Development of Bio-Inspired Distributed Pressure Sensor Arrays for Hydrodynamic Sensing Applications

by

Jeff Ernest Dusek

B.S., Florida Atlantic University (2009)
S.M., Massachusetts Institute of Technology (2011)

Submitted to the Department of Mechanical Engineering
in partial fulfillment of the requirements for the degree of

Doctor of Philosophy in Mechanical and Ocean Engineering

at the

MASSACHUSETTS INSTITUTE OF TECHNOLOGY

February 2016

Author ..... Signature redacted .....
Department of Mechanical Engineering
October 30, 2015

Certified by... Signature redacted .....
Michael Triantafyllou
William I. Koch Professor of Marine Technology
Thesis Supervisor

Accepted by ..... Signature redacted .....
Rohan Abeyaratne, Quentin Berg Professor of Mechanics
Chairman, Department Committee on Graduate Theses

Development of Bio-Inspired Distributed Pressure Sensor Arrays for Hydrodynamic Sensing Applications

by

Jeff Ernest Dusek

Submitted to the Department of Mechanical Engineering
on October 30, 2015, in partial fulfillment of the
requirements for the degree of
Doctor of Philosophy in Mechanical and Ocean Engineering

Abstract

The performance of marine vehicles is largely influenced by interactions with the flow around their hull, both self-generated and environmentally driven. To improve performance through flow control, a detailed, real-time measurement of the near-field flow is necessary, yet such sensing capability is presently unavailable. Looking to nature for inspiration, fish employ the distributed pressure and velocity sensing capability of their lateral line sensory organ to mediate navigation and control behaviors that, if replicated, could benefit engineered systems. Through a series of towing tank and field experiments, it was found that while distributed pressure measurements on marine vehicles enabled the detection of near-body flow phenomena, the size, cost, and mounting requirements of commercial sensors lead to sparse arrays and substantial gaps in the characterization of the flow field.

To address the challenges associated with obtaining spatially-dense pressure measurements on curved surfaces in marine environments, a new waterproof and conformal pressure sensor array was developed based on a closed-cell piezoresistive foam composed of carbon black-doped-silicone composite (CBPDMS foam). The response of the CBPDMS foam sensor arrays was characterized using periodic hydrodynamic pressure stimuli from vertical plunging and water waves, and a piecewise polynomial calibration was developed to describe the sensor response. The sensitivity and frequency response of the sensor arrays was also documented through a series of biologically-inspired hydrodynamic stimuli, including the flow from a dipole source, and the Kármán vortical wake flow behind a circular cylinder. The CBPDMS foam sensor arrays have significant advantages over existing commercial sensors for distributed flow reconstruction and control. They are found to have sensitivity on the order of 5 Pascal, frequency range of 0.5-35 Hertz, are contained in a waterproof and completely flexible package, and have material cost less than $10 per sensor.

Thesis Supervisor: Michael Triantafyllou
Title: William I. Koch Professor of Marine Technology

Acknowledgments

First, I would like to thank my advisor Professor Michael Triantafyllou for his advice, mentorship, and unwavering support throughout my studies at MIT. I am grateful for his encouragement to pursue my interests, both academically and recreationally, and consider myself fortunate to have gained even a portion of his vast knowledge of hydrodynamics and ocean engineering. Special thanks must be extended to Professor Jeffrey Lang for his support in the development of sensor arrays, and for answering a never-ending series of questions about electronics, research directions, and career paths. I would also like to acknowledge Professor Franz Hover and Professor Dave Barrett for lending their expertise to my thesis committee and keeping me on track with their constructive feedback.

Over the course of my time at MIT I have had the extreme pleasure to collaborate with outstanding individuals at MIT and CENSAM in Singapore. I would like to thank Frank Yaul, Mandy Woo, Jessica Herring, and Matthew D'Asaro for sharing their knowledge of CBPDMS sensor fabrication and helping in the design and fabrication of my devices. In Singapore, Ajay Kottapalli, Mohsen Asadnia, and Vignesh Subramaniam not only helped with experiments, but made me feel genuinely welcome in their country.

I can say with certainty that I would not have been able to complete my degree without the support and friendship of the members and friends of the Towing Tank group: Audrey Maertens, Haining Zheng, Vicente Fernandez, Dilip Thekkoodan, Heather Beem, James Schulmeister, Stephanie Steele, Amy Gao, Jacob Izraelevitz, Dixia Fan, Fangfang Xie, Jason Dahl, Gabriel Bousquet, Audren Cloitre, and Leah Mendelson. Not only did they provide assistance with research questions, but they became like family through multiple trips to Southeast Asia, daily group lunches, and adventures in skiing and running. I am truly grateful for their friendship.

Outside the lab, I am grateful for the staff of the MIT Sailing Pavilion and the members of the MIT Triathlon club for helping me maintain some balance in my life. I am grateful for the continuing friendship of Shmuel Link, Jenna Laurin, Brooks

Reed, Arman Rezaee, and Alexei Bylinskii, who have helped make Boston feel like home.

Finally, and most importantly, I would like to thank my family. My parents for their love, support, and encouragement in everything I have pursued. No words can express my gratitude. My brother Brad for being a role model and everyday demonstrating hard work and perseverance. To my wife Lianne, who has supported me every step of the way, thank you for always encouraging me to pursue lofty goals-without you I wouldn't be where I am today.

I would also like to acknowledge the support of NOAA's MIT SeaGrant program, The Singapore-MIT Alliance for Research and Technology (SMART), and the William I. Koch chair for making this work possible.

Contents

List of Figures

List of Tables

Chapter 1

Introduction

1.1 A Challenging Environment

Operating in the ocean environment presents a unique set of challenges to engineering systems. Marine vehicles and structures are subject to highly dynamic fluid forces, corrosive surroundings, and potentially large hydrostatic pressures amongst a multitude of physical design considerations. Along with the physical effects operating in an often times harsh environment has on vehicle design and construction, the sensory and communication capabilities of marine vehicles are defined by the surroundings. Unlike terrestrial and aerial vehicles which utilize visual feedback for local navigation and task execution, as well as radio frequency (RF) communication for receiving operating commands, and data from the global positioning system (GPS), marine vehicles often operate at a sensory deficit, especially underwater.

Unlike in air, RF signals quickly attenuate underwater, leaving underwater vehicles without a means of untethered communication with operators on the surface, or reliant on technologies like acoustic modems that often times lack the performance of radio-based communications and are subject to environmental interference. Similarly, visual feedback is severely limited in many marine applications. When operating deep underwater, vehicles are faced with a lack of natural light, forcing the use of high powered illumination, which represent a substantial drain on energy resources. Similarly, in coastal areas turbidity often impairs the use of visual systems by severely

Figure 1-1: Environmental hazards such as turbid water, strong currents, and sudden squalls, combined with large numbers of anchored vessels and heavy maritime traffic make the waters off of the East Coast of Singapore particularly challenging for marine vehicle operation.

reducing operational range. On the surface, quickly changing atmospheric conditions and the potential for large waves and spray challenge traditional communication and navigation systems.

Of particular interest for this study are the Singaporean coastal waters and the Straits of Malacca. The Straits represent the primary shipping channel between the Indian and Pacific Oceans, connecting major world economies such as Japan, China, and South Korea with India and the Middle East. Located at the tip of the Malaysian Peninsula, the strategic position of the Port of Singapore has led it to be the second busiest container port in the world according to Forbes [75]. The large volume of ships traversing the Straits and anchored off of Singapore's east coast, as seen in Figure 1-1, combined with shallow, turbid water and strong currents make these coastal waters particularly hazardous to marine vehicle operations. Additionally, the tropical climate of Singapore is conducive to the formation of strong and rapidly forming storms which bring heavy rain and greatly reduced visibility. Because of the unique environmental challenges facing marine vehicles, a need exists for additional sensory systems that allow for a better characterization of the highly dynamic surroundings, and help ensure safe and efficient operation.

1.1.1 Marine Vehicle Sensory Deficit

Overall, a significant challenge in the operation of marine vehicles off the coast of Singapore is that of a sensory deficit summed up below:

- **Can't see:**

  Turbid water and tropical squalls greatly reduce visibility.

- **Can't hear:**

  Shallow water and noise from biological and man-made sources negatively impact acoustic communication and navigation methods.

- **Difficult to communicate:**

  Seawater greatly attenuates RF signals, impairing communication with underwater vehicles.

1.2 The Role of Marine Vehicles

Despite the difficulty of operating in the marine environment, marine vehicles play a crucial role across a variety of industries and applications. In the offshore industry unmanned underwater vehicles are relied on for a variety of tasks including the identification and mapping of hydrocarbon deposits, drilling wells, construction of wellheads and blowout preventer valves, and periodic inspection of underwater structures throughout the operational life of the well [90]. Marine researchers rely on underwater vehicles, both manned and unmanned, for the collection of biological and oceanographic data crucial to gaining a better understanding of the planet's ecosystems and climate. Autonomous underwater vehicles such as the Slocum Glider are increasingly relied upon for the collection of data over geographic and temporal scales exceeding the capabilities of traditional manned research cruises [46]. Autonomous underwater vehicles equipped with forward-looking sonar systems have also been utilized for ship hull inspection, eliminating the need to put divers in harm's way and enabling hull inspection during periods of poor visibility which would restrict the

capabilities of vision-based methods [83]. While the applications of marine vehicles are diverse and wide-ranging, in the context of the Singaporean harbors and littoral zones, several specific tasks stand out.

1. Detection and sampling of harmful algal blooms

   Singapore has a strong seafood industry [43] that is dependent on the health of the coastal fisheries as well as near-shore aquaculture. Harmful algal blooms often lead to seafood kills that represent a risk to public health and the nation's economy [43, 78, 2].

2. Marine structure surveying and mapping

   There is great interest in the autonomous surveying and mapping of surface and subsurface marine structures including piers, oil platforms, and harbor structures.

3. Port security and surveillance

   As one of the busiest ports in the world, ensuring the safety and security of the Port of Singapore is a demanding task. The use of manned and unmanned marine vehicles and novel sensors to enhance and streamline port security is of great interest.

4. Data collection for environmental model development and verification

   A significant role of the Center for Environmental Sensing and Modeling (CENSAM) is the advancement of oceanographic and climate models for tropical Southeast Asia. The dynamic nature of the tropical climate creates a substantial challenge for modeling, and environmental data is needed to verify the model's performance. In general, the marine environment is highly undersampled, and utilizing unmanned marine vehicles to carry out sample collection over large spatial and temporal scales will lead to better models through improved training and verification data.

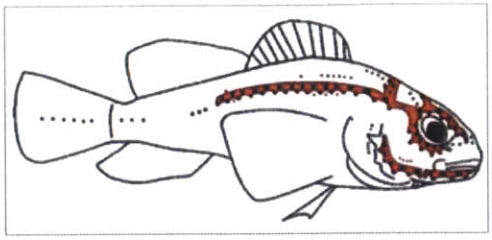

Figure 1-2: The lateral line distribution is shown for the Lake Michigan mottled sculpin. Superficial neuromasts are shown as black dots, while the extent of the canal subsystem is shown in red (adopted from [15]).

1.3 A Biological Solution: The Lateral Line

Solutions to complex engineering problems can often be found by looking to nature for inspiration. The application of biological principles to engineering systems, or biomimetics, is especially powerful when considering the marine environment which is inhospitable to humans, but contains an incredible degree of bio-diversity. The ability of fish to navigate the undersea world at high speeds and in close proximity to obstacles and other individuals is particularly attractive to ocean engineers seeking to enhance the performance of marine vehicles.

A fantastic example of a biological system overcoming a profound sensory deficit is the ability of the blind Mexican Cave Fish (*Astyanax fasciatus*) to survive in subterranean caverns devoid of light. So complete is the visual deficit in the cave environment, the fish's eyes have atrophied away, leaving the species blind. In place of sight as a primary means for detecting and avoiding obstacles, the cave fish rely on their lateral line for navigation, feeding, and other essential behaviors [82, 69, 85].

The lateral line system found in all species of fish and some amphibians is a hair-cell based mechanosensory organ comprised of two primary subsystems: superficial neuromasts and canal neuromasts, as seen in Figure 1-2. While the two subsystems share physiological elements, they provide different information to the fish about the surrounding fluid flow, allowing for a wide variety of behaviors. For an in depth review of the lateral line, the work of Coombs et al. in [16] is highly recommended.

1.3.1 Lateral Line Physiology

Descriptions of the lateral line system in fish first appeared as early as the 17th century by Stenosis, who proposed mucus production as the primary function of the organ, a view that remained largely unchanged for nearly 200 years. In the mid 19th century, the sensory nature of the lateral line was identified by German anatomist Franz Leydig based on his discovery of large and easily identifiable sense organs in the head canal of the ruffe [57] (as discussed in [16]). Around the same time, a second type of sensory organ was identified on the skin surface of fish and aquatic amphibians by Schulze [77]. These two types of sense organs are now recognized as the two distinct subsystems of the lateral line: canal neuromasts (CN) and superficial neuromasts (SN).

The main building block of the distributed lateral line system are neuromasts, small epithelial organs which are composed of both mechanosensory hair cells and non-sensory cells. Each hair cell has a bundle of cilia extending from its surface composed of a single kinocilium and several shorter stereovili that are graded in length, providing a polarity to each individual hair cell, as seen in Figure 1-3(a). When the kinocilium is deflected away from the stereocilia, an excitatory response is generated and transmitted to the brain by nerves connecting to the neuromast. When the kinocililum is deflected towards the stereocilia, an inhibitory response is produced, creating a much different signal to the brain. Within a neuromast, individual hair cells are present in opposing orientations and are spatially distributed 1-3(c); defining an axis of greatest sensitivity for the neuromast, and providing directional sensing as discussed in [16].

A single elongated cupula covers the ciliary bundles of the hair cells and provides an interface between the neuromast and the surrounding environment. The size, shape, and length of cupulas vary considerably between superficial and canal neuromasts and between species of fish, as discussed in the chapter on lateral line morphology by Coombs in [16].

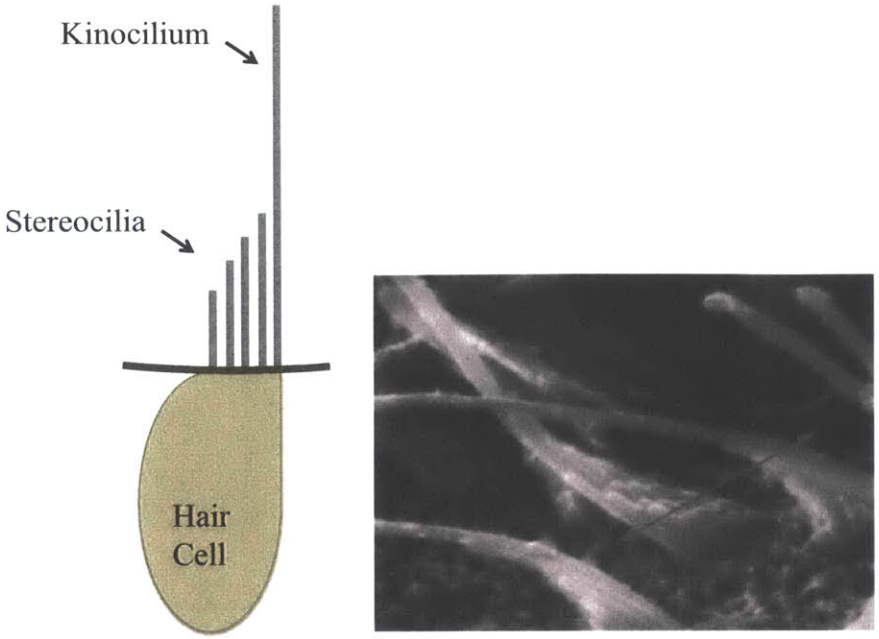

(a) Each hair cell has a bundle of cilia extending from the surface composed of a single kinocilium and several shorter stereovili that are graded in length. Each hair cell is directional depending on the orientation of the kinocilium and the graded stereovili to the flow.

(b) Scanning electron micrograph of the individual hair bundles that make up the sensory surface of the lateral line neuromast in a mottled sculpin. The single kinocilium and graded stereovili are visible, as well as the directional polarity of adjacent hair cells (from [15]).

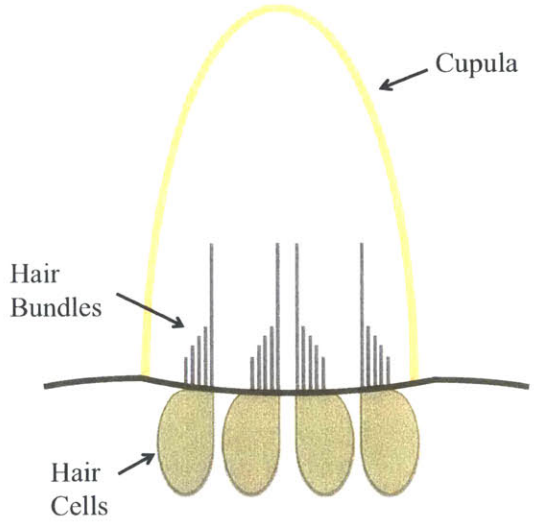

(c) Each neuromast is composed of many spatially distributed hair bundles of varying orientations contained within a single elongated cupula (orange).

Figure 1-3: Superficial and canal neuromasts are composed of many hair cells and make up the building blocks of the lateral line sensory system.

Superficial Neuromasts

Superficial neuromasts are located on the surface of the skin and are directly exposed to flow, as seen in Figure 1-4. Because the height of the superficial neuromast's cupula is generally around 50 μm tall, the superficial neuromasts reside in the boundary layer of the fish body as discussed in the chapter by McHenry and Liao in [16] and by Windsor in [85]. Superficial neuromast are generally considered as velocity sensors [7, 16], where the viscous drag of the fluid on the cupula causes deflections that stimulate the neuromast [85].

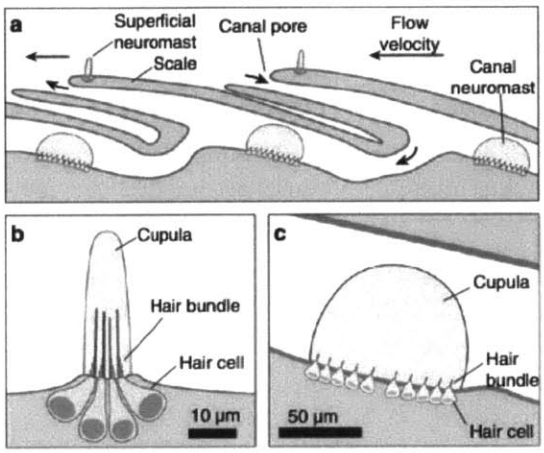

Figure 1-4: **a)** The lateral line system is composed of superficial neuromasts present on the skin of the fish and exposed to the flow field, and canal neuromasts which are present within canals beneath the skin and between pores. **b)** Superficial neuromasts are smaller than canal neuromasts and have a higher aspect ratio between base width and height. **c)** Canal neuromasts are generally the larger of the two types and slide like a rigid body along the epilthelium in the canal (from [16])

Canal Neuromasts

While the superficial neuromasts are located on the skin of the animal and are exposed to the mean flow, the canal subsystem comprises a series of canals beneath the skin, connected to the surface through an array of pores. When exposed to a pressure gradient between adjacent pores, a local flow is induced in the canal, stimulating canal neuromasts located within the canal and between the pores [85, 74]. Because

of the shape of the canals, canal neuromasts are generally hemisphere shaped and quite large, as seen in Figure 1-4. When stimulated by a local induced flow, the canal neuromasts slide like a rigid body along the epilthelium of the canal, with the motion resisted by the spring-like dynamics of the cilia bundles in the hair cells [85]. The deflection of the canal neuromasts is proportional to the velocity within the canal, which is proportional to the pressure difference between pores [85, 74]. In this way, the trunk canal subsystem acts in a similar fashion to an array of differential pressure sensors mounted on the animal's body in hydrodynamically sensitive regions [33].

Signal Filtering by the Lateral Line

The lateral line sensory system has been shown to provide a degree of 'filtering' to hydrodynamic stimulus. For the superficial neuromast subsystem, high-frequency components of the flow velocity are preferentially transmitted to the surface of the fish's body by the dynamics of the boundary layer, creating a 'high-pass' filter effect [85, 74]. Due to their location within the lateral line trunk canals, canal neuromasts are sensitive to pressure gradients between adjacent pores across a broad range of frequencies without interference from the boundary layer [85]. Because of their response in proportion to flow accelerations, CNs preferentially sense high-frequency components of the flow and have the ability to filter out direct currents. Additionally, CNs are at least an order of magnitude more sensitive than superficial neuromasts, and exhibit a degree of low-pass filtering with a cutoff frequency that is determined by the shape and size of the canal and cupula, and is generally in the hundreds of Hertz [85]. For a thorough discussion of the frequency response of the lateral line system the chapter *The Biophysics of the Fish Lateral Line* by van Netten and McHenry in [85] is highly recommended.

1.3.2 Behaviors Mediated by the Lateral Line

Throughout most of the 19th and early 20th centuries, the lateral line was viewed as an accessory to hearing, specialized for low frequency sound [16]. This view per-

sisted, despite experimental work by German ichthyologist Bruno Hofer [42] that demonstrated the ability of blind Northern Pike (*Esox lucius*) to avoid obstacles and align to water currents (rheotaxis). Hofer's work, summarized in [16], provides some of the earliest experimental evidence that the lateral line responds to flowing water, and established obstacle avoidance and rheotaxis as behaviors mediated by the lateral line system.

Evidence that the lateral line plays an important role in obstacle detection and avoidance was reinforced by Dijkgraaf [23] (described in [16]) who termed the phrase "touch-at-a-distance" to describe the function of the lateral line. This descriptor of the lateral line remains an excellent one, as the distributed nature of the lateral line sensors has more in common with touch than hearing. Following the lead of the early pioneers of lateral line research, many studies have shown the role the lateral line plays in navigation, especially in the blind cave fish [82].

Continued study has shown that the lateral line contributes to a wide range of core behaviors in fish and amphibians, including feeding, predator avoidance, and communication. In each of these cases, the lateral line is detecting the hydrodynamic fields produced by other animals, an interaction that is limited to short-ranges when compared to hearing, as described in the chapter by Bleckmann in [16]. The lateral line has also been shown to sense large-scale water flows generated by wind and gravity [16], as well as coherent flow structures generated by obstacles in the flow [58, 60]. Finally, the near-body flow sensing capabilities of the lateral line have been shown to play a role in cooperative behaviors such as spawning, parenting, and schooling [16].

Obstacle Detection and Avoidance

The blind Mexican Cave Fish provides an excellent example of the use of self-generated flows for 'hydrodynamic imaging' in low visibility environments [16, 88]. The distortion of a gliding fish's self-generated flow can be sensed by the lateral line and utilized by the animal for obstacle detection and avoidance [82, 88, 69]. Through the combined use of computational fluid dynamics (CFD) models and experimental studies utilizing particle image velocimetry (PIV) of fish swimming towards a wall [86], and

gliding parallel to a wall [87], it was found that fish could detect a wall 0.10 body lengths away, but not 0.25 body lengths away [87]. These results combined with the potential flow simulations by Hassan [39, 40], reinforce the ability of the lateral line to provide feedback for short-range object detection and avoidance.

Flow Synchronization and Alignment

The lateral line has been shown to contribute to the ability of fish to synchronize with vortex structures in a flow field in order to reduce the energy cost associated with station keeping [59, 58]. Experiments found that when placed behind a flow obstruction generating a vortex wake, trout display unique body kinematics known as the Kármán gait. Using electromyography along with a variety of visualization techniques, it was found that the trout exhibited less muscle activity when Kármán gaiting behind a D-shaped cylinder when compared to swimming in a free stream [58]. The role of vision and the lateral line during the Kármán gait behavior was studied using a pharmacologically blocked lateral line, and by performing experiments in the dark. It was found that the body kinematics of the fish Kármán gait were altered when the lateral line was impaired and the experiments were performed in the light. However, when experiments were performed in the dark, fish preferred to entrain in the suction zone behind the cylinder for both intact and impaired lateral line cases. It was concluded that vision plays a role in the preference to associate with a vortex street, but the lateral line plays a larger role in affecting body kinematics during the Kármán gait behavior [59].

The lateral line has also been found to play a role in the ability of fish to align with certain types of flows (rheotaxis). For fish in uniform flows of sufficient current to sweep them downstream, little hydrodynamic flow stimulus to the lateral line is generated, and visual stimulus is the primary source of feedback [16]. In slow moving flows insufficient to displace the fish, the lateral line is able to sense the flow relative to the body surface, enabling the fish to orient to the flow [70] (discussed in [16]). It was found that blocking the entire lateral line significantly increased the velocity threshold for rheotaxis behavior, while blocking only the canal neuromast system

had little to no effect, suggesting rheotaxis is primarily influenced by the superficial neuromast system. Further study has also suggested that the lateral line plays a role in rheotaxis in non-uniform flows [53].

Prey Detection and Predator Avoidance

The ability of surface feeding fish to localize prey trapped on the water surface by sensing concentric propagating surface waves via the lateral line was investigated by Bleckmann [6] using enucleated fish and a vibrating probe stimulus. It was found that determination of the direction of the wave source depends on the interaction of symmetrically located groups of receptors on either side of the top of the head, and that a characteristic change in the frequency spectrum of surface wave trains is the most dominant physical parameter of the stimulus relevant to localizing surface prey. Using Lake Michigan mottled sculpin, *Cottus bairdi*, Coombs found that canal neuromasts mediate the ability of fish to orient towards live pray or a vibrating sphere [17].

The impact of the difference in lateral line physiology between the ruffe, a nocturnal fish that live in turbid water, and the perch, a diurnal shallow water fish, while responding to prey was investigated by Janssen, and it was found the ruffe detected prey at a greater distance than the perch, possibly due to membranes over the lateral line canal openings inhibiting self-generated flow noise from reaching the neuromasts [45].

Just as the fish lateral line can detect the hydrodynamic signal created by prey, it can help in the detection and avoidance of predators as well. Experimental work using zebrafish larvae has shown that the accelerating flow created by a predator's strike is detected by the larvae's lateral line, allowing for an escape response that provides predator evasion during the vulnerable growing stage [68]. For a comprehensive review of prey localization on the surface and in midwater; as well as predator avoidance, the chapter by Bleckmann in [16] is recommended.

Cooperative Behaviors and Schooling

The short length scales of lateral line sensing make it an ideal candidate for enabling cooperative short range interactions between neighboring animals. The role of the lateral line in spawning synchronization, young protection, and aggression is summarized in [16]. Of particular interest for application to engineering applications is fish schooling, and the ability to navigate rapidly in close proximity to neighbors. Comparing the ability of groups of fish to shoal before and after the entire lateral line system has been suppressed with an antibiotic treatment showed the fish with impaired lateral lines were unable to maintain a shoal (note: shoaling applies to fish swimming together in an unstructured manner, whereas schooling implies synchronized and polarized swimming, although a clear dichotomy does not exist) [30].

Schooling behavior in fish is often times a response to predator threat, and the lateral line is likely involved in the transmission of threat information throughout the school. Schooling has also been shown to have hydrodynamic benefits depending on the position of an individual in the school, as investigated computationally by Maertens in [64].

1.3.3 What are the lessons of the fish lateral line?

The fish lateral line provides an excellent example of a sensory system that has evolved to overcome the challenges of survival in a marine environment. The lateral line mediates behaviors in fish that enhance performance, reduce energy expenditure, and allow for survival in harsh conditions. When considering the current state of ocean engineering systems, achieving a mere fraction of the capabilities observed in fish is highly desirable. With the goal of reducing the sensory deficit faced by marine vehicles in mind, the fish lateral provides two primary lessons that can be applied to engineering systems.

1. Fish utilize the pressure stimulus generated by **near-body hydrodynamic structures** to inform a variety of behaviors.

2. The lateral-line is an example of a **distributed** pressure and velocity sensory system.

1.4 Bringing Lateral Line Inspired Capabilities to Marine Vehicles

In order to achieve the lateral line mediated capabilities observed in fish with marine vehicles, advancements are needed in the characterization and utilization of near-body hydrodynamic pressure signals, as well as in the development of bio-inspired distributed sensor arrays. The fish lateral line and the behaviors it mediates provides an excellent motivation for the development of distributed sensor arrays, however the design requirements for arrays intended for marine vehicle use must be scaled appropriately to the hydrodynamic stimulus of interest, as shown in Table 1.1. The primary aim of this study is to answer the following questions:

1. Near-body Hydrodynamics

   (a) What are the **measurable** near-body flow structures that are **useful** for **ocean engineering applications**?

   - To answer this question, a series of towing tank and field experiments were performed using distributed arrays of commercially available pressure sensors. The results of these experiments will be presented in Chapter 2, along with a review of previous work on the impact of near-body flow structures on marine vehicle operation.

2. Distributed Pressure Sensing

   (a) What requirements should a distributed pressure sensor array fulfill for practical **ocean engineering applications** ?

   - In Chapter 3, design guidelines for distributed pressure sensor arrays intended for marine applications are formulated based on the results of previous experiments utilizing commercially available sensors.

(b) Are current sensor technologies available and sufficient ?

- Commercially available pressure sensors are evaluated for use in hydrodynamic sensing applications in Chapter 3. In particular, the size, cost, and mounting considerations of the commercial sensors used in the near-body flow sensing experiments in Chapter 2 are discussed.

(c) What sensing **principle** can be developed and demonstrated specifically for **ocean engineering applications** ?

- In Chapter 3, previous work in the development of doped-polymer 'smart-skin' pressure sensors is presented. An extension of soft-sensor fabrication techniques to marine applications, along with the development of a closed-cell foam sensing material, is introduced in Chapter 4. In Chapters 5, 6, and 7, closed-cell doped-polymer foam sensor arrays are evaluated for use on unmanned marine vehicles.

1.5 Chapter Summary

Due to the unique challenges of the maritime environment, marine vehicles face a sensory deficit compared to terrestrial and aerial vehicles. Despite limitations on the use of visual and auditory feedback systems and communication challenges underwater, unmanned marine vehicles are in high demand for applications including ship and structure inspection, port security, and scientific data collection. In nature, fish have overcome this sensory deficit by utilizing feedback from the lateral line sensory organ. Composed of two subsystems that act as distributed velocity and pressure sensor arrays respectively, the lateral line has been shown to mediate such complex behaviors as obstacle detection and avoidance, organism tracking, vortex wake synchronization, and cooperative schooling. Examples of the size scale and sensing performance of the fish lateral line system for representative applications are given in Table 1.1. With the goal of applying the lessons from nature to engineering systems, the subsequent chapters previewed below will investigate the use of distributed arrays of commercial

pressure sensors on marine vehicle hulls, and describe the development and characterization of a closed-cell foam composite pressure sensor array for marine applications.

1.6 Chapter Previews

Chapter 2: Near-Body Hydrodynamics Chapter 2 discusses the performance impacts of near-body flow structures on marine vehicles, and the need to sense and characterize these flow structures. Previous studies of the use of pressure sensing to characterize near body flow structures are discussed, and experiments conducted by the author using an instrumented model sailboat hull and instrumented hydrofoil are introduced. An experimental study of near-body flow sensing on an unmanned kayak vehicle using commercially available and experimental MEMS pressure sensor arrays is discussed in detail. Results of the laboratory and field experiments using commercial pressure sensors will provide size, dynamic range, and sensitivity guidelines for the development of distributed hydrodynamic pressure sensor arrays.

Chapter 3: Distributed Pressure Sensor Arrays In chapter 3, guidelines for the design and fabrication of distributed pressure sensor arrays for use in hydrodynamic sensing applications are outlined. The guidelines are based on experience gained from previous experiments with commercially available sensors, which are reviewed in the context of marine vehicle applications. Prior work in the development of pressure sensor arrays inspired by the fish lateral line is summarized, and the development of doped polymer 'smart-skin' pressure sensor arrays is introduced. The author's collaborative involvement in early stage 'soft-skin' sensor development and testing is discussed, and recommendations for next generation 'soft-skin' arrays are made.

Chapter 4: Closed-Cell CBPDMS Foam Development Chapter 4 presents the extension of the soft-sensor fabrication techniques and materials introduced in Chapter 3 to marine vehicle applications. The expansion of 'smart-skin' pressure

sensor arrays to marine vehicles is provided by the development of an innovative waterproof and flexible closed-cell carbon black-silicone foam piezoresistive composite. The piezoresistive behavior of the material is discussed, and the fabrication of a 4 x 1 pressure sensor array is outlined.

Chapter 5: CBPDMS Foam Sensor Array Characterization Chapter 5 describes characterization experiments conducted on the CBPDMS foam sensor arrays using oscillatory pressure stimuli from vertical plunging and water waves. The repeatability of the sensor arrays is discussed, and a piecewise polynomial calibration is generated for the sensor array's response to hydrodynamic stimulus.

Chapter 6: Dipole Experiments Chapter 6 introduces the use of an oscillating sphere as a biologically inspired pressure stimulus for testing the frequency range of the CBPDMS foam sensor array. A potential flow model of the pressure field generated by the oscillating sphere is presented for the sphere vibrating perpendicular to the CBPDMS foam sensor array, and in the vicinity of the sensor array and testing tank bottom. The frequency range of the CBPDMS foam sensor array is discussed, and the minimum RMS pressure for successful frequency identification is explored.

Chapter 7: Kármán Vortex Street Identification Chapter 7 discusses the sensing of a Kármán vortex street by the CBPMDS foam sensor array. The biological relevance of vortex sensing and the fish Kármán gait behavior is introduced, and measurements of vortex shedding frequency and pressure magnitude from the foam sensor array are compared to measurements from an array of commercial pressure sensors and measurements of the foil lift force.

Chapter 8: Conclusions Chapter 8 summarizes the need for distributed pressure sensing for near-field flow measurement, and reviews the principle contributions of the thesis. Based on the results of the current study, recommendations for future work are made and discussed.

Application Scale	Example unsteady flow	Sensor spacing	Dynamic pressure [Pa]	Frequency range [Hz]
Fish lateral line	Energy extraction from vortices [60]	$\sim$ 1-3 mm (Trout)	10-30	2-5
Fish lateral line	Prey tracking [15]	$\sim$ 2 mm (Mottled Sculpin)	0-15	30-100
Unmanned marine vehicles	Free vortex tracking [33]	$<$ 6 cm	20-100	0.5-2
Unmanned marine vehicles	Leading edge vortex shedding [27]	$<$ 4 cm	40-200	0.25-3
Unmanned marine vehicles	Separation from model sailboat hull (L= 1 m, Fr= 0.16, u= 0.5 m/s) [31]	$\sim$ 5 cm	10-100	$<$ 1 Hz
Proposed ship-scale marine application	Separation during surface vehicle maneuvering (L= 30 m, Fr= 0.16 m, u= 3 m/s)	$\sim$ 1.5 m	400 - 4000	$<$ 1 Hz

Table 1.1: The size and performance requirements for lateral line inspired hydrodynamic sensor arrays are dependent on the scale of the vehicle or unsteady flow of interest. In nature, the fish lateral line canal subsystem (highlighted in red) has pore spacing on the order of millimeters, and the dynamic pressure stimuli discussed in Section 1.3.2 are typically on the order of tens of pascals. In Chapter 2, examples of unsteady flows characteristic of unmanned marine vehicles on the scale of $\sim$1-3 m (in grey) will be discussed in detail, and will serve as the foundation of design guidelines for hydrodynamic pressure sensor arrays that will be presented in Section 3.1. Proposed sensor array characteristics for a ship-scale application based on Froude scaling are also given for comparison (highlighted in green).

Chapter 2

Near-Body Hydrodynamics

The interaction of marine vehicles with near-body flow structures has consequences for navigation in currents and cluttered environments, and for performance during maneuvers or while operating in dynamic flow conditions. Near-body flow structures can be self-generated as in the case of a helical vortex being shed from a vessel's keel line [31], or environmentally driven, as in the case of a vortex street shed behind an obstruction, or the vortex wake generated by a swimming fish. Examples of both types of interactions are present in nature and are exploited by fish, as described in Section 1.3.2. In particular, the ability of fish to identify obstacles and navigate in a cluttered environment is an excellent example of utilizing the impact on self-generated flow noise by nearby obstacles. Similarly, the ability of fish to exploit vortex wakes to reduce the energy cost of station keeping demonstrates the utility of measuring and utilizing coherent structures already present in the flow field.

In this chapter, previous work in near-body flow sensing will be reviewed, including previous studies by members of the towing tank group at MIT. Additionally, two experimental programs conducted by the author will be discussed. A brief summary of the experimental study of leading edge vortex shedding conducted in [27] will be offered, as well as a more comprehensive discussion of the experimental investigation of near-body flow sensing on an unmanned kayak conducted in Singapore and published in [26].

2.1 Prior Work in Near-Body Flow Sensing

Several studies have explored the use of pressure sensors to characterize near-body flow structures. Fish-shaped robots equipped with arrays of commercially available pressure sensors to mimic the lateral line sensory organ were used to investigate the pressure features around a fish during different swimming gaits by Liu et al. [61]. Similarly, biomimetic robots equipped with pressure sensors were used to mimic the ability of fish to station keep in steady streams and exploit the vortical structures behind obstacles in the flow field [1, 11]. Rheotactic and station keeping behaviors were demonstrated by DeVries et al. using a streamlined foil equipped with ionic polymer metal composite (IPMC) artificial superficial neuromasts for flow velocity sensing, and pressure sensors to represent the canal subsystem [22].

In an effort to accomplish the task of obstacle detection and avoidance using a small underwater vehicle named "Snookie," Franosch et al. developed flow velocity sensors based on hot-thermistor anemometry. The thermistors were covered with individual canals, as seen in Figure 2-1, and the sensors were shown to have a power law relationship between flow velocity and energy dissipation [34].

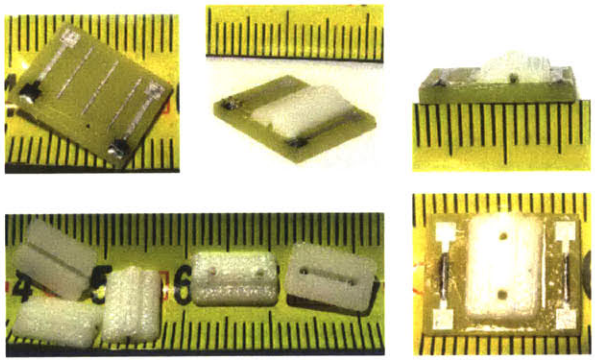

Figure 2-1: Thermistor sensors covered by a canal were used by Franosch et al. for lateral line inspired sensing on an underwater vehicle (from [34]).

Fernandez et al. investigated the use of pressure sensor arrays to passively aid in navigation and object identification [32]. Using a streamlined body instrumented with an array of seven commercially available pressure sensors, it was shown that the position and velocity of a cylinder translating near the body could be identified.

Additionally, it was shown that a differentiation could be made between a circular and square cylinder using data from a single pass of the cylinder after performing a principal component analysis on a set of training data. Expanding on the capability to identify objects, it was shown that the location and cross sectional shape of a stationary cylinder could be found using the pressure field generated by a translating instrumented hydrofoil.

The use of pressure sensor arrays on marine vehicles was further investigated in the context of optimizing vehicle performance and maneuverability [31]. The strength and position of a free vortex pair translating near a streamlined body was estimated using sparse pressure sensor measurements and a potential flow model with an extended Kalman filter. Leading edge vortex shedding was identified on an instrumented hydrofoil translating at large angles of attack, and an array of pressure sensors mounted inside a model sailboat hull was used to identify helical vortex shedding from the keel line.

Experiments with an instrumented model sailboat hull of length L=1 m discussed in [31] were conducted by the author in the MIT towing tank. An array of 10 Honeywell 19C015PG4K pressure sensors were connected to taps along the length of the model's hull 2.54 cm below the waterline via plastic tubes, as seen in Figure 2-2(a). The model was towed at 0.5 m/s at angles of attack ranging from 0 to 35 degrees with respect to the towing direction, as seen in Figure 2-2(b). At low angles of attack between 0 and 10 degrees, the experimentally measured pressure decreased along the length of the bow-mounted pressure sensors from x/L=0.05 to 0.11. At angles of attack greater than 15 degrees the trend reversed, with the pressure increasing from x/L=0.05 to 0.11. The pressure gradient indicated accelerating fluid in the bow portion at low angles, and decelerating or re-circulating fluid at high angles. It was clear that the pressure along the sailboat hull peaked at high angles in the un-instrumented midship region of the vehicle from x/L of 0.11 and 0.5. Although the precise location of this peak was not captured in the experiment due to the limited distribution of discrete pressure taps, its presence suggested vortex separation was occurring at the sharp bow and possibly also at the keel line, which was supported by the dye visu-

alization in Figure 2-5. Additionally, the pressure at the bow-most tap exhibited a consistent decreasing trend with increasing angle of attack. This information could therefore be used to accurately estimate the hull's angle of attack, demonstrating that surface pressure measurements provide useful insight to the nature of the flow field past the hull. The results of the model sailboat hull experiments, summarized in Table 2.1, were also used to inform design guidelines for continued sensor array development, as presented in Section 3.1.

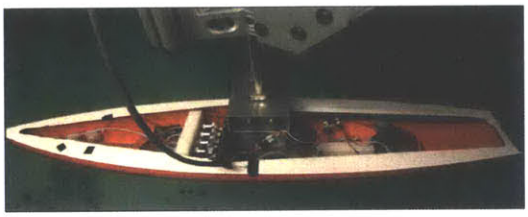

(a) A model sailboat hull was instrumented with an array of 10 Honeywell 19 mm pressure sensors connected to taps on the low pressure side of the hull using plastic tubes. The sailboat hull was attached to the towing carriage in the MIT Towing Tank and the angle of attack relative to the towing direction was varied from 0 to 35 degrees.

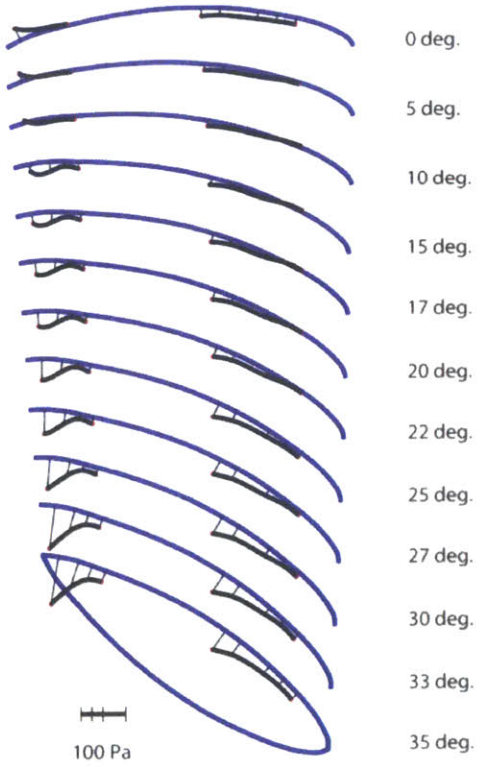

(b) The pressure distribution on the sailboat hull's surface was found to vary with the angle of attack, allowing for the estimation of towing angle (from [31]).

Figure 2-2: Study of distributed pressure sensing on a towed surface vehicle.

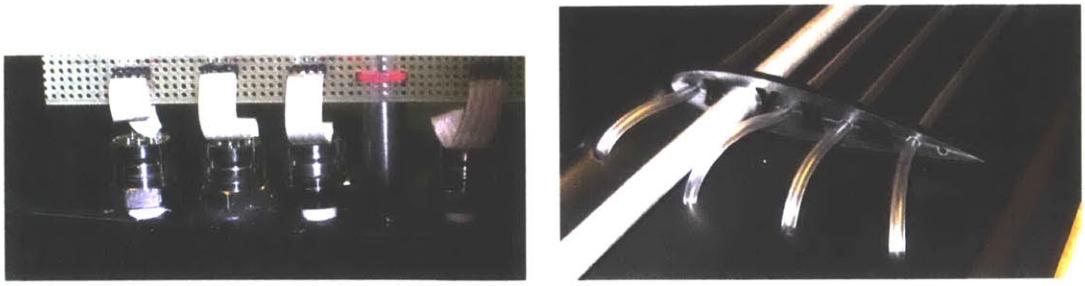

(a) Honeywell 19mm pressure sensors were used the study LEV shedding on a single element hydrofoil. Because of sensor size limitations, the array on the foil was limited to four sensors (from [27]).

(b) To transmit pressure from the foil surface to the sensors mounted on top of the foil, tubing was embedded within the urethane foil during the casting process (from [27]).

Figure 2-3: An instrumented hydrofoil was used to study the pressure distribution due to LEV shedding.

2.2 Detection of Leading Edge Vortex Shedding

An experimental study of leading edge vortex (LEV) detection using on-body pressure sensors was conducted by the author to investigate the utility of distributed pressure sensing arrays for ocean engineering applications [27]. An array of four commercially available pressure sensors (Honeywell 19mm type) were mounted on top of a rigid urethane hydrofoil as seen in Figure 2-3(a). Due to the size of the foil being constrained by experimental facilities, the thickness of the foil did not allow the pressure sensor to be mounted internally, and tubes were instead embedded within the foil connecting the sensors to the foil's surface, as seen in Figure 2-3(b).

Experiments were conducted with the foil undergoing steady translations at various angles of attack as well as sinusoidal 'flapping' motions over a range of heave and pitch parameters. Of great interest during the study was the formation and shedding of a strong LEV during the acceleration phase of the foil motion. It was found that the presence and location of the LEV was readily identifiable using surface pressure measurements at discrete locations along the foil chord. Using particle image velocimetry (PIV) techniques, the location of the LEV was determined and correlated with pressure measurements, as seen in Figure 2-4. Additionally, force measurements were used to measure the performance impact of the shed vortex in the near-body flow field.

The study of LEV detection using on-body pressure sensing demonstrated the ability to detect a near-body flow structure that has a significant impact on the foil's performance. The range of dynamic pressure signals measured during the LEV experiments, the frequency of vortex shedding, and analysis of the sensor spacing on the foil's surface all provided valuable contributions to the development of design guidelines for distributed pressure sensor arrays, as seen in Table 2.1. The study of LEV shedding was conducted in the context of optimizing performance during flapping foil energy extraction, but the lessons were applicable to a variety of marine vehicles and structures, and motivated continued investigation of near-body flow structures.

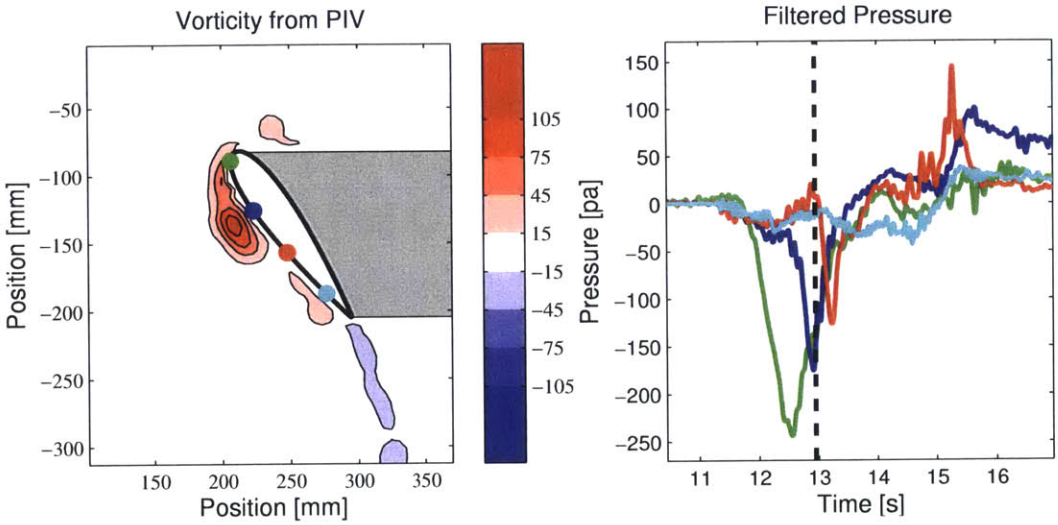

Figure 2-4: The left frame is a plot of the near-body vorticity field of a foil at 35° angle of attack and translating at 0.3 m/s. Red is counter-clockwise vorticity, and a shed LEV is clearly visible adjacent to the second pressure tap denoted by the blue colored circle. The right frame is a time trace of pressure at the four discrete taps for the entire run. The colors of the pressure traces correspond to the colored circles denoting pressure tap location. The vertical line denotes the time corresponding to the frame at left, and a characteristic drop in pressure consistent with the presence of a vortex is clearly observed in the second pressure trace shown in blue.

2.3 Near-Body Hydrodynamics of an Unmanned Kayak

The utility of near-body flow sensing on a surface vehicle was investigated experimentally by the author in collaboration with members of the towing tank group at MIT, and CENSAM researchers in Singapore [26]. The primary experimental platform for the study was an unmanned surface vehicle adapted from a rotomoulded kayak, as described in Section 2.3.3. The kayak vehicle was equipped with an array of commercially available pressure sensors, described in Section 2.3.4, as well as three experimental pressure sensor arrays inspired by the fish lateral line. Two of the experimental arrays, described in Section 2.3.2, were fabricated using silicon piezoresistive sensor dies on a flexible substrate by CENSAM researchers Ajay Kottapalli and Mohsen Asadnia. The third experimental sensor array, described in Section 2.3.2, was fabricated by MIT researcher Mandy Woo using doped silicone, and is described further in the context of continued 'smart-skin' sensor development in Section 3.4.

The author was the lead investigator for the study of the unmanned kayak vehicle, integrating the commercial and experimental pressure sensors onto the vehicle and managing the data collection hardware and software. The author also lead the analysis efforts for the data collected experimentally both in swimming pool and reservoir environments.

2.3.1 Introduction to Pressure Sensing on an Unmanned kayak

Pressure sensing on hulls

For a vehicle operating in a marine environment, enhanced situational awareness has numerous benefits to control, navigation, and performance. Marine environments are highly dynamic, and vehicle motions are impacted by waves, wind, currents, and a wide variety of surface and submerged obstructions. In order to accurately control a marine vehicle, the vehicle dynamics must be well measured in real time. While these measurements are typically accomplished using inertial motion units (IMU), or

digital compasses with built-in gyroscopes, hull mounted pressure sensor arrays offer an alternative method for measuring vehicle motions.

Experiments using a hydrofoil constructed with pressure taps on the foil surface indicated that the shape and location of stationary obstruction can be detected using pressure sensor feedback alone [33, 65]. While existing sensor technology greatly limited the distance at which an obstruction could be detected, the experiments demonstrated the potential for increasing environmental awareness by marine vehicles using a passive detection technique. Such a passive technique could be of great benefit for operation in noisy, cluttered environments, or where visual navigation is impaired due to a lack of light or poor water clarity. Passive methods for improving vehicle awareness are also attractive for missions where stealth and quiet operation is desirable.

The detection of strong vortex structures shed by a vehicle during maneuvering could be utilized to either increase vehicle maneuverability, or decrease the drag associated with rapid maneuvers [31]. During maneuvering, streamlined bodies take on a large angle of attack relative to the mean flow, resulting in a cross sectional profile that is no longer streamlined, but similar to a bluff body. Because of this change in profile, helical vortices are shed from the vehicle, resulting in strong regions of low pressure near the body, as seen in figure 2-5.

The presence of helical vortices, and their subsequent low pressure regions, near a body result in a large additional drag force on the vehicle during maneuvers. For a survey vehicle conducting a "lawnmower" search pattern, the additional drag at each maneuver can add up quickly, resulting in a reduced mission length. For an autonomous vehicle, battery life and mission endurance are the driving factors for cost, and the amount of usable data collected. If vehicle drag can be reduced through the use of active sensing and control through maneuvers, the benefit to ocean data collection would be significant [31].

Figure 2-5: When towed at an angle of attack, even well streamlined hull shapes, such as a model sailboat hull, present a bluff cross section to the incoming flow field. This drastic change in cross section results in the shedding of strong helical vortices from the hull's keel line. These helical vortices were visualized in the MIT Towing Tank by injecting fluorescent dye into the flow field at the keel line, near the bow of a sailboat hull. The dye could be clearly seen curling into a helical vortex that grew in diameter towards the stern of the model, and began to break apart due to the effects of viscosity.

MEMS Pressure Sensor Array Requirements for Hydrodynamic Sensing

While previous experimental works within the MEMS pressure sensor group [33, 31, 65, 27] used commercial off the shelf (COTF) pressure sensors, these sensors do not meet all of the requirements of the MEMS pressure sensor arrays currently under development. Of primary importance in the development of the MEMS pressure sensor arrays was to create a flexible and waterproof sensor array that could be surface mounted to a curved body, such as the hull of an underwater or surface vehicle. Additionally, it was desired to fabricate arrays of sensors that will ultimately mimic full body-length coverage of the fish lateral line [33].

The experiments conducted by Fernandez [33, 31], Dusek [27], and Maertens [65], utilized Honeywell 19mm series pressure sensors for measuring surface pressure. The Honeywell sensors were found to have excellent robustness and sensitivity, but their large size (30mm height, 19mm diameter), and lack of waterproofing made surface mounting the sensors impossible. Instead, the sensors required mounting inside a waterproof housing [33, 31], or mounting above the water surface, with pressure transmission tubes needed to transmit signals from the body surface to the sensors [27, 65]. In both cases, the size and lack of waterproofing of the sensors placed limitations on both the number of sensors that could be mounted on a body, and the size and shape

of the experimental setup. In addition, the use of pressure transmission tubes introduced an undesirable added degree of uncertainty to pressure measurements due to the dynamics of the air-water interface within the tubes.

Based on experience gained from these previous experimental studies, particular emphasis was placed on optimizing the flexibility and waterproofing of the MEMS pressure sensor arrays. Ultimately, it is desired to produce sensor arrays with sufficient flexibility, waterproofing, and robustness to allow for surface mounting on a wide variety of surfaces without the need for altering the sensing body in any permanent way. To achieve this goal, innovative, flexible, material sets were chosen for the fabrication of the MEMS sensor arrays.

2.3.2 Experimental Pressure Sensor Arrays Used on Unmanned Kayak Vehicle

Within the MEMS pressure sensor group at the Center for Environmental Sensing and Modeling (CENSAM), several sensor technologies are currently under development. During January of 2012, three experimental sensor types were tested both in the CENSAM testing tank, and on an autonomous surface vehicle (ASV) at the Pandan Reservoir in Singapore. While the three sensors were based on different technologies, all three were flexible, waterproof, and able to be surface mounted on the vehicle. Two of the sensor arrays were developed around a silicon pizeoresistive sensor die, discussed in section 2.3.2, and their individual packaging schemes will be discussed in sections 2.3.2 and 2.3.2. The field testing results for the two packaging schemes will be discussed together in section 2.3.5. The third sensor array was developed using an innovative conductive polymer material set, and will be discussed in section 2.3.2. While much work remains to further optimize each sensor, initial trials beyond the laboratory environment showed great promise.

Silicon Piezoresistive Sensors

Pressure Sensor Dies

For the two pressure sensor arrays developed at the Nanyang Technological University (NTU) in Singapore, commercially available pressure sensor dies were implemented using two different packaging schemes to create flexible and waterproof sensor arrays. Piezoresistive-based absolute silicon micro-machined pressure sensor dies (Model MS7201-A2 from Measurement Specialties Inc) were chosen as suitable for deployment in harsh environments due to the construction of the pressure port from glass and silicon that is stable in most chemicals. Applied pressure was converted into electrical signal by the implanted piezoresistors in the silicon membrane, with packaging needed to provide the sensor die power and transport the output signal off-array. Other features included 0 to 100 kPa range, output span of 110mV at 5V supply voltage, temperature range from -40° to 150° C, small die size (1.35 x 1.79 mm^2), affordability, and high reliability.

Underwater Packaging Scheme

A liquid crystal polymer (LCP) substrate was used, on which Chromium (Cr)/Gold (Au) electrical circuits were sputtered so that electrical connection via wires could be established with the bonded pressure sensor dies. Advantages of the LCP substrate included extremely low moisture absorption, superior hermetic sealing, and excellent chemical resistance. Thus, the substrate was able to maintain stable electrical, mechanical, and dimensional properties in wet, humid environments [52]. The most flexible method to process LCP is micro-machining techniques, as it is compatible with most photoresist. As a result, standard IC fabrication processes, such as photolithography, etching, and metallization, can be utilized to process the LCP substrate. As a complement to the LCP substrate, a flexible printed circuit board (PCB) substrate was also implemented to attach the sensor dies. For waterproofing and sealing purposes, polydimethylsiloxane (PDMS) (or silicone rubber) was dispensed over the LCP and flexible PCB substrates. These LCP/PDMS and flexible PCB/PDMS

combinations resulted in flexible pressure sensor arrays that could be easily deployed on the streamlined bodies of marine vehicles.

Fabrication

LCP/PDMS Packaging Scheme

For the LCP/PDMS packaging scheme, the processing of two LCP substrates was involved: (1) sensor and (2) base. For the sensor substrate, the fabrication process consisted of five steps. First, a square copper (Cu) feature (2 mm by 2 mm) was patterned on the LCP substrate by photolithography and Cu etching. Subsequently, this Cu pattern defined the location of a mechanically drilled through-hole (diameter 1.2 mm) in the substrate. Second, a metallic layer of Cr (30nm)/Au (700 nm) was sputtered onto the LCP substrate to form the electrical circuits for the sensor dies. Third, a through-hole was drilled through the LCP substrate via the Cu pattern so that the sensors backside pressure port could be accessed by water. After that, any residual Cu pattern around the through-hole was etched away. In the fourth step, after cutting out the individual sensor substrates, the sensor die was bonded to the LCP substrate using adhesive with the alignment performed under a microscope. Finally, the sensor die was wire-bonded to the Cr/Au electrode pads using Au wires. For additional mechanical protection, the entire sensor die, together with the bonded wires, was encapsulated in silicone gel. These fabrication steps resulted in a sensor module ready to be placed on the LCP base substrate during the assembly process.

For the base substrate, the fabrication process consisted of three steps, which were similar to those of the sensor substrate. For the assembly of the sensor modules to the base substrate, four steps were involved. First, the sensor modules were bonded to the LCP base substrate using adhesive with the alignment performed under a microscope. Second, individual wires and ribbon cable wires were hand-soldered on the sensor modules and the base substrate to complete the electrical circuits. Where necessary, Ag conductive epoxy was used in addition to solder to enhance the durability of the electrical connections. Third, after securing the LCP base substrate (with assembled

sensor modules) to a container, PDMS was dispensed over the whole assembly and subsequently allowed to cure under room temperature. Figure 2-6 illustrates the fabricated pressure sensor array.

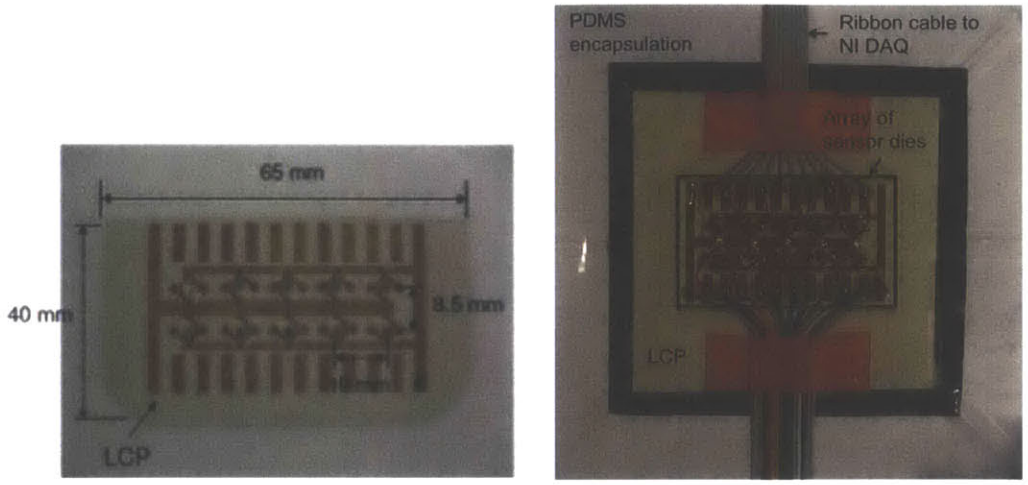

(a) A completed LCP sensor array before encapsulation

(b) The backside of an encapsulated LCP array

Figure 2-6: Fabricated pressure sensor array (2 x 5) with the LCP/PDMS packaging scheme. Size: 65 mm x 40 mm and sensor pitch: 10 mm (x-direction) and 8.5 mm (y-direction).

Flexible PCB/PDMS Packaging Scheme

For the flexible PCB/PDMS packaging scheme, the fabrication process consisted of similar steps to the LCP/PDMS array. First, the sensor die was bonded to the flexible PCB substrate using adhesive with the alignment performed under a microscope. Second, the sensor die was wire-bonded to the Au electrode pads using Au wires. For additional mechanical protection, the entire sensor array was encapsulated with silicone gel. Third, ribbon cable wires were hand-soldered on the flexible PCB substrate to complete the electrical circuits. In the fourth step, after securing the flexible PCB substrate to a container, PDMS was dispensed over the sensor array and subsequently allowed to cure under room temperature. Figure 2-7 illustrates the fabricated pressure sensor array.

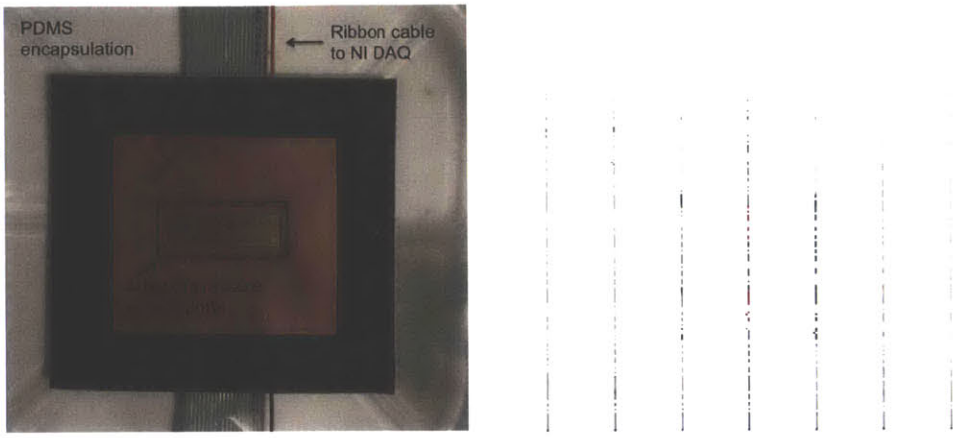

(a) The backside of an encapsulated PCB sensor array.

(b) The frontside of an encapsulated PCB sensor array

Figure 2-7: Fabricated pressure sensor array (2 x 10) with the Flexible PCB/PDMS packaging scheme. Size: 40 mm x 20 mm and sensor pitch: 3 mm (x-direction) and 5.5 mm (y-direction).

Hydrostatic Calibration

Prior to deployment of the experimental pressure sensors on a streamlined body, hydrostatic calibration was performed in the laboratory. The piezoresistive sensor dies used in both the LCP and flexible PCB packaging schemes operated on the principle of the Wheatstone bridge, and a 5V input voltage was used during calibration with the sensor output voltage recorded using a National Instruments Data Acquisition Board (Model USB-6281) and Labview software. Hydrostatic calibration was performed by placing the sensor arrays at known depths in the CENSAM testing tank, and acquiring the output signal over a 60 second period. Both sensors performed as expected, producing a linear relationship between pressure and output voltage with negligible hysteresis, as seen in figures 2-8(b) and 2-9(b).

LCP/PDMS Packaging Scheme

Figure 2-8 illustrates the voltage data acquired by the DAQ system in the time domain during the multi-step hydrostatic calibration of the LCP/PDMS sensor. The left half of the plots shows the stepwise increase in the hydrostatic pressure when the sensor array was lowered into the water tank while the right half shows the stepwise

decrease in pressure when the sensor array was raised upwards. From figure 2-8, a sensor calibration plot could be obtained as shown in figure 2-8(b). As illustrated, the average sensor sensitivity is about 0.99 μV/Pa with a 5V supply voltage. During testing, it was found that sensor channels 5 and 7 produced unreliable results due to an air bubble forming at the access hole to the sensor die, preventing water from reaching the sensing membrane. The formation of this bubble was likely due to the presence of protruding edges of LCP in the access hole, created during the manual drilling of the LCP substrate. Although deep reactive ion etching recipes were developed that could etch LCP, the etch rate was found to be too low, and etching of the mask layer was experienced in some cases. Because the pressure die access holes were large enough for manual drilling, this technique was employed with generally favorable results.

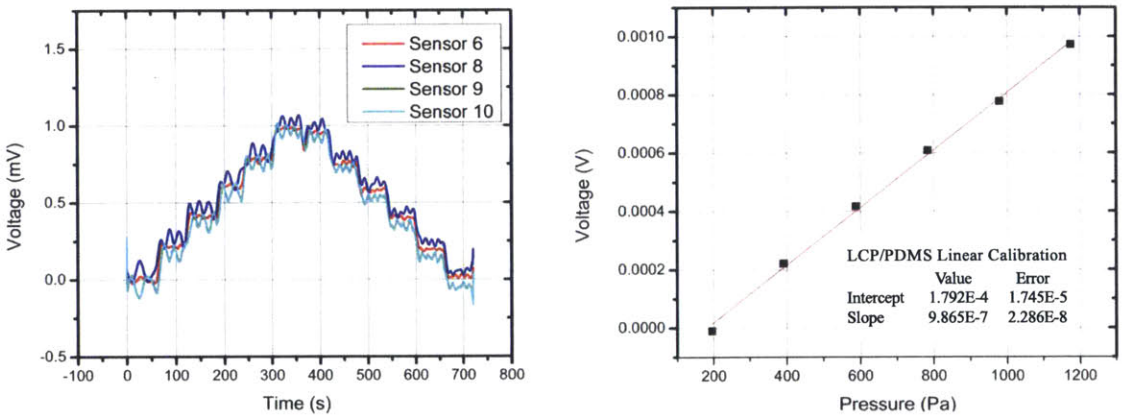

(a) Example calibration for the bottom row of the LCP sensor array.

(b) Sensor calibration plot for the LCP/PDMS packaging scheme with an average sensitivity of 0.99 μV/Pa with a 5V supply voltage.

Figure 2-8: Multi-step hydrostatic calibration results for the LCP/PDMS packaging scheme fabricated by CENSAM collaborators A. Kottapalli and M. Asadnia. During testing, array channels 5 and 7 were not operational due to the pressure access hole on the backside of the sensor being blocked by protruding edges of LCP substrate created during the manual drilling of the access holes. A discussion of the signal noise can be found in section 2.3.5

Flexible PCB/PDMS Packaging Scheme

Figure 2-9(a) illustrates the voltage data acquired by the DAQ system in the time domain during the multi-step hydrostatic calibration of the flexible PCB/PDMS sen-

sor. The plot shows the stepwise decrease in the hydrostatic pressure when the sensor array was raised upwards in the water tank. From figure 2-9(a), a sensor calibration plot could be obtained as shown in Figure 2-9(b). As illustrated, the average sensor sensitivity is about 0.92 μV/Pa with a 5V supply voltage.

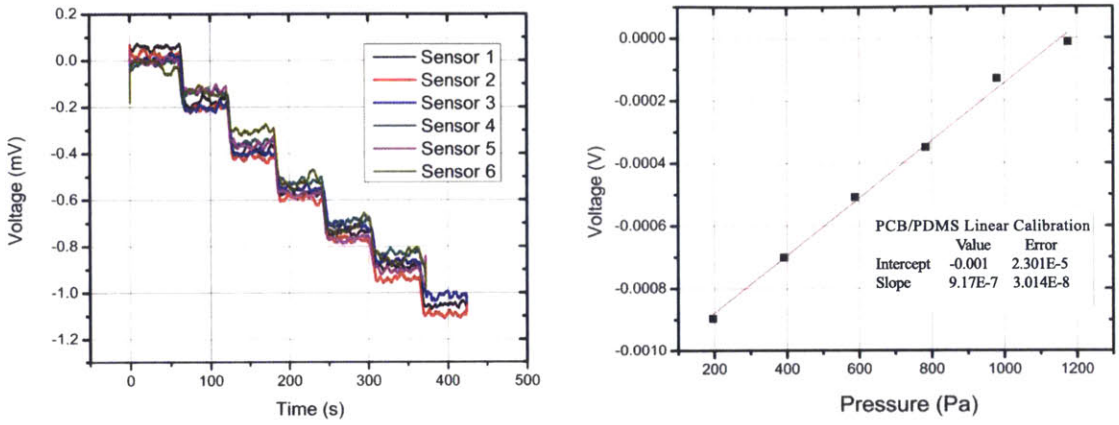

(a) Multi-step hydrostatic calibration results for the flexible PCB/PDMS packaging scheme. Only 6 channels are shown due to limitations in data acquisition. The operation and calibration of the remaining channels were independently verified.

(b) Sensor calibration plot for the flexible PCB/PDMS packaging scheme with an average sensitivity of 0.92 μV/Pa with a 5V supply voltage.

Figure 2-9: Multi-step hydrostatic calibration results for the flexible PDMS packaging scheme fabricated by CENSAM collaborators A. Kottapalli and M. Asadnia.

Hydrostatic Calibration Analysis

Although both the LCP/PDMS and PCB/PDMS packaging schemes employed the same commercially available piezoresistive sensor dies from Measurement Specialties, the sensitivity of the two sensor arrays was found to differ by approximately 7%. The difference in measured sensitivity can primarily be attributed to two reasons. The first reason was experimental errors when performing the multi-step hydrostatic calibration in the CENSAM testing tank. Although great care was taken in placing the two sensor arrays at the same depth, small errors in the measured versus actual depth of submersion could lead to differences in the measured sensitivity. Differences in array sensitivity could also be attributed to stresses generated on the piezoresistive sensor dies as the PDMS cured. The thickness of the PDMS encapsulation on the

two sensor arrays was not identical, creating the potential for different stresses on the sensor dies as the PDMS dried.

Conductive Polymer Pressure Sensor

The third pressure sensor array deployed on the ASV was developed at the Massachusetts Institute of Technology (MIT), and fabricated entirely from a polymer. Unlike the silicon piezoresistive pressure sensors that employed rigid dies on a flexible backing, the polymer-based sensor was completely flexible. The active part of each sensor cell in the array was a strain-concentrating diaphragm molded from polydimethylsiloxane (PDMS), on which a piezoresistive strain gauge was patterned ([94],[95]), as seen in figure 2-10. A pressure difference across the diaphragm caused it to deflect, and this deflection was transduced by the strain gauge. PDMS was chosen as the sensor material because its favorable chemical resistance and waterproofing characteristics are desirable for long term underwater usage. Additionally, its flexibility allows the sensor array to be compatible with the streamlined bodies of underwater vehicles, making it amenable to wide-area fabrication and deployment. The strain gauge was made of PDMS doped with carbon black. This composite was chosen because it is inexpensive, compatible with the main body of the sensor array, highly piezoresistive ([94],[95]), and because it provides for repeatable operation.

Figure 2-10(b) shows the fabrication flow. Initially, PDMS was poured into two different molds and cured for 15 minutes at 120°C. The top substrate comprised four square strain-concentrating PDMS diaphragms, as seen in figure 2-11(a), connected to a common plenum; hence each sensor array had four pressure sensors. After removing the cured PDMS substrates from the molds, the piezoresistive carbon-black-PDMS composite (composition of 1:6 in weight) was screen-patterned onto the bottom substrate ([94],[95]). After inserting copper wires into the grooves on that substrate to make strain-gauge connections, the whole assembly was cured for 20 additional minutes at 120°C. Finally, a Tygon tube was inserted into the common plenum before the top and bottom substrates were bonded together for waterproofing. The fabrication process was straightforward, with an approximate fabrication time of 3 hours and a

material cost of less than $3 per sensor array (Dow Corning).

All sensors were connected to a common plenum used to equilibrate the array against large pressure fluctuations due to hydrostatic variations. Equilibration was actuated through the Tygon tube. Before conducting underwater tests, a known positive bias pressure was applied to the plenum causing the sensor array to bulge slightly outward. This pressure biased the strain gauges into their most sensitive regions. In response to a pressure difference between the plenum and the external environment near a diaphragm, the diaphragm would deflect, and this deflection was transduced by its piezoresistive strain gauge. The center-edge of the diaphragm experiences the maximum strain during diaphragm deflection, and was thus chosen for the strain gauge location. All four strain gauges in an array were connected in series and driven with a common current. The output from each strain gauge was the voltage measured across it. A Kelvin-probe structure, seen in figure 2-11(b), was used to measure these voltages without the influence of contact resistance. Upon calibration, the measured voltage was readily converted to the deflecting pressure difference.

To demonstrate the capabilities of the polymer-based pressure sensor array, one array was mounted on the hull of a kayak, and its pressure signals were recorded during kayak maneuvers in the Pandan Reservoir. For reference, the kayak hull was also instrumented with commercial pressure sensors at nearby locations. Because the commercial and experimental pressure sensor were not exactly co-located due to mounting considerations, some variation in the measured pressure is expected between the sensors. This experimental setup is discussed further in section 2.3.3. Figure 2-12 shows two pressure signals recorded during one kayak maneuver. The pressure measured by a commercial sensor is shown in blue, and that measured by a polymer-based sensor is shown in green. During the kayak experiments, the polymer-based sensor demonstrated a sensitivity of 1.21μV/Pa with a 12V supply voltage. Note that to create Figure 2-12, the pressure signal from the polymer-based sensor has been shifted in time so as to best match the pressure signal from the commercial sensor; again, the two sensors were not co-located. The figure shows that the pressure response of the

polymer-based sensor was similar to that of the commercial sensor, demonstrating the promising functionality of the polymer-based sensor in uncontrolled conditions.

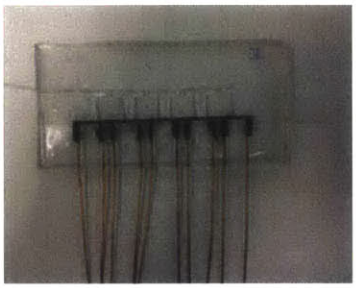

(a) A flexible polymer-based pressure sensor array (1x4) constructed from PDMS, employing four strain-concentrating diaphragms that each supported a strain gauge made from a piezoresistive carbon-black-PDMS composite.

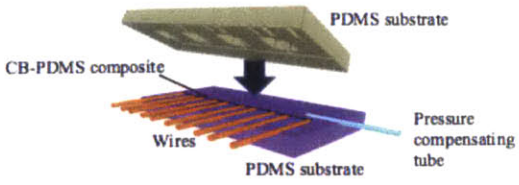

(b) An exploded view of the polymer-based pressure sensors array. During fabrication, the carbon-black-PDMS composite was screen-patterned onto one PDMS substrate, and connecting wires were inserted into molded slots, before the two substrates were bonded together.

Figure 2-10: The conductive polymer sensor array was fabricated using PDMS and PDMS-carbon black composite, creating a completely flexible array suitable for surface mounting on a variety of streamlined vehicles.

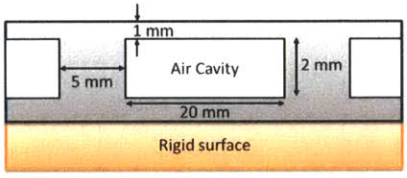

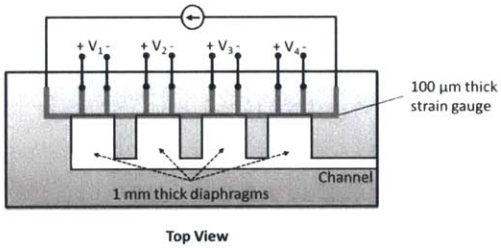

(a) Side view of the polymer-based pressure sensor array showing the sensor diaphragms with 1mm material thickness and 2mm air cavity. The 1x4 array had a sensor pitch of 25mm (x-direction).

(b) Top view of the polymer-based pressure sensor array showing the Kelvin-probe structure used to measure the voltage across each strain gauge without the influence of contact resistance. Each sensor diaphragm had a material thickness of 1mm, with a 2mm air cavity. The screen-printed carbon black/PDMS strain gauges had a thickness of 100μm.

Figure 2-11: The conductive polymer sensor array was composed of four individual sensor diaphragms, each employing a PDMS-carbon black strain gauge as the sensing element.

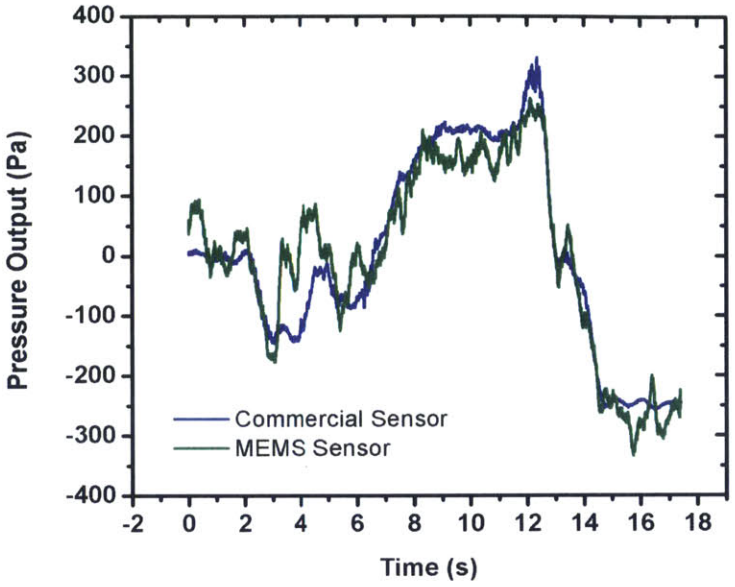

Figure 2-12: Pressure sensor output recorded during an open-water kayak test. The pressure recorded by a polymer-based sensor is shown in green, with the Honeywell SPT series sensor in blue. During the kayak experiments, the polymer-based sensor demonstrated a sensitivity of $1.21\mu V/Pa$ with a 12V supply voltage. As shown above, the polymer-based sensor captured the same trends as the commercial sensor during the experiment.

2.3.3 Unmanned Kayak Vehicle

In order to test the experimental pressure sensors outside the laboratory environment, an autonomous surface vehicle, operated with radio control, was employed. Based on a Pungo 100 rotomoulded kayak (from Wilderness Systems), the vehicle provided a platform capable of carrying multiple experimental pressure sensor arrays, along with a suite of commercial pressure sensors and vehicle navigation instrumentation, as seen in figure 2-13.

The kayak was equipped with two onboard computers within a custom waterproof electronics box. One computer was responsible for the control of the kayak's onboard sensors which include a digital compass, GPS, IMU, and DVL. This computer ran Ubuntu Linux, and was loaded with MOOS-IvP software which both managed the data collection and saving, and could provide for autonomous operation if desired (for

Figure 2-13: An unmanned kayak, used in radio control mode, was used as a platform for testing multiple arrays of experimental pressure sensors.

more information on the MOOS-IvP software, please see www.moos-ivp.org).

The second onboard computer ran a Windows operating system, allowing for the use of National Instruments Labview software to be employed for collecting data from the commercial pressure sensor suite and the experimental pressure sensors. Labview provided an easy to use interface for collecting data from a large number of sensors, while also allowing visual inspection of the signals in real-time, enabling the operation of each sensor to be verified before deployment.

2.3.4 Commercial Pressure Sensors

In order to provide a baseline against which to test the experimental pressure sensors, the kayak was outfitted with 19 Honeywell SPT series pressure sensors. Honeywell 19mm pressure sensors had been used in previous experiments by group members, and were found to be both sensitive and robust. The SPT series sensors offered similar sensitivity and robustness to the previously used sensors, while also carrying onboard amplification, allowing for easier implementation in the bow compartment of the kayak. The SPT series sensors were individually calibrated before use, and were found to have excellent consistency in both voltage offset and calibration constant. To reduce the measurement noise from the SPT sensors, a first order RC filter was used between the sensors and the National Instruments Data Acquisition Board (Model USB-6281).

While the SPT sensors were found to provide an excellent baseline for verifying the performance of the experimental sensor arrays, the size of the sensors (73mm height, 22mm diameter) was substantially larger than desired for surface mounted applica-

tions. Because of their size, mounting the sensors to the kayak was substantially more difficult than the experimental arrays. While the flexible PDMS encapsulated arrays were adhered directly to the exterior of the kayak hull using silicone adhesive, the Honeywell SPT sensors were mounted to the interior of the kayak bow section by threading the individual sensors into tapped delrin blocks that were epoxied to the kayak inner hull. Holes were drilled through the kayak hull at each sensor location, allowing for the surface pressure to be measured, but also introducing potential failure points to the kayak system.

2.3.5 Field Experiment Results

Two series of experiments were conducted using the autonomous surface vehicle outfitted with experimental surface mounted pressure sensor arrays. The first series of experiments was conducted in a pool at the National University of Singapore (NUS), allowing for simple and controlled vehicle motions without the influence of waves or the vehicle's thruster. The second series of experiments was conducted at Singapore's Pandan Resevoir, and allowed for the sensor arrays to be tested in "real world" operating conditions.

Pool Experiments

Before taking the kayak vehicle to Singapore's Pandan Reservoir, experiments were conducted in one of the swimming pools at NUS to ensure the operation of the pressure sensors, as well as remote data collection from the vehicle.

Because the pool at NUS was limited in size, experiments were restricted to simple vehicle motions that did not use the vehicle's propulsor. The conductive polymer based sensors were not working during the initial pool tests due to an electrical problem that was remedied before conducting experiments at the reservoir. The two silicon piezoresistive sensors were operating as expected, however, and responded well to various vehicle motions.

Roll Test

A roll response test was performed by forcing an oscillatory roll motion by hand in the pool. Because the silicon piezoresistive sensors were mounted on opposite sides of the vehicle, it was expected to see the signals from the two sensors 180° out of phase, as seen in figure 2-14(a). The voltage output from the silicon piezoresistive sensors was found to have high frequency noise of approximately 25% the signal magnitude, but a Butterworth filter at 20 hertz greatly improved the output signal as seen in 2-14(a).

To verify the time response of the sensors, the frequency spectrum of the sensor response, seen in figure 2-14(b), can be compared to the roll motion from the IMU data, as seen in figure 2-15.

It was observed that the primary one hertz frequency of the sensors matched the roll frequency, demonstrating that the sensors were working as expected. The frequency response of the pressure sensors also contained a 1.75 Hz component which was not observed in the frequency response of the roll motion from the IMU data. The cause of this high frequency component was not fully known, but it was theorized the higher frequency could be attributed to saturation at the extremes of the roll motion, as observed in the flattening of the top of the pressure spikes in Figure 2-14(a). Similar experiments were performed for the case of pitch and yaw, each with results matching expectations.

Pandan Reservoir Experiments

Experiments were conducted at Singapore's Pandan Reservoir January 25 and 26, 2012 to verify the operation of the experimental arrays in "real world" conditions. Pandan Reservoir is located in the southwest portion of Singapore, and is a drinking water reservoir managed by the Singapore Public Utilities Board. Located near the Singapore-MIT Alliance for Research and Technology (SMART) center at NUS, the reservoir offers an ideal setting for the testing of underwater and surface vehicles.

Unlike the experiments in the NUS pool, Pandan Reservoir provided sufficient

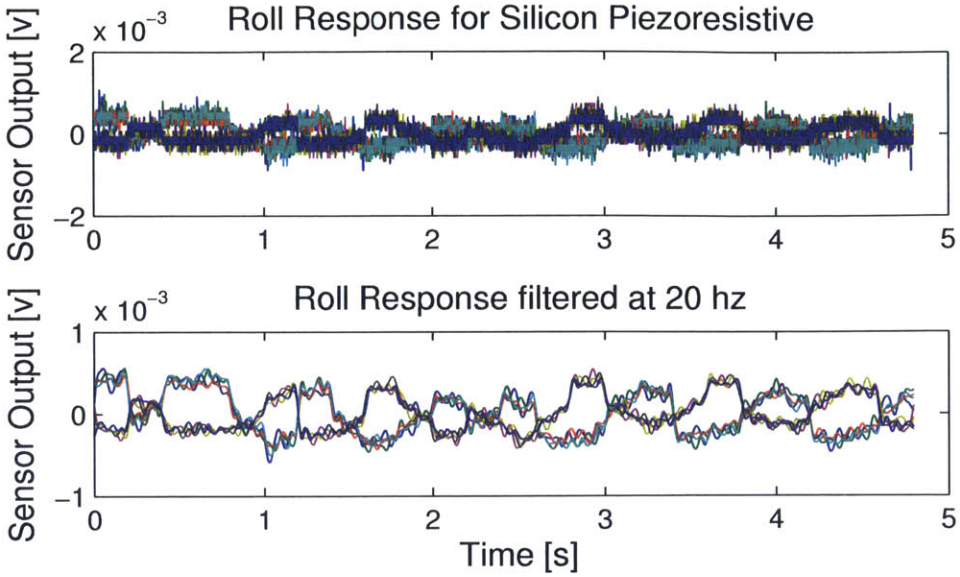

(a) A roll test was performed on the kayak in the NUS pool. The two silicon piezoresistive sensors reacted as expected, with periodic signals 180° out of phase. Variation in peak magnitude between channels could be attributed to a slight difference in depth below the kayak waterline between the PCB and LCP arrays.

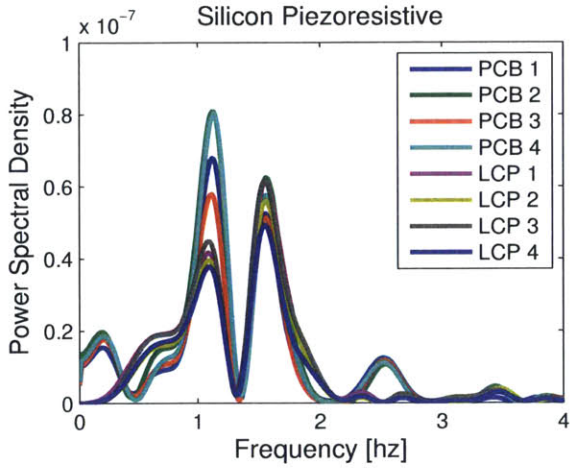

(b) Power spectrum for the silicon piezoresistive sensors during the pool roll experiment. Strong frequency components are observed at approximately 1 and 1.75 hz. Variation in power spectral density between the two arrays was due to differences in mounting position, and a slight difference in sensitivity between the LCP and PCB arrays.

Figure 2-14: A roll test was performed in the NUS pool to test the response of the experimental sensor arrays.

space to conduct self-propelled experiments using the kayak's propulsor under radio control. A variety of experiments were conducted over the two day testing period,

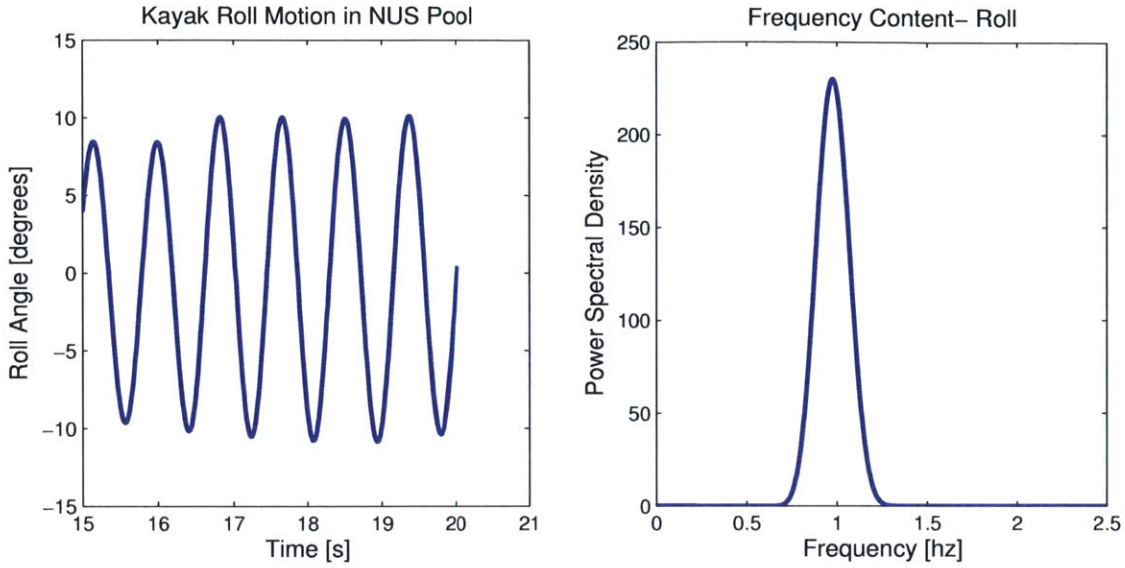

(a) A time series of the kayak roll angle from the IMU during tests in the NUS pool show a periodic roll motion with a maximum amplitude of approximately 15°

(b) Power spectrum for the IMU roll data during the pool roll experiment showing the roll motion of the kayak was forced at approximately 1hz.

Figure 2-15: The kayak inertial motion unit (IMU) was used to measure the vehicle's roll angle and verify the frequency response of the sensors.

including circles of various diameters, periodic turning motions in forward and reverse, approaches to docks and obstructions, and attempts to detect boat wakes.

For the experiments at Pandan, the electrical connection problems to the conductive polymer sensors had been resolved, enabling all of the sensors on the kayak to be used simultaneously. To ensure the conductive polymer sensors were operating as expected, the roll and pitch experiments without the thruster were repeated at the reservoir. It was found that for both the roll and pitch experiments, all three sensor types (commercial, conductive polymer, and silicon piezoresistive), worked as expected, as seen in Figures 2-16(a) and 2-16(b). The commercial sensors gave the largest signal due to their onboard amplification, but the periodic vehicle motions could be easily identified in the signals from both types of experimental sensors. In the case of both experimental sensor types, the signal to noise ratio was not as good as for the commercial sensors, revealing an area to be addressed in future iterations of the sensors.

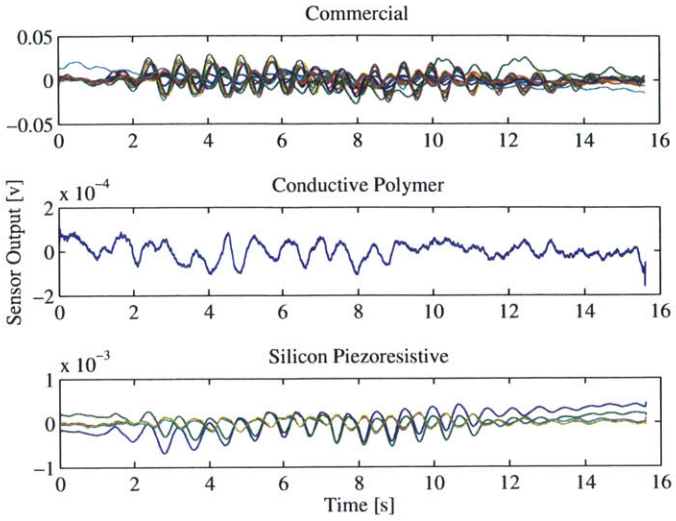

(a) The un-powered roll test was repeated at the reservoir to ensure the operation of all three pressure sensor types.

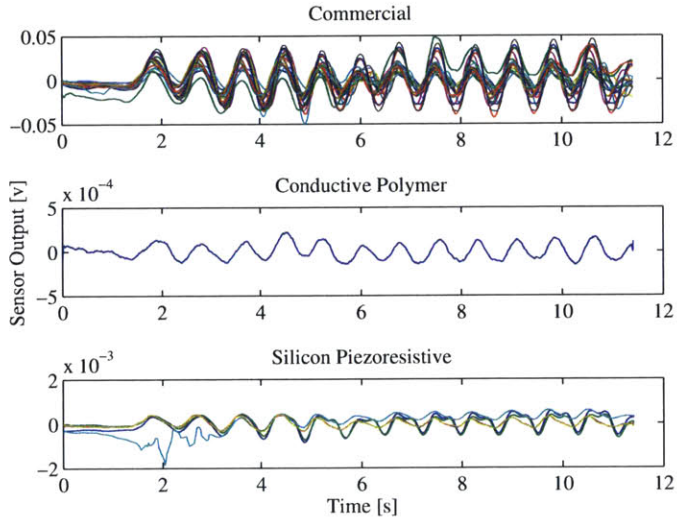

(b) The un-powered pitching experiment was repeated at Pandan.

Figure 2-16: Un-powered experiments were repeated at Pandan after the connection problems with the conductive polymer sensors were fixed. Only operational channels from the sensors arrays are shown, and an 80 point moving average was applied to the experimental data.

Self-Propelled Experiments

One of the primary goals for the Pandan Reservoir trials was to test the sensors during "real world" operating conditions. While simple vehicle motions without the thruster

demonstrated that the sensors were working as expected, the successful implementation of the sensors on a self-propelled vehicle was considered a crucial proof of concept of the utility of pressure sensors as a feedback mechanism on marine vehicles.

Several types of self-propelled tests were conducted at the reservoir, all with the intention of producing strong hydrodynamic signals for the sensors to detect. One result that was immediately apparent during the experiments was the noticeable increase in noise on the silicon piezoresistive sensors when the thruster was in operation, as seen in Figure 2-17. The increase in noise was not observed when the motor was tested in air, and the magnitude of the increased noise was found to make discerning hydrodynamic signals difficult. It is believed noise was introduced to the signals through the unshielded ribbon cable used between the sensor arrays and the NI DAQ board. Work is ongoing to incorporate filtration and amplification onboard the sensor arrays, as well as using shielded components to mitigate the effects of external noise.

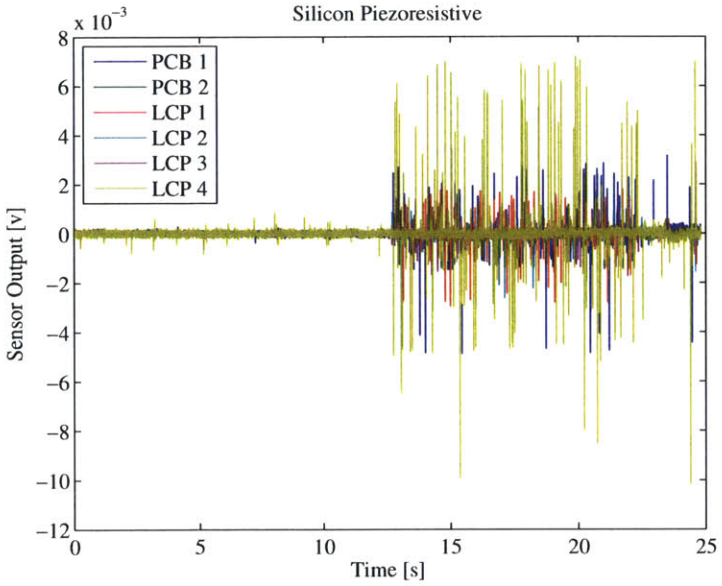

Figure 2-17: During the experiments at the Pandan Reservoir, it was found that operating the thruster added significant noise to the silicon piezoresistive sensors. In the figure above, the thruster was enabled at approximately 12 seconds. Two channels of the PCB/PDMS sensor were damaged during transport of the kayak to the Pandan Reservoir and are not plotted. A discussion of the thruster noise can be found in Section 2.3.5

Circle maneuvers were performed to both port and starboard in order to investi-

gate if the pressure sensors could be used to measure the drift angle of the vehicle. Previous experiments using a sailboat hull equipped with commercial pressure sensors and towed at various angles of attack showed that a nearly-linear relationship existed between the pressure difference across the bow of the vehicle, and the angle of attack [31]. It was believed that by conducting circle tests at various radii, the drift angle found from compass and GPS data could be compared to pressure measurements, and a similar relationship established.

Interpreting the results from the self propelled kayak experiments was complicated by the data collection system employed on the kayak. Because navigational and pressure data were recorded on two separate computers, relating features in the pressure signals to vehicle motions required special care. In the case of the circle test, coordinating the pressure and navigational data was accomplished by comparing features in the pressure data recorded using the commercial sensors, and the vehicle roll motion found from the IMU. The un-powered roll experiments in Figure 2-16(a) showed that the pressure sensors were well-suited for measuring the vehicle roll dynamics, verifying the utility of roll data as a means to coordinate pressure and navigational data. For the circle test in Figures 2-18 and 2-19, the time difference between the navigation and pressure data was found to be approximately 20 seconds.

Considering a port circle experiment, seen in Figure 2-19, all three sensor types showed an initial drop in voltage, followed by a rise to a steady value that was maintained for the remainder of the experiment. By comparing the pressure during the first 20 seconds of the turn with the yaw rate and acceleration, it was found that the pressure sensors showed a measurable change in pressure during the initiation of the port turn, when the yaw rate was changing and the acceleration was non-zero, as seen in Figure 2-18 and Figure 2-20. When the vehicle reached a steady yaw rate, the pressure recovered to a steady value, and remained constant for the remainder of the turning maneuver. The drop in voltage output from the Honeywell SPT pressure sensors in Figures 2-18 and 2-20 was indicative of a decrease in pressure on the starboard bow of the kayak, consistent with an added mass effect during the initiation of a turn to port by the vehicle.

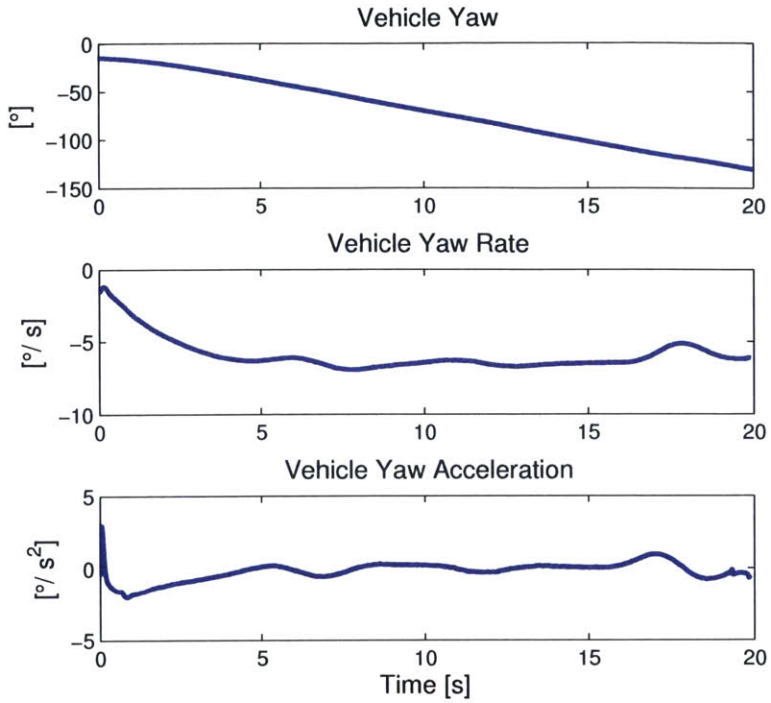

Figure 2-18: The vehicle yaw angle, rate, and acceleration were found from IMU data. From the IMU data, it was observed that the turn to port was initiated at approximately zero seconds, with a steady turning rate achieved by approximately 6-7 seconds.

In addition to the variation in pressure during the unsteady portion of the circle maneuver, oscillations in the 0.75-1 hertz range were present in the pressure signals, as seen in Figure 2-21(a). These oscillations were present whenever the vehicle was undergoing a turning maneuver, and were caused by a small amplitude, but constant frequency, rolling motion of the kayak, as seen in Figure 2-21(b).

Additional self-propelled experiments conducted with the kayak vehicle consisted of circles to port and starboard, zig-zag motions in both forward and reverse, and passes in close proximity to a stationary pier. In each case, the vehicle pitch and roll dynamics were clearly evident in the pressure data, but larger flow structures were more difficult to distinguish. These results suggest that additional optimization of sensor design is needed before the existing sensor arrays can be implemented as a feedback mechanism on an operational vehicle.

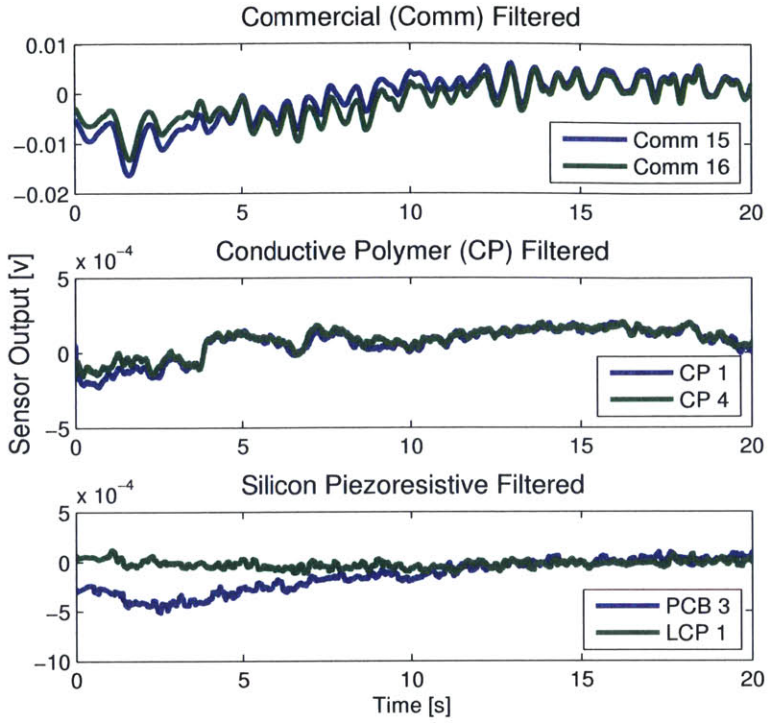

Figure 2-19: During the port circle experiments, a dip in pressure was observed during the initiation of the turn, followed by a constant value during the remainder of the maneuver. Two channels from each sensor were chosen for clarity, and an 80 point moving average was applied to each signal.

Silicon Piezoresistive Sensor Analysis

The silicon piezoresistive sensors have two main areas of need: packaging size and signal to noise ratio. While both the PCB and LCP based arrays are contained in a very small, flexible strip, the PDMS encapsulation is too large for practical application. In order for the MEMS sensors to be a viable feedback solution on a variety of marine vehicles, the sensor arrays must be robust, easy to apply, and small enough not to alter the near-body flow field. To meet these goals, the size of the encapsulated sensors must be reduced.

The signal to noise ratio is also an area of needed improvement for the silicon piezoresistive sensors. While the sensors produced a measurable signal without amplification, operating the thruster created noise that nearly masked the desired signal, as seen in Figure 2-17. In an effort to resolve the signal to noise ratio of the silicon piezoresistive sensors, work is underway to incorporate a low-pass filter and amplifier

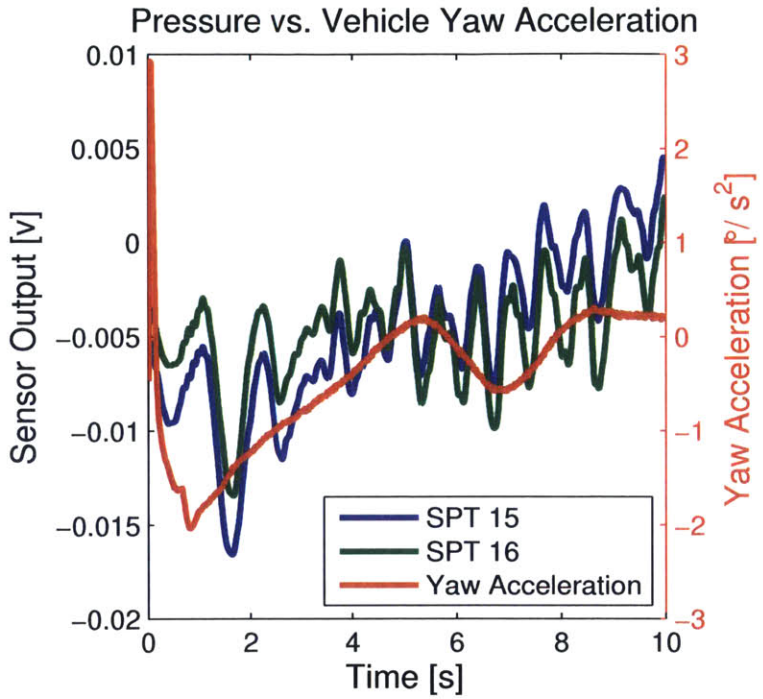

Figure 2-20: The output from the Honeywell SPT pressure sensors located on the kayak's starboard side shown with the kayak yaw acceleration during the initiation of a port turn.

onto the same strip as the sensor dies, creating an array that requires no external circuitry and delivers a strong signal to noise ratio. This design change will retain the flexibility and size benefits of the current sensor, while enhancing the usability of the output signal.

Conductive Polymer Sensor Analysis

The conductive polymer sensors demonstrated mixed results when tested on the surface of the kayak. The implementation of the sensors was straightforward, with the completely flexible sensors able to be mounted at any location on the kayak's hull. Additionally, it was found that the sensor arrays could be powered with both a 0 volt reference or a -12 volt reference, allowing them to be connected to the same set of batteries as the commercial pressure sensors.

Where the conductive polymer sensor's performance was lower was in sensitivity compared to both the commercial and silicon piezoresistive sensors. During the test-

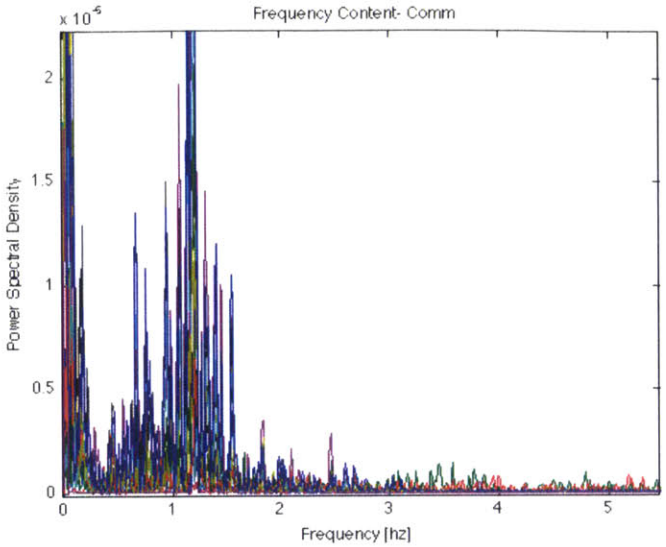

(a) The power spectrum for the commercial sensors during the port circle maneuver revealed the presence of oscillations in the range of 0.75-1 hz.

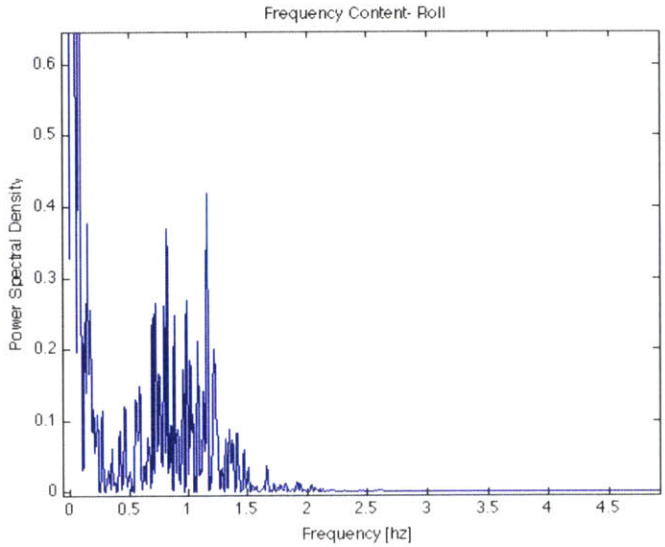

(b) The power spectrum of the IMU roll data showed the roll motion had the same frequency range as the oscillations in the commercial pressure sensor data.

Figure 2-21: The frequency content of the commercial pressure sensor data and the kayak roll motion were compared to ensure the oscillations in the pressure data could be attributed to the small amplitude kayak roll motion during the maneuver.

ing of the sensors, the conductive polymer output signals were found to be on the order of millivolts, even after amplification. As a consequence of the small amplitude response of the sensors, small variations in pressure were not detected by the array,

or masked by noise. Enhancing the sensitivity of the sensor array would improve its utility as a feedback mechanism for a marine vehicle where relevant flow structures produce pressure variations on the order of tens to hundreds of pascals.

Additionally, the question of back pressure on the conductive polymer sensor array remains an open, and relevant, question. During the experiments on the kayak vehicle, a reliable way to maintain a constant back pressure on the sensors was not achieved. In order to reliably measure pressure, the back pressure needs to be held constant, or the baseline calibration of the sensors will be in constant flux. While this requirement presents an engineering design and fabrication challenge, work is underway to resolve the issue using a micro-channel patterned into the sensor substrate that will account for variations in hydrostatic pressure.

2.3.6 Conclusions from Unmanned Kayak Experiments

The lateral line found in most species of fish is an organ without analog in humans, and makes possible many behaviors such as obstacle avoidance, schooling and prey detection. In an effort to extend these capabilities to engineering systems, several lateral line like pressure sensor array were constructed using innovative material sets. In each case, priority was placed on constructing a sensor array that was durable, flexible, and able to be surface-mounted on a marine vehicle.

Three individual pressure sensor arrays were fabricated at MIT and NTU in Singapore. The two NTU sensors were constructed from commercially available piezoresistive sensor dies that were packaged on LCP and flexible PCB substrates. The array fabricated at MIT relied on a new, and unique material set that allowed for a completely flexible sensor. The array was constructed using conductive polymer strain gauges arranged in a four point probe arrangement and utilizing four independent strain-enhancing diaphragms patterned from flexible PDMS.

Overall, the experiments conducted during January 2012 served as an important proof of concept for the experimental MEMS pressure sensors arrays. All three experimental arrays demonstrated the ability to measure dynamic pressure while mounted to the curved kayak hull. In addition, the sensors were shown to deliver a measurable

signal, despite suffering from additional noise while the thruster was in operation. Although experiments demonstrated significant progress from previous generations of the sensors, they also revealed areas of needed improvement for each sensor type.

2.3.7 Lessons from Kayak Experiments for Next Generation Sensor Arrays

While the experimental sensor arrays utilized during the kayak experiments in Singapore were successfully mounted to a marine vehicle and demonstrated their ability to measure vehicle dynamics, several areas for improvement in sensor array design and fabrication were identified. Two goals for sensor array development made clear from the field experiments were to improve device robustness and increase signal-to-noise ratio. As has been previously discussed, all of the experimental sensor arrays suffered from signal-to-noise problems when the vehicle motor was in operation. In addition, the sensor robustness was a cause for concern when transporting the kayak vehicle from the NUS campus to the Pandan reservoir. While the sensor arrays survived normal operating conditions very well, several individual sensor dies from the piezoresistive arrays were damaged when the kayak was improperly placed on its transport cart during deployment. Based on the lessons learned from the Singapore kayak experiments, it was desired for the next generation of pressure sensor arrays to be a "stick and forget" technology, utilizing waterproof, robust, and flexible materials.

2.4 Characteristic Examples of Near-Body Hydrodynamic Sensing

In the design of pressure sensor arrays, sensor spacing and dynamic pressure range is largely defined by the scale of the application and flow of interest. In Chapter 1, the fish lateral line was introduced as a biological example of distributed pressure sensing mediating complex behaviors in a marine environment. At fish-scale, dynamic pressure stimuli are on the order of tens of pascals, and the spacing between individual

pores of the lateral line trunk canal vary by fish species, but are generally on the order of millimeters, as shown in the red rows of Table 2.1. In Chapter 2, a series of towing tank and field experiments were conducted to investigate the distributed pressure sensing on the scale of typical unmanned marine vehicles in the 1-3 m length range. The sensor spacing, dynamic pressure ranges, and frequency ranges for example applications on this scale are given in the grey rows of Table 2.1. The results from these experiments serve as the foundation for design guidelines for hydrodynamic sensor array development given in Section 3.1. While the focus of the sensor development presented in this thesis is focused on the size and performance range for unmanned vehicle applications, experimental results can be scaled to predict the size and performance requirements for sensor arrays in ship-scale applications, as given in the green row of Table 2.1.

2.5 Chapter Summary

The performance of marine vehicles is greatly impacted by interactions with the flow around their hull, both self-generated and environmentally driven. In this chapter, previous studies investigating near-body hydrodynamics were reviewed, focusing on applications on the scale of unmanned marine vehicles approximately 1-3 m in length. Along with studies from the literature, several experiments conducted by the author using distributed arrays of commercial pressure sensors were introduced. Using a model sailboat hull towed in the MIT towing tank, it was shown that the angle of attack of the hull could be determined by measuring the hydrodynamic pressure gradient near the vehicle's bow. As the angle of attack increased, the pressure gradient was observed to switch directions, suggesting the onset of separation from the sharp bow which leads to increased drag during maneuvering. Similarly, an autonomous kayak vehicle was instrumented with an array of pressure sensors to study the near-body pressure field during self-propelled operation. It was found that the vehicle dynamics in pitch and roll were measurable by the pressure sensor array, as well as the initiation of vehicle maneuvers due to a characteristic pressure signature consistent

Application Scale	Example unsteady flow	Sensor spacing	Dynamic pressure [Pa]	Frequency range [Hz]
Fish lateral line	Energy extraction from vortices [60]	$\sim$ 1-3 mm (Trout)	10-30	2-5
Fish lateral line	Prey tracking [15]	$\sim$ 2 mm (Mottled Sculpin)	0-15	30-100
Unmanned marine vehicles	Free vortex tracking [33]	$<$ 6 cm	20-100	0.5-2
Unmanned marine vehicles	Leading edge vortex shedding [27]	$<$ 4 cm	40-200	0.25-3
Unmanned marine vehicles	Separation from model sailboat hull (L= 1 m, Fr= 0.16, u= 0.5 m/s) [31]	$\sim$ 5 cm	10-100	$<$ 1 Hz
Proposed ship-scale marine application	Separation during surface vehicle maneuvering (L= 30 m, Fr= 0.16 m, u= 3 m/s)	$\sim$ 1.5 m	400 - 4000	$<$ 1 Hz

Table 2.1: Examples of unsteady flow sensing using distributed pressure sensor arrays. The rows in red represent examples at the scale of the fish lateral line, as discussed in Chapter 1. Examples in grey represent applications at the scale of typical unmanned marine vehicles, and are based on experimental results using commercially available pressure sensors. The final green row represents a theoretical scaling of array requirements to ship-scale.

with added mass effects during unsteady vehicle motions.

The primary contribution of the experiments presented in Chapter 2 was to inform guidelines for the development of next generation pressure sensor arrays, as discussed in Section 2.4, and summarized in Table 2.1. The experiments conducted using commercial pressure sensor showed that the principle of distributed pressure sensing displayed by the fish lateral line could give useful information at a scale consistent with unmanned marine vehicles. By studying the measurements from the commercial sensor arrays, guidelines for the sensor spacing, dynamic pressure range, and frequency range appropriate for hydrodynamic sensing applications were developed.

Chapter 3

Distributed Pressure Sensor Arrays

3.1 Guidelines for Hydrodynamic Pressure Sensor Arrays

After conducting a series of experiments using commercially available pressure sensors to characterize near-body flow structures, as described in Chapter 2, the limitations of each type of sensor were made apparent. In general, the sensors used in previous studies were rigid and too large for surface mounting applications, and were not designed for prolonged exposure to moisture. Using the practical knowledge gained from first-hand experimental experience, the attributes of a pressure sensor array designed specifically for marine use were considered. To act as a lateral line inspired sensor on marine vehicles, pressure sensor arrays should be designed with a variety of guidelines in mind.

Flexibility: Pressure sensor arrays to be surface mounted on curved surfaces with radius of curvature ~5-10 cm, consistent with unmanned vehicle hulls [27, 26, 31].

Form Factor: Sensor spacing should be less than 5 cm for vehicles on the 1-3 m scale. Sensor thickness should be < 5 mm to avoid vortex shedding [27, 33, 31].

Robustness: Sensor arrays are meant for sustained underwater or exposed operation and may be subject to impacts.

Sensitivity: For marine vehicles of length ~1-3 m, dynamic pressure stimuli range from ~10-400 Pa with ~10 Pa sensitivity [27, 26, 33, 31].

Cost: Sensor cost should be reduced from ~ $100 per sensor to ~ $10 per sensor [26].

3.2 Review of Commercial Pressure Sensors

A variety of commercial off the shelf pressure sensors have been tested at the MIT Towing Tank for use as lateral line inspired sensor arrays. These include 19 mm series (Figure 3-1(a)) and SPT series sensors (Figure 3-1(b)) from Honeywell, and MPXV series sensors (models 5010 and 7007) from Freescale Semiconductor (Figure 3-1(c)). While the Honeywell sensors offered robust stainless steel construction, and a fully waterproof housing in the case of the SPT series, the form factor was much larger than desired. Neither Honeywell sensor was amenable to surface mounting, requiring the use of pressure transmission tubes to an off-body array of sensors [27], as seen in Figures 3-2(b) and 3-2(a), or the use of holes drilled through the test vehicle's hull [26], as seen in Figure 3-2(c). The MPXV series sensors had a reduced form factor when compared to the Honeywell sensors, which allowed for a higher density of sensors along body. The sensors were not waterproof, however, requiring them to be either potted in silicone or resin, connected to the flow via pressure transmission tubes, or contained within a watertight vehicle [35].

Additional pressure sensor technologies that were investigated for use in hydrodynamic pressure sensing included Flexiforce conductive ink sensors from Tekscan, and a disposable medical pressure sensor from Measurement Specialties. The Flexiforce conductive ink sensors from Tekscan, shown in Figure 3-3(a), were attractive for surface mounting applications because of their thin profile and high flexibility. Initial experiments with the sensors revealed difficulties with drift and sensitivity, precluding the use of the sensors from the current study of hydrodynamic stimulus. However, the use of conductive ink for highly flexible sensors remains attractive, and the Flexiforce sensors are considered an excellent choice for tactile applications with

(a) Honeywell 19mm series pressure sensor

(b) Honeywell SPT series pressure sensor

(c) Freescale Semiconductor MPXV7007 pressure sensor

Figure 3-1: Commercially available pressure sensors used in previous studies by members of the MIT Towing Tank Laboratory.

larger pressure requirements.

The model 1620 disposable medical pressure sensor from Measurement Technologies, seen in Figure 3-3(b), was also attractive for use in hydrodynamic sensing applications because of the dielectric gel barrier provided to protect the silicon piezoresistive sensor die from exposure to liquid. Despite the waterproofing of the sensor die, the form factor of the sensor was too large for surface mounting, and electrical connections required additional waterproofing.

Overall, a commercially available pressure sensor was not found that met all of the needs for near-body flow sensing described in Section 3.1, as shown in Figure 3-4. The Measurement Specialties MPXV5010 and MPXV7007 and Honeywell 19mm series and SPT sensors were utilized in experiments because of their appropriate range and excellent repeatability; however, the large form factor or lack of waterproofing required the use of pressure transmission tubes or compromises to be made in mounting position, as seen in Figure 3-3. The Honeywell pressure sensors also represented a significant financial cost during distributed pressure sensing experiments, as shown in Table 3.1. The financial challenge of achieving dense spatial resolution using commercially available pressure sensors was demonstrated during experiments using the unmanned kayak vehicle described in Section 2.3. The vehicle was equipped with 20 Honeywell SPT pressure sensors at a total cost of approximately $5000.00. Despite the substantial investment in instrumentation, sensors were limited to the bow

(a) Honeywell 19 mm pressure sensors were used to study LEV shedding on a single element hydrofoil. Because of sensor size limitations, the array on the foil was limited to four sensors (from [27]).

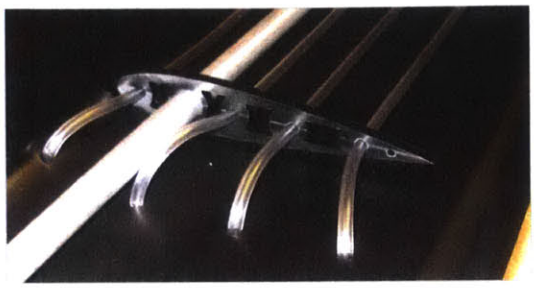

(b) To transmit pressure from the foil surface to the sensors mounted on top of the foil, tubing was embedded within the urethane foil during the casting process (from [27]).

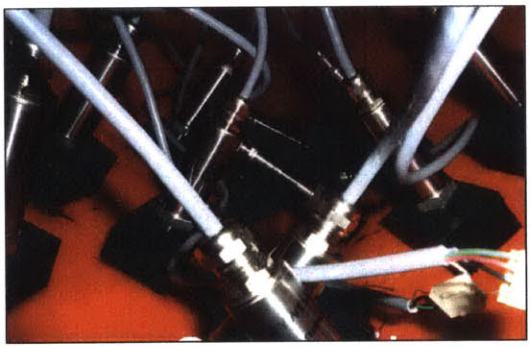

(c) Honeywell SPT sensors were used to measure the pressure distribution on the bow region of an autonomous kayak. To mount the sensors inside the vehicle, tapped delrin blocks were epoxied to the inside of the rotomoulded hull, and holes were drilled through the hull skin to access the flow.

Figure 3-2: The form factor of commercially available sensors required compromises to be made in sensor positioning and mounting, including the use of pressure transmission tubing and drilling holes through vehicle hulls.

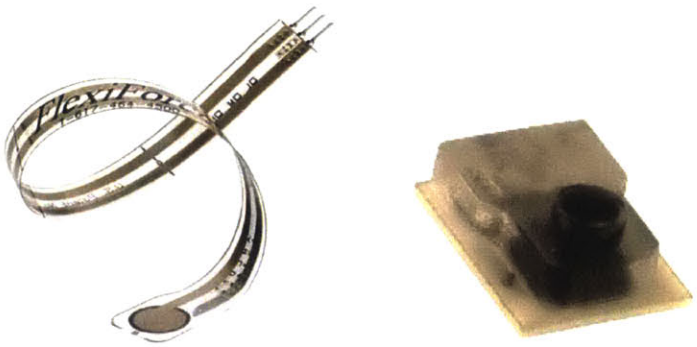

(a) Flexiforce conductive ink sensors from Tekscan showed great form factor and flexibility, but lacked the sensitivity required for near-body flow sensing.

(b) The model 1620 disposable medical pressure sensor from Measurement Technologies had a dielectric gel barrier to protect the piezoresistive sensor die from contact with fluid, but lacked the form factor for surface-mount applications.

Figure 3-3: Both conductive ink and disposable medical pressure sensor were considered for use in lateral line inspired sensor arrays, but did not meet all the requirements for use in hydrodynamic sensing applications.

section of the vehicle, leaving a large percentage of the near-body flow structures unmeasured. In order to scale the use of distributed pressure sensing to real-world applications while maintaining spacial resolution on the order of centimeters, an order of magnitude price decrease is needed compared to current commercial offerings, as discussed in Section 3.1.

Although the dielectric gel barrier protecting the sensing element in the disposable medical sensors from Measurement Specialties provided waterproofing, the sensors lacked the appropriate form factor for surface mounting applications. The Flexiforce sensors from Tekscan provided great improvements in form factor, but lacked the sensitivity needed for the specific hydrodynamic stimulus under investigation. The lack of commercially available sensors able to satisfy the guidelines given in Section 3.1 and shown in Figure 3-4 motivated the development of experimental pressure sensor arrays designed specifically for hydrodynamic sensing applications, as described in Section 3.4 and Chapter 4.

Experiment	Sensor Type	Number of Sensors	Approx. Sensor Density	Approx. Cost per Sensor [$]	Total Sensor Cost [$]
Unmanned kayak	Honeywell SPT	20	$1/900cm^2$	250.00	5000.00
Model sailboat hull	Honeywell 19mm	10	$1/160cm^2$	120.00	1200.00
Instrumented hydrofoil	Honeywell 19mm	4	$1/5cm$ (linear array)	120.00	480.00

Table 3.1: Approximate cost for use of commercially available pressure sensors in distributed sensing applications based on previous experimental studies.

3.3 Prior Work in Lateral Line Inspired Sensors

Generally speaking, lateral line inspired sensor arrays fall into two categories: those that mimic the physiology of the fish lateral line system, and those that draw on the broad principle of distributed pressure sensing. For an excellent overview of the application of biological principles from the lateral line to engineered sensors, the chapter by Bleckmann et al. [7] is recommended.

3.3.1 Sensor Arrays Mimicking Lateral Line Physiology

Looking to fish for engineering inspiration, several sensor arrays have been developed mimicking the physiology of the lateral line. Flow velocity generated by a dipole source was measured through the deflection of a vertical 'hair-cell' structure fabricated on the end of a doped cantilever piezoresistor by Chen et al. [13], and further developed by Yang et al. [93]. Using a similar standing structure mounted to a cantilever piezoresitor, McConney et al. found the addition of a hydrogel 'cupula' to the artificial neuromast, seen in Figure 3-5(a), increased the flow sensitivity by two orders of magnitude compared to the 'hair-cell' without a 'cupola' [67]. A silicon standing structure patterned on top of a liquid crystal polymer (LCP) substrate was fabricated by Kottapalli to mimic the geometry of a superficial neuromast, as seen in Figure 3-5(c) [51]. An array of standing structures was also used by Pandya et al. in the form of a linear array of 16 hot-wire anemometers, shown in Figure 3-5(b)

	Cost per Sensor	Waterproof	Size (Footprint x Height)	Flexible	Surface Mountable	~10 Pa Sensitivity
Freescale Semiconductor MPXV 	~$14.00	No	100 mm² x 13 mm	No	No	Yes
Honeywell 19mm Series 	~$120.00	Sensing Element Only	283 mm² x 31 mm	No	No	Yes
Honeywell SPT Series 	~$250.00	Yes	380 mm² x 70 mm	No	No	Yes
Measurement Specialties 1620 	~$3.50	Sensing Element Only	85 mm² x 3.5 mm	No	No	Not Verified
Tekscan Flexiforce 	~$16.00	Yes	196 mm² x 0.2 mm (sensing pad)	Yes	Yes	No

Figure 3-4: Evaluation of commercial pressure sensors for use in distributed hydrodynamic pressure sensing applications. Green coloring represents the sensor satisfied the needs of distributed pressure sensor arrays. Orange coloring signifies that the requirements were partially satisfied (e.g. the sensing element is waterproof but electrical connections would need additional encapsulation). Red coloring signifies the sensor did not not satisfy a necessary requirement for use in hydrodynamic sensing applications.

[73, 38]. The array was reported to have a flow velocity sensitivity of 10mm/s, and was used to develop algorithms for the localization and tracking of a dipole [73], and for characterizing the wake behind a cylinder in a flow channel [91].

An artificial lateral line canal, seen in Figure 3-6(a), was fabricated from plexiglass by Chen et al. [12] for use with the array of hot-wire anemometers described in [73] with the goal of acting as a high pass filter and attenuating the DC component of hydrodynamic signals. Similarly, Yang et al. [92] used stereolithography techniques to fabricate a canal, shown in Figure 3-6(b), for the hair-cell sensors developed in [13]. It was found that the artificial lateral line canal reduced the background turbulent flow noise created by a dipole source oscillating at 20 Hz, a result consistent with the noise-rejection functionality of the fish canal neuromast. Noise rejection was also observed by Kottapali at al. who used PDMS to fabricate canals for a MEMS piezoeletric hair cell sensor, as seen in Figure 3-6(c) [51]. Finally, Klein and Bleckmann developed an

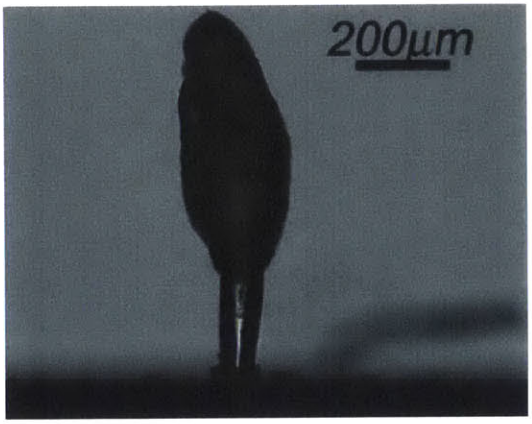

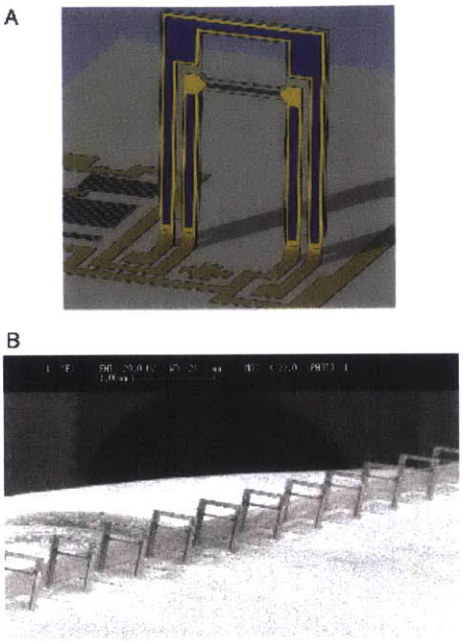

(a) An artificial hydrogel cupula was used to increase the flow sensitivity of a lateral line inspired flow sensor mimicking the phsiology of a neuromast (from [67]).

(b) An array of 16 hot wire anemometers used to Yang et al. for lateral line inspired sensing (from [91]).

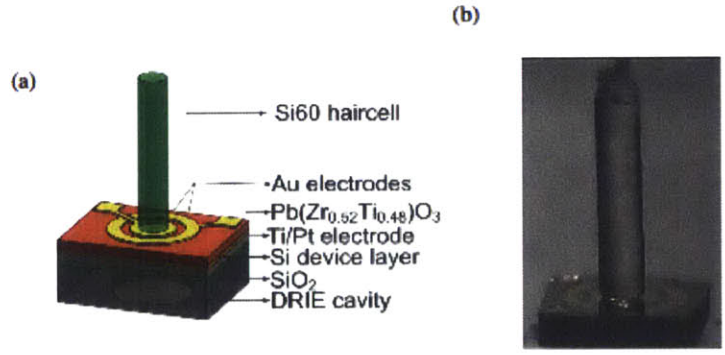

(c) Kottapalli fabricated an artificial superficial neuromast from silicon on a LCP substrate (from [51]).

Figure 3-5: Sensors developed mimicking the physiology of the neuromasts found in the fish lateral line.

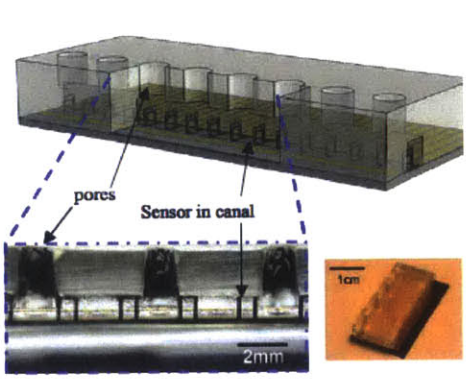

(a) Plexiglass lateral line canal for a hot-wire anemometer array (from [12]).

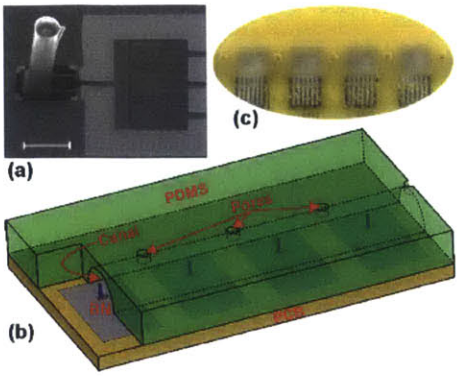

(b) Artificial canal fabricated by Yang for use with the cantilever-type artificial neuromasts shown in frame (a) (from [92]).

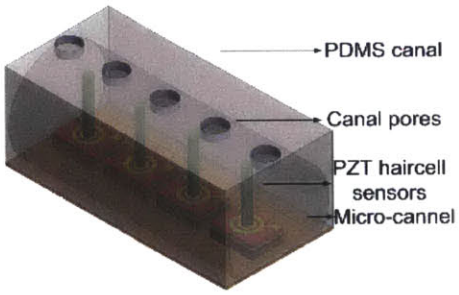

(c) Kottapalli fabricated an artificial lateral line canal using PDMS (from [51]).

Figure 3-6: Artificial lateral line canals fabricated to replicate the frequency filtering observed in the fish lateral line system.

artificial lateral line canal with artificial neuromasts that relied on optical signals for flow sensing [48].

3.3.2 Distributed Pressure Sensitive 'Smart-Skins'

Interest in the development of soft and conformal sensor arrays capable of large area coverage, generally referred to as 'smart skins', is present in multiple fields. For ocean engineering applications, thin and flexible pressure sensors are of interest for use in surface mount applications on streamlined vehicles and structures [95]. In the broader field of robotics, pressure sensitive skins to provide haptic feedback are in great demand to mediate interaction with humans [72, 9], and could also find use in

rehabilitative and assistive technology applications.

A liquid crystal polymer (LCP) membrane patterned with helical gold strain gauges was used by Kottapalli to fabricate a pressure sensor array for flow sensing applications, as seen in Figure 3-7 [52, 50]. Thin film piezoelectric pressure sensors capable of operating at very low frequencies approaching 0.1 Hz were mounted in an array on a flexible LCP substrate and tested in water using a dipole source by Asadnia [4].

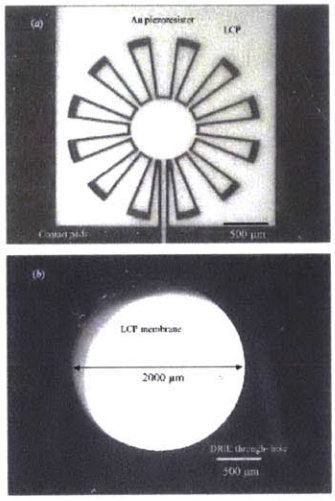

Figure 3-7: A flexible LCP substrate was patterned with serpentine gold strain gauges by Kottapalli (from [52]).

With the goal of creating thin, large area, and conformal "electronic skins," Someya et al. utilized organic field-effect transistors due to their low cost and inherent flexibility ([80],[79]). A 12 x 12 network was successfully fabricated and found to be extremely flexible and resistant to degradation, even after repeated cyclic loading. Because the focus of the network design was on accurate spacial resolution of pressure, sensitivity was not a priority, and tests were performed at 30 kPa, much higher than typical for hydrodynamic stimulus.

Microstructured PDMS thin films were used by Mannsfeld et al. as the dielectric layer in an organic field-effect transistor to create a highly pressure sensitive device [66]. The PDMS thin films were microstructured to minimize visco-elastic behavior typically exhibited by PDMS films with thicknesses of a few micrometers, as seen in

Figure 3-8. Microstructuring the PDMS thin films provided voids that enable the surface to elastically deform when subjected to external pressure, enhancing reversibility. The sensors were able to detect pressures as low as 3 Pa with a highest demonstrated sensitivity of 5.50% change in capacitance ($\Delta C/C_\circ$) per kPa. The microstructured thin films also exhibited relaxation times in the milliseconds, a significant increase in performance over unstructured PDMS thin films with relaxation times on the order of ten seconds.

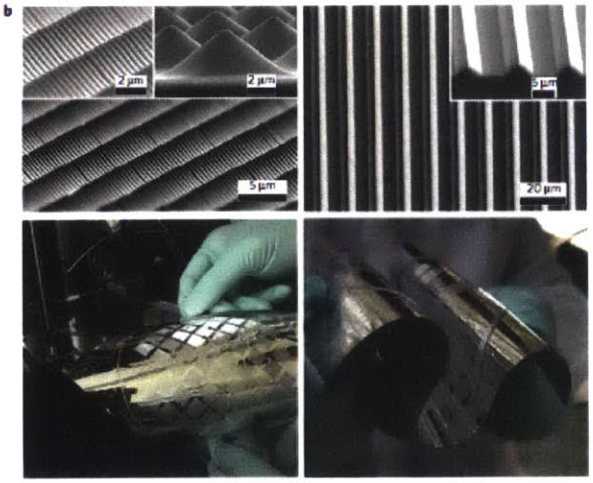

Figure 3-8: Thin PDMS films were microstructured with one and two dimensional features in order to reduce visco-elasticity (adopted from [66]).

Carbon black-PDMS (CBPDMS) composite has been studied as an active material for pressure and shear sensors due to its low Young's modulus, ease of fabrication, and low cost ([63],[62],[95],[54],[76]). The variation in piezoresisitivity as a function of carbon black concentration in carbon black filled silicone rubber composites was studied and modeled by Luheng et al. [63]. The pressure sensitive response of carbon black filled silicones, and the influence of contact resistance with electrodes was studied by Lacasse et al., and an analytical model was developed for the change in resistivity under an applied pressure [54].

The introduction of porosity into CBPDMS composites has also been studied as a method to lower Young's modulus and increase sensitivity ([47],[10]). King et al. showed a sacrificial sugar scaffold could be used in PDMS to create a porous network in

the material, reducing the Young's modulus when compared to solid PDMS. Carbon black was introduced to the pure PDMS "sponge" by dropping a solution of carbon black and water over the material, allowing the solution to percolate through the PDMS, and when dried, leaving a thin layer of carbon black coating the inside of the pores. When the porous material material was compressed, the pores were found to collapse, bringing the carbon-lined walls into contact and increasing the conductivity of the composite. The use of a sacrificial scaffold to create a porous network in PDMS was also employed by Cha et al. to create a pump for use with microfluidic devices [10].

Polyvinylidenefluoride (PVDF) was used as the sensing element in a 4x10 pressure sensor array by Lee and Sung [56]. PVDF was chosen as the sensing material for measuring small amplitude fluctuations due to its large dynamic range and large piezoelectric constant. The sensor array was validated using a speaker, and utilized to measure turbulent pressure fluctuations at the wall of a wind tunnel.

Doped-Polymer 'Smart-Skins' for Marine Applications

Based on the operational requirements for use in distributed pressure sensing on marine vehicles, and after considering previous work in bio-inspired pressure sensor development, it was determined a doped polymer 'smart-skin' array offered the best combination of performance characteristics for marine use. The use of a doped polymer would allow for the development of a completely waterproof and flexible sensor array through the careful selection of bulk matrix material and conductive dopant. The flexibility, robustness, and resistance to moisture of bulk matrix materials like PDMS (silicone) make doped composites well suited for prolonged environmental exposure while surface mounted on marine vehicle hulls. Additionally, controlling the material properties of the bulk matrix through the introduction of porosity has been shown to lead to increased sensitivity in carbon black-PDMS composites, allowing for piezoresistive composites to be optimized for pressure ranges consistent with hydrodynamic stimulus. Finally, doped polymers make use of cheap and easy to work with component materials, allowing for the scaling of distributed pressure sensor arrays to

real-world applications.

3.4 Collaborative Development of Doped Polymer 'Smart Skins'

Several iterations of 'smart-skin' pressure sensor arrays were developed at MIT using an innovative carbon black-polydimethylsiloxane (CBPDMS) composite as the active sensing material. The first version 'smart-skin' array utilized CBPDMS strain gauges on a PDMS (silicone) substrate, as seen in Figure 3-9, and was developed by MIT Masters student Frank Yaul [94, 95, 32]. MIT Masters student Mun Ee Woo continued the optimization of the strain gauge sensor arrays, and also developed a novel open-cell CBPDMS foam sensing material [89, 26, 28].

The author worked in collaboration with Yaul and Woo on the development and testing of the CBPDMS 'smart-skin' pressure sensor arrays. In particular, the author worked closely with Woo to characterize the performance of a version-one strain gauge array in the MIT towing tank [89], and to deploy and test a version-one strain gauge array on the hull of an unmanned kayak vehicle operating in the Pandan reservoir in Singapore [26]. Based on the lessons learned from the kayak experiments in Singapore [26], and experiments with commercially available sensors on hydrofoils [27], Dusek and Woo collaborated on the development and tow tank testing of a CBPDMS open-cell foam sensor array [28].

The following sections will summarize the collaborative work on the early generation CBPDMS 'smart-skins' that provided an important foundation for the development of the closed-cell CBDPMS foam sensors described in Chapter 4. For complete details of the sensor fabrication and testing, see the works by Yaul [94, 95] and Woo [89].

3.4.1 Carbon Black-PDMS Composite

To fulfill the guidelines identified for conformal pressure sensor arrays in Section 3.1, a composite of carbon black and polydimethylsiloxane (PDMS) was used as a piezoresistive sensing material. Because the primary component of the mixture is PDMS, the composite retains the flexible, robust, and waterproof characteristics for which PDMS is known.

Material Selection

A low Young's modulus was desired for the composite's polymer matrix in order to maximize the deformation of the material under compressive load [89]. In this regard, PDMS was an excellent material choice due to its low Young's modulus and very low glass transition temperature [89]. Additionally, PDMS has a low cure temperature, allowing for fabrication without specialized equipment or training, and making the material suitable for large area fabrication. Finally, the material exhibits no significant change in shear or Young's modulus with respect to frequency [94], making the material properties very stable under multiple deformations, which is important for use as a pressure sensor.

The choice of filler material was also important in achieving the sensitivity and reproducibility necessary for sensor array fabrication. After a thorough review of existing active materials for sensors [89], carbon black was judged to be the most suitable filler material for use with the PDMS matrix. From the literature, high structure carbon black was found to have high piezoresistivity and reproducibility, as well as being an inexpensive filler agent [49].

With the composite matrix and filler agents selected, the design space for optimizing the Young's modulus and sensitivity of the composite consisted of the ratio between crosslink agent and base material in the PDMS, and the ratio between PDMS matrix and carbon black filler in the final composite.

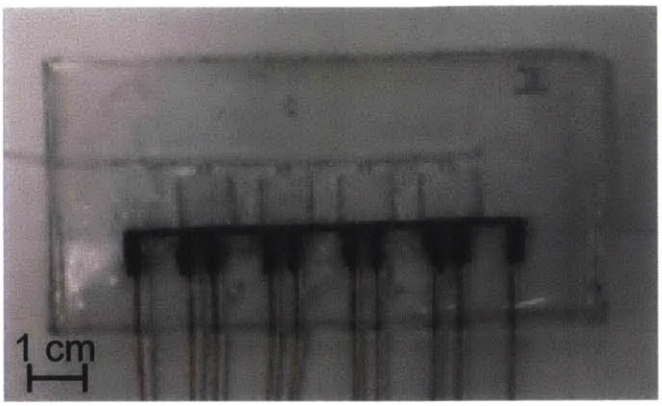

Figure 3-9: The version-one conformal pressure sensor array utilized a solid CBPDMS composite patterned in a four point probe strain gauge arrangement. To achieve the sensitivity necessary for hydrodynamic stimulus, strain enhancing diaphragms were patterned in the solid PDMS substrate. Inconsistencies in the fabrication of the diaphragms and difficulty in eliminating voids when joining substrate layers influenced the development of a new active sensing material.

Solid CBPDMS Composite

A solid CBPDMS composite was developed by Yaul et al. [94] for use as a flexible strain gauge on a PDMS sensor. For the solid composite, a mixture of PDMS (Sylgard 184) and carbon black (Cabot XC 72) was combined to produce a composition that was 14.3 percent by weight carbon black [94].

To produce a pressure sensor array, the CBPDMS composite was screen printed in a strain gauge pattern onto a pure PDMS substrate, then bonded to a second PDMS substrate containing strain-enhancing cavities to achieve the sensitivity necessary for hydrodynamic stimulus (for full fabrication details see [94] or [89]). To guard against measurement uncertainty caused by contact resistance, the four-point probe measurement technique was utilized, as shown in Figure 3-9. The resulting Version 1 sensor array, seen in Figure 3-9, achieved a sensitivity of approximately 1.21 mV/kPa during sea trials on an unmanned kayak vehicle, at a material cost of approximately $3 per sensor [26, 89]. While the solid CBPDMS composite and strain gauge geometry produced a pressure sensor array capable of operation in real-world conditions [26], it was desired to improve the active material sensitivity in order to eliminate the need for fabrication-intensive strain enhancing cavities.

Figure 3-10: The porous structure of the new active material is visible after the sacrificial sugar scaffold has been dissolved.

3.4.2 Material Development for Improved Sensitivity

Based on experience with the solid carbon black composite both in the laboratory and in the field, it was desired to develop a new composite with 1. lower Young's modulus and 2. increased piezoresistivity. Reducing the Young's modulus of the composite can be accomplished by reducing the relative amount of crosslink agent to base material in the PDMS. However, this leads to reduced creep resistance in the PDMS, impacting the reversibility of the active material and allowing for plastic deformation. For use as a pressure sensor, repeatability of measurements is of primary importance, and requires the material to behave predictably over many loading and unloading cycles. Young's modulus reduction can also be accomplished by lowering the percentage of carbon black in the CBPDMS composite. Reducing the carbon black content also has a significant impact on the piezoresistivity, and therefore the sensitivity of the composite. In order to ensure the carbon black concentration could be optimized to achieve the desired sensitivity in a new active material, it was determined that a new fabrication technique was needed to achieve reduced Young's modulus.

3.4.3 Porous (Open-Cell) CBPDMS Foam

After a review of the literature, it was determined that creating a porous CBPDMS composite would accomplish the desired reduction in Young's modulus [47, 10]. The porous composite was fabricated through the use of a sacrificial sugar scaffold which

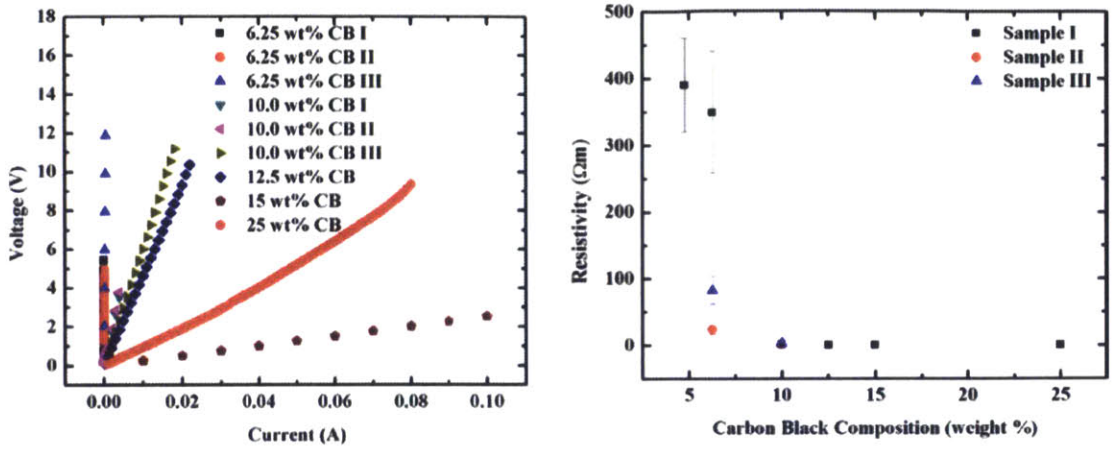

(a) The I-V plots for the various carbon black compositions for the CBPDMS composite.

(b) The resistivity of the CBPDMS composite as a function of the carbon black concentration showing the percolation threshold at 6.25% concentration by weight of carbon black.

Figure 3-11: Electrical properties of CBPDMS composite. Figures adopted from [89] and [28].

was dissolved away after the composite cured. Sugar is preferred for the creation of the sacrificial scaffold because it is inert and does not react with PDMS. Also, it can be easily removed with water, allowing for inexpensive and scalable fabrication. The fabrication of the porous composite was straightforward, adding to the appeal of the porous CBPDMS as the active material in a sensor array. First, PDMS base (Sylgard 184 from Dow Corning) was prepared and degassed in a desiccator before adding the filler particles of acetylene carbon black (catalog number 06-0026 from Strem Chemicals) and fine sugar, and mixing in a mechanical mixer. The PDMS crosslink agent was then added at a base:crosslink ratio of 10:1 by mass, and again mixed mechanically. The raw material was then cast in a mold and cured at 90°C for approximately 30 minutes. Following the complete curing of the material, the samples were soaked in a 80°C water bath for 24 hours to dissolve the sugar scaffold, leaving a porous structure as seen in Figure 3-10. To ensure all the sugar had been dissolved from the sample, acetone was used to infiltrate the porous composite. Since acetone precipitates sugar, the solution will appear to be cloudy if the PDMS-carbon black composite contains sugar, otherwise, the solution will appear to be clear.

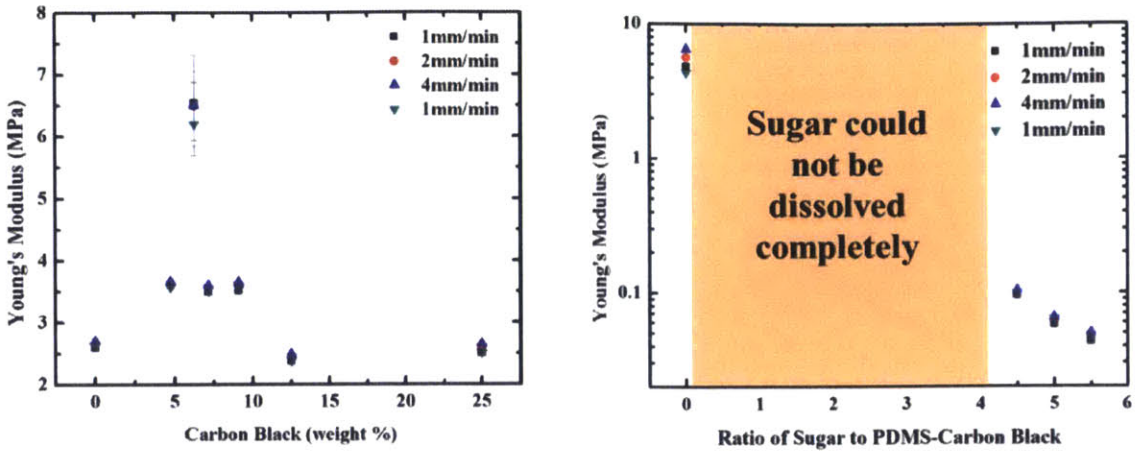

(a) The Young's moduli of different compositions of CBPDMS as a function of weight percentage of carbon black

(b) The Young's modulus of 6.25% porous CBPDMS as a function of sugar concentration.

Figure 3-12: Optimization of the mechanical properties of solid CBPDMS and CBPDMS open cell foam. Figures adopted from [89] and [28].

Carbon Black Concentration

Achieving optimal sensor performance is largely dependent on the concentration of carbon black in the CBPDMS composite. The largest change in resistivity (or the largest piezoresistivity) occurs in composites when the concentration of the conductive particles is near the percolation threshold [76, 63]. When compressive stress is applied to the composite, the deformation of the polymer matrix causes a change in distance between the conductive particles, leading to a change in conduction path and a large change in resistance [89]. To determine the percolation threshold and optimal carbon black concentration for the CBPDMS composite, current-voltage (I-V) measurements were conducted on a series of solid CBPDMS samples with varying carbon black concentrations, as seen in Figure 3-11(a). To eliminate the contribution of contact resistance to the results, a four-point probe methodology was used during all measurements to ensure accuracy [89].

From the slope of the I-V plots, the resistance (R) of each composition was determined, and the resistivity was computed as $\rho = \frac{RA}{L}$ where A was the cross-sectional area, and L the length of the sample. The largest change in resistivity, and thus the percolation threshold for the CBPDMS composite, was found to be at 6.25% by

weight carbon black concentration, as seen in Figure 3-11(b).

Following mechanical testing, it was also found that the 6.25% concentration of carbon black had the best reversibility in the change of resistance vs. pressure curve when compared to other concentrations. While the 6.25% concentration composition had optimal resistivity properties, it also had the highest Young's modulus of the tested compositions, as seen in Figure 3-12(a), reinforcing the need for the porous fabrication technique.

Sugar Concentration

Three different mass ratios of sugar in the 6.25% concentration composition were investigated (4.5:1, 5:1, 5.5:1) to determine the effect of the sugar scaffold on the Young's modulus of the composite. To create a continuous porous network in the solid CBPDMS composite, the mass of sugar must be at least four times that of the solid CBPDMS, otherwise the sugar will not completely dissolve. It was found that at a mass ratio of 5.5:1, the Young's modulus of the porous composite was reduced nearly two orders of magnitude compared to the solid composite, as seen in Figure 3-12(b).

3.4.4 CBPDMS Sensor Results

Having developed a new active material optimized for the sensitivity requirements of hydrodynamic stimulus, the material was packaged as a sensor and subjected to mechanical testing. Unlike the Version-one sensor that relied on strain enhancing diaphragms to achieve the required sensitivity for near-body flow detection, the porous CBPDMS sensor was designed as a simple 'smart skin' array with no cavities or membranes. Due to the high porosity of the new active material, it was found that special care was needed to ensure adequate contact between wires and the active material when building a sensor. Unlike the solid CBPDMS material where a single copper wire was used at each contact point of the four-point probe arrangement, the porous material used three parallel wires to maximize transmission, as seen in Figure 3-10

and Figure 3-13. To fabricate the porous CBPDMS sensors, the composite material was first mixed following the procedure outlined in Section 3.4.3. Copper wires were then embedded between successive layers of active material, as shown in Figure 3-13. After curing the active material with embedded copper wires, the entire sensor skin was soaked in warm water to dissolve the sugar matrix, leaving a porous CBPDMS array ready for electrical connections.

The experimental sensor fabricated using the porous CBPDMS material was subjected to cyclic loading on a mechanical tester with I-V measurements taken in the same four-point probe manner as during material characterization experiments. The porous material exhibited some hysteresis during the cyclic loading, but the resistance was found to return to the initial value upon unloading, demonstrating the reversibility of the material and suitability for use as a pressure sensor. With the porous CBPDMS active material and the three wire arrangement, the piezoresistivity estimated from the resistance vs. pressure plot was found to be 12 $\pm$ 1% $\Delta R/R_\circ$ per kPa for the major loop and 5.6 $\pm$ 0.2% $\Delta R/R_\circ$ per kPa for the minor loop, which represents a significant improvement over the 1.9 % $\Delta R/R_\circ$ per kPa achieved by the Version 1 sensor comprised of solid CBPDMS composite, and utilizing strain enhancing diaphragms [89].

3.4.5 Sensor Encapsulation

To enable reliable underwater operation, the porous PDMS composite required encapsulation to keep water out of the pores in the material. A successful encapsulation method provided waterproofing to the composite, while retaining the very low Young's modulus provided by the porous material. Initial testing was performed on three different encapsulation techniques: 1. pure PDMS 2. sticky wrap 3. electrical insulating spray. Of the three encapsulation methods, the use of ordinary household sticky wrap was found to be the best method due to the negligible impact its application had on the Young's modulus of the material. The pure PDMS and insulating spray, seen in Figure 3-14, decreased the Young's modulus by a factor of three and two respectively. The sticky wrap, however, allowed the Young's modulus, and thus the sensitivity of

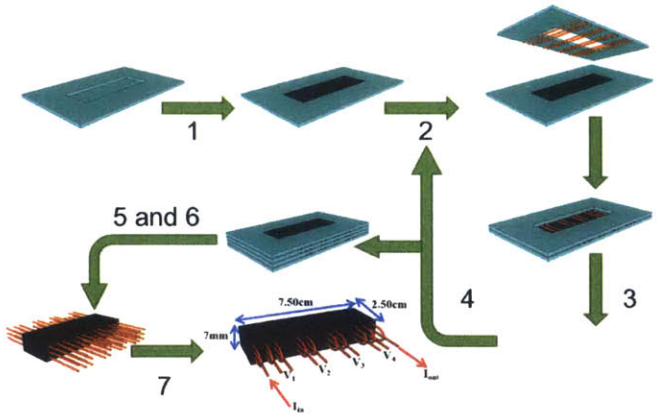

Figure 3-13: The steps involved in the fabrication of the porous CBPDMS sensor highlighting the three parallel wires used to maximize contact between the transmission wires and the active material. 1) screen print CBPDMS/sugar mixture 2) place mask with wires 3) screen print CBPDMS/sugar mixture 4) repeat for three layers 5) cure at 90°C for at least two hours 6) remove from molds 7) consolidate parallel wires and trim excess.

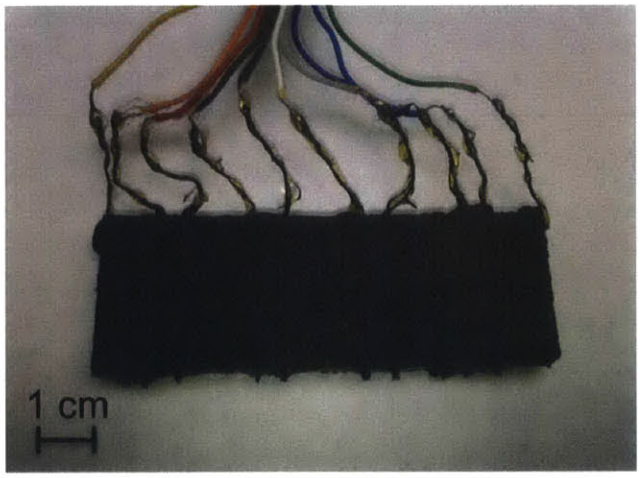

Figure 3-14: A porous CBPDMS sensor array encapsulated in a thin layer of electrical insulating spray. Insulating spray had the advantage of being very easy to apply, but was found to increase the Young's modulus of the porous active material.

the porous composite, to remain unchanged. While the sticky wrap approach worked well in mechanical testing and controlled lab experiments, the material was delicate and prone to puncture.

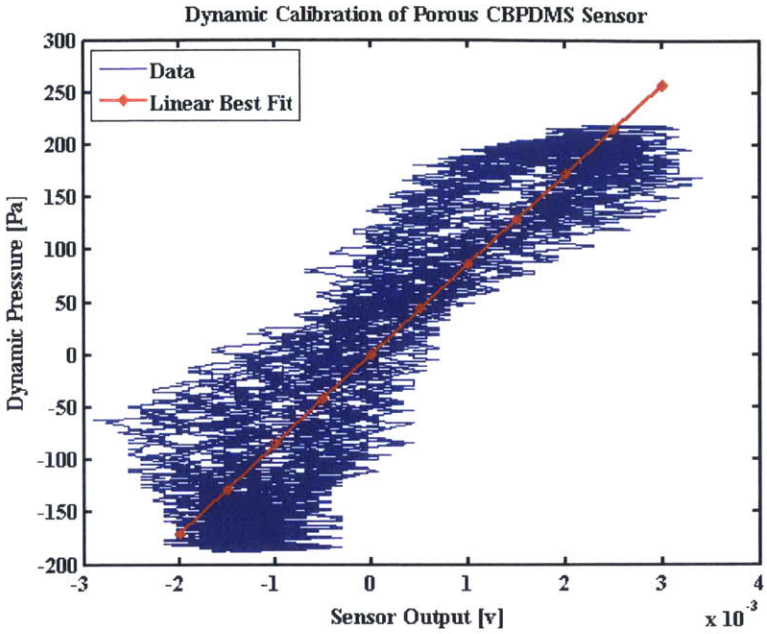

(a) A strong correlation was observed between the wave dynamic pressure and the CBPDMS voltage output. Using a linear best-fit, the sensitivity of the un-amplified sensor was found to be 11.7 mV/kPa.

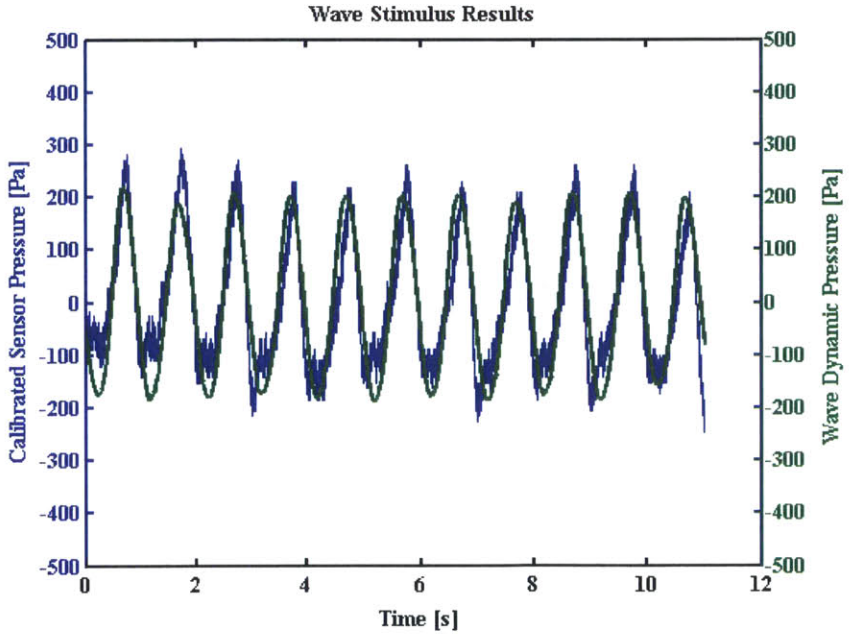

(b) After applying the dynamic calibration, the pressure sensor was found to accurately measure the magnitude and frequency of the dynamic pressure field.

Figure 3-15: Dynamic testing of a CBDPMS open cell foam pressure sensor array in the MIT towing tank using water wave stimulus.

Underwater Testing

To verify the ability of the porous CBPDMS sensor to measure hydrodynamic stimuli, the encapsulated sensors were tested in the MIT Towing Tank using a paddle-type wave maker to generate plane waves, and therefore oscillatory pressure variations at known frequencies. The experimental sensor arrays were mounted perpendicular to the wave fronts and placed at a static depth of 2.5 cm. Voltage measurements were amplified approximately 2.66 times using an AD 620 operational amplifier, and filtered using an RC filter with a cut-off frequency of approximately 100 Hz. The amplification and filtering electronics were the same as used when testing the Version 1 sensor, allowing performance comparisons to be easily made. An Op-amp circuit was used to provide a constant current source of $90\mu A$ to the sensor. Signals were collected using a National Instruments USB 6215 DAQ and Labview Signal Express software. A conductance wave probe was used to record the wave height throughout the experiments, and linear wave theory was used to calculate the dynamic pressure at the sensor array. The dynamic portion of the wave pressure is given by Equation (3.1) where η_e is the measured free surface elevation from the wave probes, k is the wavenumber, and z is the static depth of the sensor array. For the experiment shown, the wave maker was set to generate waves with a frequency of 1Hz.

$$P_{dynamic} = \rho g \eta_e e^{kz} \tag{3.1}$$

When the measured output voltage from the sticky wrap encapsulated CBPDMS sensor array was plotted against the calculated dynamic pressure, a strong correlation was present, as seen in Figure 3-15(a). To ensure an accurate assessment of the response of the the CBPDMS material to a dynamic pressure field, only the portion of the voltage time trace when a wave packet was present was used, and the mean was removed from the raw signal. Using a linear best-fit, the sensitivity of the sticky wrap encapsulated sensor without amplification was found to be 11.7 mV/kPa at a $90\mu A$ current bias. With the 2.66 times amplification included, the sensitivity was found to be 31 mV/kPa, representing a 25 times improvement over the Version 1

array sensitivity using the same amplification. Applying the dynamic calibration to the raw sensor output voltage, the pressure magnitude and frequency were found to closely match the dynamic pressure from the waves, as seen in Figure 3-15(b). Overall, it was found that the porous CBPDMS array encapsulated in shrink wrap provided an accurate measurement of the dynamic pressure field produced by water waves with an amplitude of ~400 Pa. The dynamic pressure range tested using the water wave stimulus was consistent with the range needed for unmanned marine vehicle applications, as given in Table 2.1, and demonstrated that CBPDMS foam could achieve the desired performance for hydrodynamic sensing applications. The performance of the CBPDMS sensor in response to the dynamic portion of the wave pressure demonstrates the potential for use as a conformal near-body flow sensor.

3.4.6 Two Dimensional CBPDMS Sensor Array

When considering the geometry of the lateral line on fish, it is recognized that near the head of the animal, the lateral line elements increase in density and extend vertically as well as horizontally, as seen in Figure 1-2. For many marine applications, including the helical vortex shedding on ship hulls, identifying the location of a near-body flow structure in two dimensions is necessary. To meet this need, a two-dimensional pressure sensor array was fabricated using solid CBPDMS as the active sensing material, and pure PDMS as the structural component of the sensor, as seen in Figure 3-16(a). Copper foil leads were embedded within the PDMS encapsulation to transmit power and signals, as seen in Figure 3-16(b), and the entire sensor was flexible and waterproof. The sensor array proved to be operational and responsive to manual stimulus. However, it was found that as the sensing elements were pressed manually, the contact resistance between the solid PDMS and the copper foil varied comparably to the resistance variation due to the compression of the active material. Work is ongoing to improve the two dimensional array design through the incorporation of a four-point probe measurement as used in previous iterations of the sensor, as discussed in Chapter 8. Plans also include using silver-PDMS composite transmission wires to improve flexibility and reduce contact resistance. To enhance sensitivity, it

is desired to incorporate the CBPDMS foam active material introduced in Chapter 4 into future generations of two-dimensional sensors.

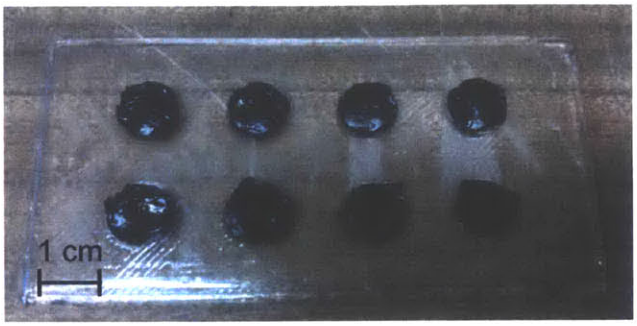

(a) Solid CBPDMS sensing elements were patterned using 3D printed molds and encapsulated within a pure PDMS matrix

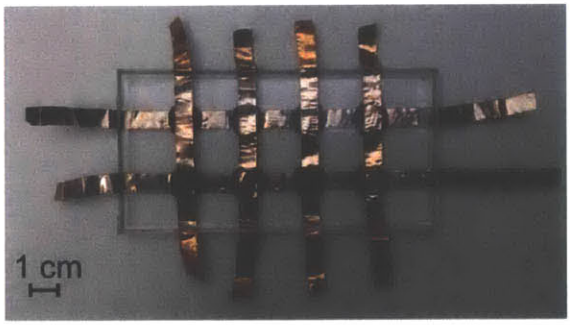

(b) Copper foil leads embedded within the pure PDMS matrix were used for power and signal transmission.

Figure 3-16: Two-dimensional pressure sensor array using solid CBPDMS composite.

3.4.7 Conclusions from First Generation CBPDMS Open-Cell Foam

Drawing on the lateral line sensory organ for inspiration, flexible, waterproof, and highly sensitive pressure sensor arrays were developed for use in marine applications. The active material used in the sensor arrays was an innovative composite of carbon black and PDMS, with an optimal concentration of 6.25% carbon black by weight. To achieve the desired sensitivity of tens of pascals required to measure hydrodynamic stimuli, porosity was introduced to the material through the use of a sacrificial sugar scaffold. This lowered the Young's modulus of the CBPDMS composite by two

orders of magnitude. Mechanical testing revealed that the porous CBPDMS composite achieved a piezoresistivity of up to 12 $\pm$ 1% $\Delta R/R_\circ$ per kPa, an increase in piezoresistivity of nearly an order of magnitude over previously reported results for CBPDMS composites.

Using the new porous CBPDMS active material, sensor arrays were tested underwater and shown to successfully measure the magnitude and frequency of the dynamic pressure field generated by water waves. During underwater experiments, a sensitivity of 31mV/kPa was recorded. This is 25 times higher than the Version 1 sensors, which utilized solid CBPDMS and strain-enhancing diaphragms. Both sensor arrays utilized the same amplification.

3.5 Lessons from Doped Polymer Smart-Skins

The development and testing of the doped polymer smart-skins conducted in collaboration with Yaul and Woo provided several lessons to be applied to the next generation of conformal hydrodynamic pressure sensor arrays. Primary among these lessons was a general need to simplify array architecture and in doing so improve robustness. The Version 1 arrays developed by Yaul [94, 95, 32] utilized a solid CBPDMS that relied on strain enhancing diaphragms to achieve the sensitivity desired for lateral line inspired hydrodynamic sensing, as described in Section 3.1. While the performance of the sensors was demonstrated in the towing tank [95] and in the field [26], the strain enhancing diaphragms were time consuming to manufacture and prone to damage, especially when the array was surface mounted on the side of a vehicle as in [26].

The benefits of the strain enhancing diaphragms were largely retained in a simplified geometry by introducing porosity into the CBPDMS composite to create an open-cell foam [28]. Without strain enhancing diaphragms, the sensor arrays were found to be extremely robust and flexible, representing an improvement over the Version 1 strain gauge arrays. The introduction of porosity introduced different problems, however, specifically the time consuming need to soak the CBPDMS for 24 hours to dissolve the sugar scaffold, and the requirement to waterproof the open-cell foam.

It was also found that the CBPDMS open cell foam sensors were thicker than desired, and required special attention to be paid to electrical connections because of the reduced contact area between the porous material and the wires. Despite these challenges, the improvement in sensitivity shown by the CBPDMS foam motivated a continued effort to develop the material for use in hydrodynamic pressure sensing applications. A summary of the lessons learned from the stage one and two development of doped polymer smart-skins is given below.

1. **Simplify**
   (a) Improvement: The development of CBPDMS foam eliminated the necessity of fabricating strain enhancing diaphragms
   (b) Failure: Dissolving a sugar scaffold was time consuming and additional wires were needed for electrical connections
2. **Improve Robustness**
   (a) Improvement: Thin diaphragms were eliminated from the sensor array
3. **Reduce Thickness**
   (a) Failure: CBPDMS open-cell foam sensors were of similar thickness to CB-PDMS strain gauge sensors
4. **Retain Sensitivity**
   (a) Improvement: A 25 times sensitivity improvement of the Version 1 array was found for CB-PDMS foam under the same amplification

3.6 Chapter Summary

Based on the results of the experiments using commercial pressure sensor arrays presented in Chapter 2, guidelines for the design of pressure sensor arrays intended for unmanned marine vehicle applications were outlined in Section 3.1. Using these

guidelines, commercially available pressure sensors were evaluated and found to not satisfy all of the needs for hydrodynamic sensing applications. In particular, most of the commercial devices were too large for surface mounting on the outside of a marine vehicle hull, and required additional waterproofing for exposed applications. The cost of commercially available devices was also a concern, with the commercial sensors used in the towing tank and unmanned kayak vehicle experiments costing between ~$100 and ~$200 per sensor, making spatially dense arrays economically infeasible.

Pressure sensor arrays inspired by the lateral line sensory organ were reviewed, and found to fall into two main categories, arrays that mimicked the physiology of the lateral line, and those that drew on the broad principle of distributed pressure sensing. Based on this review of alternative sensor technologies, the use of a doped-polymer 'smart-skin' sensor stood out as a promising approach to pressure sensing on marine vehicles. The collaborative development of soft sensor arrays using a carbon black-PDMS composite material set was discussed, and the ability to increase the sensitivity of the composite through the addition of porosity was introduced. Based on testing of first-generation open-cell foam sensor arrays in the MIT towing tank, areas of improvement for next generation hydrodynamic sensor arrays were identified.

Chapter 4

Closed-Cell CBPDMS Foam Sensor Development

4.1 Goals for Next Generation CBPDMS Foam Sensor

Experience gained from the collaborative development of the doped polymer 'smart-skin' arrays described in Section 3.4 informed and motivated the development of a next generation closed-cell CBPDMS foam array for hydrodynamic sensing applications. While previous generations of CBPDMS sensors demonstrated the validity of the material set for pressure sensing applications, several areas of improvement remained for use in ocean engineering applications. Primary among these areas of improvement was the need to develop an inherently waterproof active sensing material that retained or improved upon the sensitivity of the open-cell CBPDMS foam described in Section 3.4.3. The need to waterproof the open-cell CBPDMS foam material was detrimental to its practical use in marine applications by adding an additional fabrication step and increasing the time and cost of sensor production. After investigating several sensor array encapsulation materials, including pure silicone and aerosol insulating spray, it was found that sealing the array with household sticky wrap worked best in the laboratory environment. The sticky wrap had little to no

impact on the Young's modulus of the open-cell foam, allowing the sensitivity gains achieved by the introduction of porosity to remain. The use of sticky wrap as a long term solution to the encapsulation problem was not viewed as practical, however, as the thin film was too susceptible to damage for use in a real world environment.

Another goal of the sensor array development was to improve the contact method between the active piezoresistive sensing material and the electrodes used to provide current to the array and measure voltage drop as a response to pressure stimulus. The sensor arrays developed utilizing open-cell CBPDMS foam relied on an arrangement of three parallel wires within the thickness of the array to maximize contact area between the foam and the wires, as described in Section 3.4.4. This solution was not ideal, as it required array fabrication to be done in a time-intensive three-layer process. Additionally, the three independent parallel wires needed to be spliced together and connected to longer transmission lines to provide current or pass voltage to data acquisition equipment. Eliminating the need for multiple independent wires was viewed as an important step in improving the array's performance, reducing the fabrication time, and improving robustness.

The goals of the next-generation sensor development are summarized below:

1. Retain or improve upon sensitivity of open-cell CBPDMS foam
2. Eliminate the need for additional waterproofing layers
3. Improve contact between electrodes and piezoresistive material
4. Improve robustness of the sensor array and associated electrical wiring

4.2 Closed-Cell CBDPMS Foam Sensor Arrays

Carbon black-PDMS closed-cell foam pressure sensor arrays were fabricated using alternating segments of piezoresistive CBPDMS foam and silver-carbon black-PDMS (Ag-CBPDMS) electrodes, as seen in Figure 4-1. A four point probe arrangement was used (described in Section 4.5.2), creating a 4x1 linear array of sensor channels, as seen in Figures 4-1(b) and 4-1(c). The overall footprint of the array was 80 mm by 20mm, with each piezoresistive foam sensor channel having a width of 5 mm,

Sensor	Channels	Footprint [mm]	Active Layer Thickness [mm]	Overall Thickness [mm]	Mass [g]
Thin	4	80 x 20	3.175	6.2	15
Thick	4	80 x 20	4.763	7.8	20

Table 4.1: Physical dimensions of the CBPDMS foam sensor arrays.

and Ag-CBPMS electrodes having a width of 4 mm as seen in Figure 4-1(c). Each sensor array was composed of three layers, a pure PDMS base layer, a middle active layer that contained the electrodes and CBPDMS foam sensor channels, and a thin CBPDMS foam top layer, as seen in Figures 4-1(a) and 4-1(d). The height of the middle active layer was varied to create a thick sensor with a 4.763 mm active layer and overall thickness of 7.8 mm, and a thin sensor with a 3.175 mm active layer and overall sensor thickness of 6.2 mm. A complete description of the sensor geometry for the thick and thin CBDPMS foam sensor arrays can be found in Table 4.1. To supply current to the sensor array and allow for voltage measurements, ribbon cable ends were embedded in the Ag-CBDPMS electrodes, as seen in Figure 4-1(a).

4.3 CBPDMS Foam Array Sensing Principle

The CBDPMS foam pressure sensor arrays rely on the piezoresitivity, or variation in resistance with strain, of carbon black doped PDMS (silicone) to provide a measurement of pressure stimulus. Each component composite in the sensor array utilizes PDMS as the matrix material, ensuring strong bonding between sensor components while retaining overall array flexibility. By varying the carbon black doping and Young's modulus between sections of the sensor array, a linear four by one array of sensor channels was created. Electrodes were fabricated using a silver-carbon black-PDMS (Ag-CBPDMS) composite with a high mass fraction of silver to ensure high conductance and low piezoresistivity, as a discussed in Section 4.5.3. Sensing elements were fabricated using a closed-cell CBPDMS foam (Section 4.5.4) with a low Young's modulus and carbon black concentration near the percolation threshold to enhance piezoresistivity and improve the sensitivity of the array to hydrodynamic stimuli.

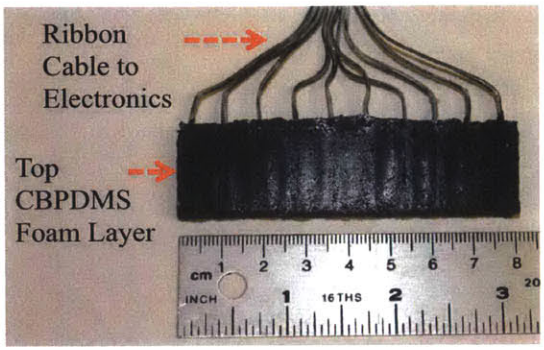

(a) The top of the CBPDMS foam sensor array is covered with a thin layer of CBPDMS foam. The ends of a ribbon cable are embedded in a Ag-CBPDMS electrodes to supply the array with a constant current and to allow for for voltage measurements to be taken across the piezoresistive CBPDMS foam sensor channels.

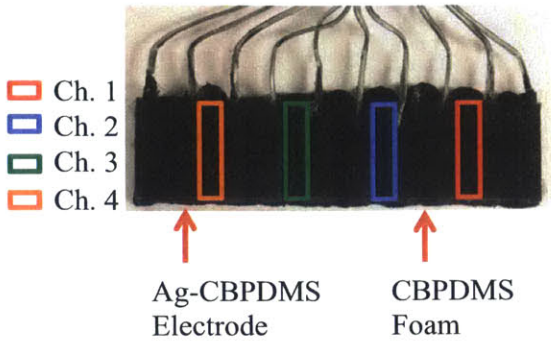

(b) Viewed from the bottom, the middle active layer of the CBPDMS foam sensor array is visible through the clear solid PDMS base layer. The active layer is composed of alternating blocks of piezoresistive CBPDMS foam, and Ag-CBPDMS electrodes. The sensor array uses a four-point measurement to eliminate the effects of contact resistance in voltage measurements and is a linear array of four channels.

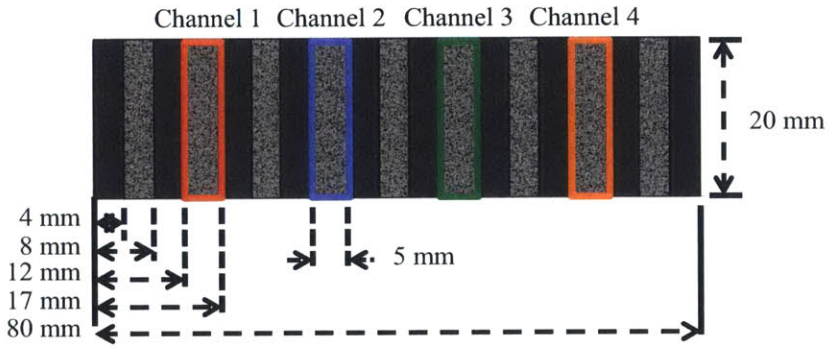

(c) The overall footprint of the CBPDMS foam array is 80 mm by 20mm, and each sensor channel is 5 mm wide while electrodes and non-sensor foam sections are 4 mm wide

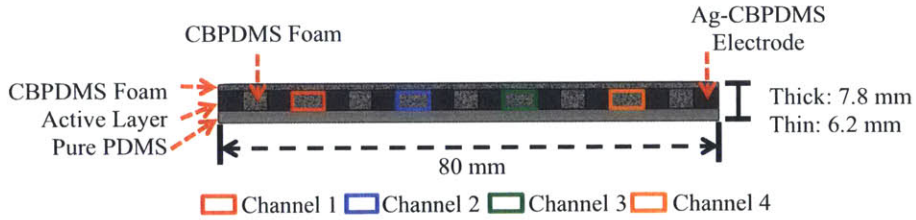

(d) Each CBPDMS foam array is composed of three layers. A 2 mm layer of pure PDMS provides a flexible base to the array and allows for surface mounting to curved surfaces. The active middle layer is composed of CBPDMS foam sensor channels and Ag-CBPDMS electrodes, and active layer thicknesses of 4.763 mm and 3.175 mm have both been tested. The top lower of the device is a 1 mm thick layer of CBPDMS foam created during the foam expansion process.

Figure 4-1: Carbon black- PDMS closed-cell foam pressure sensor arrays were fabricated using alternating segments of piezoresistive CBPDMS foam and silver-carbon black-PMDS (Ag-CBPDMS) electrodes with a pure PDMS base layer to preserve flexibility.

4.4 Models of Carbon Black Doped Silicone Piezoresistivity

Above a mass fraction of carbon black known as the percolation threshold, carbon black doped PDMS forms a conductive composite. When the percolation threshold is reached, continuous chains of carbon black particles create conductive pathways through the PDMS bulk material; while below the percolation threshold, CBPDMS composite behaves like an insulator. The piezoresistive behavior of CBPDMS relies on the formation and breakdown of these conductive chains as the PDMS matrix material is deformed due to external stimulus.

Two primary models are used to describe the resistance change of CBPDMS composite when subjected to an external pressure stimulus, as summarized by Lacasse [54] and shown in Figure 4-2. Both piezoresistive effects have been observed in CBPDMS composites, and the relationship between resistance and strain is highly dependent on the filler material, the type of polymer matrix, and the nature of the loading [54].

Compressible Model The compressible model of CBPMS piezoresistivity, shown in Figure 4-2(a), states that as the PDMS matrix is compressed due to external pressure stimulus, the volume fraction of CB particles within the composite is increased, allowing for the formation of new continuous conductive pathways and decreasing the resistance of the composite ([54, 44, 5]). When the external pressure stimulus on the composite is decreased, the material relaxes, and the newly formed conductive pathways are broken, leading to a recovery of the composite resistance.

Incompressible Model The incompressible model of CBPMS piezoresistivity, shown in Figure 4-2(b), states that small deformations in the PDMS matrix due to compressive strain cause a breakdown of conductive pathways within the CBPDMS composite, leading to an increase in resistance ([54, 24]). When strain is relieved from the composite, the conductive pathways reform in a reversible process.

For the CBDPMS foam used in the fabrication of the distributed pressure sensor arrays, piezoresistive behavior consistent with both the compressible and

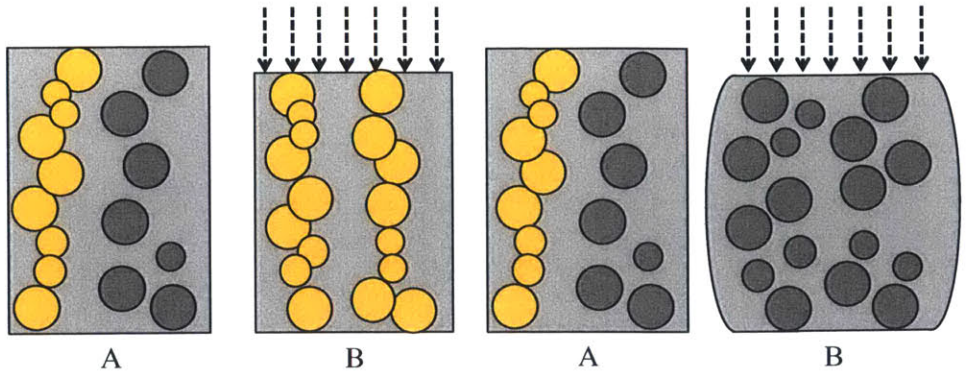

(a) The compressible model of CBPDMS piezoresistivity in which the PDMS matrix is compressed under load, leading to an increased volume fraction of CB particles in the composite and the formation of new conductive pathways, leading to a decrease in resistance.

(b) The incompressible model of CPDMS piezoresistivity in which small deformations of the PDMS matrix leads to reversible destruction of carbon black conductive pathways within the composite, leading to an increase in resistance.

Figure 4-2: Comparison of the two primary models used to explain the change in resistance in CBPDMS composites when subjected to a pressure stimulus. The light grey boxes represent the PDMS foam bulk material, and dark grey circles represent free carbon black (CB) particles that have not formed conductive chains. The gold circles represent CB particles that have linked together to form continuous conductive pathways through the bulk PDMS foam matrix. For the CBDPMS foam pressure sensor array responding to isotropic hydrodynamic stimulus, the resistance is expected to change in accordance with the compressible model.

incompressible models has been observed for different sample geometries and loading cases. For cubes of CBPDMS foam tested in pure compression on a mechanical tester, the piezoresistivity was consistent with the incompressible model, as discussed in Section 4.6.2. For the complete CBPDMS foam pressure sensor array responding to isotropic hydrodynamic stimuli, the resistance was found to change in accordance with the compressible model, as discussed in Chapter 5.

4.4.1 DC Response of CBPDMS Composite

Carbon black-PDMS composites provide a reversible piezoresistive response to dynamic pressure stimulus, but are not well suited for low frequency, DC type stimulus.

Over time at a continuous strain, conductive pathways reform within the material, leading to a gradual decrease in resistance [24]. This recovery of conductive pathways takes place over a period on the order of tens of minutes[24], effectively acting as a high pass filter. Efforts have been made to characterize the low frequency behavior of CBDPMS composites through the use of Burger models and modifications of the Burger model by Yaul [95] and Lacasses [54]. The hydrodynamic pressure stimuli of interest to marine vehicles typically have frequencies ranging from 0.5 Hz (water waves, vortex shedding) to 35 Hz (predator and prey detection), and the dynamic response of the CBPDMS foam sensor arrays will be the focus of this study.

4.5 Sensor Fabrication

4.5.1 CBPDMS Foam Array Fabrication Steps

The general steps associated with the fabrication of a closed-cell CBPDMS foam sensor array are given below and in Figure 4-3. The details of the fabrication steps will be described in subsequent sections.

1. Prepare ribbon cable for current and voltage transmission by separating ribbon into individual cable ends and winding bare wire into helical "pig tails" which improve the electrical and mechanical connection to the Ag-CBPDMS electrodes.

2. Mix silver-carbon black-PDMS (Ag-CBPDMS) composite for electrodes using a mechanical mixer, as discussed in Section 4.5.3.

3. Apply uncured Ag-CBPDMS electrode material to delrin electrode mold and cure in oven (Figures 4-3(a) and 4-5(a)). The overall thickness of the CBPDMS foam array is determined by choosing an electrode thickness of 3.175 mm (1/8") or 4.763 mm (3/16").

4. After trimming the cured electrodes and returning them to the mold, apply a 2 mm layer of pure PDMS over the electrodes to serve as a flexible base for the

sensor array (Figures 4-3(b)).

5. Remove electrodes and pure PDMS base layer from delrin mold. With the electrodes facing up and the pure PDMS base layer on the bottom, return electrodes to the mold in preparation for the CBPDMS foam (Figures 4-3(c) and 4-5(b)).

6. Mechanically mix CB into part A of foaming silicone to ensure uniform distribution of conductive CB particles throughout the composite.

7. Mix A and B components of foaming silicone to initiate the expansion reaction, and manually spread the CBPMS foam into the gaps between Ag-CBPDMS electrodes (Figure 4-3(d)).

8. Cap the mold with an aluminum top plate, leaving a 1mm gap to allow CBPDMS foam to escape the mold during the expansion process.

9. After allowing for the complete cure of the CBPDMS foam, de-mold the array and trim the excess foam created during the expansion reaction.

4.5.2 Electrode Layout and Material Selection

Electrode layout and material selection were driven by the need to eliminate the effects of contact resistance and maximize the conduction between the electrodes and the CBPDMS foam active sensing material while retaining overall array flexibility. To eliminate contact resistance, a four point probe arrangement was utilized. In a four point probe, a pair of outside leads act as a constant current source, while inner lead pairs are used to take voltage measurements, as seen in Figure 4-4. In this arrangement, virtually no current flows in the measurement leads, meaning the voltage drop due to the contact resistance between the measurement leads and the CBPDMS foam is negligible, allowing the the resistance variation with strain of the CBDMS foam to be isolated.

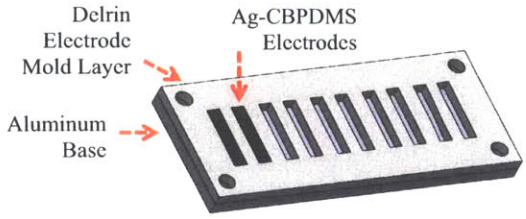

(a) After mixing the components of the Ag-CBPDMS, the uncured composite was spread into a delrin mold, taking special care to ensure no voids were present in the material. Stripped ribbon cable ends were embedded in the uncured composite, and the delrin mold was capped with an aluminum plate to compress the Ag-CBPDMS into any remaining gaps and hold the wires in place during the curing process. The electrodes were cured in an oven at 120°c for approximately two hours, then allowed to cool completely before being removed from the mold.

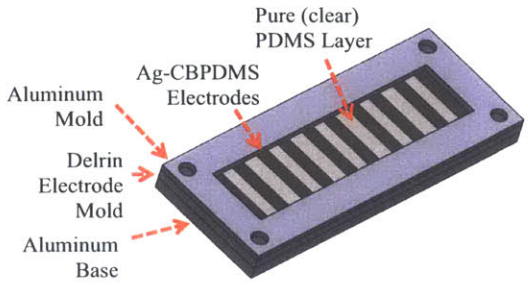

(b) After the Ag-CBPDMS electrodes were cured, they were individually removed from the delrin mold, trimmed, and returned to the cleaned mold. A 2mm layer of pure PDMS was then applied on top of the electrodes to hold them in place during the remainder of the fabrication process and to serve as a flexible base for the finished sensor array.

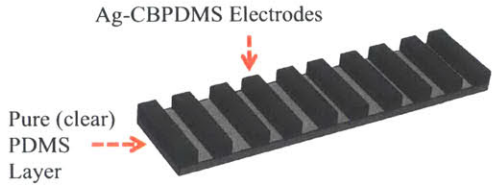

(c) After the pure PDMS base layer was cured in the oven for 20 minutes, the electrodes and base layer were removed from the mold and flipped over so the pure PDMS was on the bottom and gaps between the electrodes were accessible.

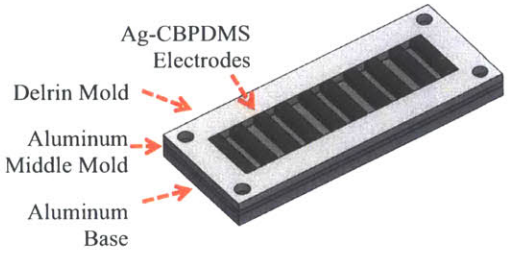

(d) After returning the electrodes and base layer to the mold, uncured CBPDMS foam was manually spread into the gaps between the electrodes before the foam expansion process took place. With the uncured CBPDMS foam expanding to fill the electrode gaps, an aluminum top plate was placed on the mold with a small gap preserved by washers to allow the excess foam to escape during expansion.

Figure 4-3: Fabrication steps for CBPDMS foam sensor arrays.

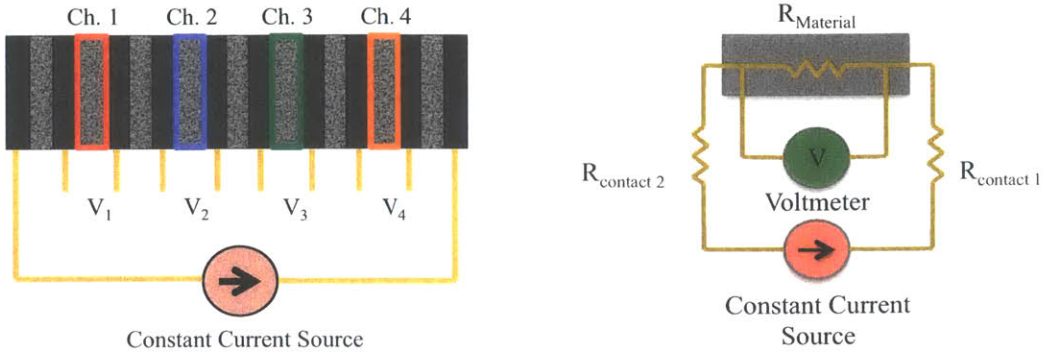

(a) The CBDPMS foam sensor arrays were connected in a four point probe arrangement to eliminate the impact of contact resistance on the voltage measurements. The leads connected to the outside electrodes provided constant current to the array, while pairs of inner leads and electrodes provided a voltage measurement across each of the CBPDMS foam sensor channels.

(b) In a four point arrangement, virtually no current flows in the measurement leads, meaning the voltage drop due to the contact resistance between the measurement leads and the CBPDMS foam is negligible, allowing the the resistance variation with strain of the CBDMS foam to be isolated.

Figure 4-4: A four point probe measurement was used to eliminate the impact of contact resistance on voltage measurements.

When making electrical connections to CBPDMS foam, the contact area between the electrode and the foam sensing material plays a large role in the quality of voltage measurements [28]. To maximize contact between the electrodes and the CBPDMS foam, electrodes spanned the full height of the sensor array and were embedded within the foam, as seen in Figure 4-5(c). To retain array flexibility and maximize adhesion between the electrodes and the CBPDMS foam, electrodes were fabricated from a silver-carbon black-PDMS composite (Ag-CBPDMS). The use of silver and a high carbon black concentration within the electrode ensured a composite with high conductivity that was insensitive to strain. By retaining PDMS as the bulk material in the composite, the electrodes remained flexible and excellent adhesion was observed between the electrodes and CBPDMS foam.

To allow for communication with the sensor arrays, ribbon cables were embedded in the AG-CBDPMS electrodes. Prior the embedding the stripped wire ends in the composite, the wires were tightly wound into "pigtails", which both maximized the contact area between the wire and the AG-CBPDMS, and enhanced the mechanical bond between the components.

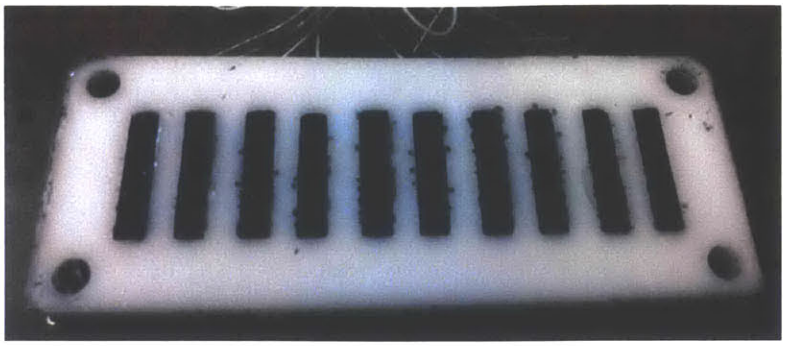

(a) Following initial difficulties removing Ag-CBPDMS electrodes from aluminum molds, delrin molds were machined using a water jet for use in electrode fabrication. It was found that electrode quality was improved by removing the Ag-CBPDMS electrode blocks from the delrin mold after curing, trimming the electrodes and cleaning the mold, then returning the electrodes to the mold for application of the pure PDMS base layer.

(b) A 2 mm thick pure PDMS base was used to hold the electrodes in place during the fabrication process and to give the finished array a smooth and flexible base for mounting to marine vehicles. The use of PDMS throughout the fabrication process ensured reliable bonding between sensor components while preserving a high degree of flexibility. A prototype sensor array is shown before wiring was switched to ribbon cables.

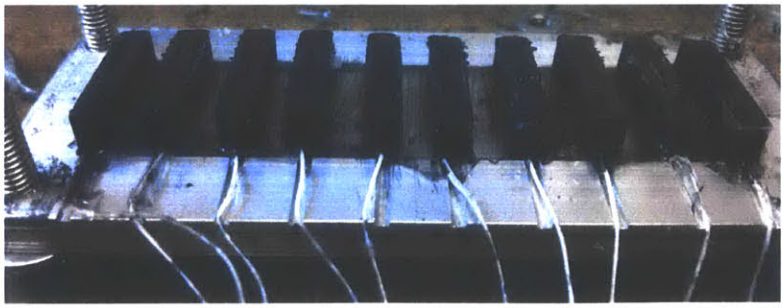

(c) After the pure PDMS base layer was applied to the Ag-CBPDMS electrodes and allowed to cure, the electrodes were returned to the mold in preparation for the gaps between the electrodes being filled with piezoresistive CBPDMS foam.

Figure 4-5: To maintain overall sensor array flexibility while providing maximum conductivity and adhesion with the CBPDMS foam piezoresistive material, electrodes were fabricated from a Ag-CBPDMS composite.

4.5.3 Electrode Fabrication

The first step of the sensor array fabrication process was to mold the electrodes from AG-CBPDMS. To prepare the AG-CBDPMS, silver powder (Number 11402 from Alfa Aesar) was mixed with PDMS (Sylgard 184 from Dow Corning) and carbon black (from Denka Elastomer and Performance Plastics) at a composition of 72.94% AG, 3.79% CB, and 23.27% PDMS by mass in a Kurabo Mazerustar KK series mixer. The uncured AG-CBPDMS mixture was manually spread into a delrin mold with an aluminum base plate, as seen in Figure 4-5(a). Wires were embedded in each uncured electrode, and the mold was capped with an aluminum top plate before being cured in an oven at 120°c for approximately two hours.

Following curing and cooling, excess AG-CBPMS was carefully trimmed using a razor, and the electrodes were individually removed from the delrin mold, allowing any excess material to be trimmed using a razor blade. After the delrin mold was cleaned, electrodes were reinserted, and a 2 mm layer of pure PDMS was applied over the electrodes to serve as a structural base for the sensor array, as seen in Figure 4-5(b). After curing the pure PDMS in the oven for approximately 20 minutes, the completed electrode layer was able to be removed from the mold, as seen in Figure 4-5(c).

4.5.4 CBPDMS Foam Fabrication

The CBPDMS foam used in the pressure sensor arrays was fabricated using Soma Foama 15 from Smooth-On. Soma Foama is a two-component platinum silicone casting foam that is available in both 240 kg/m^3 (15 lb/ft^3) and 400 kg/m^3 (25 lb/ft^3) densities, as seen in Figure 4-6(a). The Soma Foama 15 was found to be the more compressible of the two weights, and it expanded 3-4 times its initial volume when mixed, as seen in Figure 4-6(b). Because the foaming reaction was rapid when the two components of the silicone were mixed, working time was very limited, and advanced preparation of all molds was required to ensure successful fabrication. Soma Foama 15 is the lower density of two versions of Soma Foama offered by Smooth-On,

and used a 2:1 ratio of the A:B silicone components by volume or weight. Because part A of the mixture is used in higher volume than part B, carbon black particles were mechanically mixed into Part A in advance of the foaming reaction using the Mazerustar mixer shown in Figure 4-6(c).

When ready to mold the CBPDMS foam sensing layer, Soma Foama Part B was mixed into the Soma Foama Part A-carbon black mixture by hand, taking care to ensure thorough mixing of the two components. The mixture was then spread into the gaps between the AG-CBPDMS electrodes, and the molds were capped with an aluminum plate. A small gap was maintained between the electrode layer and the top plate using aluminum washers, allowing the foam mixture to expand out the sides of mold after the electrode gaps were filled and leaving a uniform layer of foam across the top of the array, as seen in Figure 4-1(a). After allowing the completed array to cure for approximately 12 hours, the excess foam was trimmed away from the array, and the edges of array were coated in a thin layer of pure PMDS to insulate the exposed electrode edges from exposure to the environment.

After completing the fabrication process, sensor arrays were initially tested on the bench top to verify the operation of each array channel. The CBPDMS foam sensor arrays were found to have a high degree of flexibility, as seen in Figure 4-7(a), and the operation of the sensor arrays underwater was confirmed by testing the arrays while submerged in a shallow petri dish. A more comprehensive experimental characterization of the CBPDMS foam arrays can be found in Chapter 5.

4.6 CBPDMS Foam Material Properties

The material properties of PDMS foam and CBPDMS foam composite were studied by MIT undergraduate Jessica Herring for her Bachelor's thesis in the Materials Science Department [41]. The mechanical and electrical properties of the CBPDMS Foam, shown in detail in Figure 4-8, were investigated using an Admet mechanical tester capable of recording position and force, as seen in Figure 4-9(a). To measure the electrical properties of the material, a Keithly 2602 System SourceMeter was

(a) Closed-cell CBPDMS foam was produced using Soma Foama, a two part platinum silicone foam from Smooth-On.

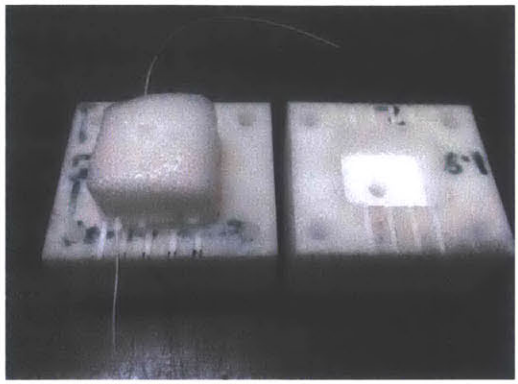

(b) Without CB particles mixed into the material, the bubbles generated during the Soma Foama expansion were clearly visible. Pure Soma Foama 15 was found to expand 3-4 times its initial volume, and the expansion was found to decrease as the percentage of CB was increased.

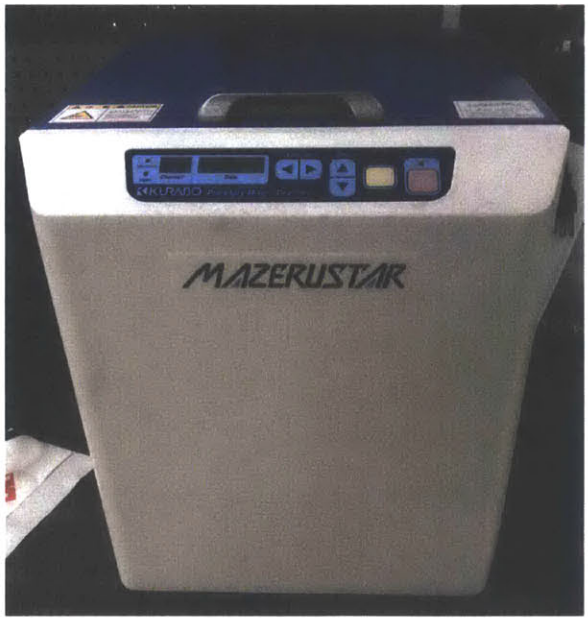

(c) During fabrication, CB particles were mixed into Part A of the Soma Foama silicone foam using a Mazerustar high speed mixer to ensure even distribution of particles throughout the composite.

Figure 4-6: The commercially available silicone foam "Soma Foama" from Smooth-On was the base material used in the fabrication of closed-cell CBPDMS foam. The silicone foam is available in 240 kg/m^3 (15 lb/ft^3) and 400 kg/m^3 (25 lb/ft^3) densities, and the 240 kg/m^3 density material was chosen for use in the fabrication of CBPDMS foam pressure sensor arrays.

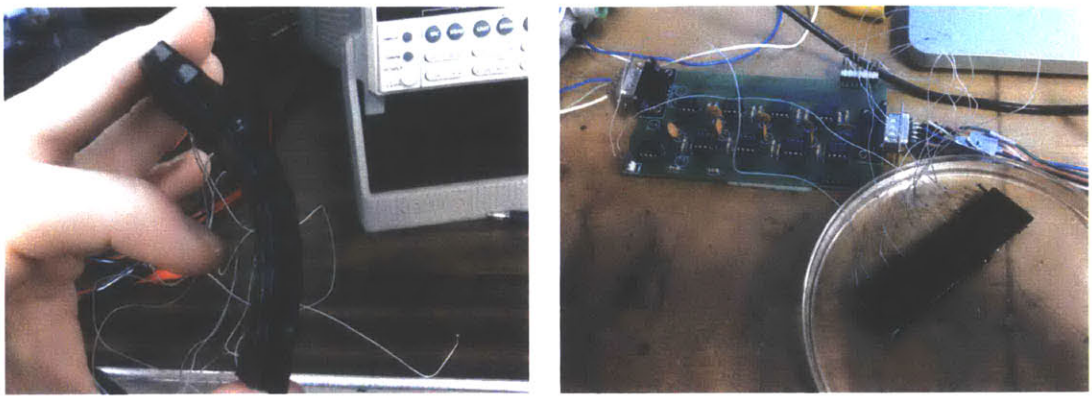

(a) Initial confirmation of the array flexibility. (b) Initial bench top testing of the array underwater using a petri dish.

Figure 4-7: Initial tests of prototype closed-cell CBPDMS foam sensor array.

used to generate a constant current and capture voltage measurements in a four-point arrangement as shown in Figure 4-4. Samples for testing were 25.4 mm cubes prepared in a delrin mold with wires embedded within the material at the half-height plane, as seen in Figure 4-9(b).

4.6.1 CBPDMS Foam Mechanical Properties

Using the ADMET mechanical tester, stress-strain curves were developed for pure 240 kg/m^3 (15 lb/ft^3) Soma Foama, and for composites with carbon black concentrations ranging from 4% to 5.5%, as seen in Figure 4-10. As expected for a silicone composite, the stress-strain curve for each sample was found to be non-linear, particularly at low levels of stress consistent with the hydrodynamic stimulus of interest. Additionally, it was found that the stiffness of the composite increased with the introduction of carbon black dopant in the composite. This result reinforced the desire to keep the weight percentage of carbon black as low as possible while staying above the percolation threshold.

4.6.2 CBPDMS Foam Electrical Properties

The piezoresistivity of the CBPDMS foam composite was tested using four wires inserted into the mid-plane of the composite blocks in a four-point probe arrangement,

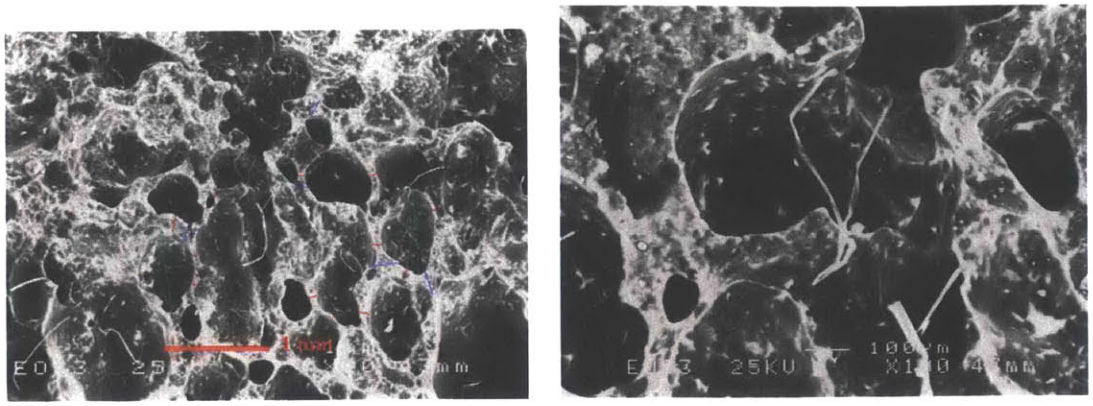

(a) Under 20x magnification, the cell structure of the closed-cell CBPDMS foam is clear.

(b) Under 100x magnification the non-uniform shape of the cell walls within the material is revealed. The non-uniformity of the cellular structure has an impact on mass percentage of the percolation threshold for the composite, and contributes to slight variations in sensitivity between the array channels.

Figure 4-8: Under magnification the cellular structure of the CBPDMS foam structure is apparent. The cellular structure reduces the Young's modulus of the material compared to solid PDMS, enhancing the sensitivity of the CBPDMS foam active material. The use of a waterproof closed-cell foam is of great importance in the use of the sensor arrays in marine applications.

as seen in Figure 4-9(b). Of primary interest was determining the percolation threshold for the CBPDMS composite before fabricating complete sensor arrays. Based on previous studies by Woo [89] and Yaul [95], tests were restricted to weight percentages of carbon black of 4% to 5.5%. Samples were tested in pure compression on the ADMET mechanical using sinusoidal and ramp stimulus. The CBPDMS foam was found to react to the compressive stimulus in accordance with the incompressible model discussed in Section 4.4, with the resistance increasing with stress, as shown in Figure 4-11 for the composite with 5.5% by weight of carbon black. It was also found that the 5% and 5.5% carbon black by weight samples performed the best, leading to the use of 5% carbon black in the final sensor arrays.

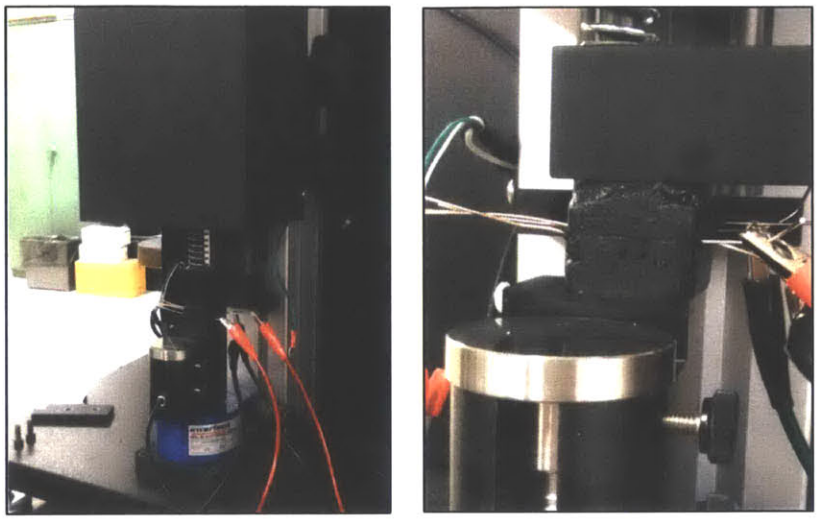

(a) An Admet mechanical tester was utilized to measure the stress-strain relationship and electrical properties of CBPDMS foam samples.

(b) Wires were embedded in the mid-plane of the CBPDMS cubes in a four-point probe arrangement in order to measure the change in resistance of the material when subjected to compressive strain.

Figure 4-9: Cubes of CBPDMS foam with varying concentrations of carbon black were tested for mechanical and electrical properties using an ADMET mechanical tester.

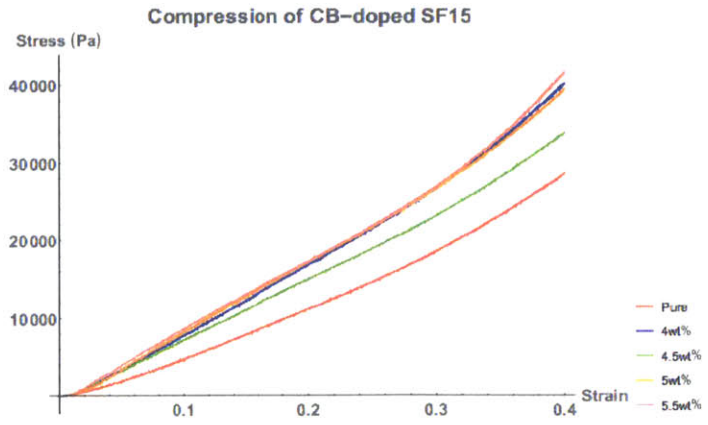

Figure 4-10: Stress-strain curves for 240 kg/m^3 (15 lb/ft^3) Soma Foama platinum silicone with increasing weight percentage of carbon black. The stress-strain curve was found to be non-linear, and the stiffness of the composite was found to increase with presence of carbon black dopant. Results suggest that the weight percentage of carbon black may be proportional to the composite stiffness, although variations in molding and the presence of air pockets in the samples may also have an effect on the stress-strain curve.

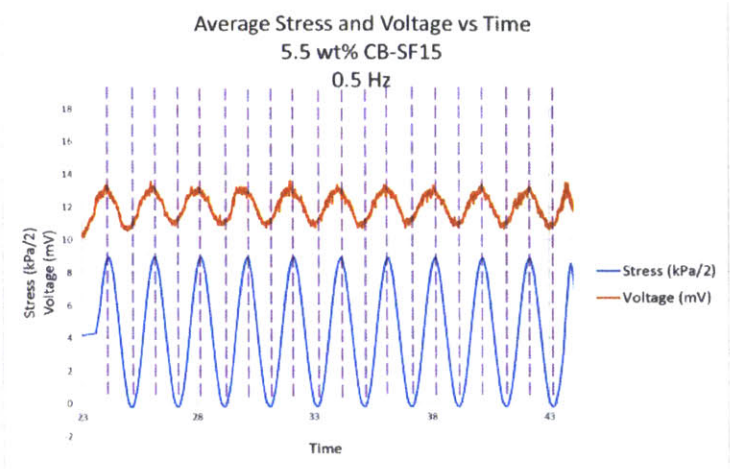

Figure 4-11: The response of 5.5 % by weight CBPDMS foam composite in compression is consistent with the incompressible model of piezoresistive response.

4.7 Chapter Summary

Conformal pressure sensor arrays for use in a marine environment were fabricated using a silicone-based material set. The pressure sensitive components of the array utilized a closed-cell piezoresistive CBPDMS foam, while the sensor array electrodes were composed of a silver-carbon black-PDMS composite that displayed high conductivity with low piezoresistivity. The array utilized a pure PDMS base layer to provide support during the fabrication process, and to allow for surface mounting using silicone adhesives. The array utilized a four-point probe measurement technique to mitigate the effects of contact resistance, and electrical connections were provided by a ribbon cable embedded in the Ag-CBPDMS electrodes. Overall sensor array dimensions were 80mm x 20mm with thicknesses of 7.8 and 6.2 mm, and four sensor channels were contained in the array.

The physical dimensions and cost of the CBPDMS foam sensor array compared favorably to commercially available sensor options, as seen in Figure 4-12. For use in hydrodynamic sensing applications, the need for the sensor array to be waterproof is of great importance, as is the ability to surface mount the array on a curved surface typical of marine vehicles and structures. Additionally, for large-area distributed sensing, the price per sensor is vital and the material cost of the CBDPMS foam array

	Cost per Sensor	Waterproof	Size	Flexible	Surface Mountable	Sensitivity ~10 Pa
Closed Cell CBPDMS Foam 	~$10.00 (4x1) ~$5.75 (7x1)	Yes	5 mm x 20mm per channel X 6-8 mm height	Yes	Yes	Yes
Freescale Semiconductor MPXV 	~$14.00	No	10 mm x 10mm footprint X 13 mm height	No	No	Yes
Honeywell 19mm Series 	~$120.00	No	19mm diameter X 31 mm height	No	No	Yes
Honeywell SPT Series 	~$250.00	Yes	22 mm diameter X 70 mm height	No	No	Yes

Figure 4-12: The physical dimensions and cost of the CBPDMS foam sensor array compare favorably to commercially available sensor options.

(~$10) represents an order of magnitude decrease over the stainless steel piezoresistive sensors offered by Honeywell (19mm and STP series), and a slight reduction over the MPXV series sensors from Freescale Semiconductor. The dynamic performance of the CBPDMS foam sensor arrays will be discussed in detail in subsequent chapters.

Chapter 5

CBPDMS Foam Sensor Array Characterization

5.1 Introduction

To characterize the performance of the CBPDMS foam sensor arrays, a series of experiments were conducted with the sensor arrays operating underwater and using biologically-inspired hydrodynamic stimulus. Experiments using the CBPDMS arrays could be broadly categorized into three main types:

1. Characterization and calibration experiments using periodic stimulus (Chapter 5)

2. Dipole experiments using a vibrating sphere (Chapter 6)

3. Vortex detection in the wake of a circular cylinder (Chapter 7)

In Chapter 5, experiments using simple periodically varying pressure stimulus meant to investigate sensor response characteristics and develop a sensor calibration will be discussed. In Section 5.3, a time-varying hydrostatic pressure was created by oscillating the sensor arrays vertically in the water column using a computer controlled linear stage. From these experiments the basic operating characteristics of

the sensor arrays were studied, and the dynamic range of the arrays was investigated. The repeatability of the sensor arrays was confirmed, and a sensor calibration was developed. In Section 5.4, the CBPDMS sensor arrays were placed at a fixed depth and surface water waves were generated by the wave maker in the MIT towing tank, creating an oscillatory pressure stimulus that is ubiquitous in nature. From the water waves experiments the performance characteristics established during the plunging experiments were confirmed, the operation of the sensor arrays while surface mounted on a curved body was investigated, and the sensor calibration found during the plunging experiments was verified.

5.1.1 Characteristics of a Successful Sensor

During the experiments to characterize the CBPDMS foam sensor arrays, the success of the sensor design was evaluated based on a set of desired characteristics:

1. Sensors must demonstrate repeatable results
2. Sensors must be able to be calibrated
3. Sensors should have enough dynamic range to measure useful flows for ocean engineering applications
4. Sensors must be robust

Repeatability

To be valuable as a sensor, a device must demonstrate three types of repeatability:

- Sensor is repeatable over the course of a single experiment. For example, multiple oscillations of a periodic stimulus should give consistent measurements.
- Sensor is repeatable across multiple independent trials using the same stimulus.
- Sensor is repeatable across various types of stimulus

Calibration

In order to act as a sensor, a relationship between an input stimulus such as pressure, and the device output voltage, must be able to be developed. This relationship does not need to be linear, and may include hysteresis.

Dynamic Range

A prototype device must demonstrate a large enough dynamic range to be useful for measuring flows within a designated range of interest. For the CBPDMS foam sensor arrays, the flows of interest were at the scale of unmanned marine vehicles as given in Table 2.1 and Section 3.1, and the dynamic range should reflect this.

Robustness

For use in ocean engineering applications a sensor must be able to withstand extended periods of submergence, the potential for impact, and repeated deformations.

5.2 Sensor Power and Amplification Electronics

For the CBPDMS foam sensor array characterization experiments, custom electronics were designed to provide a current source for the four-point probe arrangement discussed in Section 4.5.2, and to amplify voltage measurements from the array. The current source and amplification circuits were built on a custom PCB board designed and printed for the experiments, as seen in Figure 5-1.

5.2.1 Constant Voltage Source

During the plunging (Section 5.3) and Dipole (Chapter 6) experiments conducted in Singapore, the CBPDMS foam sensor arrays were powered with a constant voltage source as shown in the equivalent circuit diagrams in Figure 5-2. As shown in Figure 5-2(b), the CBPDMS foam sensor array was found to have a total resistance of $\sim$28 kΩ which can be largely attributed to the contact resistance between the ribbon

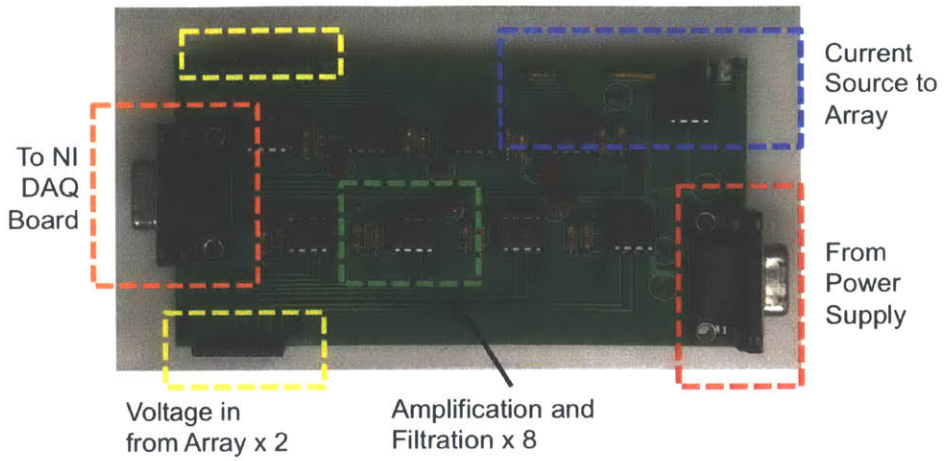

Figure 5-1: A custom PCB board was designed and printed for sensor array characterization experiments that contained a constant current source circuit using an LM741 Op-Amp and signal amplification using AD620 Op-Amps.

cables and the Ag-CBPDMS electrodes. With the $\sim$ 28 kΩ array resistance in series with a 112 kΩ resistor, the current through the sensor array was $\sim$ 0.17 mA. Because the voltage source was constant in this arrangement, variations in the sensor array resistance could lead to variations in the current being supplied to the array, introducing uncertainty to the voltage measurements taken across the sensor channels. The magnitude of this uncertainty can be calculated using the voltage measurements taken during a characterization experiment and knowledge of the voltage source and in-series resistor.

To quantify the effect of the changing resistance of the sensor channels on the array source current, a case of periodically varying hydrostatic pressure, shown in Figure 5-3, was analyzed (for a complete discussion of the varying hydrostatic pressure experiments see Section 5.3). In this analysis, it was assumed that the total resistance of the CBPDMS sensor array when measured across the two outermost electrodes of the four-point probe arrangement was a summation of the individual resistance of each block of Ag-CBPDMS and CBPDMS foam (for details of sensor layout and fabrication see Chapter 4). If this was the case during experiments, a variation of resistance in the CBPDMS foam sensor material would cause a change in the total resistance of the sensor array, and subsequently cause variation of the current in the

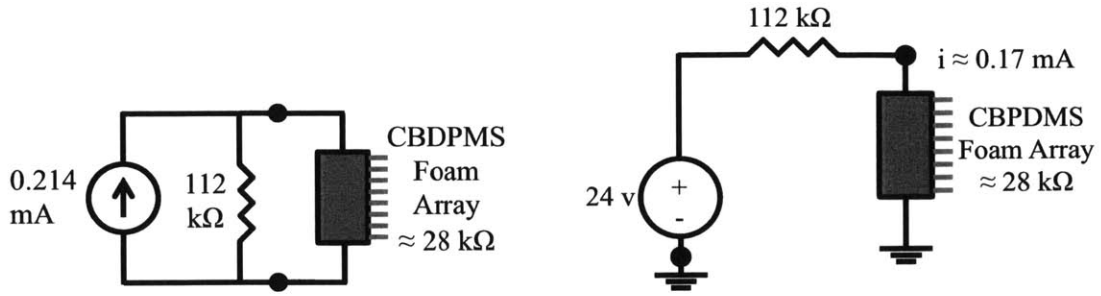

(a) Norton equivalent circuit for the sensor array current source when using a constant 24 volt power source.

(b) Thevenin equivalent circuit for the sensor array current source when using a constant 24 volt power source.

Figure 5-2: For the experiments conducted in Singapore, the CBPDMS foam sensor array was powered with a constant voltage source of 24 volts. Because the resistance variations of the sensor array were substantially smaller than the in-series 112 kΩ resistor, the sensor array was provided with a nearly constant current of approximately 0.17 mA.

circuit. The measured voltage and corresponding resistance values for each sensor channel is summarized in Table 5.1, assuming a 24 volt constant voltage source and initial current of 0.17 mA based on a measured total array resistance of $\sim$ 28 kΩ.

From the results shown in Table 5.1, it was observed that during a typical experiment, the variation in CBPDMS foam resistance could cause an $\sim$ 1% change in supply current. Additionally, if the total measured resistance of the CBPDMS foam array was primarily due to contact resistance between the ribbon cable and the Ag-CBPDMS electrodes, the effect of resistance change in the CBPDMS is further reduced. Because the potential change in current was found to be minor, it will be noted as a source of experimental measurement error during experiments, as discussed in Section 5.3.4.

5.2.2 Constant Current Source

For experiments conducted at MIT including water wave stimulus (Section 5.4) and Kármán vortex street identification (Chapter 7), the CBDPMS foam sensor array was powered using a constant current source circuit composed of a LM 741 operational amplifier in an inverting amplifier configuration, as seen in Figure 5-4. In this configuration, the constant current supplied to the sensor array was found using Equation

Ch.	Offset Volt. [v]	R [Ω]	% Total R	Δ v	Δ R [Ω]	Δ i [mA]	% Total i
2	0.2917	1715.9	1.23	0.008	47	0.0015	0.88
3	0.4312	2536.6	1.82	0.01	58	0.0017	0.88
4	0.3726	2191.8	1.57	0.01	58	0.0017	0.88

Table 5.1: The nominal resistance of each CBPDMS foam sensor channel was found using the average offset voltage at the beginning of the characterization experiment shown in Figure 5-3 and a supply current of 0.17 mA. The supply current was calculated from a 24 v constant voltage source and a total resistance for the sensor array and in-series resistor of 140 kΩ. '% Total R' is the percentage of the total circuit resistance (140 kΩ) of each sensor channel. 'Δ v' is the peak-to-peak voltage variation during the oscillatory component of Figure 5-3, and 'Δ R' was the resistance change assuming i=0.17 mA. 'Δ i' is the change in supply current based on the total circuit resistance changing by 'Δ R' with a 24 v constant voltage.

5.1, where V_{in} was the supply voltage from a DC power supply, i_{in} was the desired input current to the array, and R was the resistance value chosen to achieve the desired input current. For the CBPDMS foam sensor array, V_{in}=12v and R=56 kΩ, giving a constant current of i_{in}=0.2 mA.

$$i_{in} = \frac{V_{in}}{R} \tag{5.1}$$

5.2.3 Signal Amplification and Filtering

Signal amplification was provided for each sensor channel by an AD620 operational amplifier, as shown in Figure 5-5. The amplification was set by a gain resistor according to Equation 5.2, where R_G was the value of the gain resistor and G was the gain. During the CBDPMS foam array characterization experiments a 30 kΩ gain resistor was used, giving an amplification gain of 2.66.

$$R_G = \frac{49.4k\Omega}{G-1} \tag{5.2}$$

Following amplification, signals were filtered using an RC low pass filter with a cutoff frequency (f_c) given by equation 5.3. For the CBPDMS foam array experi-

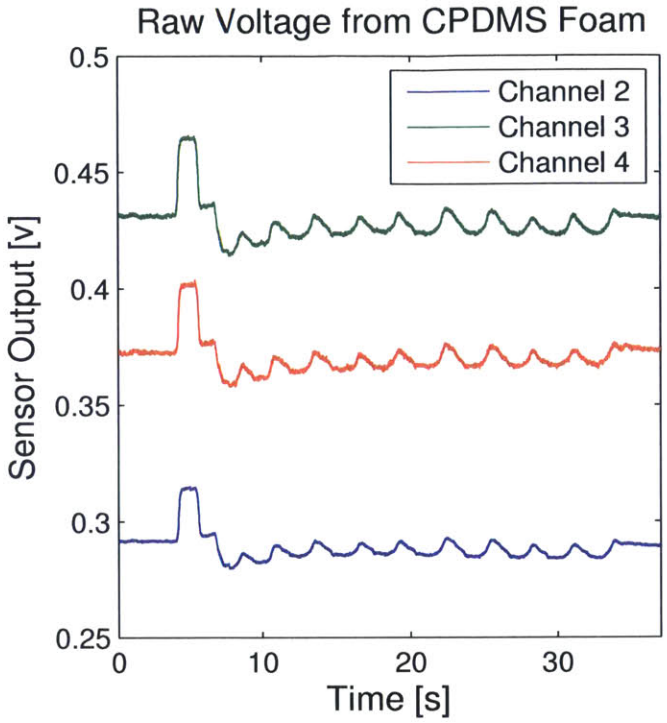

Figure 5-3: The initial resistance of each channel of the 7.8 mm thick CBDPMS foam sensor array at a starting depth of 10mm can be found by calculating the average steady voltage output before the start of an oscillatory characterization experiment (0-4s) and dividing by the supply current. The variation in resistance of each channel can similarly be determined using the voltage fluctuations in response to an oscillatory pressure stimulus. With the magnitude of resistance variation known, the effect on the supply current can be quantified. Sensor array channel 1 was not operational during the plunging experiments in Singapore and results for that channel will not be shown. Sensor channel 1 was subsequently repaired upon return to Boston, and discussion of the sensor channel's performance during water waves tests at MIT can be found in Section 5.4.5.

ments, the resistor was R=300 $k\Omega$ and the capacitor was C=4700 pF giving a cutoff frequency of 112.88 Hz.

$$f_c = \frac{1}{2\pi RC} \tag{5.3}$$

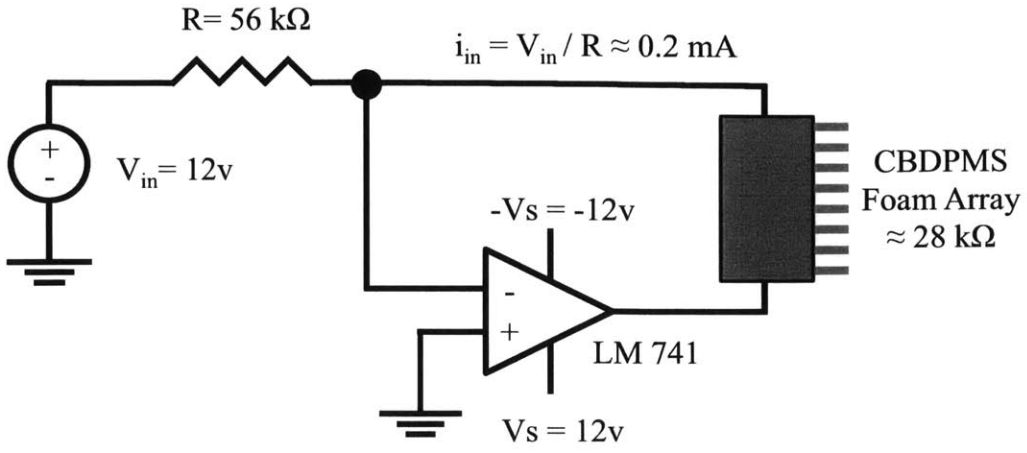

Figure 5-4: For all experiments conducted at MIT, the CBPDMS foam sensor array was provided a constant 0.2 mA current using a constant current source cicruit composed of a LM741 Op-Amp and a 56 kΩ resistor. Voltage was supplied to the current source electronics using a DC power supply.

5.3 Vertical Plunging Experiments

To demonstrate the operation of the CBPDMS Foam pressure sensor arrays, a time-varying hydrostatic pressure stimulus was used. The goals of the experiment were to verify the operation of the closed cell CBPDMS foam sensor arrays when submerged, characterize the sensitivity of the arrays, and develop a set of calibration curves for each sensor channel. To do this, two types of experiments were conducted using well-characterized dynamic pressure stimulus. First, sinusoidal plunging motions were carried out using a computer controlled linear stage to create a time-varying hydrostatic pressure. Second, a sensor array was surface mounted on a foil shape and tested using the dynamic pressure field generated by surface water waves in the towing tank at MIT.

5.3.1 Plunging Experimental Setup

To allow for vertical plunging of the sensor arrays, a Zaber T-Series linear stage (Model T-LSQ300B) was mounted vertically above CENSAM's large vehicle testing tank in Singapore, as seen in Figure 5-6(a). The CBPDMS foam pressure sensor arrays were mounted in a 3-D printed holder which was attached to the linear stage

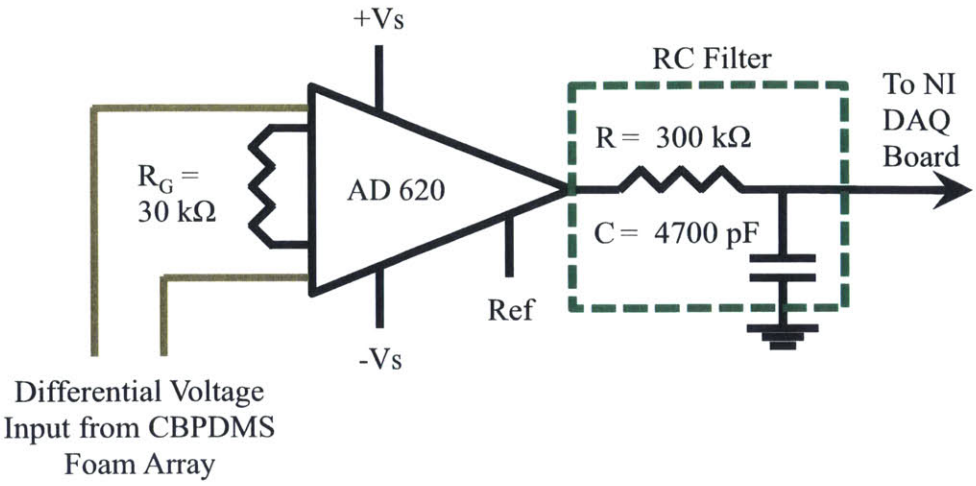

Figure 5-5: Differential voltage measurements from the CBPDMS foam sensor array were amplified 2.66 times using an AD 620 operational amplifier. An RC filter with a cutoff frequency of $\sim$ 113 Hz was included to reduce electrical noise during the experiments.

using an aluminum plate, as seen in Figure 5-6(b). Because the aluminum plate was thin, oscillation of the sensor holder due to actuator vibrations or fluid interactions was a consideration, but were found to be negligible for the low frequencies (0.5-1 hz) being investigated.

The motion of the linear stage was controlled using proprietary Zaber Console software running on a laboratory laptop, and connected to the stage via a USB-serial converter. Motion of the Zaber stage was provided by a stepper motor, and stage position and velocity values were reported by the Zaber Console software in terms of microsteps. Proper use of the stage required conversion between the output *Data* reported by the control software for the desired parameter, and metric units. For the stage used in the experiments, the microstep size M was found to be $M = 0.49609375 \frac{\mu m}{microstep}$. The conversions between output values from the Zaber Console software *Data* and metric units are given in Equations 5.4 and 5.5.

$$Distance(m) = \frac{Data \times M}{10^6} \tag{5.4}$$

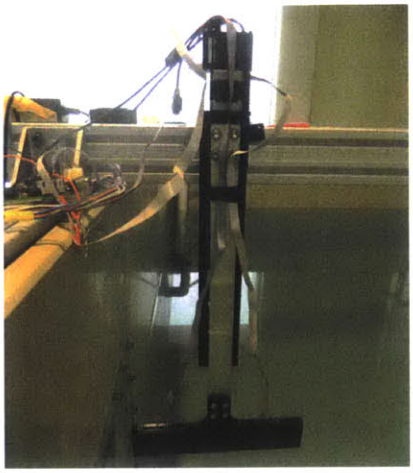

(a) A computer controlled Zaber T-Series linear stage was mounted vertically above the large vehicle testing tank on the CREATE campus in Singapore in order to provide an oscillatory hydrostatic stimulus. Two CBDPMS foam sensor arrays were secured in a 3D printed holder and attached to the stage using an aluminum plate.

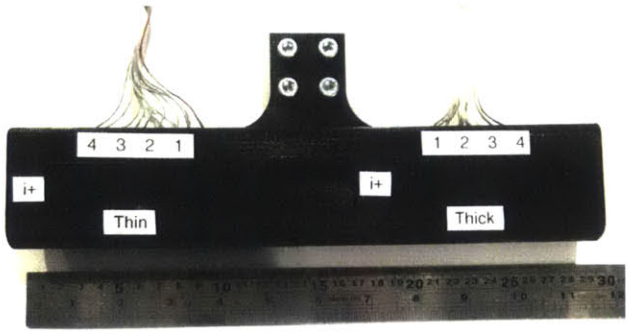

(b) During plunging experiments the two CBPDMS foam sensor arrays were secured in a 3D printed holder that was attached to the Zaber stage by an aluminum plate. The sensor arrays were mounted so they were flush with the surface of holder, and the bottom of the holder was streamlined to reduce vibrations due to vortex shedding. The ribbon cable that supplied current to the sensor arrays and facilitated voltage measurements exited through a slit in the top of the holder.

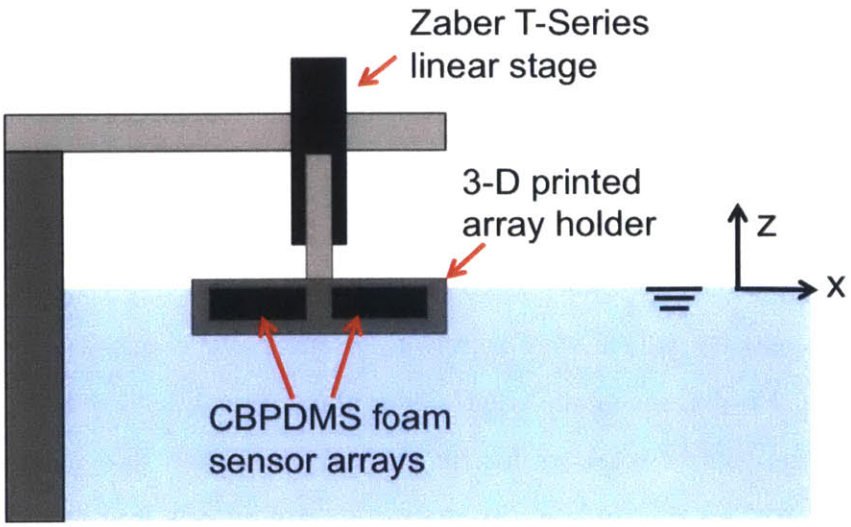

(c) To begin each plunging experiment, the stage was positioned so the top of the CBPDMS foam sensor arrays was level with the tank free surface. The initial position of the array represented the peak of the stage oscillatory motion, with subsequent stage motions increasing the submergence depth of the arrays.

Figure 5-6: The response of the CBDPMS foam sensor arrays to a time-varying hydrostatic stimulus was tested by periodically raising and lowering the arrays in a water tank. The vertical oscillation of the arrays was provided by a computer-controlled linear stage mounted above the tank, and the stage position was recorded along with voltage measurements from the sensor array.

$$Velocity(m/s) = \frac{Data \times 9.375 \times M}{10^6} \tag{5.5}$$

During the plunging experiments, the sensor arrays were powered using two 12v batteries, and signals were amplified using the electronics described in Section 5.2. The position of the linear stage was written to an output file throughout each experiment to allow the actual hydrostatic pressure acting on the arrays to be determined. The output voltage from the the pressure sensor arrays was recorded using an NI USB-6218 data acquisition board and National Instruments Labview software running on a laboratory laptop. The complete data flow for the experiment can be seen in Figure 5-7.

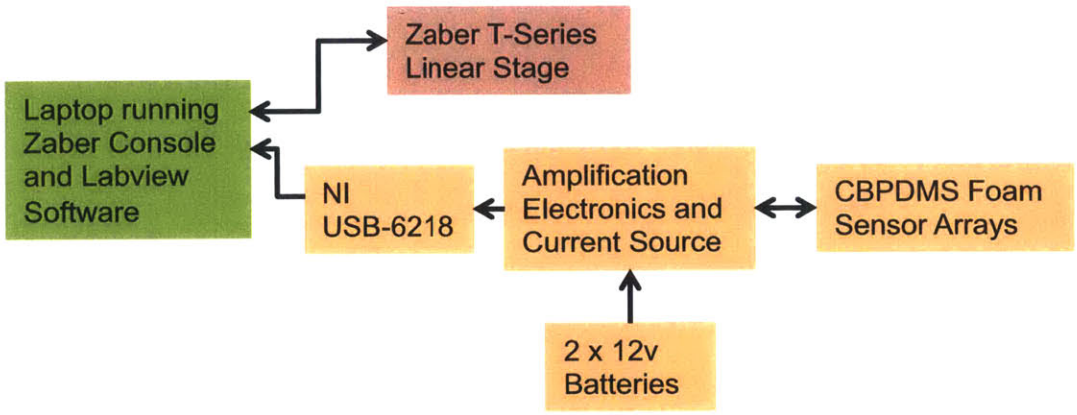

Figure 5-7: For the plunging experiments using the Zaber linear stage, both the Zaber Console software for controlling the stage motion and Labview software for data acquisition were run on a laboratory laptop. Data acquisition from the CBPDMS foam sensor arrays was provided by a Nationals Instruments USB 6218 data acquisition board, and signals were amplified 2.66 times using AD620 operational amplifiers. Power was provided to the sensor array by two 12v batteries.

5.3.2 Experiment Description and Parameters

To characterize the dynamic response of the CBPDMS foam pressure sensor arrays, oscillatory plunging motions were used to generate a time-varying hydrostatic stimulus. Because of the limitations of the Zaber stage, and to minimize the impact of spurious vibrations on the experimental results, experiments were restricted to frequencies of 0.5 Hz and 1 Hz. In each experiment, the initial position of the array was

with the still waterline level with the top of the array, as seen in Figure 5-6(c). To allow time synchronization between the stage position and the sensor voltage output, a step in the positive z direction was executed at the beginning of each experiment to create an easily identifiable feature in both signals, as seen in Figure 5-8. Following the step move, ten oscillatory cycles were executed with peak-to-peak amplitudes ranging from 5mm to 30mm. A complete description of the parameter space covered can be found in Table 5.2.

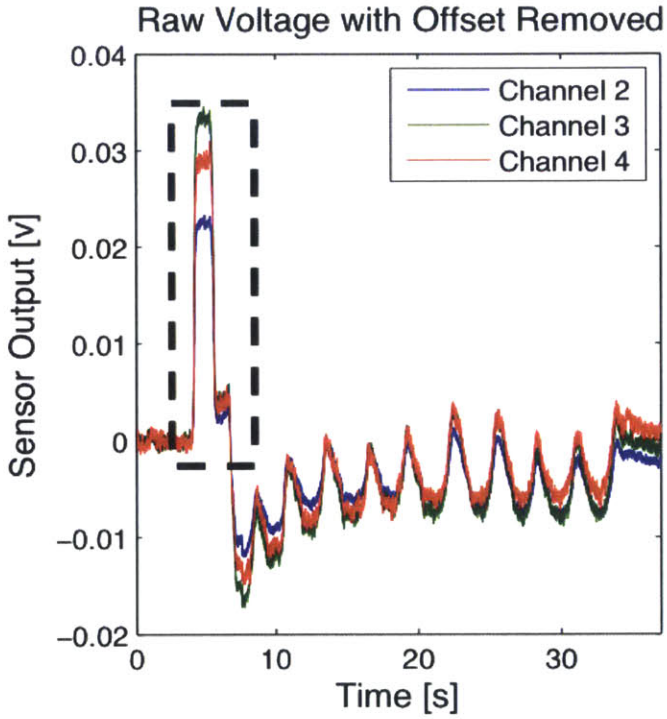

Figure 5-8: To allow for synchronization between the Zaber stage position and the CBPDMS foam array output voltage, the stage carried out a 5 mm step move in the positive z-direction at the beginning of each experiment, creating a clear signal in the voltage measurement. The voltage measurement shown has had the initial offset voltage of each sensor removed to highlight the step motion.

The total time-varying pressure during the plunging experiments (P_{pt}) was composed of both a hydrostatic (P_{ph}) and dynamic component (P_{pd}), as shown in Equation 5.6. In Equation 5.6, u is the plunging velocity and z is the vertical position of the sensor array midpoint. When considering the time-varying pressure from a simulated sinusoidal motion with a 5mm peak-to-peak amplitude at 0.5 Hz and 30mm peak-to-

Frequency [hz]	5mm	10mm	20mm	30mm
0.5	Tx1	Tx2	Tx2	Tx2
		tx2	tx2	tx3
1.0		Tx2	Tx2	Tx2
		tx2	tx2	tx3

Table 5.2: Parameter space for oscillatory plunging experiments. The thick sensor is represented by capitol T, and the thin sensor is represented by lower case t. The number of runs for each parameter combination is also specified. The amplitude is given as peak-to-peak amplitude.

peak amplitude at 1 Hz, the dynamic pressure component was found to be at least two orders of magnitude smaller than the hydrostatic component, as seen in Figure 5-9, and therefore the dynamic pressure component was neglected from future analysis.

$$P_{pt} = P_{ph} + p_{pd} \tag{5.6}$$
$$P_{ph} = -\rho * g * z$$
$$P_{pd} = \frac{1}{2} * \rho * u^2$$

It was observed during the course of the experimental program that the sinusoidal motion created by the Zaber stage was not always consistent in amplitude and frequency, as seen in Figure 5-10(a). This was particularly evident during low frequency motions were the stage would occasionally hesitate at the peak or trough of a cycle. These slight errors in amplitude and frequency were accounted for by making sure to utilize the actual position output information recorded from the stage during each experiment instead of relying on the anticipated frequency and amplitude values.

5.3.3 CBPDMS Foam Array Response Characteristics

The periodic plunging experiments conducted at the CENSAM lab in Singapore using the Zaber linear stage provided an excellent platform for studying the response of the CBDPMS foam sensor arrays. During the experiments, it was found that sensor

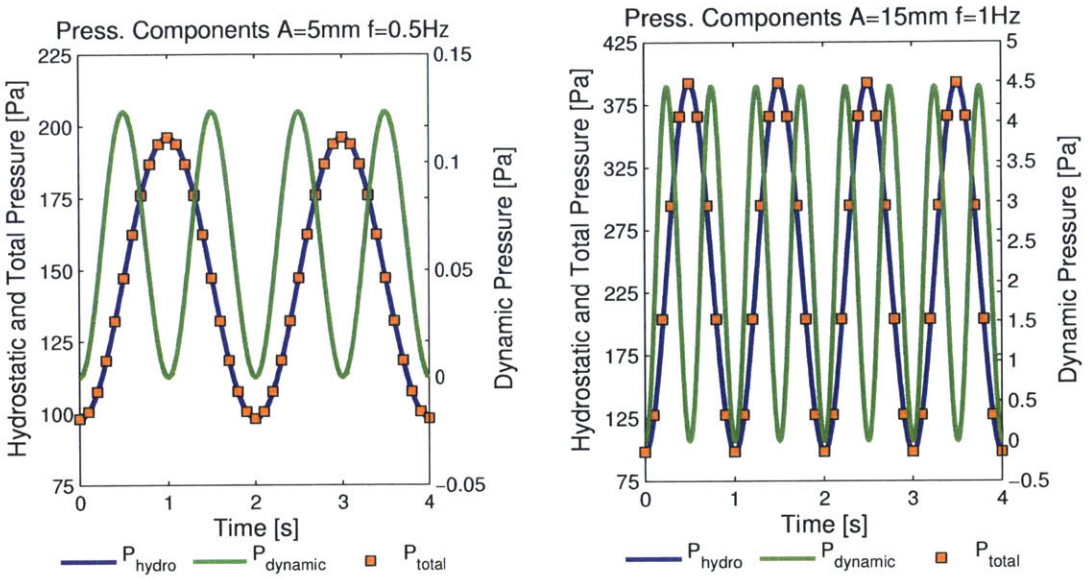

(a) The pressure components for a simulated sinusoidal plunging motion with a 10 mm peak-to-peak amplitude at 0.5 Hz starting from an initial depth of 10mm. The dynamic component of pressure (green line) was found to be approximately three orders of magnitude less than the time-varying hydrostatic pressure (blue line), making its contribution to the total pressure (orange squares) negligible.

(b) The pressure components for a simulated sinusoidal plunging motion with a 30 mm peak-to-peak amplitude at 1 Hz starting from an initial depth of 10mm. The dynamic pressure component was found to be greater than the case of 10 mm and 0.5 Hz due to the larger peak stage velocities, but still two orders of magnitude less than the hydrostatic component.

Figure 5-9: The hydrostatic (blue line) and hydrodynamic (green line) components of the total pressure (orange squares) was found for simulated sinusoidal plunging motions. The hydrostatic component of the pressure was found to be the dominant component, and the dynamic component was neglected during the CBPDMS foam sensor characterization.

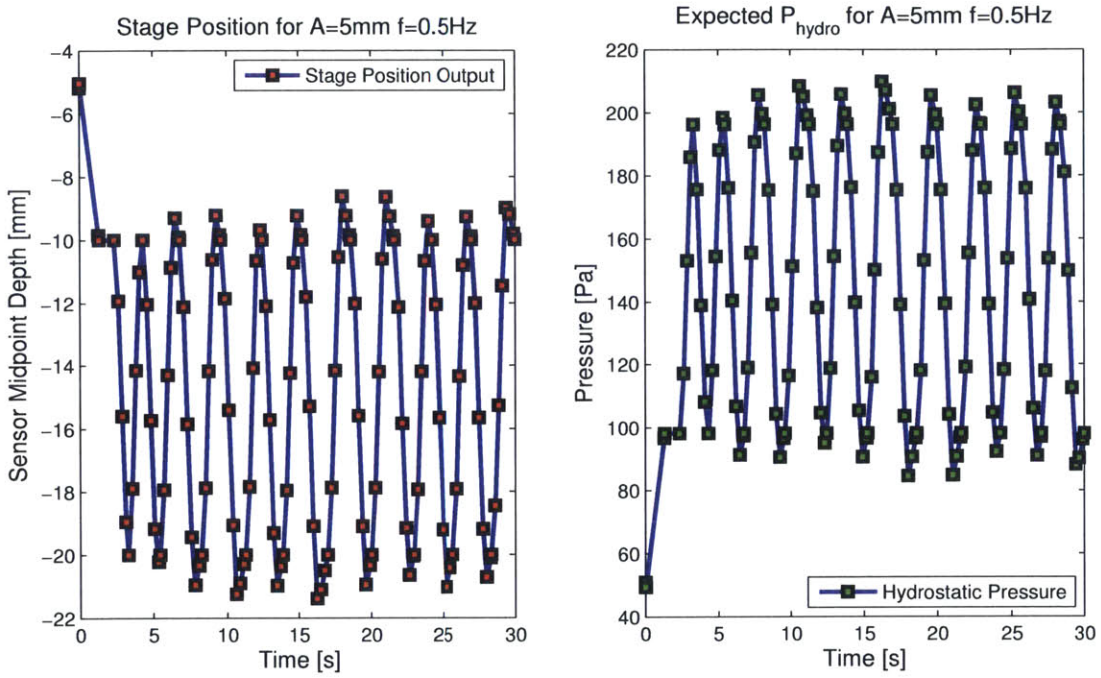

(a) The Zaber stage output position throughout the periodic plunging experiments, denoted here by red squares for the case of a 10mm peak-to-peak motion at 0.5 Hz. The first position output value from the stage was after an initial 5mm step move in the positive z direction used to sync the position and pressure signals was completed. Despite the stage position being under-sampled, it is evident that some variation in amplitude and period occurred throughout the experiment.

(b) Using the position output values from the Zaber stage, the hydrostatic pressure at the midpoint of the CBPDMS foam sensor array was calculated. Due to the low frequency and small oscillation amplitudes, the hydrostatic component of pressure was dominant in the experiments, as shown in Figure 5-9

Figure 5-10: The pressure values used to characterize the CBPDMS foam sensor array were the hydrostatic component of pressure found using the position output from the Zaber linear stage.

channel one on both the 7.8 mm and 6.2 mm thick sensor arrays was not operational. The sensor channels were subsequently repaired upon returning to MIT and were found to be operational and consistent with channels two through four, as discussed in Section 5.4.5. For the plunging experiments, results for sensor channels two, three, and four will be presented.

CBDPMS Voltage Output Filtering

The voltage output signals from the CBPDMS foam sensor were bandpass filtered using the *idealfilter* function in Matlab. The filter is non-causal with sharp cutoffs in the frequency domain and non-realizable in real time. The bandpass interval was chosen to be 0.2 to 3.0 Hz for the plunging experiments in order to remove any low frequency DC drift from the signals, as well as high frequency electrical noise.

Inverse Pressure-Resistance Relationship

Studying the voltage output from the CBPDMS foam arrays when subjected to an oscillatory pressure stimulus revealed several important sensor characteristics. The first of these was that an inverse relationship existed between voltage output and pressure magnitude under an approximately isotropic stimulus, as seen in Figure 5-11(a). For a constant current, voltage is proportional to resistance through Ohm's law (v=iR), so it follows that the resistance change in the CBPDMS foam sensing material is inversely related to pressure.

The inverse relationship between pressure and resistance follows the compressible model of CBPDMS piezoresistivity discussed in Section 4.4, but is opposite of the pressure-resistance relationship observed when CBPDMS foam cubes were tested on a mechanical tester in Section 4.6.2. During the investigation of the CBPDMS foam composite's electrical properties using the ADMET mechanical tester, the pressure stimulus was anisotropic compression, as opposed to the isotropic hydrodynamic pressure experienced during the plunging experiments. The difference in the loading condition of the foam composite is believed to play a crucial role in determining if the piezoresistive response of the CBPDMS foam follows the compressible or incom-

pressible model of CBPDMS piezoresistivity.

For an anisotropic stimulus like the compressive force from the mechanical tester, it was observed that the PDMS matrix material 'bulged' in the off-loading direction, consistent with the graphical description of the incompressible model in Figure 4-2(b). For an isotropic stimulus like hydrostatic pressure, no off-load direction exists, and it is expected that the CPDMS foam undergoes a volume reduction consistent with the compressible model in Figure 4-2(a). Additionally, the boundary conditions on the CBPDMS foam are believed to contribute to the piezoresistive response by influencing the material deformations. During the ADMET mechanical testing, the CBPDMS foam cubes were unconstrained in the off-loading direction, as seen in Figure 4-9(b), while the CBPDMS foam sensor channels in the complete array were constrained by the presence of the Ag-CBPDMS electrodes and the pure PDMS base layer, as seen in Figure 4-1(b). Throughout extensive testing of the CBPDMS foam sensor array using multiple hydrodynamic stimuli, the inverse relationship between the resistance and pressure remained consistent and repeatable, and it was concluded that for isotropic hydrodynamic stimulus, the CBPDMS foam sensor arrays follow the compressible model of piezoresistivity.

Sensor Array Repeatability

As discussed in Section 5.1.1, a prototype sensor must demonstrate repeatability in order to be considered successful. To evaluate the repeatability of the CBPDMS foam arrays, voltage was plotted versus hydrostatic pressure for the periodic plunging experiments. From the plunging experiments the repeatability of the sensor array over the course of a single experiment could be verified, as well as the repeatability of the sensor when the plunging motion was changed. To be considered repeatable, the pressure-voltage pairs from multiple plunging cycles should fall on the same curve or hysteretic loop.

As mentioned previously, the oscillatory motion of the Zaber stage varied slightly in amplitude and period throughout an experiment, as seen in Figure 5-10(b). To account for these variations, sensor output voltage values were selected for the times

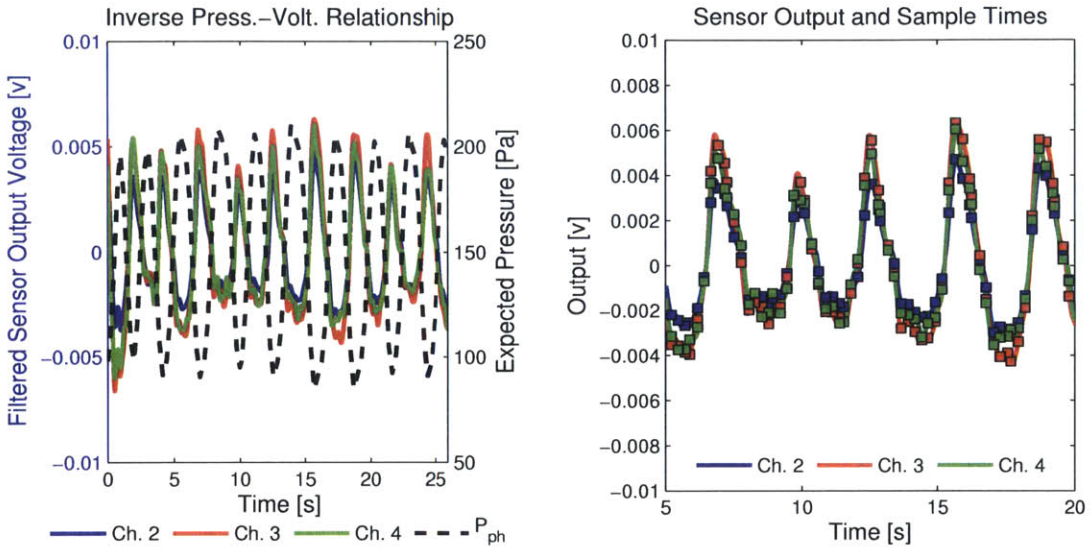

(a) Plotting the hydrostatic pressure stimulus (black dotted line) and the CBPDMS foam sensor voltage output (solid colored lines) together shows that an inverse relationship exists between hydrostatic pressure and output voltage for the CBPDMS foam sensing material. Because output voltage is proportional to resistance, it follows that the resistance change in the material is inversely proportional to pressure.

(b) A subset of the array voltage output values (squares) was selected to correspond with the position samples from the Zaber stage in order to account for any variations in amplitude or period in the stage motion. The mean voltage from each channel has been removed for easier visualization.

Figure 5-11: The voltage output from the CBPDMS foam sensor array during oscillatory plunging revealed an inverse relationship between pressure and resistance. The voltage time series was sampled at discrete times corresponding with position outputs from the Zaber stage in order to generate pressure-voltage pairs for use in sensor calibration.

corresponding to the position outputs from the Zaber stage, as seen in Figure 5-11(b). In this way, an accurate picture of the pressure-voltage relationship for the array could be found.

A qualitative assessment of sensor array repeatability was found by plotting the results from six independent plunging experiments with the 7.8 mm thick sensor array on the same pressure vs. voltage axes, as seen in Figure 5-12(a). Within each experiment, the data points were found to follow a consistent trend, as seen in Figure 5-12(b), qualitatively fulfilling the requirement of repeatability within a given experiment, as described in Section 5.1.1. Although the dynamic response of the sensor array appeared consistent between independent experiments, variations in the DC offset voltage were observed, leading to a distinct spread in the data points, as seen in Figure 5-12(b).

DC Offset Voltage When the results from six independent plunging experiments with the 7.8 mm thick sensor array were plotted on the same pressure vs. voltage axes, it was observed that the DC voltage offset varied between independent experiments, as seen in Figures 5-12(a) and 5-12(b). Because the CBDPSM foam sensor array is intended for the measurement of AC pressure signals, the dynamic response of the array is of primary concern. In order to verify the repeatability of the dynamic response of the sensor array between independent experiments, the DC voltage offsets were adjusted for consistency, as seen in Figures 5-12(c) and 5-12(d). With the DC voltage offset corrected, the results from all six independent experiments were found to have a repeatable non-linear pressure vs. voltage response, as seen in Figure 5-12(c).

5.3.4 Experimental Error in Plunging Results

Error in Voltage Measurement During the plunging experiments conducted in Singapore, the CBPDMS foam sensor array was powered using a constant voltage source, as described in Section 5.2.1. Based on the analysis presented in Section 5.2.1 and summarized in Table 5.1, it was found that the supply current to the sensor array

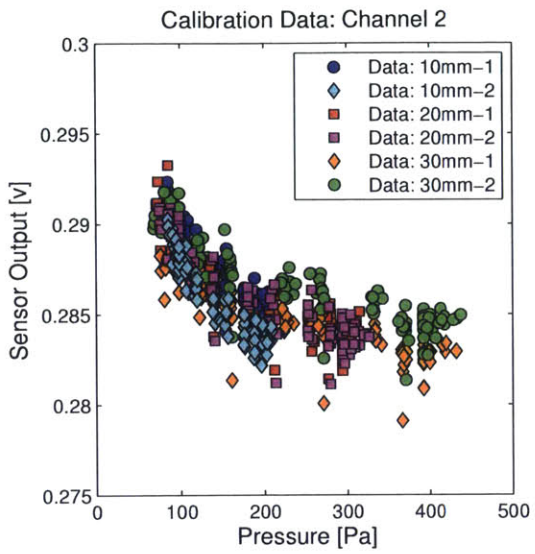

(a) The pressure-voltage data pairs from channel 2 for six independent plunging experiments were plotted together to demonstrate the repeatability of the 7.8 mm thick CBPDMS foam sensor array.

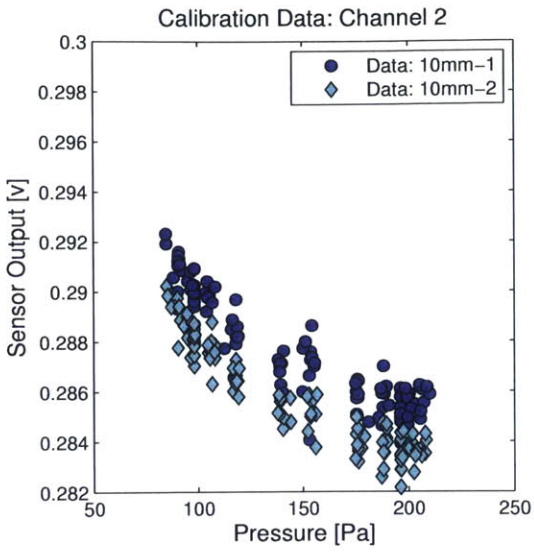

(b) Pressure-voltage pairs from channel 2 of the 7.8 mm thick CBPMDS foam array for two plunging experiments with a 10mm peak-to-peak amplitude.

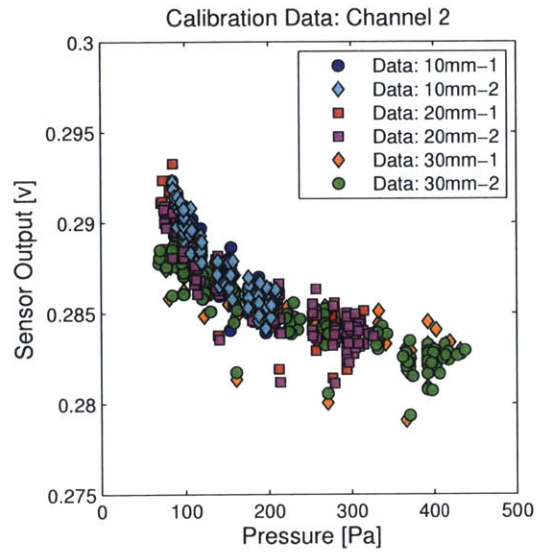

(c) When the DC offset was adjusted for data sets '10mm-2' (light blue diamonds) and '30mm-2' (green circles), the spread in data points between the six plunging experiments was reduced.

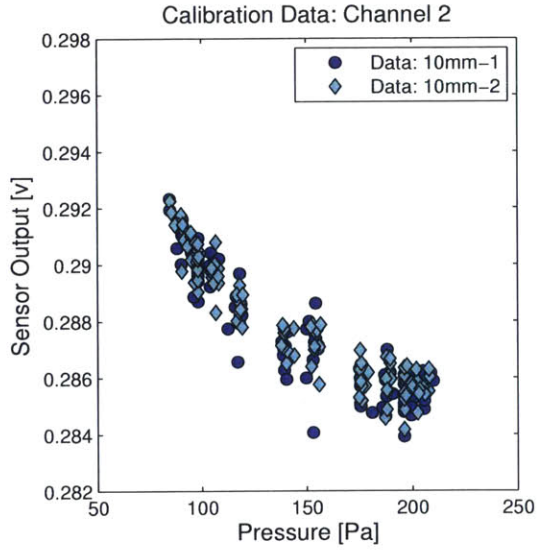

(d) With a 2 mV shift applied to the second 10mm peak-to-peak data set (light blue diamonds), the results from the two experiments were found to show strong agreement.

Figure 5-12: Six independent plunging experiments were conducted using the 7.8 mm thick CBPDMS foam sensor array, two each at 10 mm, 20 mm, and 30 mm peak-to-peak amplitude. Pressure-voltage pairs were found by sampling the foam array voltage output at the Zaber stage position output times, as described in Section 5.3.3.

could vary by ~1% if the total resistance of the sensor array was a summation of the resistance of each individual electrode and sensor channel resistance. To account for this possible variation, the error in voltage, given by the red shaded boxes in Figure 5-13, was found by scaling each voltage measurement based on a supply current increase and decrease of 1%, as given in Equation 5.7. For the 6.2 mm thick (Thin) sensor array, the magnitude of voltage fluctuation was found to be approximately twice that of the 7.8 mm (Thick) array for the same pressure stimulus. To account for the larger change in resistance with pressure, the error in voltage as found by assuming a 2% variation in supply current as seen in the plots in Appendix B.

$$v_{error} = v \pm 0.01 * v \tag{5.7}$$

Error in Theoretical Hydrostatic Pressure As described in Section 5.3 the pressure used to generated pressure-voltage pairs in Figures 5-11 and 5-12 was the hydrostatic component of pressure based on the position output from the Zaber linear stage. Two likely sources of error in the theoretical hydrostatic pressure were the presence of surface waves in the tank generated by the motion of the sensor holder beneath the surface, and measurement error in the initial position of the sensor. Because the position output from the Zaber stage was in Microsteps with a conversion to meters given by Equation 5.4, small errors in the stage output value would cause negligible errors in the submergence depth and theoretical hydrostatic pressure.

The possible error in hydrostatic pressure due to free surface fluctuations in the tank was characterized by considering the voltage measurements from the CBPDMS foam array after the motion of the stage had completed it's motion, as shown in the period after ~35 seconds in Figure 5-8. Because the stage motion was complete and the array was at rest, fluctuations in the voltage measurements were likely due to residual free surface motion in the tank. After applying the calibration described in Section 5.3.5 to the raw voltage measurements, the pressure fluctuations were found to be <~10 Pa for the 30 mm peak-to-peak case, where maximum free surface disturbances were expected. Because the maximum submergence depth in the plunging

experiments was 40 mm, the decay of the pressure fluctuations due to free surface deformation was found to be small, and a constant ±10 Pa error was applied to the pressure values in Figure 5-13. Additional error in the theoretical hydrostatic pressure may have been present due to errors in the initial measurement of sensor array position before the plunging motion was initiated. Because careful attention was paid to aligning the the top of the sensor array with the free surface before each set of experiments, as shown in Figure 5-6, measurement error was assumed to be of similar magnitude or less than the ±10 Pa error assumed for free surface deformations.

Plunging Experiment Data Plots With Error Examples of the experimental data from the plunging experiment with boxes representing error in the voltage measurement and theoretical hydrostatic pressure are given in Figure 5-13 for the channel 2 of the 7.8 mm thick (Thick) sensor array. Similar plots for each of the six plunging experiments and the three operational sensor channels (channels 2, 3, and 4) can be found in Appendix A for the 7.8 mm (Thick) array and Appendix B for the 6.2 mm (Thin) array.

5.3.5 Calibration of 7.8 mm (Thick) CBPDMS Foam Array

As described in Section 5.1.1, an experimental device must be able to be calibrated in order to be considered a viable sensor. For the CBPDMS foam arrays, a relationship between voltage output and stimulus pressure was required for use of the device as a hydrodynamic pressure sensor. To find this relationship, the curve fitting function *fit* in Matlab was used to fit polynomials of increasing order to the experimental data plotted as voltage vs. pressure.

Cross-Validation of Polynomial Order

The output of the CBPDMS foam array in response to a time-varying hydrostatic stimulus was found to be repeatable and non-linear, as seen in Figure 5-12. To determine the order of polynomial fit best suited to represent the sensor response, a cross-validation was performed, as described in Figure 5-14(a). For each iteration

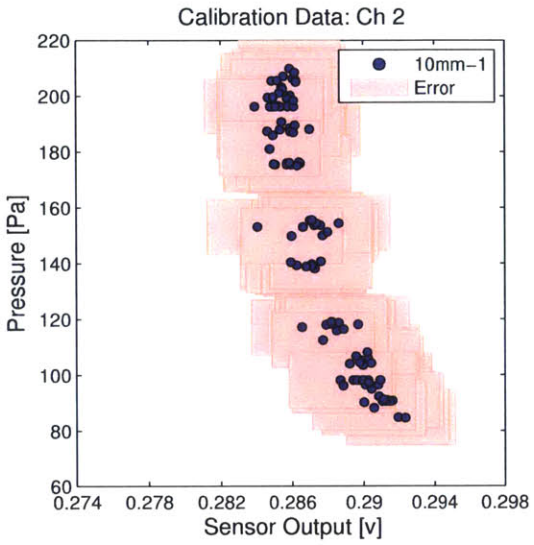

(a) Plunging results for 10mm peak-to-peak amplitude run 1 channel 2.

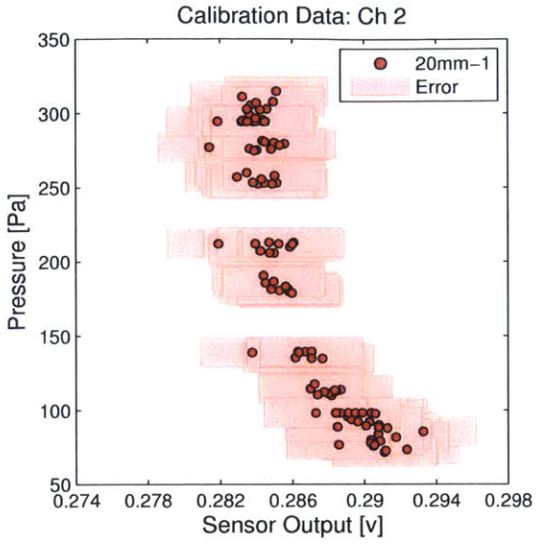

(b) Plunging results for 20mm peak-to-peak amplitude run 1 channel 2.

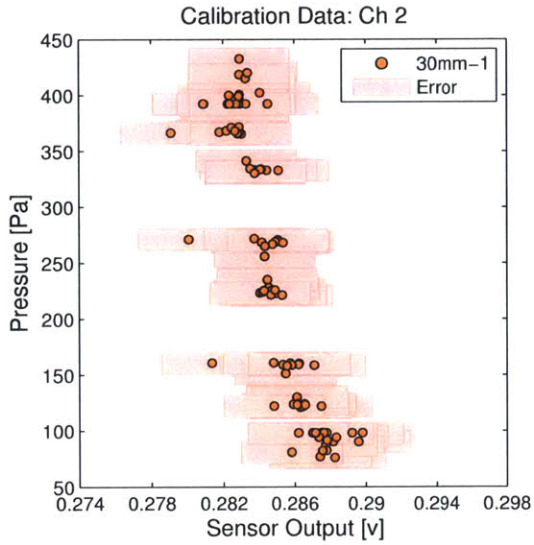

(c) Plunging results for 30mm peak-to-peak amplitude run 1 channel 2.

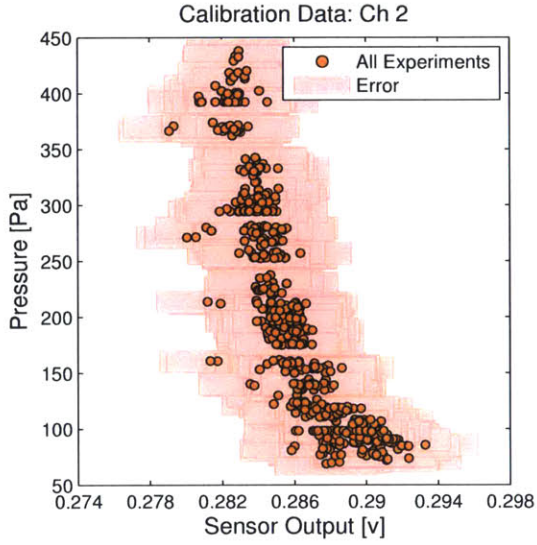

(d) Plunging results for all experiments channel 2.

Figure 5-13: Plunging data for 7.8 mm thick array channel 2. The light red shaded boxes designate the experimental error in pressure and voltage. Data is plotted as voltage vs. pressure to reflect the orientation of the data for calibration of the CBPDMS foam array.

of the cross-validation analysis, the complete set of experimental data from the six independent plunging experiments discussed in Section 5.3.3 was divided into four subsets based on randomly selected sample indices. One subset (1/4 of the total data) was set aside to be used for validation, while the remaining voltage-pressure pairs (3/4 of the total data) were used as training data to fit a polynomial curve. The polynomial fit was then applied to the validation subset, and the percent root-mean-square error (%RMSE), given in Equation 5.8, was calculated. For each polynomial order, 100 iterations of the cross-validation procedure were performed, and the mean and standard deviation of the %RMSE was found, as shown in Figures 5-14(b) and 5-14(c) .

$$\%RMSE = \sqrt{\frac{1}{n}\sum_{i=1}^{n}\left(\frac{\hat{y}_i - y_i}{y_i}\right)^2} \times 100 \tag{5.8}$$

For the CBPDMS foam array voltage output, it was found that the average %RMSE decreased as the polynomial order increased to four, and then stabilized or increased as the data became over-fit, as seen in Figure 5-14(b). When outliers were removed from the data set, as discussed in Section 5.3.5, the %RMSE was found to stabilize for polynomials of second order and on. Based on the cross-validation of polynomial order, curve fits of second, third, and fourth order were pursued for further analysis.

Polynomial Fits for Full Data Set

Using the curve fitting function *fit* in Matlab, robust polynomial fits of order 2-4 were found for the 7.8 mm thick CBPDMS foam plunging data, as seen in Figure 5-15. It was observed that while the 2nd (red) and 3rd (black) degree fits were very similar in shape, the 4th degree fit displayed non-physical characteristics at the high-pressure extreme of the training data range due to the influence of outliers at particularly low voltage values. The coefficients for an n degree polynomial of form $P = C_n * v^n + C_{n-1} * v^{n-1} + ... + C_0$, as well as the RMS error (Equation 5.9), normalized RMS error (Equation 5.10), and R^2 values (Equation 5.11) can be found in Tables 5.3,

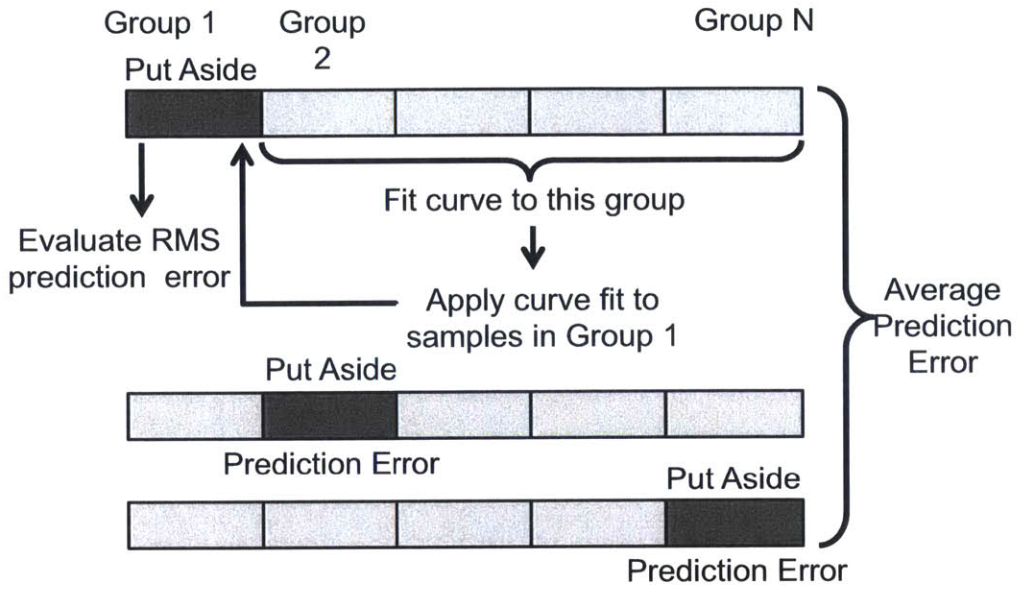

(a) The full data set from six independent plunging experiments was divided into four subsets (n=4), with one subset used as a validation set and the remainder used as training data. One hundred iterations were performed to find the average prediction error for each polynomial order.

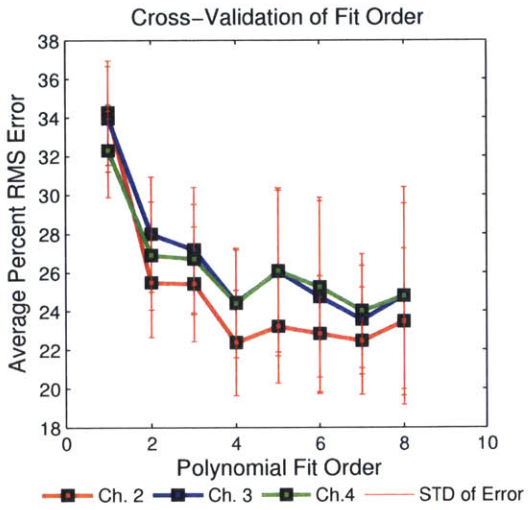

(b) Cross validation for the complete plunging data set.

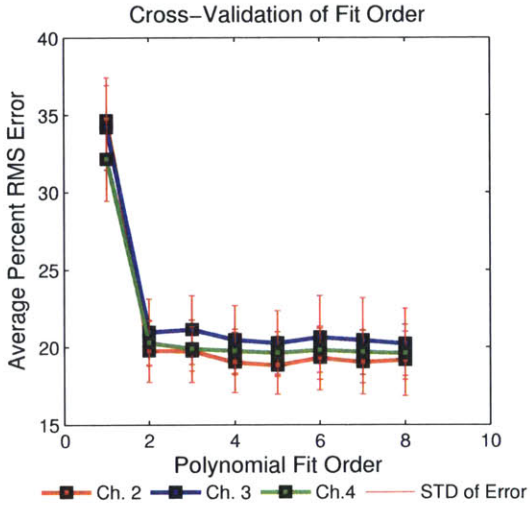

(c) Cross validation for the plunging data set with outlier points removed. A complete discussion of outliers can be found in Section 5.3.5.

Figure 5-14: Cross-validation was used to determine the optimal degree of polynomial fit for the CBDMS foam array plunging data.

n	C_4	C_3	C_2	C_1	C_0
2	NA	NA	4.883e+06	-2.834e+06	4.114e+05
3	NA	-1.33e+08	1.195e+08	-3.572e+07	3.559e+06
4	-1.271e+11	1.459e+11	-6.281e+10	1.202e+10	-8.62e+08
n	R^2	RMSE [Pa]	NRMSE [%]		
2	0.8823	33.73	9.14		
3	0.8853	33.32	9.02		
4	0.8882	32.92	8.92		

Table 5.3: Polynomial coefficients and goodness of fit measures for the 7.8mm CBPDMS foam sensor array Channel 2 with outliers included.

n	C_4	C_3	C_2	C_1	C_0
2	NA	NA	2.369e+06	-2.046e+06	4.418e+05
3	NA	1.766e+07	-2.025e+07	7.617e+06	-9.337e+05
4	-4.747e+10	8.115e+10	-5.201e+10	1.482e+10	-1.582e+09
n	R^2	RMSE [Pa]	NRMSE [%]		
2	0.8512	37.92	10.27		
3	0.8495	38.17	10.34		
4	0.8508	38.03	10.30		

Table 5.4: Polynomial coefficients and goodness of fit measures for the 7.8mm CBPDMS foam sensor array Channel 3 with outliers included.

5.4, and 5.5. Based on the results for second, third, and fourth degree polynomials, it was decided that the third degree polynomial provided the best representation of the voltage-pressure relationship without the end effects observed for the fourth degree fit.

$$RMSE = \sqrt{\frac{1}{n}\sum_{i=1}^{n} w_i \left(\hat{y}_i - y_i\right)^2} \tag{5.9}$$

$$NRMSE = \frac{RMSE}{y_{max} - y_{min}} \times 100 \tag{5.10}$$

$$R^2 = \frac{SSR}{SST} = \frac{\sum_{i=1}^{n} w_i \left(\hat{y}_i - \bar{y}\right)^2}{\sum_{i=1}^{n} w_i \left(y_i - \bar{y}\right)^2} \tag{5.11}$$

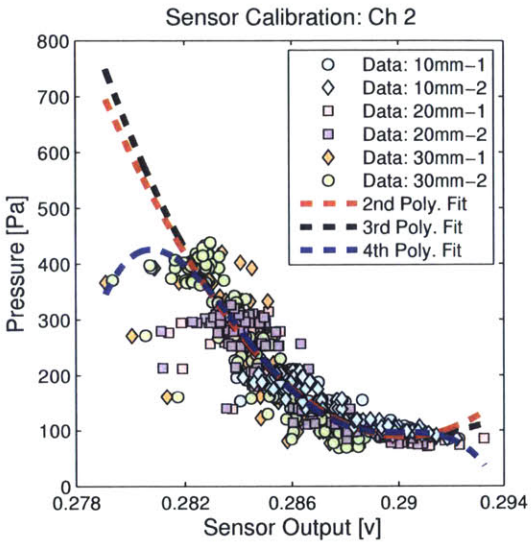

(a) Polynomial curve fits for Channel 2

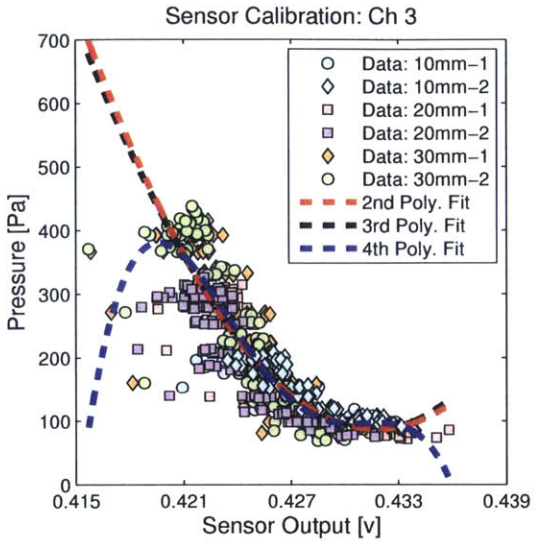

(b) Polynomial curve fits for Channel 3

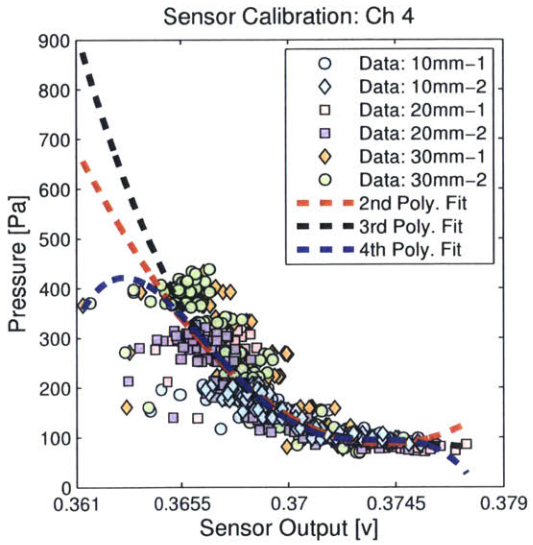

(c) Polynomial curve fits for Channel 4

Figure 5-15: Second, third, and fourth order polynomial curve fits were found for the plunging experiment results from the 7.8 mm thick CBPDMS foam sensor array.

n	C_4	C_3	C_2	C_1	C_0
2	NA	NA	3.515e+06	-2.629e+06	4.917e+05
3	NA	-2.767e+08	3.116e+08	-1.169e+08	1.463e+07
4	-7.434e+10	1.101e+11	-6.111e+10	1.508e+10	-1.395e+09
n	R^2	RMSE [Pa]	NRMSE [%]		
2	0.8485	38.26	10.37		
3	0.8688	35.64	9.65		
4	0.8596	36.89	9.99		

Table 5.5: Polynomial coefficients and goodness of fit measures for the 7.8mm CBPDMS foam sensor array Channel 4 with outliers included.

Identification and Removal of Outliers

When considering the CBPDMS foam array plunging data, outliers were considered samples that fell greater than 1.5 standard deviations away from the third degree polynomial fit found using the complete data set in Section 5.3.5. In Figure 5-16, the points that satisfied the criteria for being considered an outlier are designated with large red asterisks, and were removed from the training data set when generating the refined curve fits shown in black. The third degree polynomial coefficients and the goodness of fit metrics for the refined curves can be found in Table 5.6. In Figure 5-17 the refined third degree polynomial fits are shown with 95% confidence bounds for each sensor array channel. The outliers present in the experimental data were attributed to the first oscillation of each plunging experiment which consistently produced a lower sensor output voltage than subsequent oscillations, as seen in Figure 5-11(b). The source of this transient behavior in the output voltage should be considered as a direction for future study.

Calibration Applied to Time-Series Results

The refined third order polynomial calibration curves were tested by applying the calibration to the voltage output measurements from plunging experiments at 10 mm, 20 mm, and 30 mm peak-to-peak amplitude, as seen in Figure 5-18. The RMS error (RMSE), percent RMS error (%RMSE), and Normalized RMS error (NRMSE) were then calculated between the theoretical hydrostatic pressure determined by the

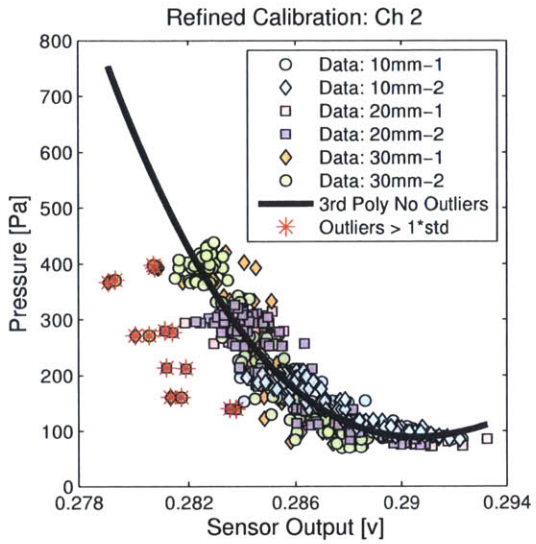

(a) Outliers and refined third order polynomial fit for channel 2.

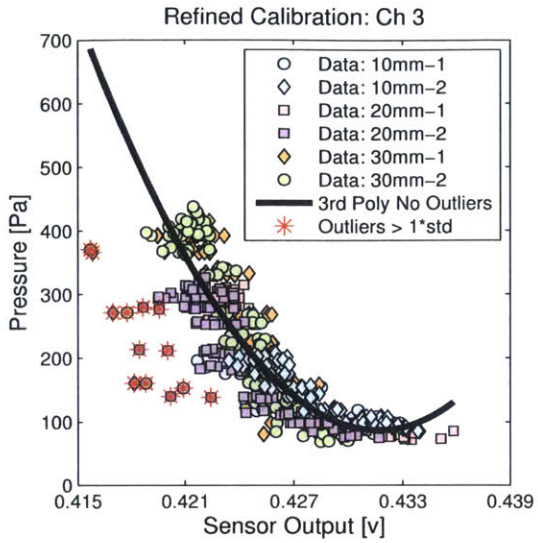

(b) Outliers and refined third order polynomial fit for channel 3.

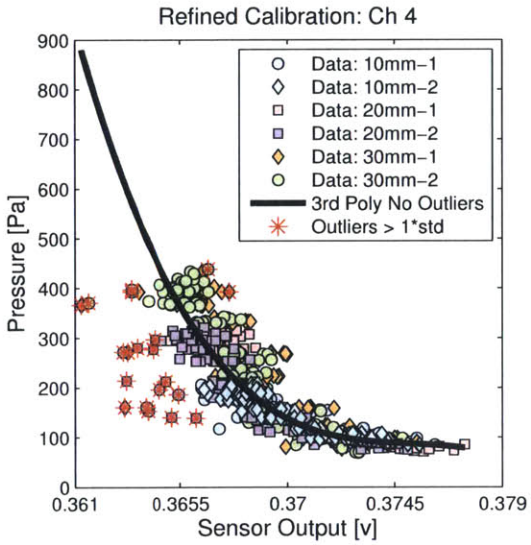

(c) Outliers and refined third order polynomial fit for channel 4.

Figure 5-16: Outliers were designated as samples falling further than 1.5 standard deviations away from the third degree polynomial fits shown in Figure 5-15. A refined third degree polynomial fit was found for each sensor channel with the outliers excluded.

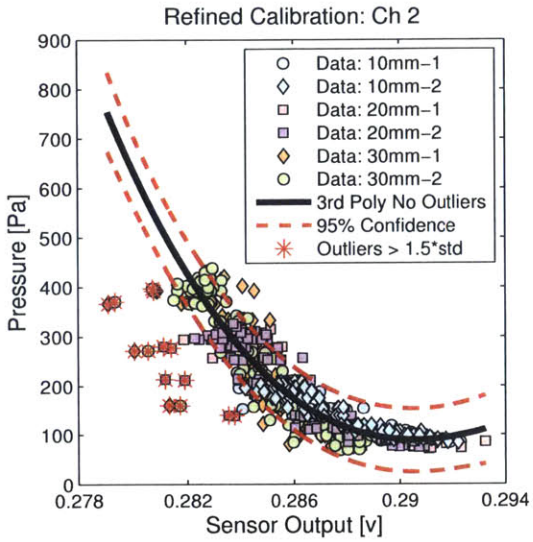

(a) Refined third degree polynomial fit for channel 2 with 95% confidence bounds.

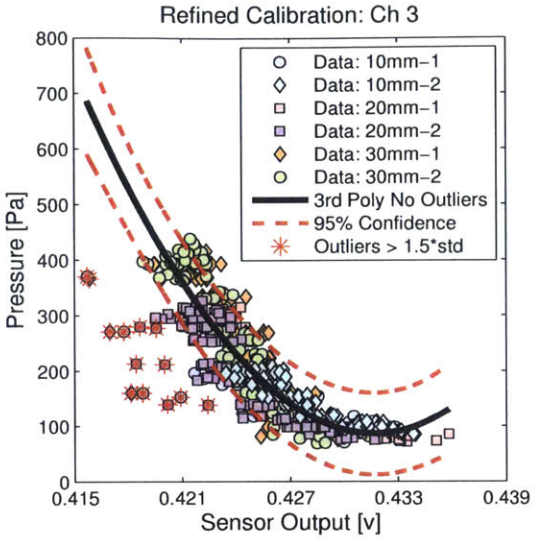

(b) Refined third degree polynomial fit for channel 3 with 95% confidence bounds.

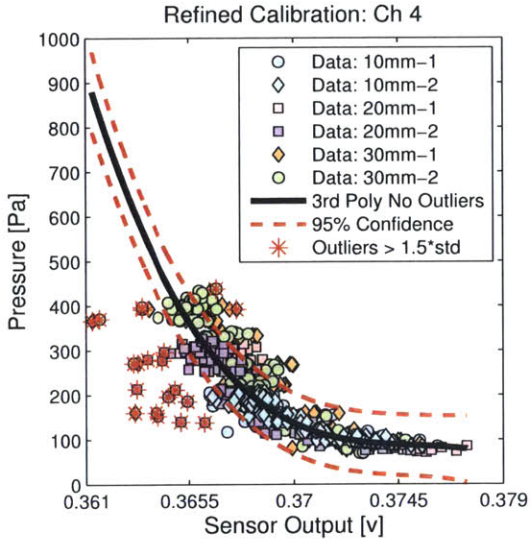

(c) Refined third degree polynomial fit for channel 4 with 95% confidence bounds.

Figure 5-17: Polynomial fits for the CBDPMS foam sensor array refined through the removal of outliers.

Channel	C_3	C_2	C_1	C_0
2	-1.426e+08	1.277e+08	-3.809e+07	3.785e+06
3	1.152e+07	-1.239e+07	4.254e+06	-4.548e+05
4	-2.846e+08	3.203e+08	-1.202e+08	1.503e+07
Channel	R^2	RMSE [Pa]	NRMSE [%]	
2	0.8881	32.80	8.89	
3	0.8551	37.54	10.17	
4	0.8752	34.49	9.34	

Table 5.6: Refined third degree polynomial coefficients and goodness of fit measures for the 7.8mm CBPMDS foam sensor array

Ch.	Experiment	RMSE [Pa]	%RMSE	NRMSE [%]
2	10 mm	19.83	12.18	13.23
2	20 mm	35.21	16.7	12.77
2	30 mm	47.41	28.04	13.34
3	10 mm	22.04	13.19	12.52
3	20 mm	47.77	27.32	15.09
3	30 mm	55.08	25.96	16.43
4	10 mm	32.58	18.23	15.27
4	20 mm	38.14	19.46	12.66
4	30 mm	71.82	24.86	24.92

Table 5.7: RMS error and Percent RMS error for the refined third degree polynomial calibration applied to time series plunging results.

vertical location of the Zaber stage, and the calibrated sensor results, as given in Table 5.7. The first oscillation of the stage was removed from each data set due to the first plunging oscillation generating a lower voltage response from the CBPDMS sensor array than the remainder of the oscillations within the experiment, as seen in Figure 5-11(b) and discussed in Section 5.3.5.

Piecewise Calibration with First-Order Correction

When considering the third order polynomial curve fits shown in Figure 5-17 it was observed that the behavior of the curves at the low pressure and high voltage end of the training data set was non-physical.While the slope of the polynomial curve changes from negative to positive, the pressure-voltage relationship in the physical sensor is

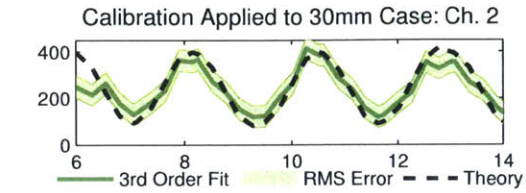

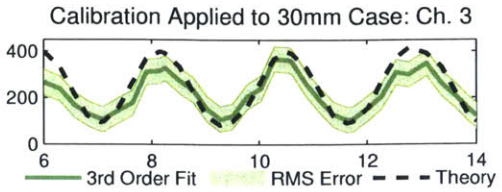

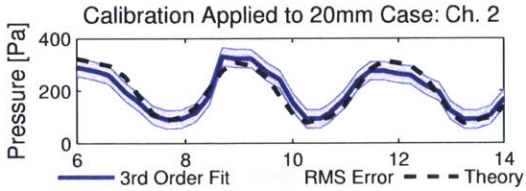

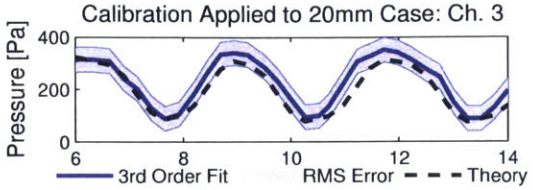

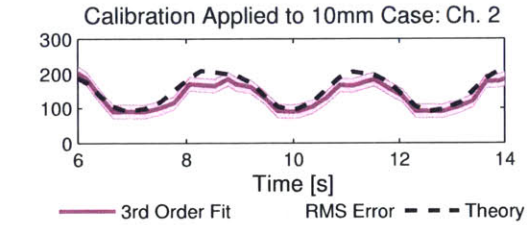

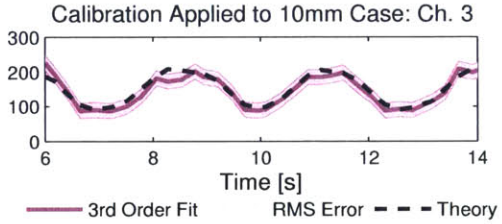

(a) Channel 2 polynomial calibration applied to plunging time series data.

(b) Channel 3 polynomial calibration applied to plunging time series data.

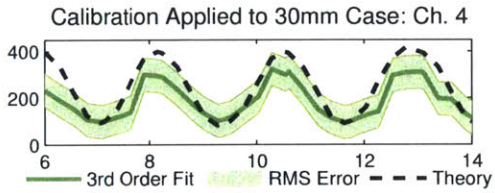

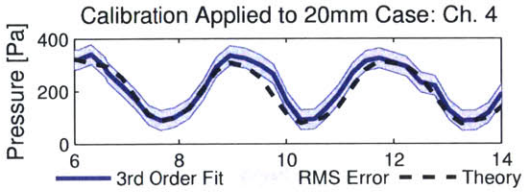

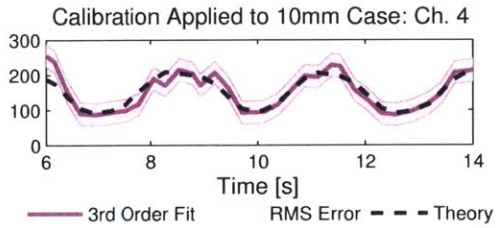

(c) Channel 4 polynomial calibration applied to plunging time series data.

Figure 5-18: The refined third degree polynomial calibration was applied to time series data from plunging experiments.

always inverse with a sensitivity that decreases at high levels of strain (pressure). To better represent the physical performance of the sensor array, a first-order correction of the form shown in Equation 5.12 was added to the calibration curve in the low pressure region to create a piecewise calibration.

$$P = C_3 * v^3 + C_2 * v^2 + C_1 * v + C_0, v \leq v_{inflection} \tag{5.12}$$
$$P = D_1 * v + D_0, v > v_{inflection}$$

To determine the curve fit for the first-order correction, the inflection point in the refined third degree polynomial fit was found. A linear fit was then performed on the subset of the data for $v > v_{inflection}$ with a condition put on the linear fit that it needed to pass through the point $(v_{inflection}, P_{inflection})$ from the third degree polynomial. The linear fit was found using the *slmengine* function in Matlab which allows for curve fitting with prescriptions on shape, piecewise segments, etc. The calibration curves with first and third degree polynomial regions for each channel of the 7.8 mm thick CBPDMS foam array can be seen in Figure 5-19, and the calibration curve parameters are given in Table 5.8. The piecewise polynomial calibration was also applied to the same time series data used to evaluate the refined third order polynomial fit in Section 5.3.5, and the results for the RMS error, %RMSE, and Normalized RMS error (NRMSE) are given in Table 5.9. While the the RMS error was not found to improve significantly between the refined third degree polynomial fit and the the piecewise polynomial fit, the piecewise fit eliminated the non-physical behavior of the third degree polynomial curve at low pressures, and is expected to provide more accurate results for low pressure stimulus outside of the training data range.

Ch.	C_3	C_2	C_1	C_0
2	-1.426e+08	1.277e+08	-3.809e+07	3.785e+06
3	1.152e+07	-1.239e+07	4.254e+06	-4.548e+05
4	-2.846e+08	3.203e+08	-1.202e+08	1.503e+07
Ch.	$v_{inflection}$ [v]	$P_{inflection}$ [Pa]	D_1	D_0
2	0.2906	89.25	-2362.43	775.74
3	0.4317	86.46	-553.09	325.23
4	0.376	84.99	- 3437.60	1377.53

Table 5.8: Coefficients and break points for the piecewise polynomial calibration of the thick array. For channel 4, an inflection point did not occur within the training data range, so a linear correction was added for v > 0.376 to ensure extrapolated values followed expected behavior.

Ch.	Experiment	RMSE [Pa]	%RMSE	NRMSE [%]
2	10 mm	19.78	12.06	12.84
2	20 mm	35.20	16.70	12.73
2	30 mm	47.41	28.04	13.34
3	10 mm	22.04	13.19	12.52
3	20 mm	47.77	27.32	15.09
3	30 mm	55.08	25.96	16.43
4	10 mm	32.58	18.23	15.27
4	20 mm	38.14	19.46	12.66
4	30 mm	71.82	24.86	24.92

Table 5.9: RMS error, Percent RMS error, and normalized RMS error for the piecewise polynomial calibration applied to time series plunging results for the thick array.

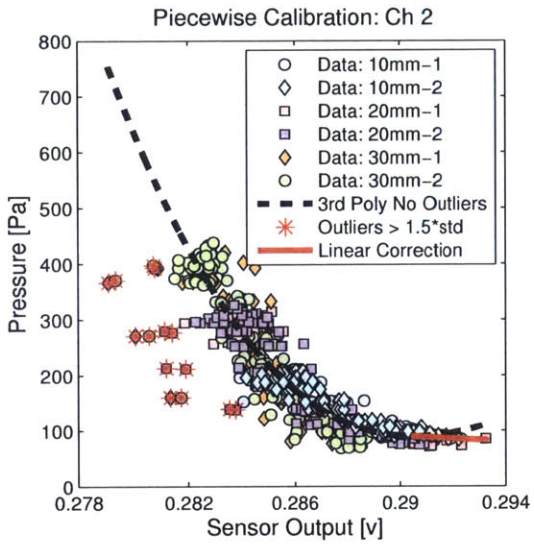

(a) Piecewise polynomial calibration for 7.8 mm thick CBPDMS foam array Channel 2.

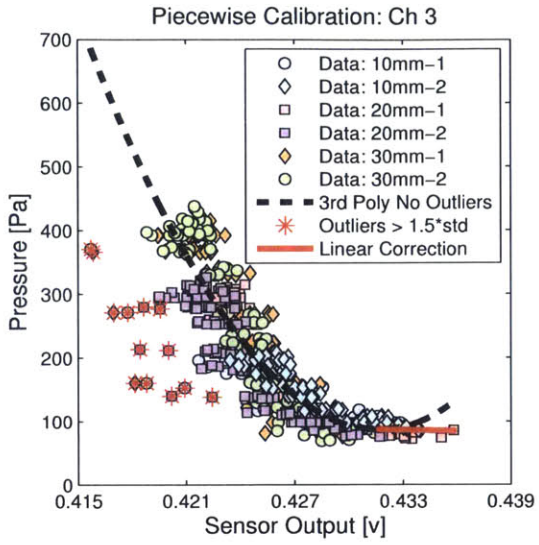

(b) Piecewise polynomial calibration for 7.8 mm thick CBPDMS foam array Channel 3.

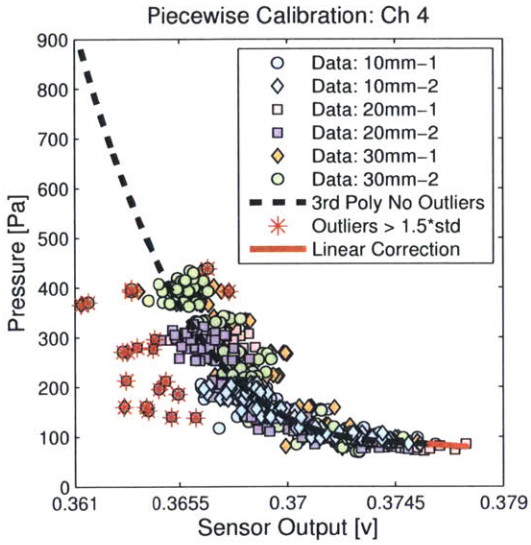

(c) Piecewise polynomial calibration for 7.8 mm thick CBPDMS foam array Channel 4.

Figure 5-19: Piecewise polynomial calibrations for the 7.8 mm (Thick) CBPDMS foam sensor array.

Ch.	C_3	C_2	C_1	C_0
2	-9.875e+05	9.223e+05	-2.678e+05	2.487e+04
3	-8.004e+05	8.296e+05	-2.791e+05	3.077e+04
4	-9.771e+05	1.045e+06	-3.721e+05	4.418e+04
Ch.	$v_{inflection}$ [v]	$P_{inflection}$ [Pa]	D_1	D_0
2	0.2305	60.20	0	60.20
3	0.2898	58.15	0	58.15
4	0.3437	62.81	0	62.81

Table 5.10: Coefficients and break point for piecewise polynomial calibration for the 6.2 mm (Thin) array.

5.3.6 Calibration of 6.2 mm (Thin) CBPDMS Foam Sensor Array

The 6.2 mm thick CBPDMS foam sensor array (referred to as "Thin") was calibrated using the same approach as the 7.8 mm thick array. A third degree polynomial was fit to the plunging data and refined through the exclusion of outliers falling further than 1.5 times the standard deviation away from the third degree fit curve. A linear correction was then added to the low pressure region of the training data to form a piecewise polynomial fit with the break point located at the third degree polynomial inflection, as seen in Figure 5-20. As in the case of the 7.8 mm thick sensor array, Channel 1 of the 6.2 mm (Thin) array was not working during the plunging experiments in Singapore. The parameters of the piecewise polynomial calibration for the Thin array can be found in Table 5.10, and the results of applying the calibration curves to time series plunging data is shown in Table 5.11.

5.3.7 Conclusions from Plunging Experiments

The periodic plunging experiments using the Zaber linear stage demonstrated the CBPDMS foam sensor array's repeatability and ability to be calibrated. The repeatability of the sensor arrays was demonstrated by considering the pressure-voltage trend exhibited by the array during six independent plunging experiments at increasing oscillation amplitudes, as seen in Figure 5-12. It was observed that pressure-voltage

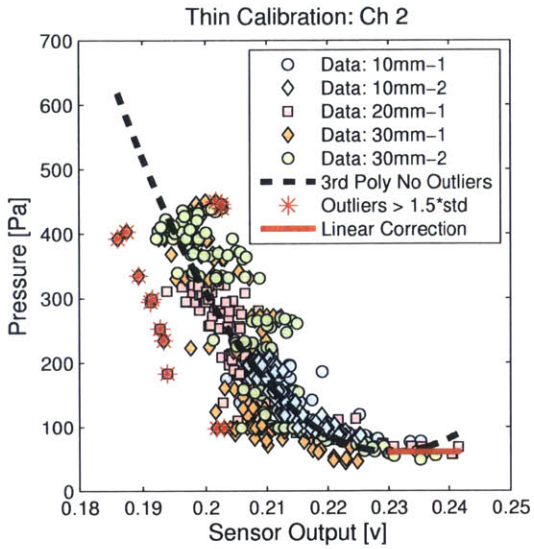

(a) Piecewise polynomial calibration for 6.2 mm thick CBPDMS foam array Channel 2.

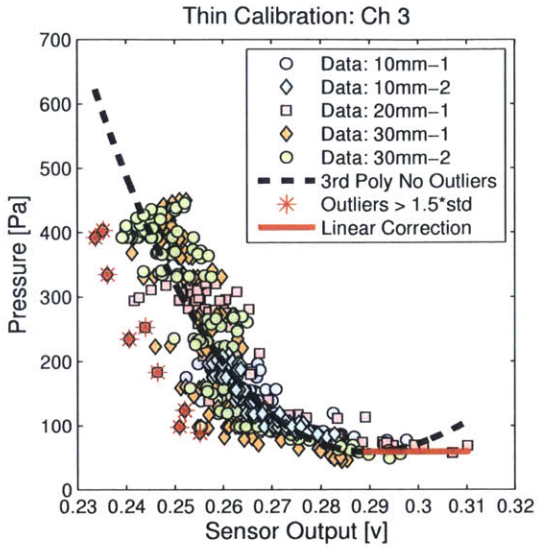

(b) Piecewise polynomial calibration for 6.2 mm thick CBPDMS foam array Channel 3.

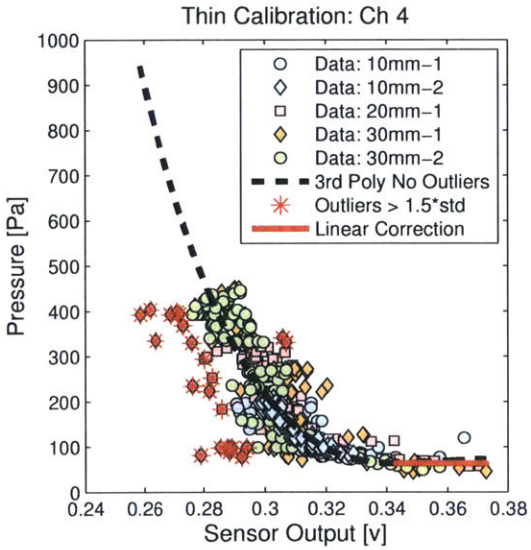

(c) Piecewise polynomial calibration for 6.2 mm thick CBPDMS foam array Channel 4.

Figure 5-20: Piecewise polynomial calibrations for the 6.2 mm (Thin) CBPDMS foam sensor array.

Ch.	Experiment	RMSE [Pa]	%RMSE	NRMSE [%]
2	10 mm	26.16	18.72	13.37
2	20 mm	53.75	30.26	12.56
2	30 mm	61.96	22.80	15.29
3	10 mm	28.36	20.15	12.37
3	20 mm	49.82	25.03	12.28
3	30 mm	56.65	26.97	12.67
4	10 mm	28. 97	20.08	12.17
4	20 mm	53.10	23.56	13.21
4	30 mm	58.89	29.20	12.54

Table 5.11: RMS error, Percent RMS error, and normalized RMS error for the piecewise polynomial calibration applied to time series plunging results for the thin array.

samples from multiple oscillations within the same experiment followed a consistent trend, as seen in Figure 5-12(b), and that with the DC offset voltage adjusted for consistency, the sensor response was consistent across multiple trials with the same parameters, as seen in Figure 5-12(d). Finally, it was observed that consistency was maintained across all six independent trials, as seen in FIgure 5-12(c).

The pressure-voltage measurements from the plunging experiments made clear that the relationship between hydrodynamic pressure stimulus and sensor voltage output was inverse and non-linear. Using a cross-validation methodology, it was determined that a polynomial fit of second, third, or fourth order could represent the sensor behavior. After refining the calibration through the removal of outlier values, a third degree polynomial was determined to best capture the sensor response, and a first order correction was added to the calibration for low pressures to eliminate non-physical behavior of the third-order curve. Using the piecewise polynomial calibration curves, time-varying hydrostatic pressure was reproduced from sensor voltage measurements with $\sim$15% NMRSE for the 7.8 mm thick sensor array, and $\sim$13% NMRSE for the 6.2 mm thick array when compared to the theoretical hydrostatic pressure based on sensor depth.

5.4 Water Wave Stimulus

5.4.1 Introduction

The ability to sense variations in free surface elevation is of great value in ocean engineering applications. Sensors may be employed to gather pressure data in order to characterize the frequency spectrum and significant wave heights of a random sea-state, or identify the free surface deformations caused by the wake of a passing surface vessel. Surface waves generated by wind are generally found at low frequencies, while the frequency of the waves generated by a surface vessel are related to the vessels speed [21].

In nature, both fish and toads utilize the lateral line sensory organ to perceive and localize the source of high frequency surface waves [6, 8, 36]. The perception of toads was tested by dipping a rod in the water to generate surface waves, and it was found toads were more likely orient to the wave source when the lateral line was intact compared to cases with the sensory organ disabled [36]. In the case of surface feeding fish, prey struggling on the water surface is localized based on the direction of the wave front sensed using symmetric lateral line receptors on opposite sides of the fish's head, as well as the curvature of the wave front and the change in frequency spectrum due to dispersion. The surface waves generated by insects trapped on the water surface are typically at frequencies above 20 Hz and have amplitudes less than 1 mm, a range very different from waves generated by surf, wind, and the fish's own movements [6, 8]. This distinction in frequency content, and the adaptation of the laterally line of surface feeding species to sense high-frequency and low-amplitude signals, allows fish to distinguish between waves signals from prey and environmental "noise".

5.4.2 Water Wave Experimental Setup

Characterization of a closed-cell CBPDMS foam pressure sensor array was conducted in the MIT towing tank using water waves as a dynamic pressure stimulus, similar

to the experiments described in Section 3.4.5. The MIT towing tank is a 100ft x 8ft x 4ft basin and waves were provided by a paddle type hydraulic wave maker capable of producing waves between 0.5 and 2.5 Hz, as seen in Figure 5-21(a). The wave maker frequency was controlled via a Labview interface, and wave amplitude was governed by an analog signal amplifier. Free surface elevation was accurately measured using two capacitance style wave probes located ahead of the foil's leading edge and separated by 4.5 cm, as seen in Figures 5-21(b) and 5-21(c). The output voltage from a CBPDMS foam pressure sensor array surface mounted on the foil was recorded simultaneously with the wave probe voltage output using a National Instruments USB-6289 data acquisition board and Labview software.

Two wave probes were used in the experiment and spaced at a distance less than the expected wavelength to allow for the measurement of the phase velocity during each experiment. In addition to the CBPDMS foam pressure sensor array, an array of four commercially available pressure sensors was mounted on the top of the foil and connected to the foil's surface via tubes within the foil for use in subsequent experiments. Additional details of the hydrofoil and commercial pressure sensor array can be found in Section 7.3.

Unlike the plunging experiments where the sensor array was tested while mounted flat in the 3D printed holder, during the wave experiments the array was glued into the surface of a NACA 0020 hydrofoil with a chord length of 0.12 m and composed of multiple individual sections along the span, as seen in Figure 5-22(a). Experiments were conducted using the 7.8mm thick array, and the array was held in place using Sil-Poxy silicone adhesive from Smooth-On. Experiments were conducted with the sensor array mounted on the foil section for two reasons:

1. To determine the effect of steady-state curvature on the array's output and sensitivity

2. To characterize the sensor in the foil used for the Kármán vortex street identification experiments discussed in Chapter 7

The 7.8mm thick array was chosen for integration into the foil surface due to its

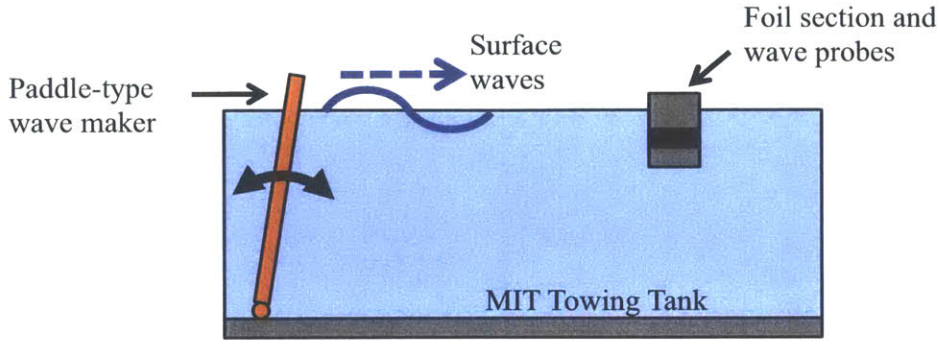

(a) Water waves were generated in the MIT towing tank by a paddle-type wave maker controlled via Labview. The sensor array was mounted in a 3D prointed NACA 0020 foil section and submerged at 1-1.5 cm below the mean waterline.

(b) Two capacitance style wave probes were mounted adjacent to the closed-cell CBDPMS foam sensor array to provide an accurate measurement of the free surface elevation and wave speed.

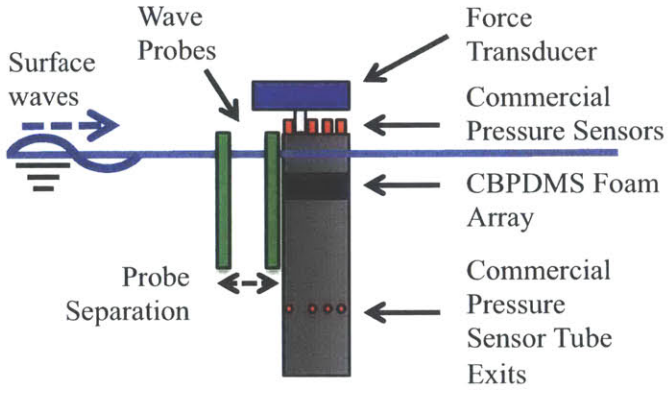

(c) The CBPDMS foam sensor array was mounted on a NACA 0020 hydrofoil secured so the array was submerged between 1-1.5 cm. The hydrofoil also contained an array of commercially available pressure sensors that were connected to the foil's surface via tubes within the foil. Additional details about the hydrofoil and commercial pressure sensor array can be found in Section 7.3.

Figure 5-21: A closed-cell CBPDMS foam sensor array was tested in the MIT towing tank using water waves as a dynamic pressure stimulus.

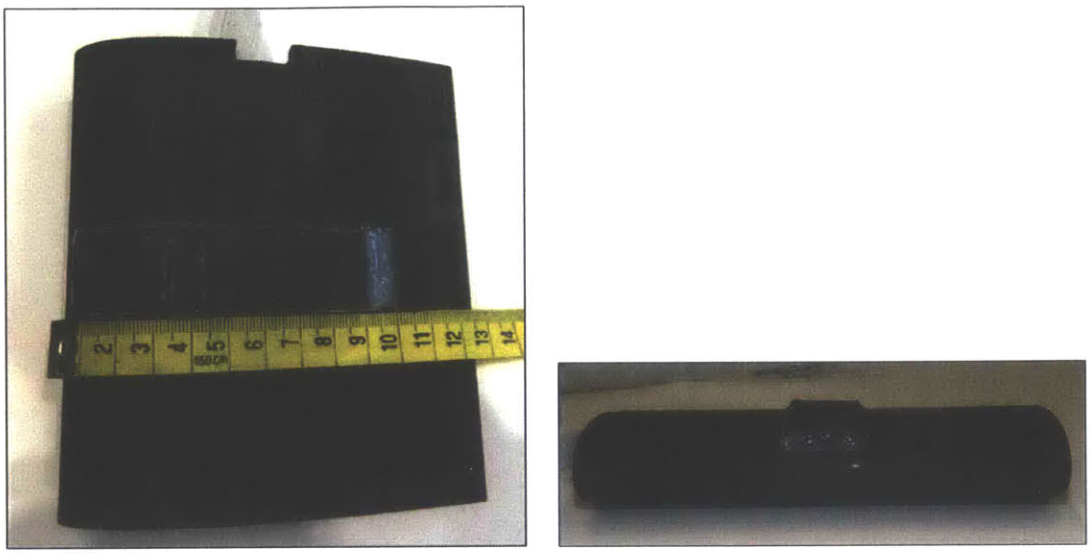

(a) For testing in the towing tank, a closed-cell CBPDMS foam sensor array was mounted on the surface of a foil section.

(b) Because of the presence of a mounting shaft within the foil section, the foam array could not be mounted flush with the foil surface. Silicone adhesive was used to secure the array and to fair the edges of the array with the foil surface.

Figure 5-22: A closed-cell CBPDMS foam sensor array was mounted on the surface of a NACA 0020 foil section for testing in the towing tank.

reliability during the plunging phase of array characterization. However, due to the presence of an aluminum support shaft that served to hold the 3D printed sections together and allow for mounting to the towing tank carriage, the array was not able to be positioned flush with the foil surface, as seen in Figure 5-22. To mitigate the effect of the protrusion from the foil surface, additional Sil-Poxy adhesive was used to fair the edges of the array and fill in any gaps between the array and the cutout in the foil surface. The effect of the sensor array protrusion from the foil surface is discussed in greater detail in Section 7.5.

5.4.3 Water Wave Pressure Field

The pressure field generated by the surface waves produced in the towing tank was calculated using linear wave theory, with the velocity potential given in Equation 5.13.

$$\phi = \frac{Ag}{\omega}\frac{cosh(k(z+h))}{cosh(kh)}sin(kx - \omega t) \tag{5.13}$$

With the free surface elevation (η_e) measured experimentally using the capacitance wave probes, the time-varying pressure due to the surface wave was given by Equation 5.14, where z was the depth of the sensor array below the mean free surface, ω was the wave frequency, and k was the wavenumber.

$$\begin{aligned} p_{total} &= p_{dynamic} - \rho g z \\ p_{dynamic} &= p_d = -\rho\frac{\partial\phi}{\partial t} \\ p_d(t) &= \rho g A\frac{cosh(k(z+h))}{cosh(kh)}cos(kx - \omega t) = \rho g\frac{cosh(k(z+h))}{cosh(kh)}\eta(t) \end{aligned} \tag{5.14}$$

For the wave maker oscillations used in the sensor array characterization experiments, $\sim h > \lambda/2$ satisfying the condition for the waves to be considered deep water, and allowing the simplification given in Equation 5.15 to be made.

$$\begin{aligned} &\sim h > \lambda/2 \\ &\therefore \omega^2 = gk \\ &P_d(t) = \rho g \eta_e(t) e^{kz} \end{aligned} \tag{5.15}$$

5.4.4 Data Analysis

Wave Probe and CBDPMS Foam Voltage Output Filtering

The voltage outputs from the capacitance style wave probes and the CBPDMS foam pressure sensors were bandpass filtered using the *idealfilter* function in Matlab. The cutoff frequencies were chosen by considering the frequency spectrum of the wave probe and CBPDMS foam array measurements. For both the wave probes and the sensor array, the primary frequency component aligned with the wave maker fre-

quency. In the case of the CBPDMS foam sensor array, a low frequency drift was present below 0.25 Hz, which was expected based on previous experiments and the design of the sensor for use in the measurement of AC signals. For both the wave probes and the pressure sensor array, high frequency noise was also present in the signals at 60 Hz and 34.65 Hz respectively. Based on the frequency spectra of the experimental data, the bandpass filter cutoffs were set at 0.3 and 3 Hz.

Temporal Shift of Pressure Measurements

As discussed in Section 5.4.2, two capacitance style wave probes were mounted in the water tank in front of the foil section to measure the free surface elevation. Using linear wave theory, the time-varying free surface elevation was used to determine the total pressure at the location of the CBPDMS foam sensor arrays. Because the wave probes were mounted closer to the wave maker than the sensor array, the voltage output from each sensor array channel needed to be shifted to ensure the proper phase alignment between the wave-generated pressure field, and the sensor output voltage. The data was shifted based on the measured distance between the wave probe closest to the foil leading edge and the location of each sensor channel (Δ_{probe}), the phase velocity (V_p) of the water wave, and the sampling rate of the National Instruments DAQ board.

The phase velocity of the water waves was determined experimentally by comparing zero crossing times of the two independent wave probes separated by 4.5 cm, as shown in Figure 5-23. With the phase velocity of the wave and the separation between the wave probe and the channels known, the time lag between the wave arriving at the probe and at the sensors was calculated. The number of data points to shift the CBPDMS foam pressure measurements was then determined based on the sampling rate of 1000 Hz, as outlined in Table 5.12.

Sensor Voltage Output Scaling and Offset Adjustment

As discussed in Section 5.2.1, during the plunging experiments conducted in the CENSAM laboratory in Singapore, the CBPDMS foam sensor array was powered by

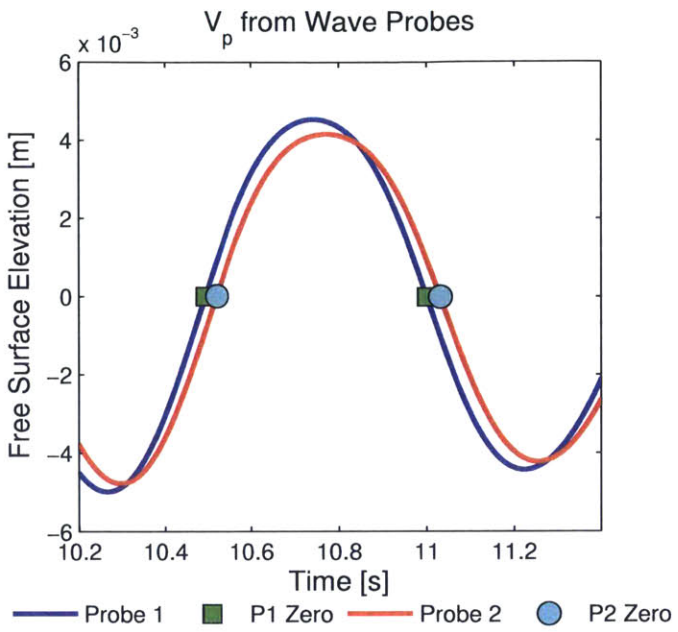

Figure 5-23: The phase speed of the water waves generated in the towing tank was found by comparing zero crossing times between the two capacitance wave probes separated by 4.5 cm. Shown above is the way probe measurements for a water wave at 1 Hz.

a supply current of $\sim$ 0.17 mA. For the wave experiments conducted at the MIT Towing Tank, a constant current circuit producing $\sim$ 0.20 mA was used to power the sensor array, as discussed in Section 5.2.2. In order to use the piecewise polynomial calibration found during the plunging experiments and described in Section 5.3.5, the voltage measurements from the wave experiments were scaled by (0.17/0.20) to account for the difference in supply current.

In addition to scaling the voltage output values to maintain consistency with the

Array Channel	Δ_{probe} [m]	V_p [m/s]	Time Lag [s]	Samples to Shift
Channel 1	0.0308	1.54	0.020	20
Channel 2	0.0478	1.54	0.031	31
Channel 3	0.0648	1.54	0.042	42
Channel 4	0.0818	1.54	0.053	53

Table 5.12: Example of the shifting of pressure sensor array measurements for a 1 Hz water wave. The distance Δ_{probe} is given from the wave probe closest to the foil leading edge to the center of the CBPDMS foam sensor channel.

Array Channel	Hydrostatic Pressure [Pa]	DC Voltage Offset [v]
Channel 1*	200	0.2854
Channel 2	200	0.2854
Channel 3	200	0.4249
Channel 4	200	0.36815

Table 5.13: The DC offset of the sensor voltage output from the water wave experiments was adjusted for hydrostatic pressure according to the piecewise calibration found during the plunging experiments in Singapore. In Singapore channel 1 was not operational, and therefore a piecewise calibration was not developed. Instead the calibration from sensor channel 2 was used, as discussed in Section 5.4.5

calibration experiments, the DC offset of the voltage output values was shifted to align with the piecewise calibration for each channel, as seen in Figure 5-24. The DC offset value was set to be the voltage that corresponded to the 200 Pa hydrostatic pressure at the sensor array submergence depth, as given in Table 5.13. With the DC offset voltage adjusted for the hydrostatic pressure, the dynamic response of the sensor array to water wave stimulus was found to be consistent with the plunging experiment data, as seen in Figure 5-24. The consistency of the dynamic response of the CBPDMS foam sensor array between the plunging and water wave experiments satisfied the requirement for repeatability across various types of stimulus as outlined in Section 5.1.1.

5.4.5 Calibrated Water Wave Results

To test the applicability of the piecewise calibration developed using plunging data to other hydrodynamic pressure stimulus, the calibration was applied to the sensor output voltage from water wave experiments, as seen in Figures 5-26 and 5-27. For Channels 2, 3, and 4 which were calibrated using the plunging experiments, the percent RMS error between the calibrated sensor output and the theoretical wave pressure found using linear wave theory was less than 10 %, as seen in Table 5.15. While the calibrated sensor results contained additional high frequency components compared to the theoretical wave pressure, the peak frequency of each channel's frequency spectra was found to match the wave frequency at 1 Hz, as shown by

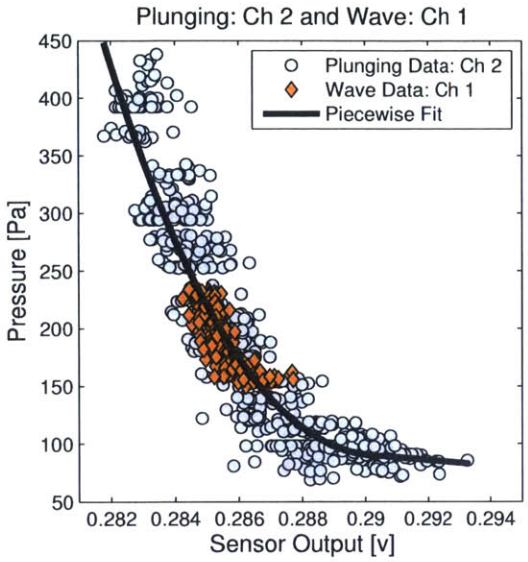

(a) Sensor output data from water wave stimulus Thick channel 1 overlaid on the plunging data and piecewise polynomial calibration for channel 2.

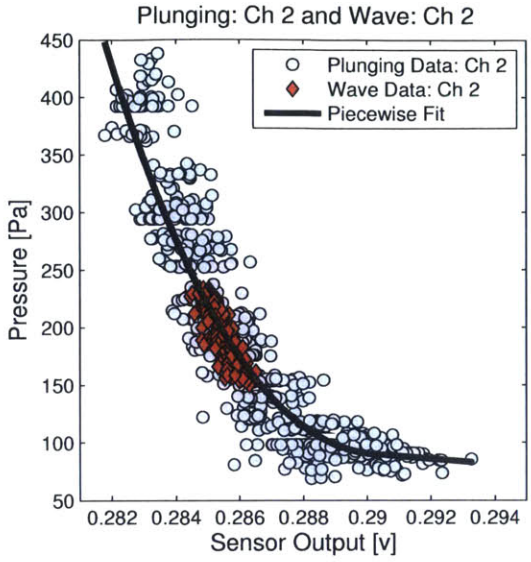

(b) Sensor output data from water wave stimulus Thick channel 2 overlaid on the plunging data and piecewise polynomial calibration for channel 2.

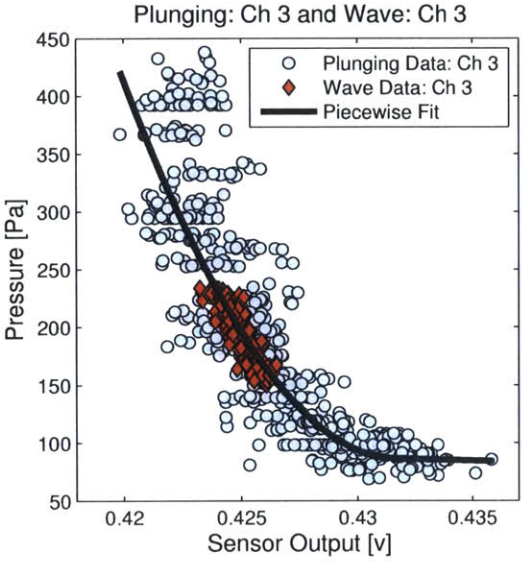

(c) Sensor output data from water wave stimulus Thick channel 3 overlaid on the plunging data and piecewise polynomial calibration for channel 3.

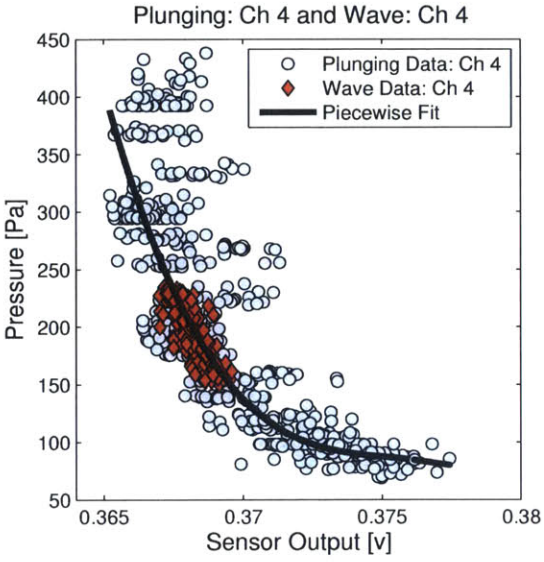

(d) Sensor output data from water wave stimulus Thick channel 4 overlaid on the plunging data and piecewise polynomial calibration for channel 4.

Figure 5-24: To demonstrate the repeatability of the 7.8 mm thick CBPDMS foam sensor array output across differing pressure stimulus, the voltage output from a water wave stimulus was compared to the data from six plunging experiments. Array channel 1 was not operational during the plunging experiments, so the output from the wave stimulus was compared to the plunging data and calibration from array channel 2. Voltage output from the water wave experiments has been scaled according to the ratio of supply current between the wave and plunging experiments, and every one-hundredth sample is shown.

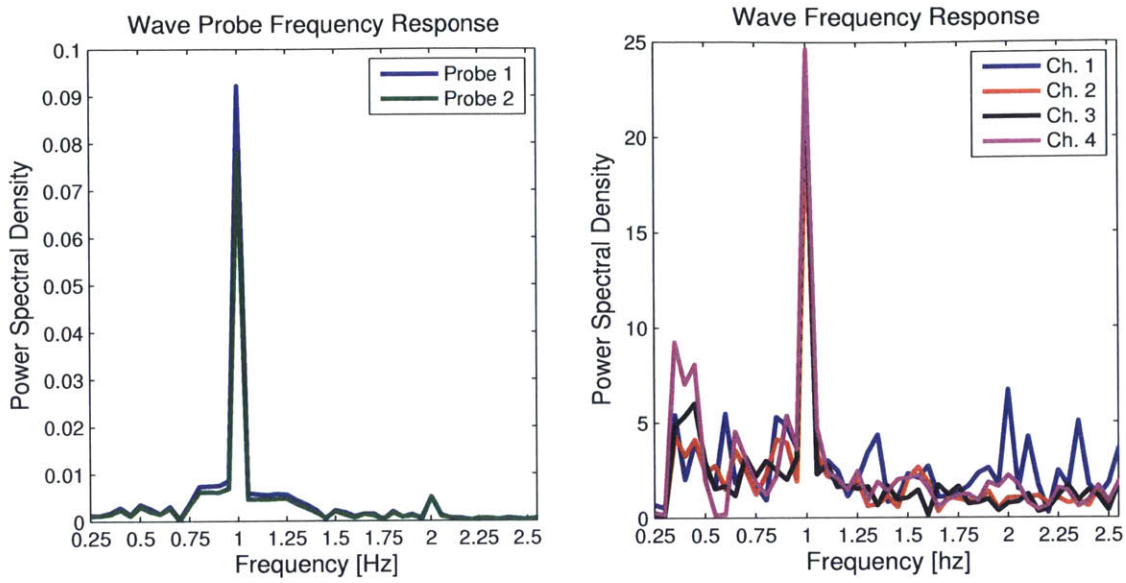

(a) Frequency spectra for the wave probe voltage outputs showing peak frequencies at 1 Hz.

(b) Frequency spectra for the four channels of the CBPDMS foam sensor array showing peak frequencies matching the wave stimulus at 1 Hz.

Figure 5-25: The peak frequency in the spectra of the CBDPMS foam sensor array channels was found to match that of the capacitance wave probes.

comparing the sensor array spectra to the wave probe spectra in Figure 5-25.

Calibration of Sensor Channel 1

During the plunging experiments conducted at the CENSAM laboratory in Singapore, channel 1 of the 7.8 mm thick CBPMDS foam sensor array was not operational, and therefore a piecewise polynomial calibration was not developed in Section 5.3.5. Upon return to MIT in Boston, channel 1 was restored to operation for use in the water wave and subsequent experiments. In order to convert the voltage measurements from channel 1 to pressure values, the calibrations from channels 2, 3, and 4 were applied to the channel 1 voltages and compared against the theoretical wave pressure found using linear wave theory, as seen in Table 5.14. It was found that the the wave pressure was reproduced with less than 10 % RMS error using the calibration from channel 2, a result significantly better than the calibration curves from channels 3 or 4. In subsequent experiments, the calibration curve developed for channel 2 will be applied to channel 1.

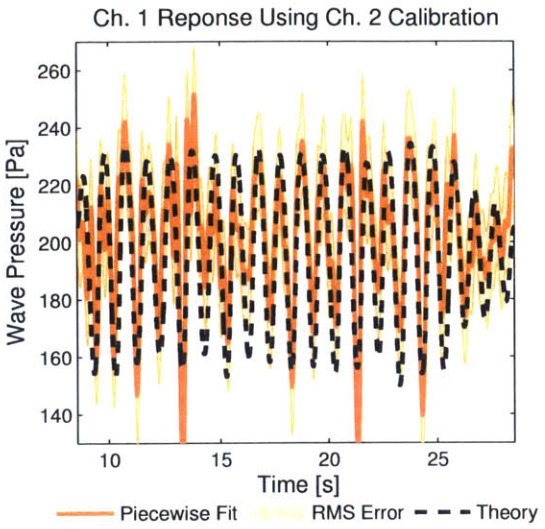

(a) Polynomial calibration for 7.8 mm thick CBPDMS foam array channel 2 applied to sensor channel 1 voltage output from water waves in the MIT Towing Tank.

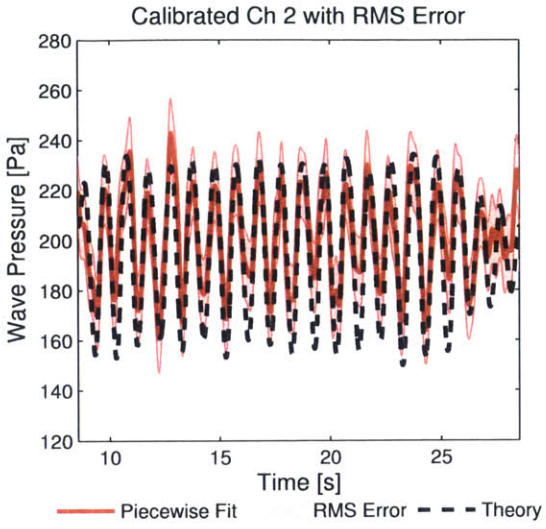

(b) Polynomial calibration for 7.8 mm thick CBPDMS foam array channel 2 applied to sensor channel 2 voltage output from water waves in the MIT Towing Tank.

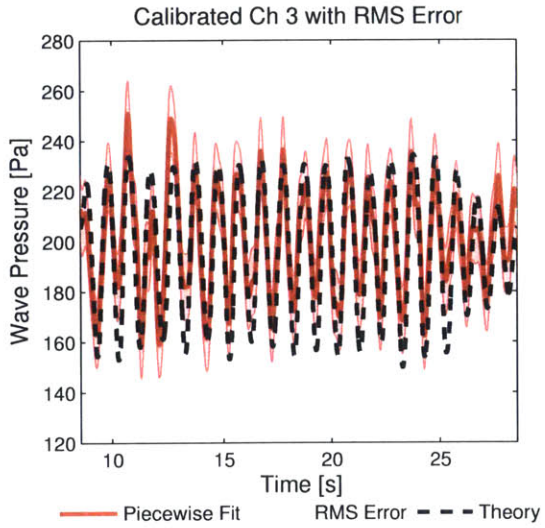

(c) Polynomial calibration for 7.8 mm thick CBPDMS foam array channel 3 applied to sensor channel 3 voltage output from water waves in the MIT Towing Tank.

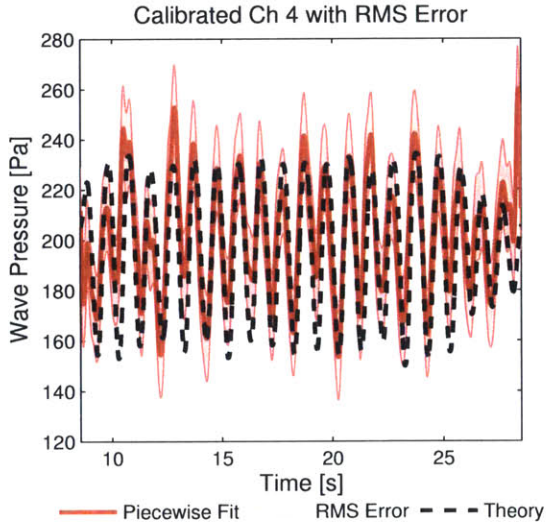

(d) Polynomial calibration for 7.8 mm thick CBPDMS foam array channel 4 applied to sensor channel 4 voltage output from water waves in the MIT Towing Tank.

Figure 5-26: The piecewise polynomial calibration found during the plunging experiments was applied to the time series voltage output from the 7.8 mm thick CBPDMS foam sensor array in response to water wave stimulus. The water wave pressure measurements for sensor channel 1 were found using the piecewise calibration curve found for channel 2 during the plunging experiments.

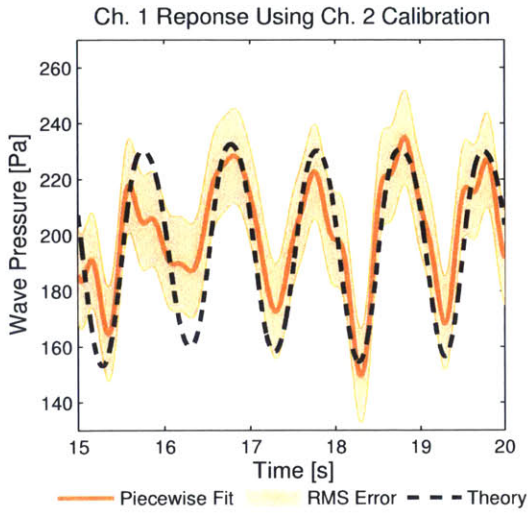

(a) Detailed view of the polynomial calibration for 7.8 mm thick CBPDMS foam array Channel 2 applied to sensor Channel 1 voltage output from water waves in the MIT Towing Tank.

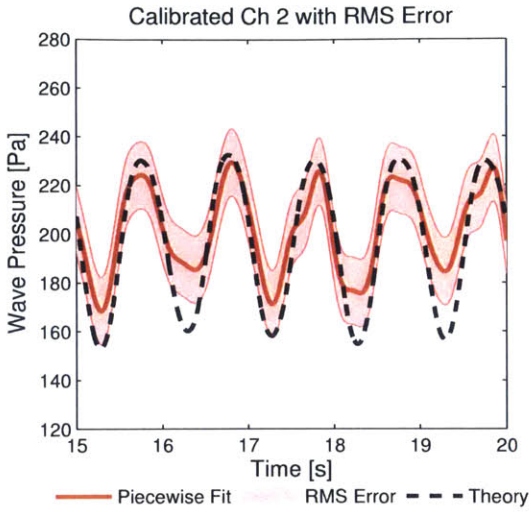

(b) Detailed view of the polynomial calibration for 7.8 mm thick CBPDMS foam array Channel 2 applied to sensor Channel 2 voltage output from water waves in the MIT Towing Tank.

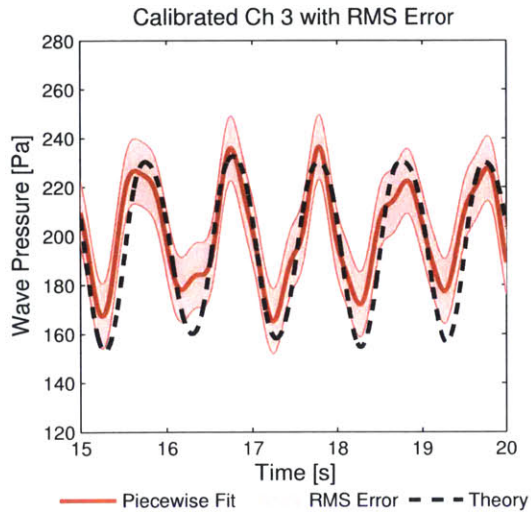

(c) Detailed view of the polynomial calibration for 7.8 mm thick CBPDMS foam array Channel 3 applied to sensor Channel 3 voltage output from water waves in the MIT Towing Tank.

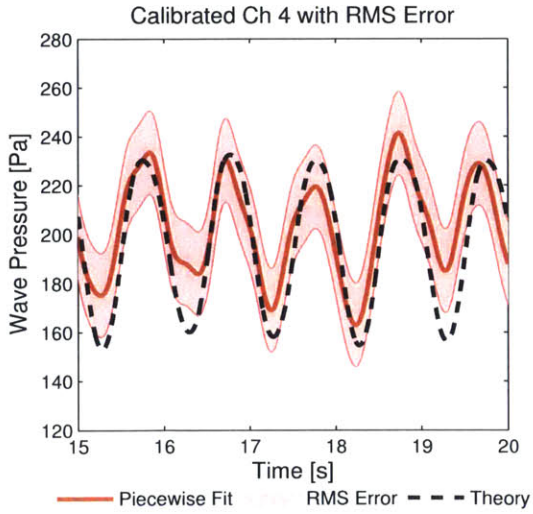

(d) Detailed view of the polynomial calibration for 7.8 mm thick CBPDMS foam array Channel 4 applied to sensor Channel 4 voltage output from water waves in the MIT Towing Tank.

Figure 5-27: Detailed view of the water wave pressure measured using the 7.8 mm thick CBPDMS foam sensor array.

Calibration	RMS Error [Pa]	% RMS Error
Channel 2	17.02	9.43
Channel 3	109.03	53.56
Channel 4	87.73	42.60

Table 5.14: The piecewise calibration for each channels 2, 3, and 4 found using the plunging experiment data was applied to channel 1, and the RMS error when compared to the theoretical wave pressure was calculated. It was found that the calibration for channel 2 provided the best fit for channel 1 by a considerable margin.

Array Channel	RMS Error [Pa]	% RMS Error	NRMSE [%]
Channel 1*	17.02	9.43	12.96
Channel 2	13.88	7.89	16.91
Channel 3	13.30	7.39	14.48
Channel 4	17.15	9.39	16.13

Table 5.15: Using the piecewise calibrations developed from the plunging experiments, the water wave pressure was found from the sensor array voltage output and compared to the theoretical pressure found from linear wave theory. For channel 1, the calibration from sensor channel 2 was used, as discussed in Section 5.4.5

5.5 Chapter Summary

Sensor characterization experiments using time-varying pressure from vertical plunging and surface water waves revealed fundamental characteristic of the CBPDMS foam array performance. Primary among these was the non-linear and inverse relationship between hydrodynamic pressure and sensor voltage output that is consistent with the compressible model of CBPDMS piezoresistivity presented in Section 4.4. The response of the sensor arrays across multiple plunging experiments with increasing amplitude was found to be repeatable, and using the results from the plunging experiments, a piecewise polynomial calibration was developed for each channel of the 7.8 mm and 6.2 mm thick arrays.

When exposed to the hydrodynamic pressure field generated by surface water waves, the voltage output from the 7.8 mm thick CBPDMS foam sensor array was found to exhibit a consistent trend to the plunging experiments when the DC voltage offset was corrected for changes in experimental setup, as shown in Figure 5-24. When

the piecewise polynomial calibration curves found from the plunging experiments were applied to the sensor voltage output recorded during the water wave experiments, the hydrodynamic pressure was reproduced with less than 17% Normalized RMS error (NRMSE) when compared to the theoretical pressure based on free surface elevation recorded using wave probes. The success of the CBPDMS foam sensor array in measuring the hydrodynamic pressure field from surface water waves demonstrated the repeatability of the sensor array across varying stimulus types, and confirmed the ability of the sensor array to be calibrated using a piecewise polynomial curve.

The success of the CBDPMS foam arrays as a hydrodynamic sensor for use on unmanned marine vehicles can be evaluated by comparing the performance of the arrays during plunging and wave experiments against the applications identified in Table 2.1. Based on previous experiments in vortex tracking on an AUV shaped body [33] and a single-element hydrofoil [27], sensor spacing of less than 5 cm was recommended in order to properly resolve vortex location. The spacing of individual sensor channels in the CBPDMS foam arrays is 1.7 cm, satisfying the sensor spacing guidelines for the unmanned vehicle applications presented. In Table 2.1, the example hydrodynamic pressure stimuli were found to have dynamic pressure amplitudes between 10 and 200 Pa. During the plunging and wave experiments, the dynamic range demonstrated by the CBPDMS foam pressure sensor array was approximately 50-500 Pa, with a resolution of $\sim$10 Pa. In these experiments, the low end of the dynamic range was limited by the experimental setups and the minimum depth necessary to fully submerge the sensor array. In Chapter 6, experiments will be discussed which utilized a dipole stimulus with RMS pressure approaching $\sim$3 Pa. Based on these experiments, it is expected that the CBPDMS foam arrays would be capable of detecting hydrodynamic stimuli consistent with the examples presented in Table 2.1.

The low frequency range of 0.25-3 Hz identified for the example unmanned marine vehicle applications was verified through plunging experiments at 0.5 Hz and wave experiments at 1 Hz. Evaluation of the high frequency sensing capabilities of the sensor array will be discussed in Chapter 6. Based on the results of the plunging and wave experiments, the CBPDMS foam sensor arrays were found to be well suited for

the unmanned marine vehicle applications identified in Table 2.1.

For the proposed ship-scale application in Table 2.1, additional optimization work would be needed to increase the dynamic range of the CBPDMS foam sensors. During the plunging experiments, it was observed that the sensitivity of the sensor arrays decreased at pressures greater than approximately 500 Pa. In ship-scale applications, foam sensor arrays would likely be subjected to dynamic pressures on the order of several kilopascals, as well as potentially large hydrostatic pressures due to the increased draft of large scale vessels. To be useful for these applications the material properties of the CBPDMS foam would require optimization for higher pressure ranges.

Chapter 6

Dipole Experiments

6.1 Introduction and Literature

A vibrating sphere generating a so-called dipole flow is one of the most commonly used stimuli in both biological studies of the fish lateral line, and efforts to characterize the performance of biomimetic sensor arrays. Any vibrating object of constant volume located in the far field appears like a dipole, leading to the the dipole being used generically for identification of flapping or vibrating bodies. Details of the dipole flow can be found in Lamb [55] and Newman [71], and the potential flow model of the flow field will be discussed in Section 6.3.

6.1.1 Dipole use in Biological Studies

When studying the sensory abilities of the fish lateral line, the dipole flow is often used as a hydrodynamic stimulus. The dipole source has been a primary stimulus method used when studying the lateral line capabilities of fish both experimentally [20, 37, 18, 19, 14, 69] and in simulation [20, 15, 85, 74]. In particular, an extensive study of the response to a dipole stimulus by blinded *Mottled Sculpin* was carried out by Coombs and Conley [18, 19, 14]. It was found that the lateral line line played a crucial role in the ability of the fish to orient towards a dipole source, and that the variation in excitation patterns across the spatially distributed lateral line was

especially important. The importance of the spatial distribution of the lateral line when localizing and orienting towards a dipole source adds to the motivation for developing spatially distributed sensor arrays for use in hydrodynamic applications.

6.1.2 Dipole use in Sensor Characterization

The dipole flow generated by a vibrating sphere is commonly used in the characterization of biomimetic sensor arrays, both due to the well known flow characteristics, and the broad use of the dipole stimulus in biological lateral line studies. The generation of a dipole flow by a vibrating sphere has been used extensively to study the response of experimental lateral line inspired pressure sensor arrays in water [48, 91, 92, 93, 73, 67, 12] and in air [25]. The particular experimental setup used in this study has been previously utilized by CENSAM researchers to characterize the performance of bio-inspired MEMS pressure sensors [3, 51, 4].

6.2 Experimental Setup

A 15.83 mm diameter brass sphere was attached to a Brüel and Kjaer Type 4810 mini shaker using a 4.70 mm diameter rod, as shown in Figure 6-1(b). The mini shaker was secured above a water tank using a T-slot aluminum frame, as shown in Figure 6-1(a). A Tektronix function generator (model AFG3102) was used to produce a sinusoidal signal at the desired testing frequency, and amplification was provided by a Brüel and Kjaer Type 2718 power amplifier, as seen in Figure 6-1(c).

The velocity of the brass sphere was a function of both the frequency and amplitude settings on the function generator, as well as the gain setting on the power amplifier. The velocity of the sphere was measured experimentally for the settings used in the characterization by taking high speed video of the sphere at each testing frequency, as shown in Figure 6-2(a). The average amplitude A of the sphere oscillation was found from individual video frames, and the sphere velocity was found as $U_{sphere} = \omega A$, where $\omega = 2\pi f$. It was found that the velocity of the sphere increased nearly linearly with frequency from 10-35 Hz, as seen in Figure 6-2(b).

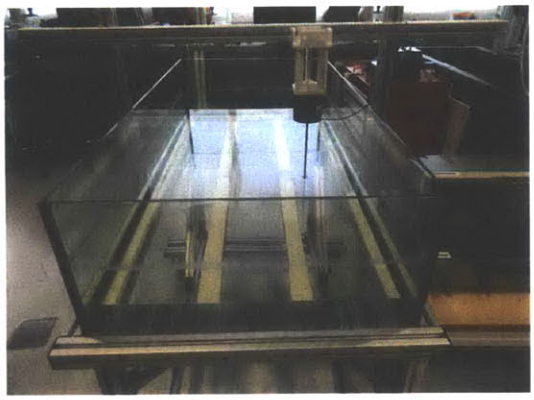

(a) Dipole experiments were conducted using a vibrating sphere mounted above a shallow glass water tank in the CENSAM lab in Singapore.

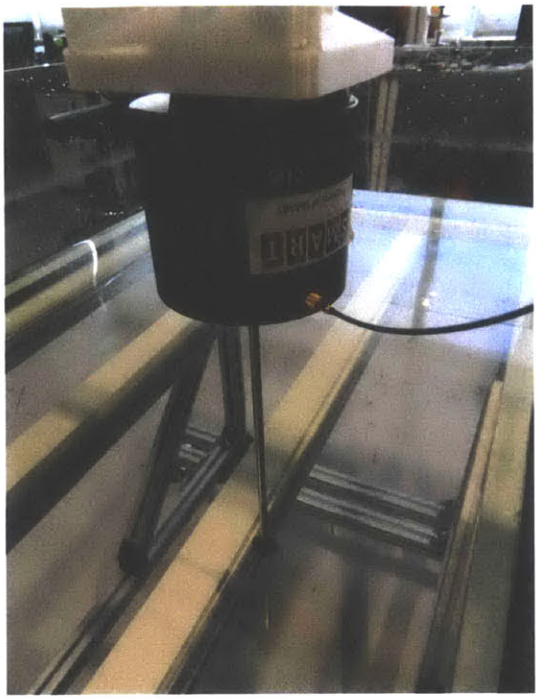

(b) A 15.83 mm diameter brass sphere was attached to a Brüel and Kjaer Type 4810 mini shaker which provided oscillations from 5-100 Hz

(c) Power amplification for the mini shaker was provided by a Brüel and Kjaer Type 2718 power amplifier.

Figure 6-1: Dipole experimental setup in the CENSAM laboratory in Singapore.

For the dipole experiments, the thin CBPDMS foam sensor array was used with a total sensor thickness of 6.2 mm. The sensor array remained in the 3-D printed holder used during the plunging experiments, and was held on the bottom of the tank using a dive weight, as seen in Figure 6-3.

During the dipole experiments, the vibrating sphere was oriented in a perpendic-

(a) High speed images of the sphere oscillations at various frequencies were captured using a Phantom V10 camera. The calibration image shown was used to convert from image pixels to physical units, and the intersection between the vertical shaft and the brass sphere provided an easily identifiable and consistent location to measure sphere position in the image frame.

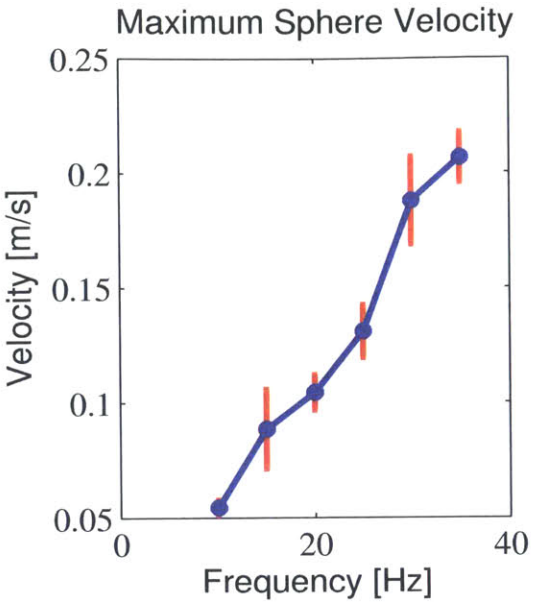

(b) The sphere peak velocity was calculated from the sinusoidal oscillation frequency and amplitude and was found to vary approximately linearly with frequency. Velocity was not calculated for a frequency of 5 Hz

Figure 6-2: The peak velocity of the oscillating sphere was measured using high speed imagery and found to vary approximately linearly with frequency.

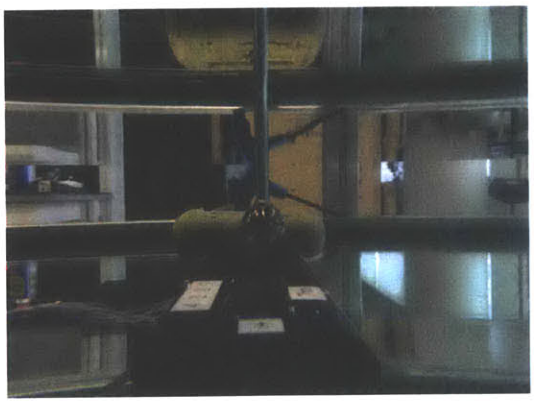

Figure 6-3: In the perpendicular configuration the dipole sphere was positioned directly above the thin CBPDMS foam sensor array at separation distances of 5 mm and 18 mm. The sphere oscillated vertically, perpendicular to the foam array

ular configuration to the sensor array, as shown in Figure 6-3. To accomodate the perpendicular orientation, the 6.2 mm thick CBPDMS foam sensor array was placed flat on the bottom of the testing tank with the sphere oscillating vertically above it inline with the z axis. In this orientation, the separation distance between the surface of the sensor array and the vibrating sphere was varied, as was the lateral position of the sphere relative to the array, as seen in Figure 6-4 and Table 6.1. For the perpendicular orientation the total water depth was 9 cm, and the submergence depth of the sensor was 7 cm, corresponding to a hydrostatic pressure of 686 Pa. During the experiments, the sinusoid amplitude generated by the Tektronix function generator was kept constant at 707 mV peak-to-peak, and the frequency of oscillation was varied from 10-35 hz as seen in Table 6.1.

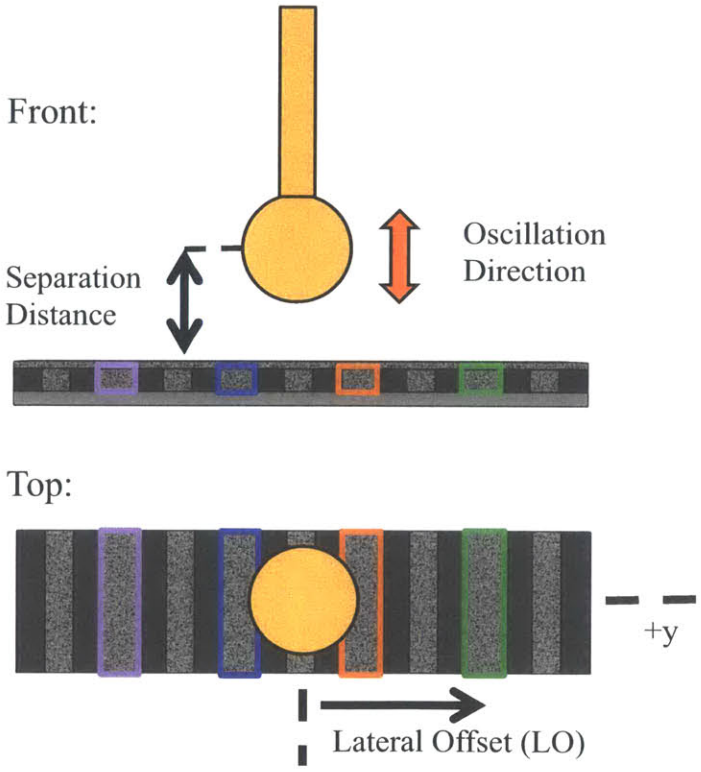

Figure 6-4: The dipole was positioned in a perpendicular arrangement above the 6.2 mm thick CBPDMS foam sensor array, and the lateral offset and separation distance were varied.

Orientation	Separation Distance [mm]	Lateral Offset [mm]	Frequency Range [hz]
Perpendicular	18	0	10:5:35
Perpendicular	18	20	10:5:35
Perpendicular	18	-20	10:5:35
Perpendicular	5	0	10:5:35
Perpendicular	5	20	10:5:35

Table 6.1: Dipole experiment parameters.

6.3 Dipole Flow Field

The pressure distribution generated by the dipole can be found by modeling an oscillating sphere in potential flow, as found in [20, 19, 18, 37, 25, 93, 15, 4, 73]. The position of the dipole was initially defined in a cartesian coordinate system with the sphere located at the origin and oscillating along the z axis, as seen in Figure 6-5. The cartesian coordinate system can be converted to spherical coordinates using Equation 6.1.

$$\begin{aligned} r &= \left[x^2 + y^2 + z^2\right]^{\frac{1}{2}} \\ \gamma &= \tan^{-1}\left(\frac{y}{x}\right) \\ \theta &= \cos^{-1}\left(\frac{z}{r}\right) \end{aligned} \tag{6.1}$$

In spherical coordinates, the velocity potential for the horizontal translation of a sphere with fluid at rest at infinity is given in Equation 6.2, where a is the radius of the sphere, and U is the sphere velocity. For the case of the vibrating sphere, the sinusoidal velocity profile in Equation 6.3 is used where $U_\circ$ is the velocity amplitude. The time-varying velocity potential ($\phi(t)$) for the vibrating sphere is then given in Equation 6.4.

$$\phi(r,\theta) = -\frac{1}{2}\frac{Ua^3}{r^2}\cos(\theta) \tag{6.2}$$

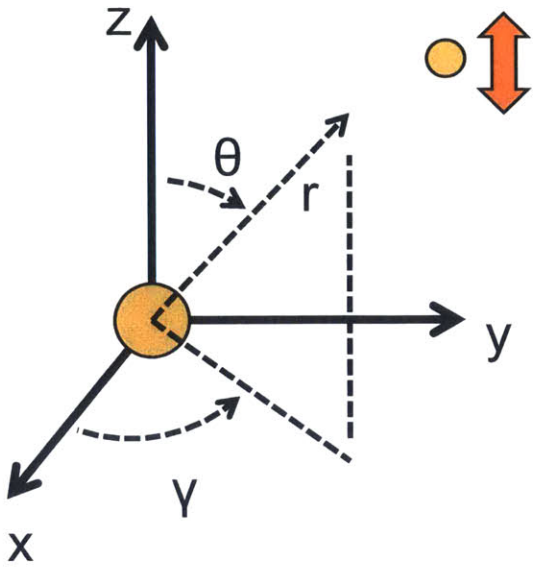

Figure 6-5: Coordinate system for perpendicular dipole potential flow model. The sphere oscillates along the z-axis.

$$U = U_\circ \sin(\omega t) \tag{6.3}$$

$$\phi(r, \theta, t) = -\frac{1}{2} \frac{U_\circ \sin(\omega t) a^3}{r^2} \cos(\theta) \tag{6.4}$$

The pressure field can then be found from the unsteady Bernoulli equation, as given in Equation 6.5. For the oscillating sphere, the pressure is dominated by the unsteady term $\frac{\partial \phi}{\partial t}$ as $\frac{\partial \phi}{\partial t} \gg |\nabla \phi|^2$. This is due to the unsteady term being proportional to $\frac{a^2}{r^2}$ while the steady term is proportional to $\frac{a^6}{r^6}$ as seen in Equation 6.6 and Equation 6.7.

$$P = -\rho \left(\frac{\partial \phi}{\partial t} + \frac{1}{2} |\nabla \phi|^2 + gz \right) + c(t) \tag{6.5}$$

$$\frac{\partial \phi}{\partial t} = -\frac{1}{2} \frac{U_\circ \omega a^3 \cos(\omega t)}{r^2} \cos(\theta) \tag{6.6}$$

$$|\nabla\phi|^2 = \left(\frac{\partial\phi}{\partial r}\right)^2 + \left(\frac{1}{r}\frac{\partial\phi}{\partial\theta}\right)^2 + \left(\frac{1}{r\sin(\theta)}\frac{\partial\phi}{\partial\gamma}\right)^2 \tag{6.7}$$

$$|\nabla\phi|^2 = \left(\frac{U_\circ \sin(\omega t)a^3\cos(\theta)}{r^3}\right)^2 + \left(\frac{1}{2}\frac{U_\circ \sin(\omega t)a^3\sin(\theta)}{r^3}\right)^2$$

The total pressure at a point in the vicinity of a vibrating sphere is therefore given by Equation 6.8, and the dynamic component (P_d) is given by Equation 6.9.

$$P = -\rho\left(\frac{\partial\phi}{\partial t} + gz\right) \tag{6.8}$$

$$P_d(r,\theta,t) = -\rho\frac{\partial\phi}{\partial t} = \frac{\rho\omega a^3 U_\circ \cos(\omega t)}{2r^2}\cos(\theta) \tag{6.9}$$

6.3.1 Flow Field Near a Wall

Sensor Array on Tank Bottom- Perpendicular Case

For the dipole experiments, the oscillating sphere was in close proximity to the CBPDMS foam sensor array, the array holder, and the water tank bottom. To ensure the no flux condition was satisfied at these walls, an image sphere was used as shown in Figure 6-6(b) and with velocity potential given in Equation 6.10. In general, the velocity potential for the image sphere is a function of θ_2 and r_2, as seen in Figure 6-6(a). For the special case of the sensor array located at the symmetry plane for the image sphere, it can be observed from Figure 6-6(b) that $r_1 = r_2 = r$ and $\theta_2 = \pi - \theta_1$. The total velocity potential ($\phi_\perp$) is then found to be the summation of the velocity potential for the vibrating sphere (ϕ_1) and the image sphere potential (ϕ_2) $\phi_\perp = \phi_1 + \phi_2$ as shown in Equation 6.11. The pressure can then be found from the total velocity potential $\phi_\perp$ using the unsteady Bernoulli equation from Equation 6.5 as seen in Equation 6.12.

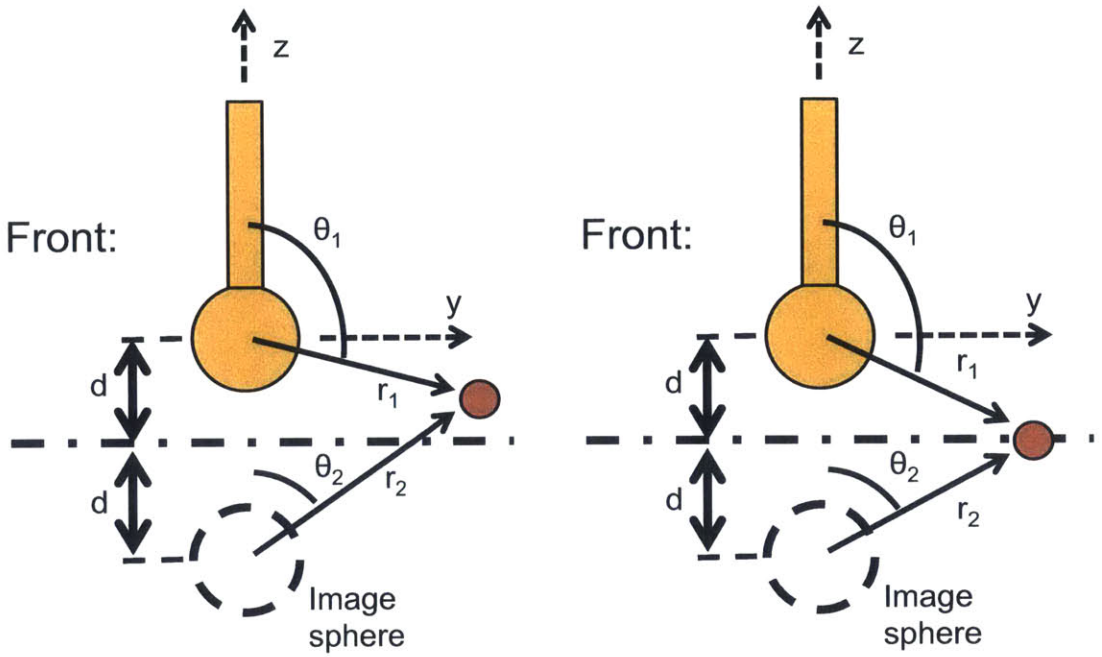

(a) Position of the potential flow image sphere, and radius and inclinations angles for a general point in the fluid domain.

(b) Position of the potential flow image sphere, and radius and inclinations angles for the special case where the point of interest is located at the symmetry plane (wall).

Figure 6-6: To properly model the flow field in the vicinity of a wall, an image sphere was utilized to satisfy the no flux boundary condition.

$$\phi_2(r_2, \theta_2, t) = \frac{1}{2} \frac{U_\circ \sin(\omega t) a^3}{r_2^2} \cos(\theta_2) \tag{6.10}$$

$$\phi_\perp(r, \theta, t) = \frac{1}{2} U_\circ \sin(\omega t) a^3 \left[-\frac{\cos(\theta_1)}{r_1^2} + \frac{\cos(\theta_2)}{r_2^2} \right] \tag{6.11}$$

$$P_d(r, \theta, t) = -\frac{1}{2} \rho \omega a^3 U_\circ \cos(\omega t) \left[-\frac{\cos(\theta_1)}{r_1^2} + \frac{\cos(\theta_2)}{r_2^2} \right] \tag{6.12}$$

The pressure amplitude contours for the field generated by the vibrating sphere can be seen in Figure 6-7(a) for the cases where the sphere is located at the middle of the array and with a separation distance of 18mm. If the image sphere is neglected, as shown in Figure 6-7(b), the pressure field is considerably altered. The pressure distribution at the array surface can be seen in Figure 6-7(c), and as expected, the

largest pressure is observed directly beneath the sphere and decays symmetrically to either side. It was also observed that the magnitude of the pressure at the sensor surface differs by a factor of two due to the presence of the image sphere.

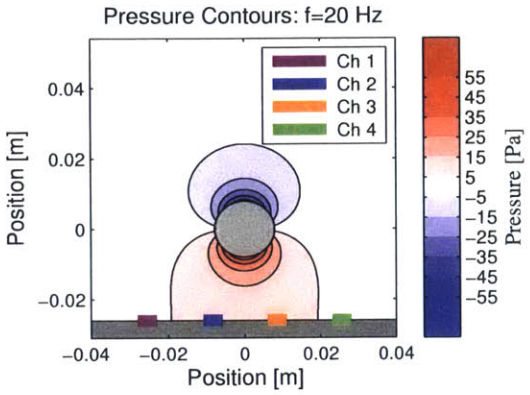

(a) Potential flow simulation of the dipole pressure field for the sphere oscillating at 20 Hz positioned in the center of the CBPDMS foam sensor array and with a separation distance of 18 mm.

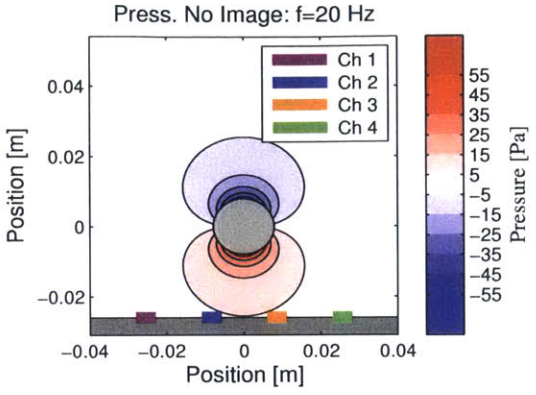

(b) Potential flow simulation with the image sphere neglected from the model.

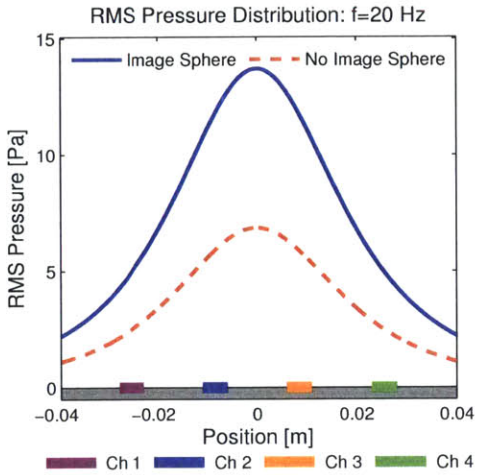

(c) RMS pressure distribution on the surface of the sensor array for the sphere vibrating at 20 Hz positioned in the center of the CBPDMS foam sensor array and with a separation distance of 18 mm.

Figure 6-7: Potential flow model for the sphere positioned in the center of the CBPDMS foam sensor array and with a separation distance of 18 mm.

When the vibrating sphere was shifted laterally, the pressure field shifted as well, as seen in Figure 6-8(a) and Figure 6-8(b).

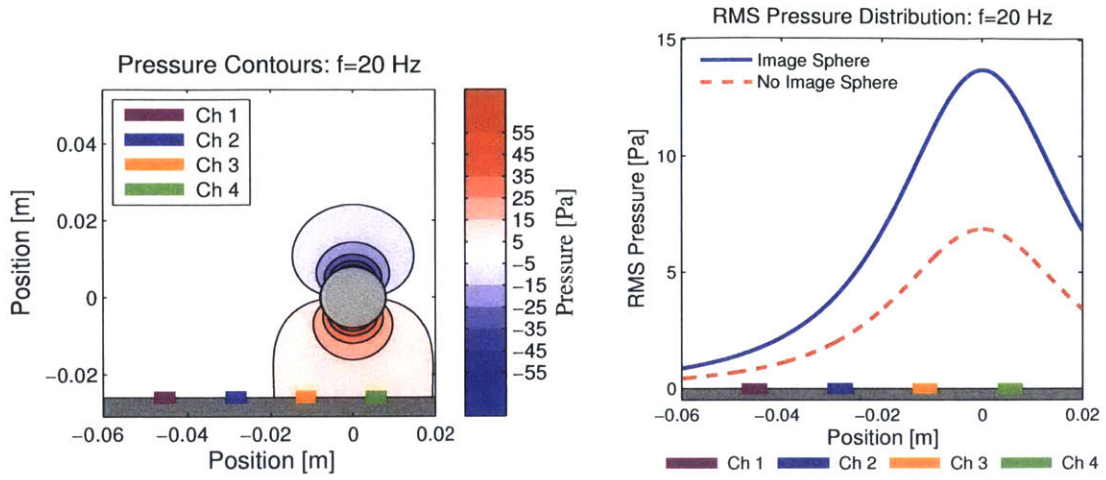

(a) Potential flow simulation of the dipole pressure field for the sphere vibrating at 20 Hz positioned 20 mm to the right of the CBPDMS foam sensor array center, and with a separation distance of 18 mm.

(b) Pressure distribution on the surface of the CBDPMS foam array for the sphere vibrating at 20 Hz positioned 20 mm to the right of array center, and with a separation distance of 18 mm.

Figure 6-8: When the vibrating is sphere is shifted away from sensor array center, an asymmetric pressure distribution is established on the sensor surface.

When the separation distance between the vibrating sphere and the array was decreased, the pressure magnitude observed at the sensor surface beneath the sphere increased, but the width of the pressure distribution decreased, as seen in Figure 6-9(b).

6.4 Dipole Experiment Results

For the perpendicular dipole arrangement, experiments were conducted at two separation distances and three lateral offset positions, as shown in Table 6.1. For each combination of separation distance and lateral offset position, the sphere oscillation frequency was increased from 10 to 35 Hz in increments of 5 Hz, then stepped back down from 35 to 10 Hz. Each frequency step represented a separate experiment with the micro-shaker stopped between steps, allowing the frequency to be reset on the signal generator and giving the water in the tank time to settle.

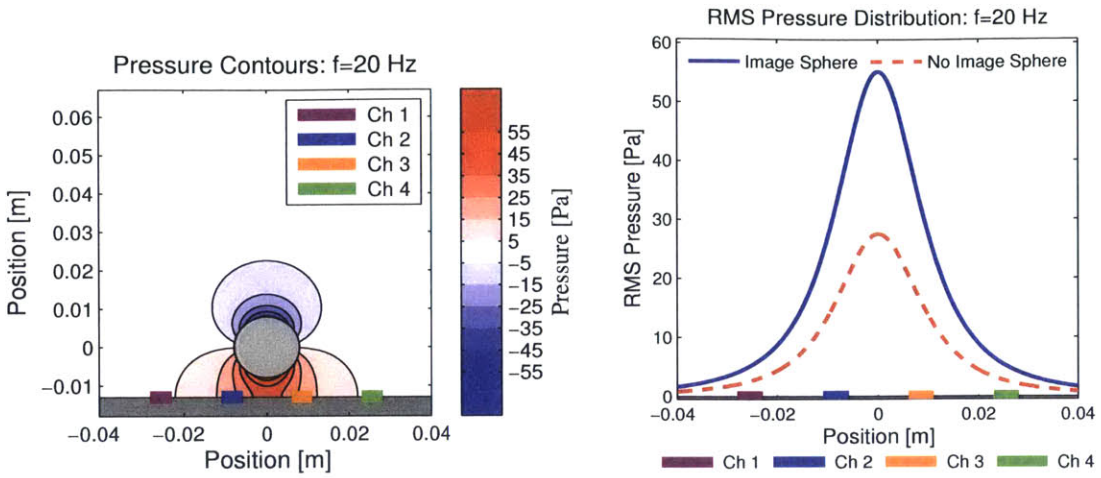

(a) Potential flow simulation of the dipole pressure field for the sphere vibrating at 20 Hz positioned in the center of the CBPDMS foam sensor array and with a separation distance of 5 mm.

(b) Pressure distribution one the surface of the senor array for the sphere vibrating at 20 Hz positioned in the center of the CBPDMS foam sensor array and with a separation distance of 5 mm.

Figure 6-9: Potential flow model for the sphere positioned in the center of the CBPDMS foam sensor array and with a separation distance of 5 mm.

6.4.1 Frequency Domain Results

Of primary interest during the dipole experiments was the frequency range of the 6.2 mm thick CBPDMS foam sensor array. Using the dipole stimulus, a large range of stimulus frequencies were available, particularly high frequencies above 10 Hz that were not able to be tested using the plunging experiments or water waves. As shown in Figure 6-2(b), the velocity of the oscillating sphere was proportional to the frequency of vibration, with the vibration amplitude remaining nearly constant across the 10 to 35 Hz frequency range where the amplitude was directly measured using high speed imagery.

In Figures 6-11, 6-13, and 6-15, the composite frequency spectra are shown for the case of the sphere vibrating perpendicular to the sensor array at changing separation distances and lateral offsets. Each composite spectrum was formed by combining the frequency spectra from individual experiments conducted at each test frequency (10, 15, 20, 25, 30, 35 Hz) for the three operational sensor channels of the 6.2 mm thick CBDMS foam array (Channels 2-4). Therefore, the composite spectrum for

each channel was composed of six independent component spectra shown in different colors in Figures 6-11, 6-13, and 6-15. The power spectral density for each component frequency spectra was normalized by the maximum power spectral density in the channel's composite spectrum, allowing for easier comparison of frequency response between channels. As in previous experiments, the signals were filtered using an ideal band pass filter with a low-frequency cutoff of 7 Hz to remove low-frequency variations in DC offset or free-surface oscillations in the testing tank, and a high-frequency cutoff of 40 Hz to account for the 50 Hz electrical noise experienced during experiments conducted in Singapore.

Results for Separation= 18 mm and Lateral Offset= 0 mm

For the sphere vibrating perpendicular to the sensor array with a separation of 18 mm and a centered (0 mm) lateral position (Figure 6-10), the pressure distribution on the sensor surface was symmetric, as seen in Figure 6-7(c). Considering the composite power spectra in Figure 6-11, it was observed that a prominent frequency peak was present at the dipole oscillation frequency for trials at frequencies greater than 20 Hz for all three sensor channels, as summarized in Table 6.2. Because the pressure field generated by the vibrating sphere is proportional to the sphere velocity, and therefore the vibrational frequency, the ability to properly identify the sphere frequency is dependent on the RMS pressure at the sensor surface exceeding a threshold value.

In Table 6.2, the frequency trials designated in green correspond to successful identification cases where the maximum power spectral density occurred at the sphere oscillation frequency. The trials highlighted in yellow correspond to cases where a prominent peak was present in the power spectrum at the sphere vibration frequency, but the maximum power spectral density occurred at a different frequency due to noise in the signal. An example of this scenario can be seen in the power spectrum for channel 2 in Figure 6-11 where a peak is clearly visible at 30 Hz (green line), but a slightly larger peak is also present at $\sim$10 Hz. The source of the noise at lower frequencies during the dipole experiments was not fully determined, and additional investigation is recommended for future studies. Finally, the trials designated in red

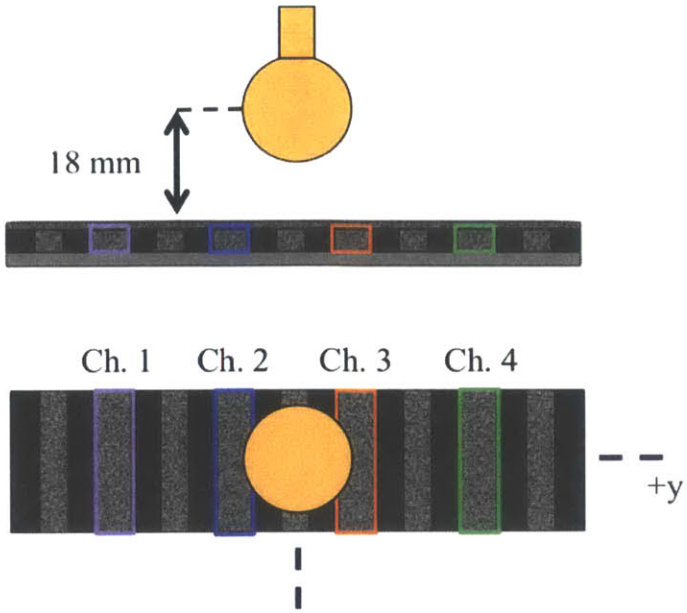

Figure 6-10: The orientation of the vibrating sphere relative to the sensor channels for the case of 18 mm separation and 0 mm lateral offset.

correspond to unsuccessful cases where a frequency peak could not be identified at the expected frequency.

Based on the results in Table 6.2, the threshold RMS pressure for signal frequency identification appeared to be ~12 Pa for channels 2 and 3, while channel 4 exhibited a lower threshold, successfully identifying a signal with a predicted RMS pressure of ~5 Pa. To refine these estimates of threshold RMS pressure and to gain a more complete understanding of the sensor's frequency range, the analysis was repeated for additional separation and offset orientations.

Results for Separation= 18 mm and Lateral Offset= +20 mm

When the lateral offset of the vibrating sphere was increased to +20 mm with the separation distance maintained at 18 mm (Figure 6-12), the peak pressure on the sensor surface was found to shift towards sensor channel 4, as seen in Figure 6-8(b). With the pressure distribution no longer symmetric about the middle of the sensor array, it was expected that the sensor channels closest to the sphere (channels 3 and 4) would successfully identify lower-frequency signals than sensor channel 2 due to

Channel	f_{dipole} [Hz]	f_{sensor} [Hz]	Percent Difference in f	Predicted P_{RMS} [Pa]
2	10	7.90	20.99	3.06
2	15	7.70	48.66	7.47
2	20	12.00	39.99	11.75
2	25	25.00	0.01	18.43
2	30	10.10	66.33	31.71
2	35	35.00	0.01	40.68
3	10	13.30	33.01	3.06
3	15	8.00	46.66	7.47
3	20	11.50	43.49	11.75
3	25	25.00	0.01	18.43
3	30	9.40	68.66	31.71
3	35	7.30	79.14	40.68
4	10	7.90	20.99	1.29
4	15	9.00	39.99	3.15
4	20	20.00	0.01	4.96
4	25	25.00	0.01	7.78
4	30	30.00	0.01	13.39
4	35	35.00	0.01	17.17

Table 6.2: Dipole frequency domain results for 18 mm separation and 0 mm lateral offset. Trials designated in green correspond to successful identification cases where the maximum power spectral density occurred at the sphere oscillation frequency. The trials highlighted in yellow correspond to cases where a prominent peak was present in the power spectrum at the sphere vibration frequency, but the maximum power spectral density occurred at a different frequency due to noise in the signal. Trials designated in red correspond to unsuccessful cases where a frequency peak could not be identified at the expected frequency.

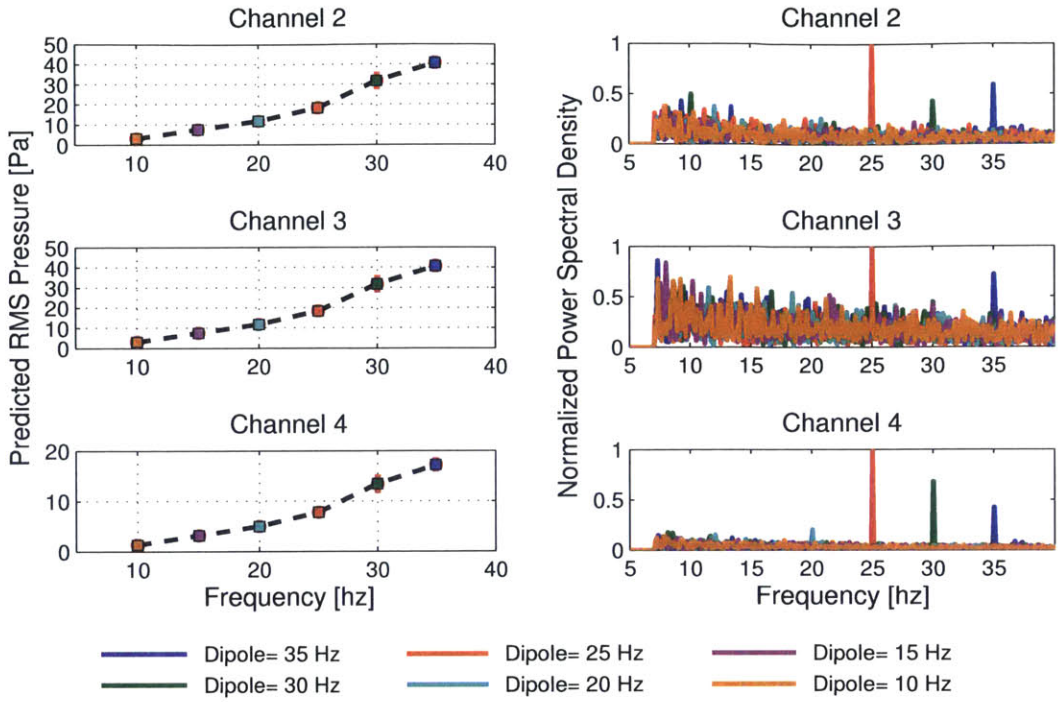

Figure 6-11: Frequency domain results for the case of 18 mm separation and 0 mm lateral offset. The plots at left give the predicted RMS pressure at the sensor surface as a function of sphere vibration frequency as found using the potential flow model in Section 6.3. The composite frequency spectrum plots at right show the normalized frequency spectra for independent experiments performed at discrete sphere oscillation frequencies as designated by the line color.

the higher RMS pressure at those channels. Additionally, based on the experiments with the sphere centered over the array, channel 4 was expected to be particularly sensitive to low RMS pressure values when compared to the other sensor channels.

Considering the results for the case of 18 mm separation and lateral offset of +20 mm in Figure 6-13 and Table 6.3, all three sensor channels showed increased success at identification of low frequency signals, especially sensor channel 4 which exhibited successful frequency detection over the full tested frequency range of 10 to 35 Hz. When comparing the threshold RMS pressure value to the centered case, sensor channel 3 was consistent, exhibiting a threshold RMS pressure of $\sim$10 Pa for the trial at 20 Hz. Sensor channel 2 showed an improved threshold compared to the previous experiment, potentially due to an increased signal to noise ratio during the trials at 18 mm separation and lateral offset of +20 mm. While the threshold

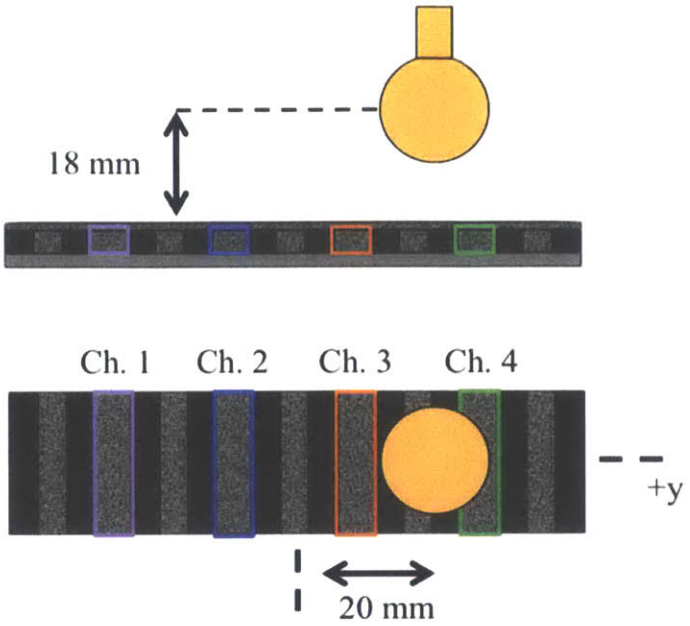

Figure 6-12: The orientation of the vibrating sphere relative to the sensor channels for the case of 18 mm separation and +20 mm lateral offset.

RMS pressure during trials with the sphere centered gave a value of ~13 Pa, the threshold with the sphere offset +20 mm was found to be ~4 Pa. Sensor channel 4 also exhibited a slight improvement in the threshold RMS pressure, with a successful identification of a 10 Hz signal at a predicted RMS pressure of ~3 Pa.

Results for Separation= 5 mm and Lateral Offset= 0 mm

When the vibrating sphere was moved closer to the surface of the pressure sensor array center, as in the case of 5 mm separation distance and 0 mm lateral offset, the RMS pressure distribution from the potential flow model showed a large increase across the frequency range at sensor channels 2 and 3 relative to the 18 mm separation case. However, due to the sharp drop-off of the RMS pressure with lateral distance, the RMS pressure at sensor position 4 was similar to the experiments at a larger separation distance. Because of this variation in pressure distribution with separation distance, it was expected that sensor channel 4 would exhibit a similar frequency detection range as the experiments at 18 mm separation, while sensor 2 and 3 were expected to benefit from the higher RMS pressure values and exhibit greater success identifying

Channel	f_{dipole} [Hz]	f_{sensor} [Hz]	Percent Difference in f	Predicted P_{RMS} [Pa]
2	10	11.60	16.02	1.09
2	15	8.10	46.00	2.65
2	20	20.00	0.01	4.17
2	25	25.00	0.01	6.54
2	30	30.00	0.01	11.25
2	35	35.00	0.01	14.43
3	10	11.60	16.01	2.73
3	15	8.00	46.66	6.65
3	20	20.00	0.01	10.46
3	25	25.00	0.01	16.41
3	30	30.00	0.01	28.23
3	35	35.00	0.01	36.21
4	10	10.00	0.01	3.34
4	15	15.00	0.01	8.15
4	20	20.00	0.01	12.82
4	25	25.00	0.01	20.11
4	30	30.00	0.01	34.60
4	35	35.00	0.01	44.38

Table 6.3: Dipole frequency domain results for 18 mm separation and +20 mm lateral offset.

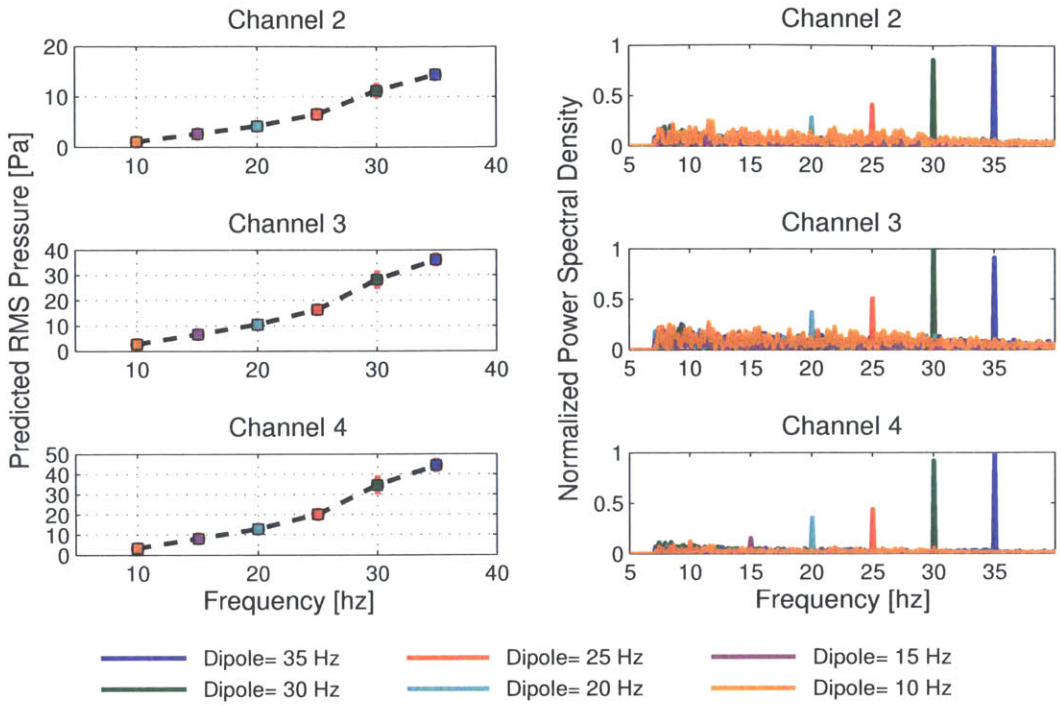

Figure 6-13: Frequency domain results for the case of 18 mm separation and +20 mm lateral offset. The predicted RMS pressure from potential flow is given at left, while the experimental frequency spectra are given at right.

low frequencies.

When viewing the results for the 5 mm separation distance and 0 mm lateral offset experiments in Figure 6-15 and Table 6.4 it was observed that sensor channel 2 was able to detect frequencies as low as 10 Hz. This improvement over the case of 18 mm separation and 0 mm offset (Table 6.2) was expected due to the predicted RMS pressure for the 10 Hz case being 8.38 Pa, which was higher than the ~4 Pa cutoff frequency shown during the experiments with 18 mm separation and +20 mm offset (Table 6.3). Sensor channel 2 exhibited slightly worse performance than previous experiments, failing to detect a signal a 15 Hz with a predicted RMS pressure of ~20 Pa. It was found in previous experiments that the cutoff RMS Pressure for channel 2 was ~10 Pa, suggesting the difficulties in frequency identification during the 5 mm separation experiments may have been due to a lower signal to noise ratio, as seen in Figure 6-15. The source of the additional noise may have been due to the increased proximity of the sphere to the sensor sphere, as both channels 2 and 4 exhibited

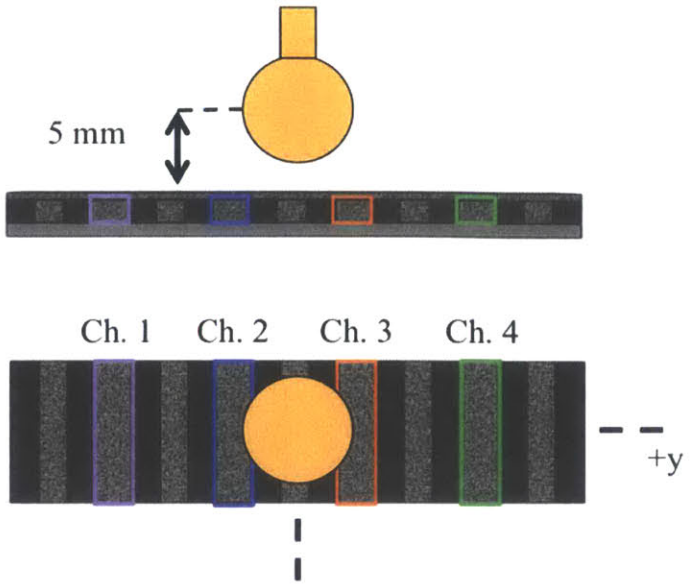

Figure 6-14: The orientation of the vibrating sphere relative to the sensor channels for the case of 5 mm separation and 0 mm lateral offset.

increased noise at low frequencies in Figure 6-15.

As discussed previously, the RMS pressure variation with frequency at sensor channel 4 was similar for both the 18 mm and 5 mm separation cases with lateral offset of 0 mm, and the range of frequency identification was expected to be similar between the two experiments. Channel 4 was initially found to successfully identify frequencies down to 25 Hz, or an RMS pressure of ~8 Pa. Upon closer inspection, it was observed that a clear frequency peak was present at 20 Hz, or an RMS pressure of ~5 Pa, but low frequency noise was also present in the 20 Hz frequency spectrum and masked the identification of the sphere vibration frequency (therefore highlighted in yellow in Table 6.4). Despite low frequency noise similar to that observed in Channel 2, the identification of the 20 Hz signal with an expected RMS pressure of ~5 Pa by Channel 4 demonstrated consistency of threshold pressure with previous experiments and different sphere orientations.

Channel	f_{dipole} [Hz]	f_{sensor} [Hz]	Percent Difference in f	Predicted P_{RMS} [Pa]
2	10	9.10	8.99	8.38
2	15	8.00	46.66	20.44
2	20	7.90	60.50	32.15
2	25	25.00	0.01	50.42
2	30	30.00	0.01	86.74
2	35	35.00	0.01	111.28
3	10	10.00	0.01	8.38
3	15	15.00	0.01	20.44
3	20	20.00	0.01	32.15
3	25	25.00	0.01	50.42
3	30	30.00	0.01	86.74
3	35	35.00	0.01	111.28
4	10	9.10	8.99	1.33
4	15	7.60	46.66	3.23
4	20	8.80	56.00	5.09
4	25	25.00	0.01	7.98
4	30	30.00	0.01	13.72
4	35	7.30	79.14	17.61

Table 6.4: Dipole frequency domain results for 5 mm separation and 0 mm lateral offset.

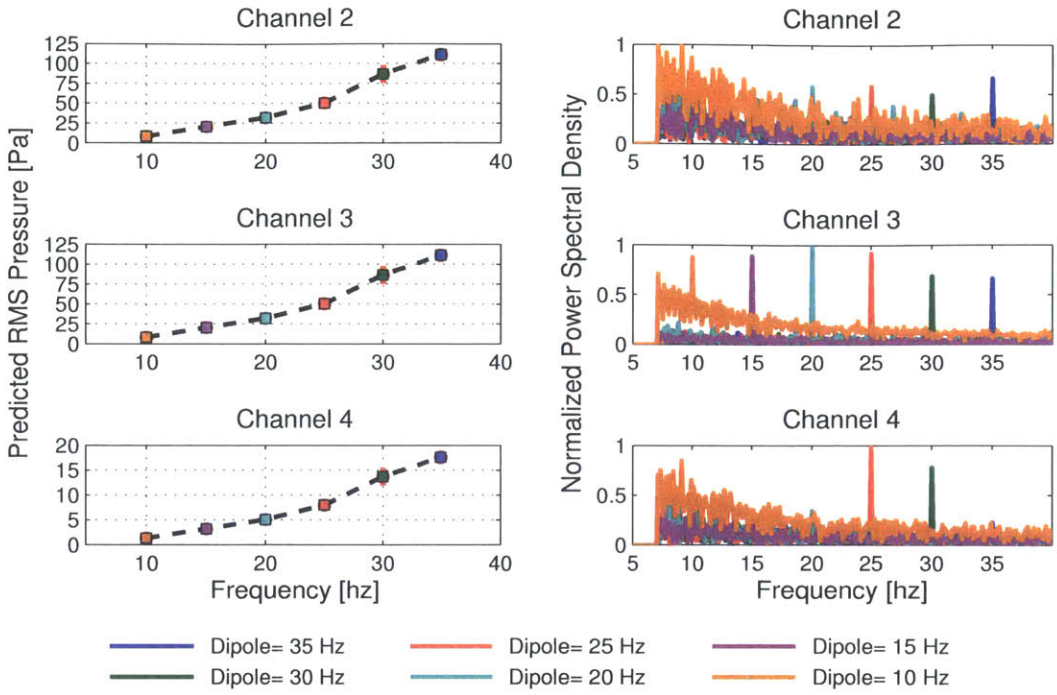

Figure 6-15: Frequency domain results for the case of 5 mm separation and 0 mm lateral offset. The predicted RMS pressure from potential flow is given at left, while the experimental frequency spectra are given at right.

6.4.2 Time Domain Results

Based on the CBPDMS foam sensor array characterization performed using periodic plunging and water waves and discussed in Chapter 5, it was expected the the RMS voltage from the sensor array would scale with RMS pressure. While a non-linear inverse relationship was found to exist between pressure and sensor voltage output, increasing pressure oscillation amplitude was still found to lead to increasing voltage amplitude. For the experiments conducted using the vibrating sphere as a pressure stimulus, the submergence depth of the sensor array was 7 cm, corresponding to a hydrostatic pressure of ~700 pa, outside of the training data range for the calibration curves developed in Section 5.3.6. According to the piecewise calibration curves, shown in Figure 6-16 for channel 4, a hydrostatic pressure of 700 Pa places the response in the third-degree polynomial portion of the calibration curve, and large variations in pressure were found to produce very small changes in voltage output, consistent with the sensitivity of the array decreasing at higher values of pressure.

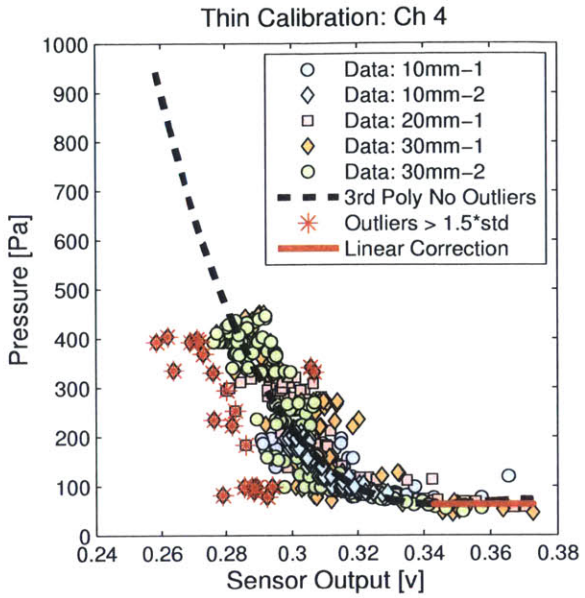

Figure 6-16: Piecewise calibration curve for thin array channel 4 found during plunging experiments.

When the predicted RMS pressure was plotted against the RMS of the output voltage for the dipole experiments, a consistent relationship between pressure and voltage was not observed, as seen in 6-17. When considering the pressure-voltage results for channel 3, it was observed that the RMS voltage output from the sensor remained nearly constant with RMS pressure, suggesting that the sensor was operating in a semi-saturated state where it was responsive to dynamic pressure stimulus, as observed in the frequency domain results, but the voltage output of the sensor was dominated by the large hydrostatic pressure value and did not scale with the RMS of the dynamic component of pressure. Because the sensor array was outside of it's calibrated range range during the dipole experiments, the piecewise calibration curves developed in Section 5.3.6 did not provide for an accurate reproduction of the time-series results for the dipole pressure field. This suggests that at larger values of hydrostatic pressure, the CBPDMS foam sensor arrays were useful for frequency domain measurements of hydrodynamic stimulus above a cutoff RMS pressure, but were not suited for time-domain measurements of pressure magnitude.

From the pressure-voltage curves from the dipole experiments it was also observed

that the magnitude of the RMS voltage varied considerably between the three working sensor channels on the array, with the magnitude of the voltage output corresponding with the sensitivity of the channels. When investigating the frequency response of the sensor array, it was observed that sensor channel 4 had the lowest cutoff RMS pressure, consistent with having the largest RMS sensor voltage output. Similarly, Channels 2 and 3 were found to have higher cutoff RMS pressure values, and RMS voltage outputs lower than found for channel 4. The variation in performance between the sensor array channels was likely due to variations in the distribution of carbon black particles within the composite, as well as closed-cell pore distribution, and the need for fabrication improvements will be further discussed in Section 8.3.

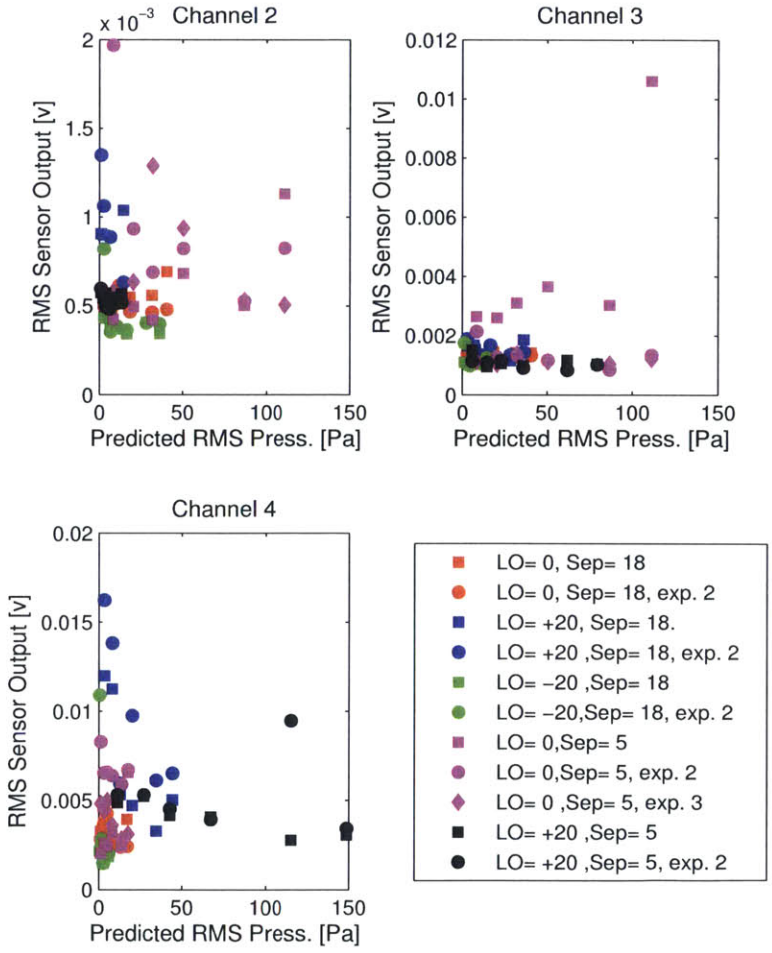

Figure 6-17: Predicted RMS pressure versus RMS voltage output for dipole experiments. In the figure legend, 'LO' designates the lateral offset in mm, and 'Sep' designates the separation distance in mm.

6.5 Conclusions from Dipole Experiments

6.5.1 CBPDMS Foam Array Frequency Range

Using the vibrating sphere as a hydrodynamic pressure stimulus, the frequency range for the CBPDMS foam sensor array was found to cover the full 10-35 Hz tested range. Added to the periodic plunging experiments at 0.5 Hz and the the wave experiments at 1 Hz, the frequency range for the sensor arrays was shown experimentally to be 0.5-35 Hz, comparable to the range of stimulus frequencies measured by the fish lateral line.

6.5.2 CBPDMS Foam Array Sensing Threshold

By comparing the predicted RMS pressure at the surface of the sensor array found using a potential flow simulation to the frequencies at which the CBPDMS foam sensor array was able to successfully identify the sphere vibration frequency, an approximate RMS pressure threshold for each sensor channel could be found. For channel 2, the lowest pressure during a successful frequency identification was $\sim$4 Pa, although the channel was observed to exhibit lower signal to noise ratio than the other two channels, inhibiting the frequency detection in some experiments. The cutoff RMS pressure for Chapter 3 was found to be as low as $\sim$8 Pa, and similar to channel 2, the signal to noise ratio suffered for the case of 18 mm separation and 0 mm lateral offset. Channel 4 was found to have the lowest RMS pressure cutoff of the array, successfully identifying a signal at 10 Hz with a predicted RMS pressure of $\sim$3 Pa.

6.5.3 CBPDMS Foam Array Saturation

When considering the relationship between predicted RMS pressure and RMS voltage output, it was found that a consistent relationship was not present for the sensor operating at a hydrostatic pressure of 700 Pa, and that the array was likely operating in a semi-saturated state. While the frequency domain results demonstrated conclusively that the sensor array was responding to the dipole hydrodynamic stimulus, the

time-series results for the pressure field amplitude were unable to be reproduced. It can be concluded from the dipole experiments that at large hydrostatic pressures, the CBPDMS foam array is capable of accurately identifying the frequency of oscillatory stimuli with RMS pressure as low as ~3 Pa, but the ability to reproduce pressure time-series results is impaired.

6.6 Chapter Summary

In Chapter 6, the ability of the CBPDMS foam sensor array to detect high frequency stimuli was investigated using the dipole flow created by an oscillating sphere. Experiments were conducted with the sphere vibrating perpendicular to the sensor array surface at variable separation distance and lateral offset, and with oscillation frequencies ranging from 10 to 35 Hz. A potential flow model of the dipole flow in the vicinity of the tank bottom was used to predict the RMS pressure at the sensor surface in order to determine the threshold RMS pressure necessary for identification of an oscillatory signal.

From the experiments, it was found that the 6.2 mm (Thin) CBDPMS foam sensor array was capable of measuring the sphere's frequency of oscillation across the 10 to 35 Hz range as long as the RMS pressure exceeded a threshold value. The threshold value varied between sensor channels, and ranged from 3 - 8 Pa, consistent with the pressure resolution of $\sim$ 5 Pa identified during the plunging and wave experiments. The success of frequency identification was also highly dependent on the signal to noise ratio in the pressure signal. In several cases, as seen in Figure 6-11, low frequency noise was present in the pressure signal power spectra, obstructing the identification of a clear frequency peak at the sphere vibration frequency. The ability of the CBPDMS foam sensor array to identify high frequency stimuli at RMS pressures below 10 Pa is consistent with the energy extraction and prey tracking capabilities of the fish lateral line identified in Table 1.1, and suggest the sensor arrays could be used in organism tracking applications.

The time domain results from the dipole experiments, discussed in Section 6.4.2,

revealed the saturation of the CBDPMS foam sensors at large hydrostatic pressures. During the dipole experiments, the sensor arrays were subjected to a ~700 Pa hydrostatic pressure, and the voltage output from the arrays was not found to consistently correspond to the predicted RMS pressure from the potential flow model, as discussed in Section 6.5.3. Despite this saturation, the sensor arrays exhibited excellent frequency domain results, demonstrating that useful information about the flow field could still be obtained outside of optimal operating conditions. The saturation of the CBDPMS foam arrays is an avenue for continued investigation and may be delayed through the optimization of material properties for various operating conditions.

Chapter 7

Kármán Vortex Street Identification

7.1 The Kármán Vortex Street

When present in a flow field, bluff bodies periodically shed vortices in an oscillatory pattern known as the Kármán vortex street, as seen in Figure 7-1. Named after Theodore von Kármán, this flow pattern is ubiquitous in fluid dynamics, and the forcing from these periodically shed vortices is responsible for the well known fluid-structure interaction known as vortex induced vibrations (VIV).

The frequency of Kármán vortex shedding is related to the fluid velocity and the significant length of the flow obstruction through the Strouhal number (St), given in Equation 7.2. The Strouhal number is largely regime dependent on Reynolds number, given in Equation 7.1, as seen in Figure 7-2 for a circular cylinder.

$$Re = \frac{UD}{\nu} \tag{7.1}$$

$$St = \frac{f_{st}D}{U} \tag{7.2}$$

$$f_{st} = \frac{StU}{D} \tag{7.3}$$

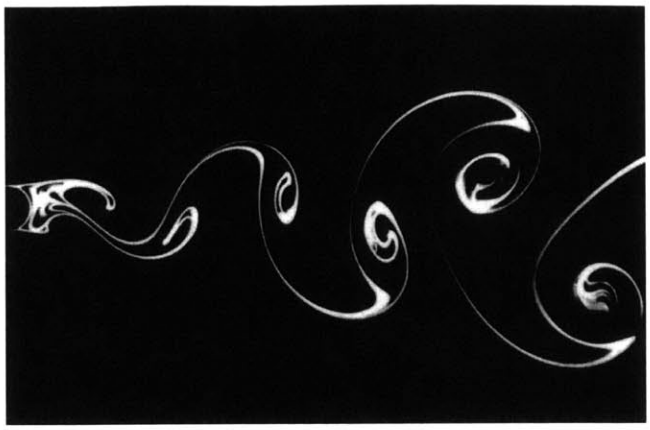

Figure 7-1: The periodic shedding of vortices behind a bluff body in a flow field is know as the Kármán vortex street, and has a shedding frequency related to the flow velocity and body size by the Strouhal number (adopted from [29]).

7.2 Biological Influence

In nature, fish have been observed to utilize the Kármán vortex wake behind obstructions in the flow field to reduce the amount of energy required for station keeping, as discussed in Section 1.3.2. Unlike the largely passive behavior of sitting in the suction zone immediately behind an obstruction, the so-called "Kármán gait" is an active behavior where the fish 'slaloms' between the shed vortices to extract energy, as seen in Figure 7-3. The energy contained in the periodically shed vortices is sufficient to allow for a dead fish to 'swim' upstream against a current following a passive synchronization with the vortex shedding, although this passive synchronization is unstable and the body kinematics differ slightly from the case of the living fish [58].

The active Kármán gait behavior is enabled by a combination of both visual cues and sensory feedback from the lateral line system. Experiments conducted with live trout in the wake of a D-shaped cylinder showed that while vision has a large influence on whether an individual decides to entrain in the suction zone (vision impaired) or Kármán gait (no vision impairment), during periods where the fish has visual cues the likelihood of Kármán gaiting is much higher when the lateral line is functioning compared to experiments when the lateral line was pharmacologically impaired [59]. The higher rate of Kármán gaiting when the lateral line is functioning suggests that

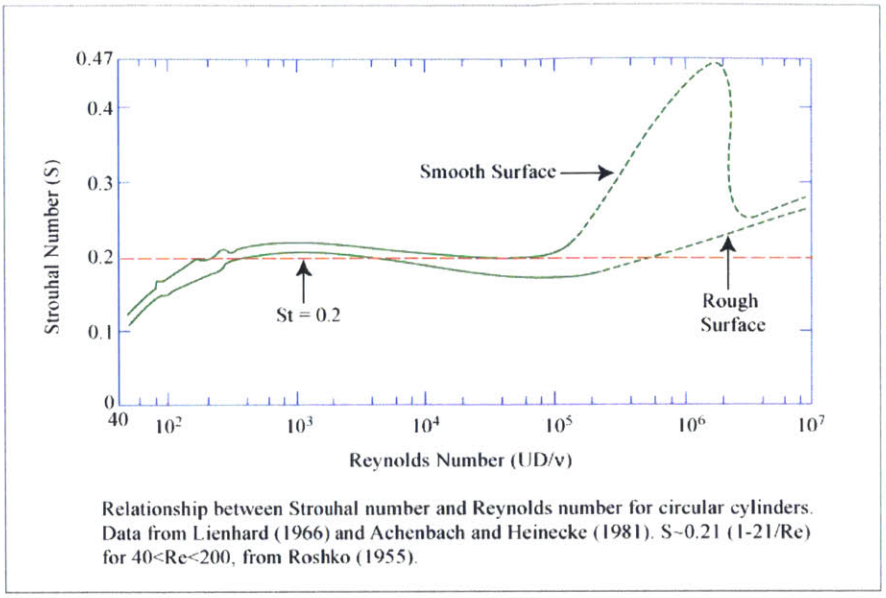

Figure 7-2: The Strouhal number which relates the Kármán shedding frequency to the fluid velocity and cylinder diameter is dependent on the Reynolds number. For the experiments conducted in the towing tank, the Strouhal number is expected to fall between St=0.18 and St=0.22 (adopted from [81]).

the sensory organ plays a role in the localization of, and synchronization with, shed vortices.

7.3 Experimental Setup

To investigate the identification of a Kármán vortex street by a CBPDMS foam sensor array, an array was glued into the surface of a NACA 0020 foil and towed in the wake of a circular cylinder in the MIT towing tank, as seen in Figures 7-4 and 7-7. The foil was placed three diameters downstream from the circular cylinder to allow for the formation of the vortex street, and was offset from the cylinder centerline so that the shed vortices would pass near the CBPDMS foam and commercial pressure sensor arrays, as seen in Figure 7-4 and described in Table 7.1. Experiments were conducted at towing speeds from 0.1 to 0.3 m/s, and the Reynolds number for each experiment was subcritical as shown in Table 7.1. Based on the Reynolds numbers of the experiments, and considering the cylinder used in the experiments to be rough, the Strouhal number was expected to fall in the range of 0.18-0.22.

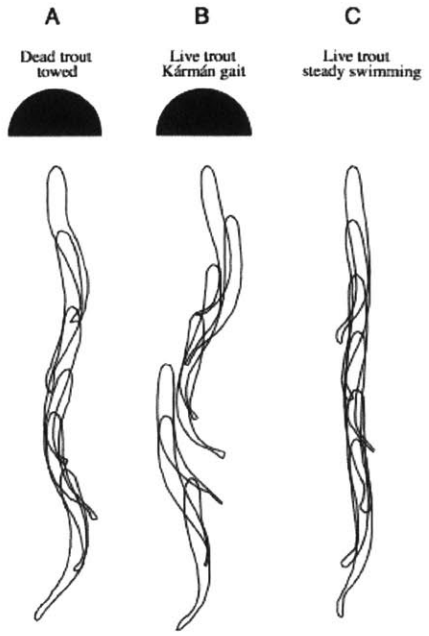

Figure 7-3: When station keeping behind an obstruction in a flow field, fish have been observed to extract energy from the shed vortex wake to reduce swimming energy. This behavior is know as the "Kármán Gait" and is characterized by 'slaloming' between the shed vortices. While experiments have shown this behavior can take place passively, enabling a dead fish to overcome fluid drag and travel upstream (a), the body kinematics are exaggerated in the live animal (b) (adopted from [58]).

Surface pressure measurements were taken on the foil using the 7.8 mm thick experimental CBPDMS foam pressure sensor array, as well as four commercially available pressure sensors from Freescale Semiconductor. Three of the sensors were model MPXV5010 (part number MPXV5010GC7U), and one sensor was model MPXV7007 (part number MPXV7007GC6U). The commercial sensors were silicon piezoresistive type sensors, and had a range of ± 7 kPa for model MPXV7007, and 0-10 kpa for model MPXV5010, with an output voltage for both of 0.5-4.5 volts. Both sensor models had the same form factor and packaging, as seen in Figure 7-5(a). The sensors were powered using the +5 volts output from an NI-USB 6289 data acquisition board, and the analog output signals were also acquired using the USB-6289. Each commercial sensor was calibrated by submerging the foil to known depths and recording the voltage output over a period of several seconds. A linear fit was then found for the hydrostatic pressure versus average voltage curve for each sensor, as seen in Figure

U [m/s]	D [m]	Separation [m]	Separation [diameters]	Offset [m]	Re_{cyl}	Trials
0.1	0.0381	0.1143	3	0.06	3810	3
0.15	0.0381	0.1143	3	0.06	5715	3
0.2	0.0381	0.1143	3	0.06	7620	3
0.3	0.0381	0.1143	3	0.06	11430	3

Table 7.1: Parameter space for Kármán vortex street identification experiments.

7-5(b). It was found that the steady voltage offset varied between the MPXV7007 and MPXV5010 model sensors, but that the sensitivity was similar and both sensor models performed reliably during the experiments. The calibration curves for the commercial sensors can be found in Appendix D.

The Freescale Semiconductor pressure sensors were not waterproof, and therefore needed to be located on the top of the foil above the waterline, as seen in Figure 7-7(a). To transmit pressure from the foil surface to the pressure sensors, flexible PVC tubes with an inner diameter of 2.38 mm were run from the pressure sensor locations to taps along the chord length of the foil, as seen in Figure 7-6.

An experimental CBPDMS foam pressure sensor array was mounted on the surface of the foil above the pressure taps for the commercial sensors, as seen in Figure 7-7(a). A foil section was 3D printed with a channel cutout from the surface to allow for the CBPDMS foam array to be glued into the foil surface, and to allow for the array's wires to pass into the interior of the foil, as seen in Figure 7-8(a). The CBPDMS foam array was glued into the foil surface using Sil-Poxy silicone rubber adhesive from Smooth-On, and the silicone adhesive was also used to fill in the remaining gaps between the array and the edges of the cutout. Due to the presence of the aluminum shaft inside the foil, the cutout depth was limited to 5 mm, which was not deep enough for the 7.8 mm thick CBPDMS sensor array to lay completely flush with the foil surface, as seen in Figure 7-8(b). The effect on the flow field by the sensor protrusion is discussed in detail in Section 7.5.

Power to the CBPDMS foam sensor array was supplied by the constant current source electronics described in Section 5.2.2, and the electronics were powered by a

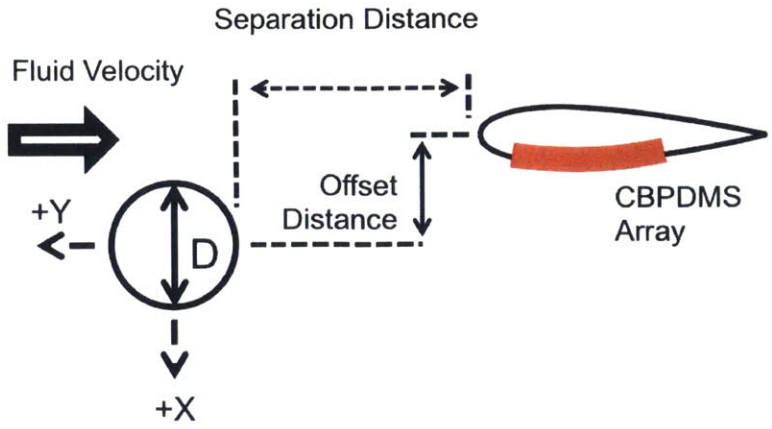

(a) Top view of the experimental setup for Kármán vortex street identification. The offset distance between the cylinder and foil centerline in the x-direction was varied to ensure the shed vortices passed on the side of the foil with the commercial and CBPDMS pressure sensor arrays.

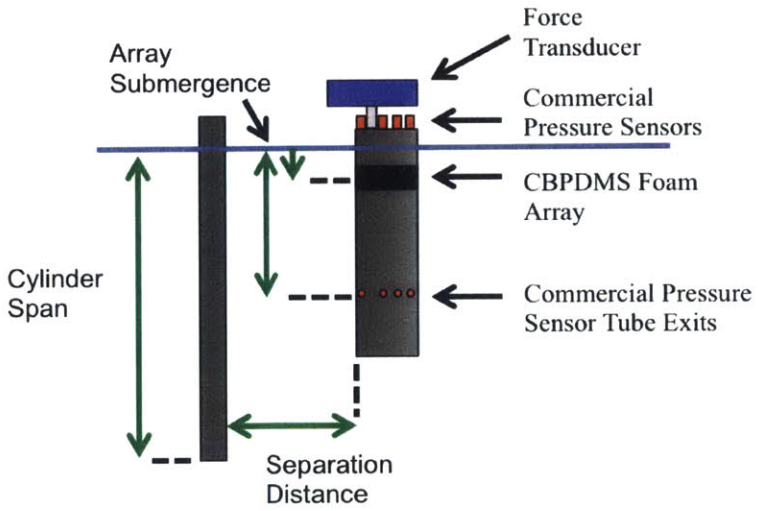

(b) Side view of the experimental setup for Kármán vortex street identification. The cylinder used in the experiments had a diameter of D=0.0381m and a submerged span of approximately 19D to reduce 3D effects on the flow structures. The submergence of the CBPDMS array was varied to minimize free surface effects while avoiding saturation. An ATI force transducer was used to measure the fluid forces acting on the foil during the experiment.

Figure 7-4: To investigate the ability of the CBPDMS foam sensor array to detect the vortex wake generated by a circular cylinder, a foil instrumented with commercial and CBPDMS pressure sensor arrays was towed behind a circular cylinder as the separation distance, offset distance, and towing speed were varied.

DC power supply on the towing tank carriage. Voltage signals were amplified using the amplification circuit described in Section 5.2.3, and measurements were taken

(a) Sensor model MPXV7007 and MPXV5010 share the same packaging, power requirements, and output voltage range, but differ in pressure range. The MPXV5010 sensors have a 0-10 kPa range, while the MPXV7007 sensors have a ±7 kPa range. Both sensor types were well suited for the expected experimental pressure.

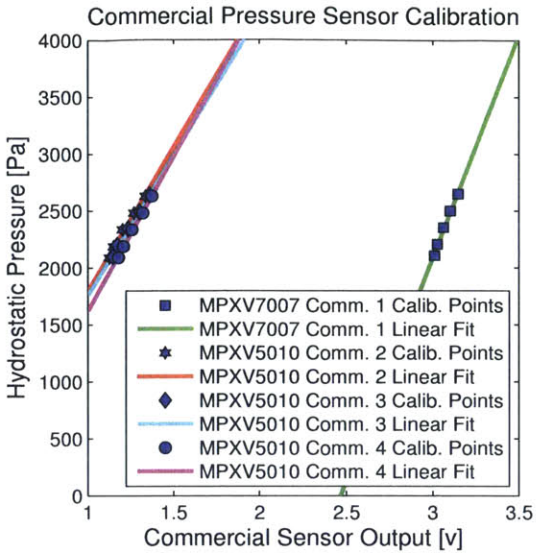

(b) A linear calibration was found for the commercial pressure sensors using discrete steps in hydrostatic pressure. It was found that the steady voltage offset varied between the MPXV7007 and MPXV5010 model sensors, but that the sensitivity was similar.

Figure 7-5: The NACA0020 foil used in the Kármán vortex street identification experiments was equipped with an array of four commercially available pressure sensors from Freescale Semiconductor to allow for comparison with the measurements from the CBPDMS foam array.

using an NI USB-6289 data acquisition board mounted on the towing carriage and connected to a carriage-mounted computer running Labview software.

During the Kármán vortex street identification experiments the foil was mounted to an ATI Gamma force transducer (Model US 30-100, SN: FT 14184), as seen in Figure 7-9, to allow for the measurement of the fluid forces acting on the foil. Of particular interest was an expected oscillatory lift force due to the presence of low pressure regions from the shed vortices near the foil surface.

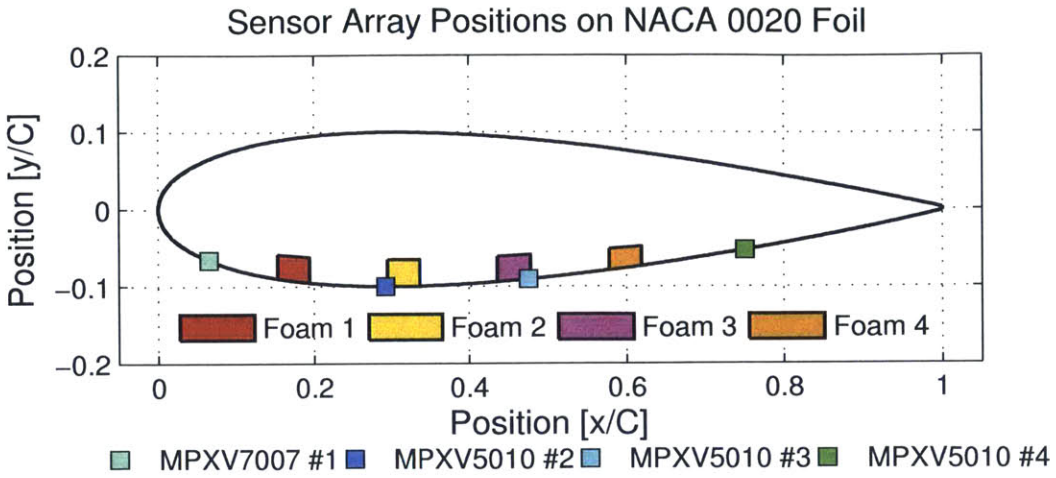

Figure 7-6: The positions of the tube exits for the commercial pressure sensors (squares) and the sensing channels of the CBPDMS foam array (filled rectangular regions) given as a fraction of overall chord length.

7.4 Kármán Vortex Street Three-Dimensionality

The periodic shedding of vortices by a circular cylinder is not uniform along the span of the cylinder in three dimensions, as seen in Figure 7-10. Instead, variations in phase and vortex strength occur along the length of the cylinder due to three dimensional instability, as seen in Figure 7-10(b). For the Kármán vortex street identification experiments, this three dimensionality meant that variations in the the phase and magnitude of the pressure stimulus felt by the CBPDMS foam sensor array and commercial pressure sensors was expected, as seen in Figure 7-10(a).

7.5 Effect of Sensor Protrusion on Flow Field

As discussed in Section 7.3, the 7.8 mm CBPDMS foam array array protruded from the foil surface approximately 2.8 mm during the Kármán vortex street identification experiments, as seen in Figure 7-8(b). The presence of the lip on the foil surface at the leading edge of the foam sensor array was expected to disrupt the near-body flow field in the vicinity of the sensor array, adding additional noise to the CBPDMS

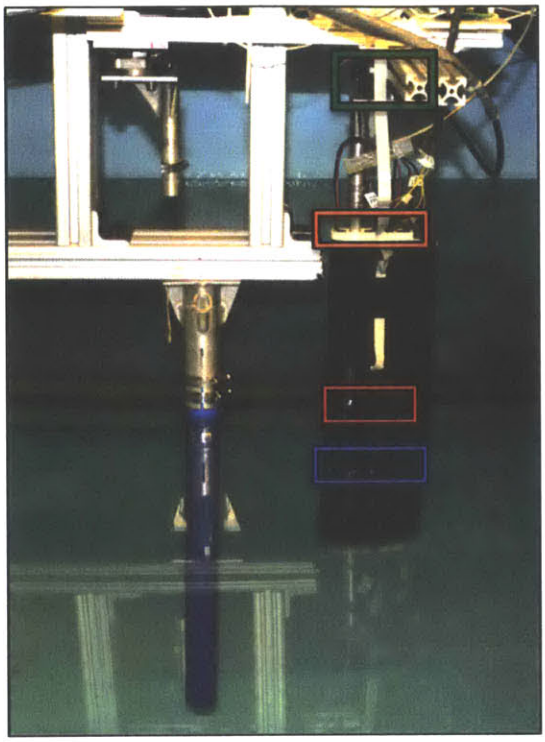

(a) A NACA 0020 foil (right) was mounted on an ATI force transducer (green frame) to allow for fluid forces to be measured during the experiment. Four commercial pressure sensors (orange frame) were mounted on top of the foil and attached to tubes leading to the exterior of the foil beneath the free surface (blue frame). A CBPDMS pressure sensor array was mounted on the surface of the foil, as seen in the red frame. The cylinder ahead of the foil (blue, left) was 0.0381m in diameter with a span of 0.72 m.

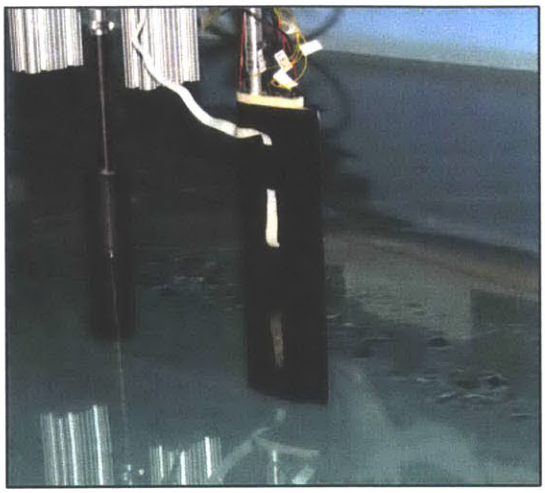

(b) Kármán vortex street identification experiments were performed in the large towing tank at MIT. During experiments with a 0.0508 m circular cylinder translating at 0.1 m/s, the periodic vortex shedding consistent with a Kármán vortex street was clearly visible when observing the tank's free surface.

Figure 7-7: Experiments to demonstrate the identification of a periodic vortex shedding from a circular cylinder, the Kármán vortex street, were conducted using the large towing carriage in the MIT towing tank.

foam pressure measurements. To understand the effect of the sensor array protrusion, experiments were conducted in the towing tank in the absence of the circular cylinder to isolate the noise contributions for the sensor strip, and CFD simulations were performed using the altered foil shape to help visualize the near-body flow structures.

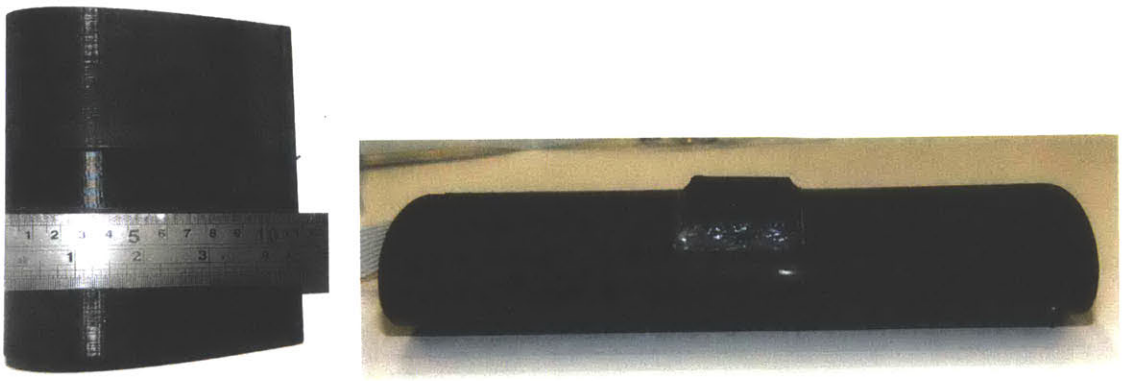

(a) A NACA 0020 foil section (b) Due to the presence of an aluminum mounting rod running was 3D printed with a cutout through the foil center, cutout depth was limited to 5 mm, leaving to allow for the mounting of the a 2.8 mm protrusion from the foil surface.
CBPDMS foam sensor array.

Figure 7-8: During the Kármán vortex street identification experiments, the 7.8 mm thick CBPDMS foam sensor array was mounted in a cutout in the surface of a NACA 0020 foil section.

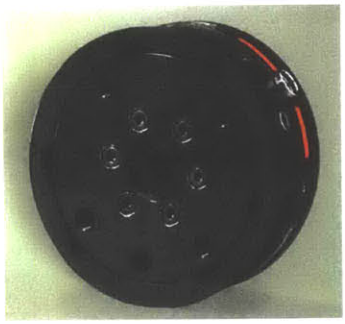

Figure 7-9: The foil was attached to an ATI Gamma force transducer to allow for the fluid forces acing on the foil to be measured. The presence of the periodically shed vortices caused an oscillatory lift force in the positive x direction.

7.5.1 Experimental Measurements with Cylinder Absent

Measurements were taken of the near-body flow field on the NACA 0020 hydrofoil using the 7.8 mm thick CBPDMS foam pressure sensor array in the absence of the upstream circular cylinder. At all four speeds tested, noise was present in the pressure signals across the frequency spectra. The noise level was found to be highest on sensor channel 1, which was the channel closest to the the protruding lip at the leading edge of the sensor array, indicating that flow separation or turbulence generation was likely taking place.

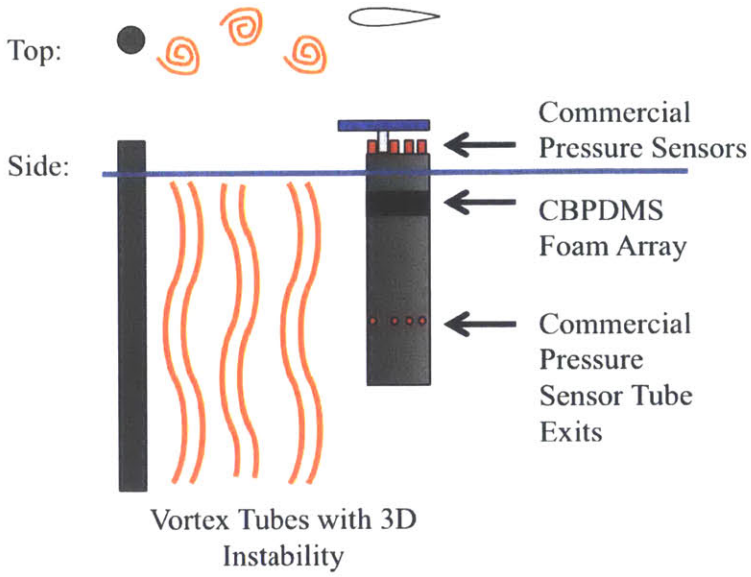

(a) The three dimensional instability of Kármán vortex shedding creates phase differences along the span-wise direction of the circular cylinder. Because the CBPDMS foam and commercial sensor arrays are located at different locations along the hydrofoil span, phase differences are expected in the surface pressure time trace.

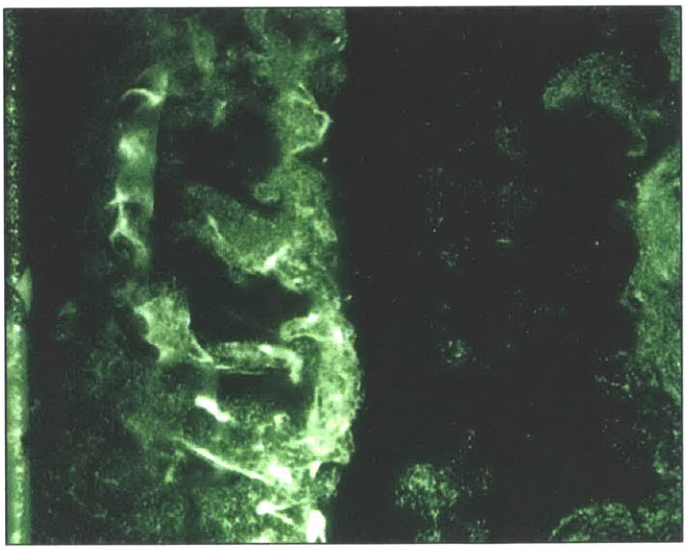

(b) The three dimensional instability of Kármán vortex shedding was demonstrated at Re=12000 using hydrogen bubble imaging in a circulating water tunnel. The fluid flow is moving left to right in the image, and a circular cylinder is on the left edge of the frame (Screenshot from a video by Gustavo R.S. Assi).

Figure 7-10: The three dimensional instability of Kármán vortex shedding creates phase differences along the span-wise direction of the circular cylinder.

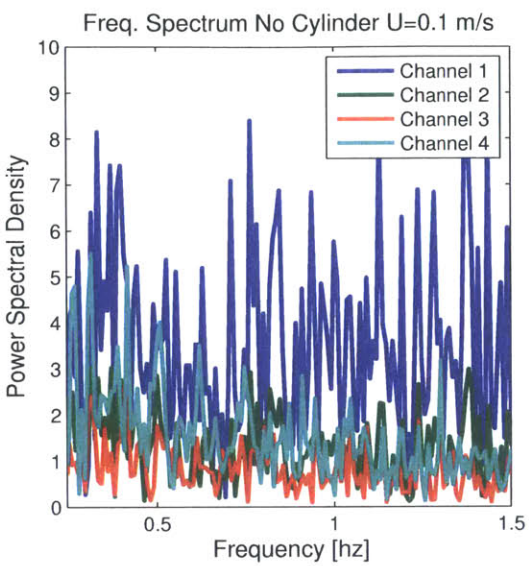

(a) Frequency spectra for the CBPDMS foam sensor array in the absence of the circular cylinder at U=0.1 m/s.

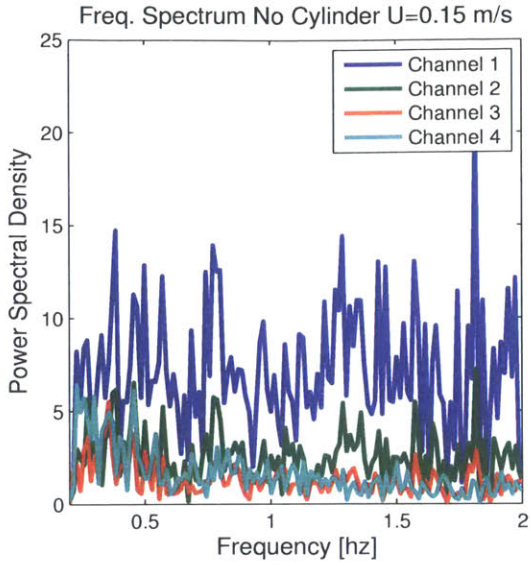

(b) Frequency spectra for the CBPDMS foam sensor array in the absence of the circular cylinder at U=0.15 m/s.

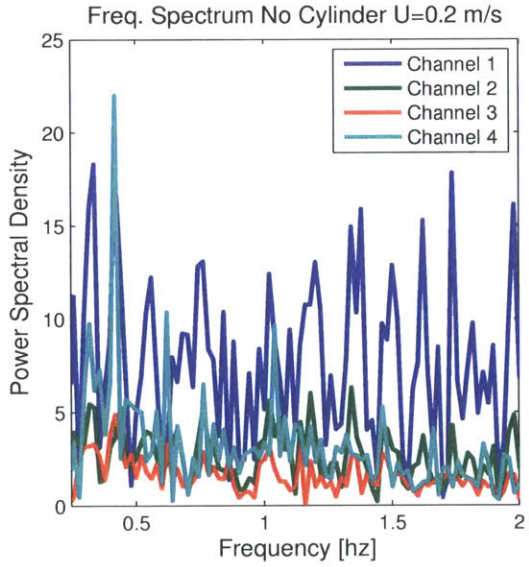

(c) Frequency spectra for the CBPDMS foam sensor array in the absence of the circular cylinder at U=0.2 m/s.

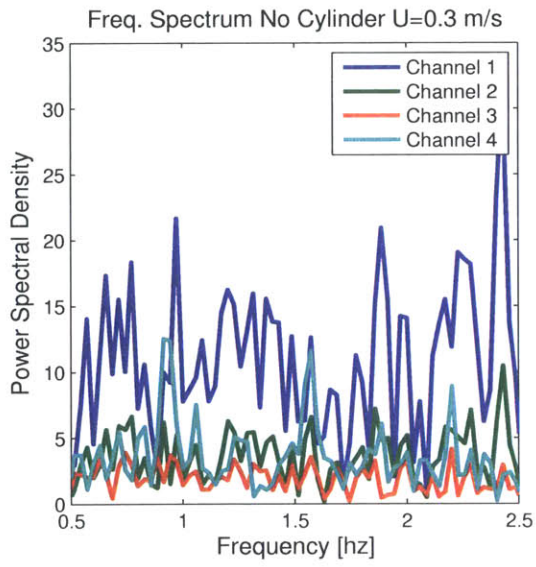

(d) Frequency spectra for the CBPDMS foam sensor array in the absence of the circular cylinder at U=0.3 m/s.

Figure 7-11: The impact of the CBPDMS foam sensor array protrusion from the foil surface was characterized by finding the frequency spectra of measurements taken in the absence of the circular cylinder.

7.5.2 Numerical Simulations

To get a qualitative picture of the near-body flow structures generated in the Kármán vortex street identification experiments, numerical simulations were performed. In

particular, it was desired to observe the effect the protruding lip of the CBPDMS foam sensor array would have on the near-body flow.

Numerical simulations of the Kármán vortex street identification experiments were conducted using the Computational Fluid Dynamics (CFD) solver Lily-Pad, which is well suited for fluid-structures interaction problems. Lily-Pad uses the Boundary Data Immersion Method (BDIM) to immerse solid bodies in the fluid domain, and allows for simulations to be setup and run extremely efficiently [84]. For additional details and references about the Lily-Pad solver and BDIM, see the Lily-Pad project page on Github (https://github.com/weymouth/lily-pad/wiki).

For both the simulation of a clean NACA 0020 foil in the wake of a circular cylinder, and for the case of the foil with the protruding sensor array, the simulation parameters were the same. The domain size was chose as 20D x 20D with the circle positioned 4D from the upstream boundary (16D from the downstream boundary) and 12D from the side boundary. The Reynolds number based on circle diameter (0.0381m) and free stream (0.2 m/s) was Re=7620, and the resolution was 50 grid points spanning the circle diameter with a total of 1 million grid points in the domain.

Lily-pad simulations of the NACA 0020 trailing a circular cylinder provided an excellent visualization of the flow field to qualitatively confirm the separation and offset values used in the towing tank experiments. The location of the cylinder and foil vortex wakes was clear when plotting the vorticity of the flow field, as seen in Figure 7-12(a). From the vorticity plot, it was confirmed that the periodic vortices shed from the circular cylinder remain inside the offset distance of the foil, causing the vortices to pass the pressure sensor arrays on the foil's surface. The vorticity plot also made clear the formation of the foil's own vortex wake, although the wake vortices don't begin to take shape until downstream of the foil, suggesting the pressure signal from the foil's own vortices will not be present in the measurements taken on the foil surface.

In Figure 7-12(b), the foil section was simulated with the CBPDMS sensor strip protrusion on the surface of the foil. It was observed that flow separation was present at both the leading and trailing edges of the sensor strip, and vortices generated

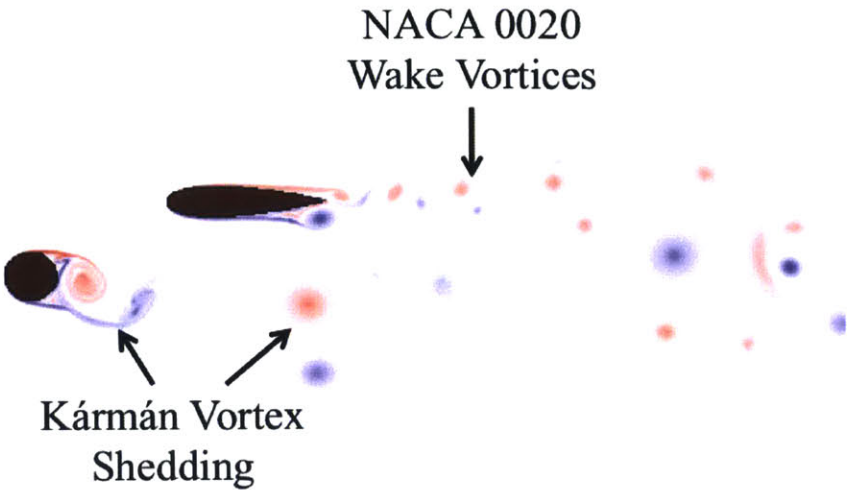

(a) Lily-Pad simulation of a clean NACA 0020 foil section in the wake of a circular cylinder. Clockwise vorticity is given in red, and counterclockwise vorticity is given in blue. The Kármán vortex shedding is clearly visible from the leading cylinder, and is observed to pass to the inside of the foil section.

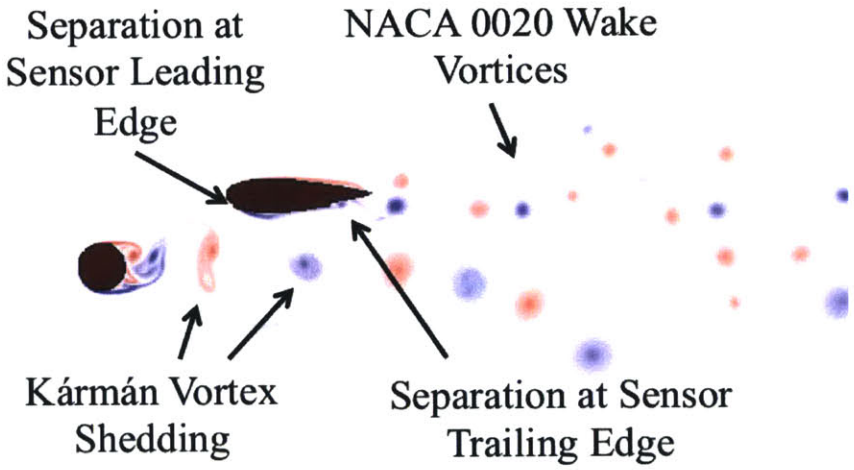

(b) Lily-Pad simulation of the NACA 0020 foil section with sensor strip protrusion in the wake of a circular cylinder. Clockwise vorticity is given in red, and counterclockwise vorticity is given in blue. Separation is visible at both the leading and trailing edges of the CBPDMS foam sensor strip, and is expected to contribute to the noise measured by the pressure sensor array.

Figure 7-12: A clean NACA 0020 foil section and a foil section with a sensor strip protrusion were simulated in the wake of a circular cylinder. The separation and offset distances were consistent with the experimental setup in the MIT towing tank, and the simulated fluid velocity corresponds to an experiment at U=0.2 m/s.

at the sensor's trailing edge were being shed into the foil's wake. The visualization of separation at the leading edge of the sensor array supports the observation of increased noise on sensor channel 1 from Figure 7-11.

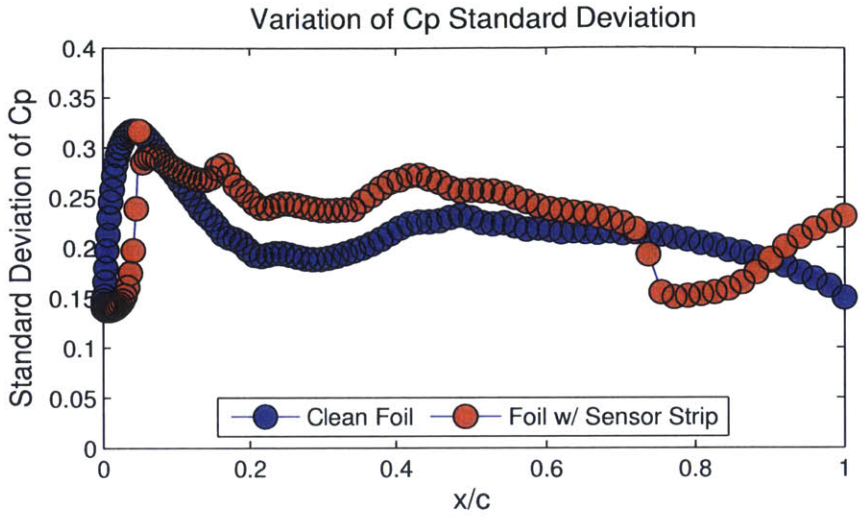

Figure 7-13: The standard deviation of the coefficient of pressure (Cp) provides an indication of the magnitude of pressure fluctuations along the foil chord. In a uniform flow in the absence of an upstream cylinder, the standard deviation of Cp on a clean foil would be small. For both the clean NACA 0020 foil and the the foil with sensor protrusion, it was observed that the standard deviation of Cp was highest near the leading edge, indicating that CBPDMS sensor channel 1 and MPXV sensor 1 would 'feel' the shed Kármán vortices more than the other sensors.

Along with providing a visualization of the shed vortex wake from the circular cylinder, the Lily-Pad simulations provided an expected pressure profile on the surface of the trailing foil. Of particular interest was the variation in how the shed vortices were 'felt' from the leading edge to the trailing edge. One means of characterizing this variation was to plot the standard deviation (STD) of the coefficient of pressure on the foil surface as a function of chord-wise position along the foil, as seen in Figure 7-13. It was expected that locations along the foil where the interaction with the shed vortex wake is significant would have large standard deviations as the periodically shed vortices caused large variations in the foil surface pressure. Similarly, the standard deviation was expected to be low in areas where the impact of the shed vortices was less apparent and surface pressure variations were small. It was observed that the standard deviation of the pressure coefficient was largest in the leading third of the foil, and dropped off towards the trailing edge for both the clean NACA 0020 and sensor protrusion cases, as seen in Figure 7-13. This result suggested that the Kármán vortex street would be most visible on sensor channel one

for both the commercial and CBPDMS sensors, and that the signal would diminish substantially towards the trailing edge sensor positions. Additionally, the observation that the largest hydrodynamic signals were present near the leading edge of the foil was consistent with lateral line physiology, where a concentration of neuromasts is often present near the head of the fish, as seen in Figure 1-2.

For the case of the foil with the sensor strip protrusion, an additional peak in STD was observed at approximately x/c=0.17 where the leading edge of the sensor strip was located. The presence of increased pressure fluctuations at the sensor strip leading edge is consistent with the observation of separation in 7-12(b). It was also observed that the STD of Cp was increased along the mid-section of the foil where the sensor strip was present (x/c=0.17-0.7) when compared to the clean foil. This indicated that the likelihood of increased noise in the CBPMDS pressure measurements compared to the pressure measurements from the MPXV sensors taken on a clean section of the foil.

7.6 Experimental Results with Cylinder

During the Kármán vortex street identification experiments, force and pressure were recorded simultaneously while the towing carriage was in motion. Between experiments, the towing carriage was returned to the starting position at the end of the tank, and the tank was given time to settle before starting the next run in order to avoid extraneous force and pressure signals. The submergence depths of the CBPDMS and commercial sensor arrays were recorded before each set of experiments, and time was given after placing the foil in the tank to allow for temperature equilibration. Additional data collection runs were conducted at each test velocity with the circular cylinder absent to allow for the identification of noise sources.

7.6.1 Data Analysis

Measurements from the ATI Gamma force transducer, commercial pressure sensors, and CBPDMS foam array were collected at 1000 Hz using the analog input channels

on a NI USB-6289 data acquisition board and Labview software. Measurements were saved to a text file and analysis was performed in Matlab.

Conversion to physical units

Following the separation of the voltage values for individual sensor channels, calibrations were applied to convert from voltage to units of force or pressure. For the ATI Gamma force transducer, a factory provided 6x6 calibration matrix (provided in Appendix D) was used to convert voltage measurements to force and torque in pounds and pound-foot respectively. An additional conversion to SI units was performed to remain consistent with the rest of this study.

For the commercial pressure sensors, the linear calibration for each sensor described in Section 7.3 was applied to the raw voltage signals before any additional post-processing. The voltage measurements from the 7.8 mm thick CBDPMS foam sensor array were converted to pressure using the piecewise polynomial calibration curves developed in Section 5.3.5. As in the experiments using water wave stimulus, the DC offset voltage was adjusted for the initial hydrostatic pressure at the CBPDMS array submergence depth.

Selection of data subset

During the Kármán vortex street identification experiments, the tow tank carriage motion and the data collection from the force and pressure sensors were facilitated by two separate computers. To run an experiment, data recording was started on one computer, then the carriage motion was subsequently started. Because of this experimental sequence, pressure and force data was recorded for periods when the carriage was not in motion, as well as during the acceleration and deceleration phases of the carriage motion. To allow for proper analysis of the CBPDMS foam sensor array's ability to detect a Kármán vortex street, a subset of data was selected for each experiment during the period where the carriage velocity was steady. Due to the length of the towing tank, data subsets ranged from 30-90 seconds depending on the towing velocity, allowing for the analysis of many vortex shedding cycles. Selection

of data subsets was based on analysis of the raw force signals, which displayed a clear and characteristic response at the start and stop of the carriage motion due to the foil's inertia, as seen in Figure 7-14(a)

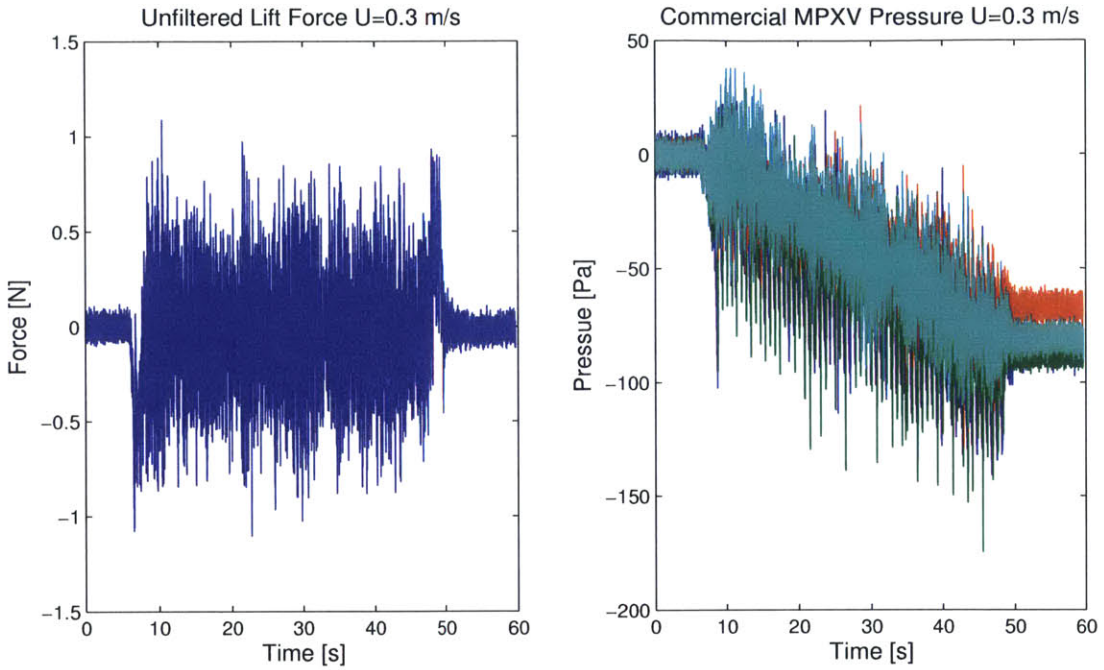

(a) The data subset for the period where the carriage was moving at a steady velocity was identified using the raw lift force. The initiation of the carriage motion is visible from the inertial spike at approximately 6 seconds, and the carriage stopping is identified by a similar spike at approximately 49 seconds.

(b) With the initial hydrostatic pressure offset removed, the variation in hydrostatic pressure caused by a change in submergence depth throughout the course of a run is evident in the un-filtered commercial pressure sensor measurements.

Figure 7-14: The subset of the pressure data where the carriage was moving was selected by observing the raw lift force measurements. Cutoff frequencies for filtering were chosen to eliminate the low frequency effect of the tank slope.

Data Filtering

Experimental data was filtered with a non-causal bandpass filter using the *idealfilter* function in Matlab. The *idealfilter* function makes any input signal zero-mean before filtering, so the mean of of each signal was taken before filtering and added back into the signal after the filtering function was complete. In the experimental signals, three primary sources of noise were identified:

1. High frequency electrical noise at $\sim$ 60 Hz
2. Low frequency drift due to change in submergence depth throughout each run
3. Mechanical vibration of the foil at $\sim$ 3 Hz

The low frequency drift due to a time-varying submergence depth is clearly visible in the un-filtered commercial pressure sensor measurements shown in Figure 7-14(b) where the initial pressure offset has been removed to emphasis the effect of the change in the submergence depth along the length of the tank. From the plot, it is clear that the submergence depth changes approximately 8mm over the course of the experiment, likely due to a very slight mis-alignment between the carriage support rail and the water free surface.

Comparing the frequency spectra for the un-filtered lift force signal in the absence of the circular cylinder (Figure 7-15(a)), and with the cylinder present (Figure 7-15(b)), allowed for the identification of frequency contributions of relevance to the detection of Kármán vortex shedding. In Figure 7-15(b), the expected frequency range for Kármán vortex shedding calculated using Equation 7.2, and based on the towing velocity and a Strouhal number range of 0.18-0.22, is designated by the grey region. Frequency contributions that fell near or within this region were considered relevant when choosing cutoff frequencies for the bandpass filter. In Figure 7-15(a) no significant frequency contributions were observed within the Strouhal region of interest, as expected. The presence of a frequency peak at $\sim$ 3 Hz in both the cylinder and no cylinder cases suggested that the contribution was due to a mechanical vibration of the foil setup, and not a hydrodynamic stimulus of interest. The cutoff frequencies for the bandpass filter were chosen based on the known noise sources discussed above, along with the expected vortex shedding frequency range, and are given in Table 7.2.

7.6.2 Frequency Domain Results for U=0.1 m/s

At U=0.1 m/s the MPXV commercial pressure sensors and lift force measurements both indicated a primary frequency component at 0.50 Hz, corresponding to a Strouhal

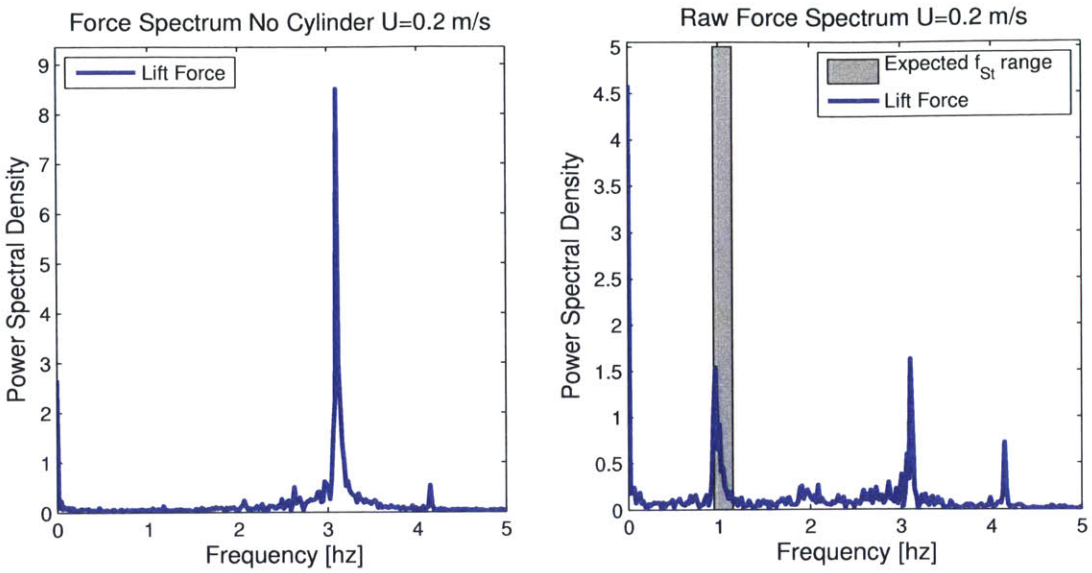

(a) Frequency spectrum for the un-filtered lift force in the absence of the circular cylinder. The low frequency component can be attributed to the variation in submergence depth along the length of the tank, while the frequency component at ~3 Hz is observed across all experiments and can be attributed to a mechanical vibration of the foil.

(b) Frequency spectrum for the un-filtered lift force with the circular cylinder present. The gray area represents the expected frequency range for Kármán vortex shedding with a Strouhal number range of 0.18-0.22.

Figure 7-15: Comparing the frequency spectra for the NACA 0020 foil lift force with and without the circular cylinder present allows for the identification of noise sources. Across a range of towing velocities, a consistent frequency contribution was identified at approximately 3 Hz which was attributed to a mechanical vibration of the foil.

number of 0.1905 that fell within the expected range for Kármán vortex shedding. The frequency spectra from the CBPDMS foam sensor array was found to be much noisier than the commercial pressure sensor and force measurements, which was expected due to the presence of the sensor protrusion on the foil surface, and consistent with the measurements taken without the circular cylinder present (Figure 7-11(a)). A minor frequency peak was present in the CBPDMS foam array measurements at 0.48 Hz, corresponding to a Strouhal number of 0.1829. However, the signal-to-noise ratio was not sufficient to make a conclusive judgement if the frequency component was due to vortex shedding from the circular cylinder.

U [m/s]	D [m]	f_{st} for St=0.18 [Hz]	f_{st} for St=0.22 [Hz]	Bandpass low [Hz]	Bandpass high [Hz]
0.1	0.0381	0.472	0.577	0.25	1.5
0.15	0.0381	0.709	0.866	0.2	2
0.2	0.0381	0.945	1.155	0.25	2
0.3	0.0381	1.417	1.732	0.5	2.5

Table 7.2: Expected vortex shedding frequencies based on towing velocity and St=0.18-0.22, and bandpass filter cutoff frequencies.

Measurement	f_{peak} [Hz]	St_{peak}
Lift Force	0.50	0.1905
Commercial Sensors (Ch. 1)	0.50	0.1905
CBDPMS Array (Ch. 1)	0.48*	0.1829

Table 7.3: Peak frequency and corresponding Strouhal number for towed cylinder experiments at U=0.1 m/s. For the CBPDMS foam sensor array, the peak frequency was chosen as the peak frequency within the expected vortex shedding range (grey region). At U=0.1 m/s, the frequency content of the CBPDMS foam signal is dominated by noise, as seen in Figure 7-16(c).

7.6.3 Frequency Domain Results for U=0.15 m/s

For experiments at U=0.15 m/s, the MPXV commercial pressure sensors and lift force measurement both had a peak frequency component at 0.743 Hz, corresponding to a Strouhal number of 0.1887. As in the case of U=0.1 m/s, the noise in the CBPDMS sensor array measurements made identification of a clear frequency peak difficult. Three frequency peaks at 0.70, 0.743, and 0.814 Hz were observed to fall within the expected frequency range of Kármán vortex shedding. The peaks at 0.70 and 0.743 were closest to the primary frequency component measured by the commercial pressure and force sensors, and corresponded to Strouhal numbers of 0.1778 and 0.1887 respectively. While it is likely that the peaks within the expected vortex shedding frequency range were due to the presence of the upstream circular cylinder, the signal-to-noise ratio was still insufficient for conclusive identification.

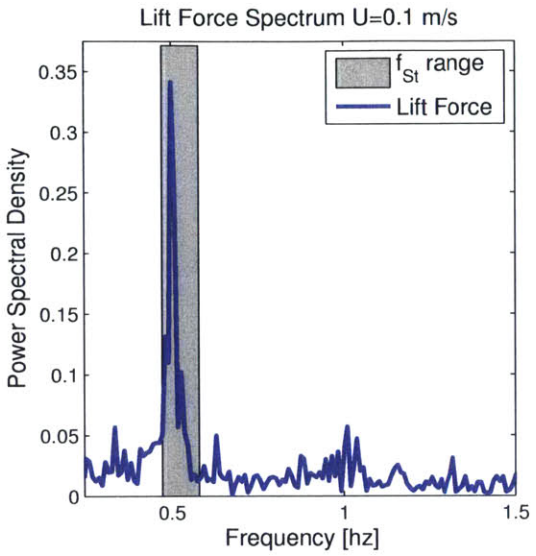

(a) Frequency spectrum of the bandpass filtered lift force for U=0.1 m/s.

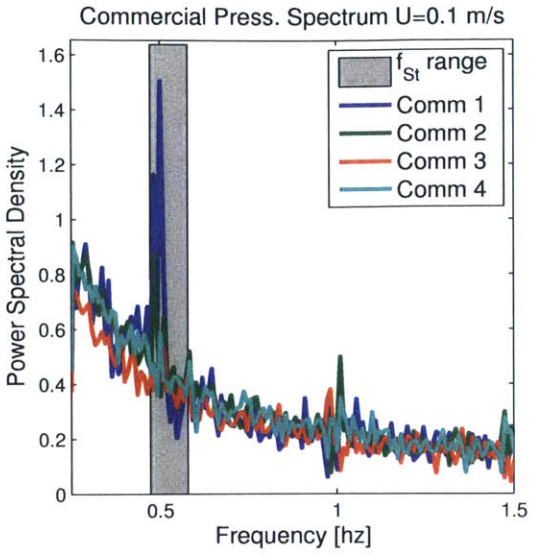

(b) Frequency spectrum of the bandpass filtered commercial pressure sensor output for U=0.1 m/s.

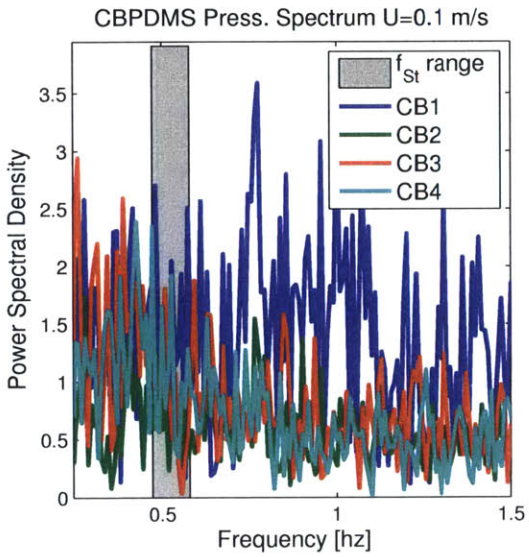

(c) Frequency spectrum of the bandpass filtered CBPDMS foam pressure sensor output for U=0.1 m/s.

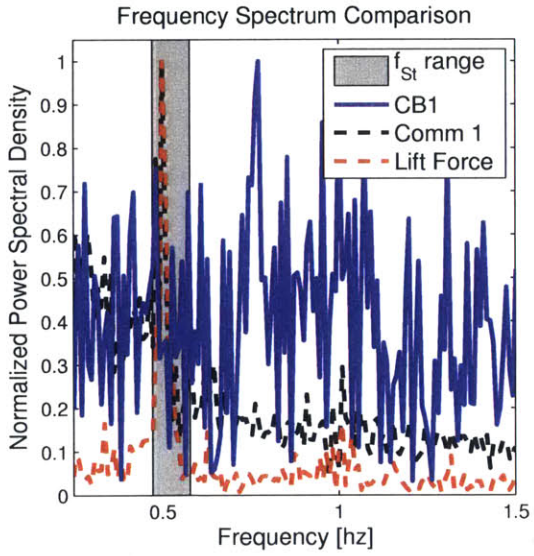

(d) Normalized lift force, commercial pressure sensor, and CBPDMS foam frequency content for U=0.1 m/s.

Figure 7-16: Frequency spectra for pressure and force measurements at U=0.1 m/s.

7.6.4 Frequency Domain Results for U=0.2 m/s

At U=0.2 m/s the CBPDMS pressure sensor arrays exhibited a clear frequency peak within the expected range for Kármán vortex shedding. When compared to the dominant frequency peaks in the lift force and commercial pressure sensor data, the

Measurement	f_{peak} [Hz]	St_{peak}
Lift Force	0.743	0.1887
Commercial Sensors (Ch. 1)	0.743	0.1887
CBDPMS Array (Ch. 1)	0.70 and 0.743	0.1778 and 0.1887

Table 7.4: Peak frequency content results for U=0.15 m/s. For the CBPDMS foam sensor array, two peaks of near equal magnitude were present within the expected frequency range for vortex shedding and in close proximity to the peak frequency measured by the commercial pressure and force sensors.

CBPDMS peak frequency was lower by approximately 2%, as seen in Table 7.5. Considering the three-dimensionality of Kármán vortex shedding and the potential for variations in phase and pressure magnitude along the span of the instrumented foil, a 2% difference in the peak frequency detected by the CBDPMS foam array and the commercial sensors was considered a successful Kármán vortex street identification. Compared to experiments at U=0.1 m/s and U=0.15 m/s, the CBPDMS foam sensor signal to noise ratio was greatly improved at the increased towing speed, although the CBPDMS sensor array measurements were still found to exhibit a lower signal-to-noise ratio than the commercial pressure sensors, as seen in Figures 7-18(c) and 7-18(d).

Measurement	f_{peak} [Hz]	St_{peak}
Lift Force	0.960	0.1829
Commercial Sensors (Ch. 1)	0.960	0.1829
CBDPMS Array (Ch. 1)	0.940	0.1791

Table 7.5: Peak frequency content results for U=0.2 m/s. The peak frequency at 0.2 m/s was much more clear than experiments at lower flow velocities.

7.6.5 Frequency Domain Results for U=0.3 m/s

At U=0.3 m/s a clear frequency peak in the expected frequency range for Kármán vortex shedding was present in the the lift force, commercial pressure sensor, and CBPDMS foam array data, as seen in Figure 7-19. Additionally, the strength of the periodic pressure signal generated by the shed vortices dropped rapidly from the lead-

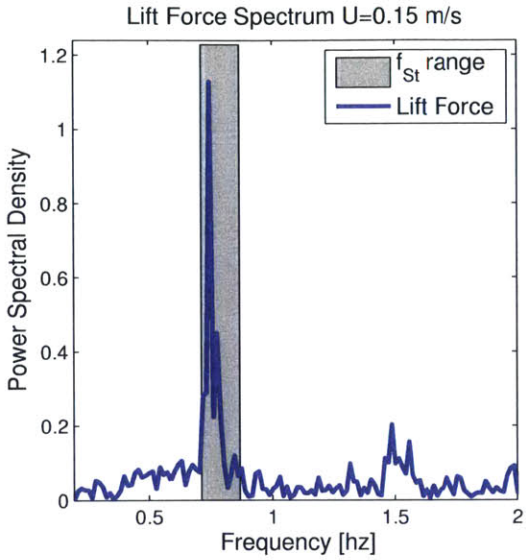

(a) Frequency spectrum of the bandpass filtered lift force for U=0.15 m/s.

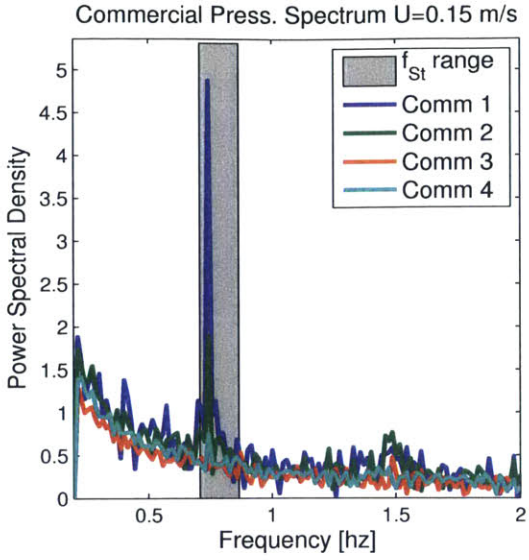

(b) Frequency spectrum of the bandpass filtered commercial pressure sensor output for U=0.15 m/s.

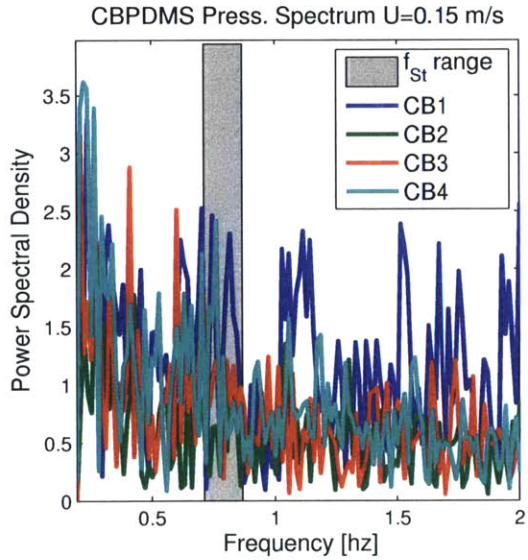

(c) Frequency spectrum of the bandpass filtered CBPDMS foam pressure sensor output for U=0.15 m/s.

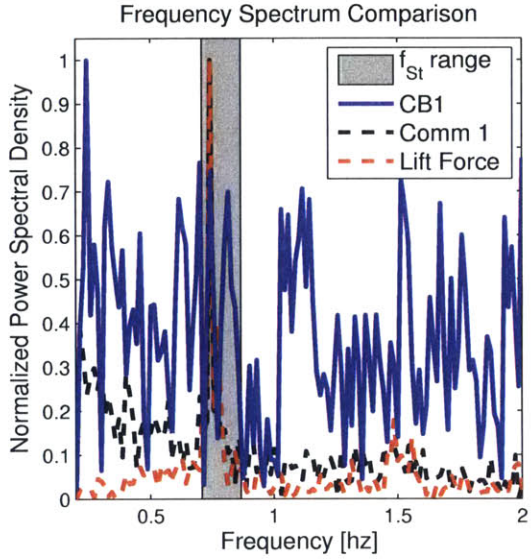

(d) Lift force, commercial pressure sensor, and CBPDMS foam frequency content for U=0.15 m/s.

Figure 7-17: Frequency spectra for pressure and force measurements at U=0.15 m/s.

ing to the trailing edge of the foil, as expected based on the results of the Lily-Pad simulations shown in Figure 7-13. The peak frequency contribution and associated Strouhal number for each measurement is given in Table 7.6, with the percent difference of the frequency measured by the CBPDMS array from the frequency measured

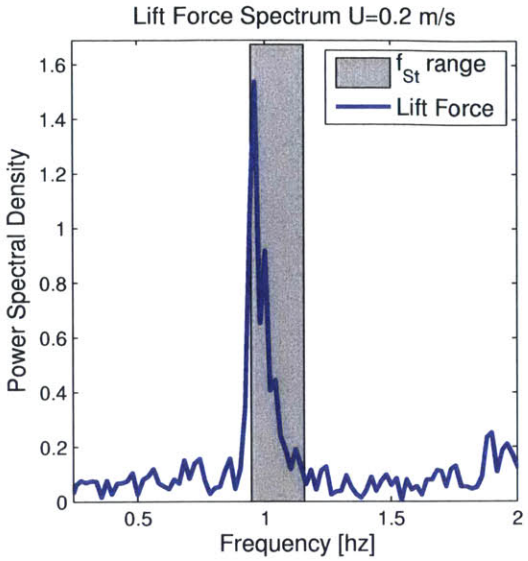

(a) Frequency spectrum of the bandpass filtered lift force for U=0.2 m/s.

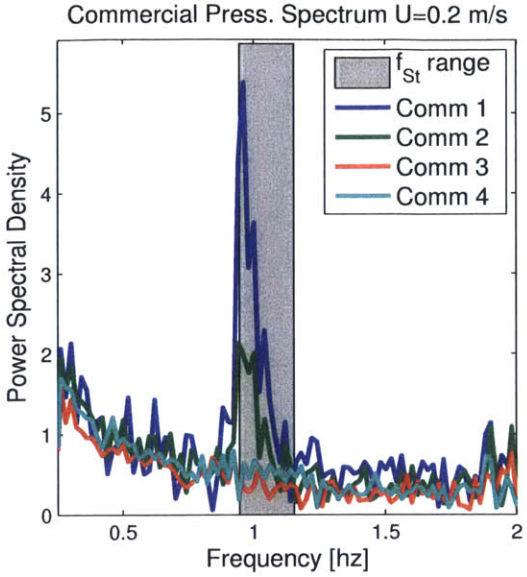

(b) Frequency spectrum of the bandpass filtered commercial pressure sensor output for U=0.2 m/s.

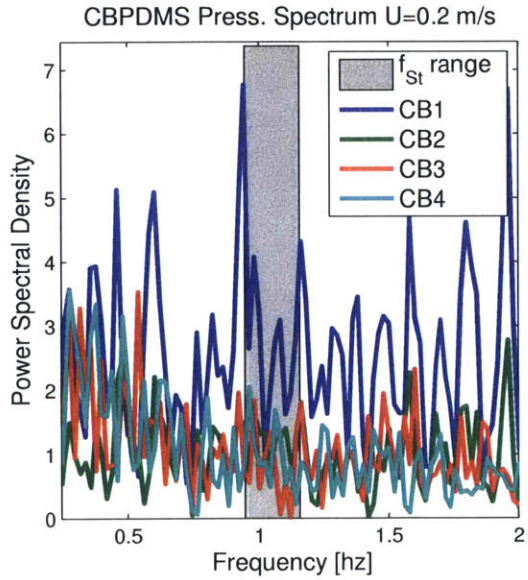

(c) Frequency spectrum of the bandpass filtered CBPDMS foam pressure sensor output for U=0.2 m/s.

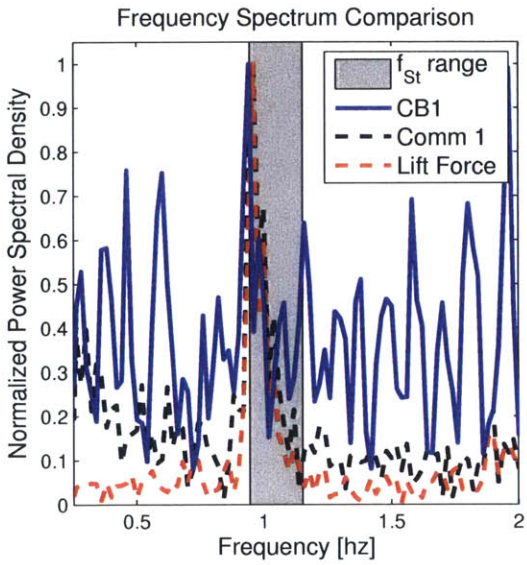

(d) Lift force, commercial pressure sensor, and CBPDMS foam frequency content for U=0.2 m/s.

Figure 7-18: Frequency spectra for pressure and force measurements at U=0.2 m/s.

by the force transducer and commercial pressure sensors being 2.03%. As in the lower towing speed cases the signal to noise ratio for the CBPDMS array was lower than the commercial pressure sensors, but it was observed that the ratio improved with

towing velocity and the magnitude of the periodic pressure signal.

Measurement	f_{peak} [Hz]	St_{peak}
Lift Force	1.429	0.1815
Commercial Sensors (Ch. 1)	1.429	0.1815
CBDPMS Array (Ch. 1)	1.400	0.1778

Table 7.6: Peak frequency content results for U=0.3 m/s.

7.7 Time Series Pressure Results

The voltage measurements from the 7.8 mm thick CBPDMS foam pressure sensor array were converted to pressure using the piecewise polynomial calibration curves developed from the plunging experiments. The time series pressure fluctuations from CBPDMS channel 2 were compared against the pressure measurements from the MPXV commercial pressure sensor number 2, which were co-located along the chord-wise direction of the NACA 0020 foil, as seen in Figure 7-6. The CBPDMS foam sensor array and the pressure transmission tube exit for the MPXV commercial pressure sensors were located at different positions along the span of the foil, as seen in Figure 7-7(a). Because of the 3D instability of Kármán vortex shedding, as discussed in Section 7.4 and shown in Figure 7-10, differences in phase and pressure fluctuation magnitude were expected between the measurements from the CBPDMS foam array and the commercial pressure sensors, as seen in Figure 7-20.

Considering the time series results at increasing free stream velocities in Figure 7-20, it was observed that at U=0.1 and U=0.15 m/s the CBPDMS foam sensor array over-predicted the RMS value of pressure fluctuations when compared to the MPXV commercial pressure sensors. At U=0.2 and U=0.3 m/s, the RMS pressure showed better agreement between the CBPDMS foam array and the MPXV sensors, as seen in Table 7.7, and consistent with the results of the frequency analysis above.

The difference in the RMS pressure between the CBPMDS foam sensor array and the MPXV sensors can be partially explained by the presence of the sensor array protrusion in the foil surface. Channel 2 of the CBPMDS sensor and MPXV sensor

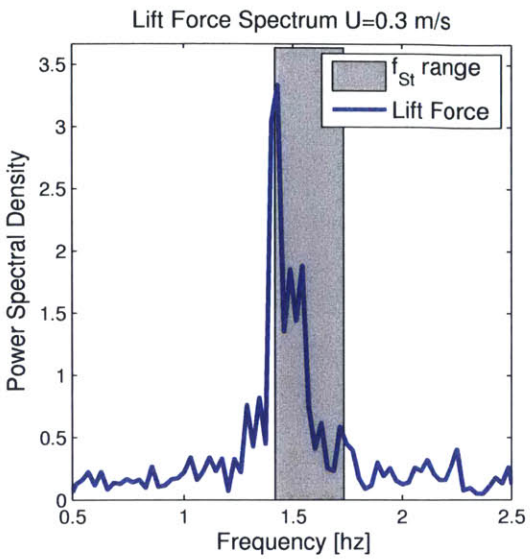

(a) Frequency spectrum of the bandpass filtered lift force for U=0.3 m/s.

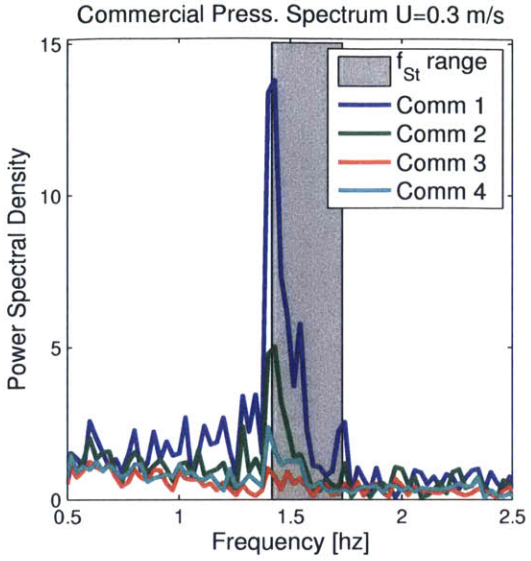

(b) Frequency spectrum of the bandpass filtered commercial pressure sensor output for U=0.3 m/s.

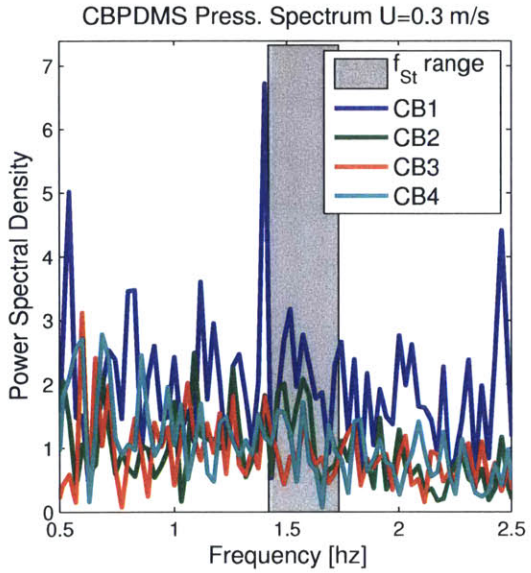

(c) Frequency spectrum of the bandpass filtered CBPDMS foam pressure sensor output for U=0.3 m/s.

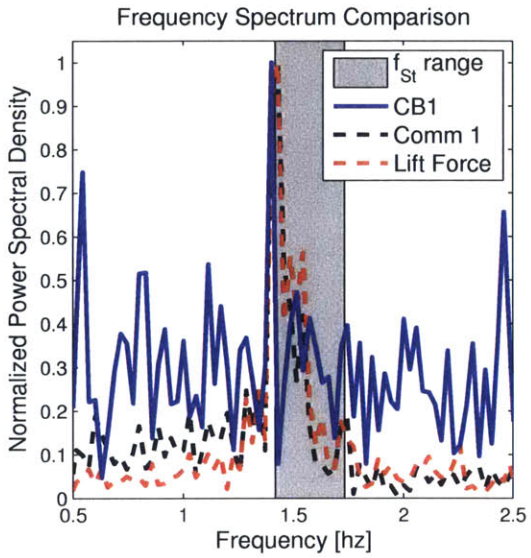

(d) Lift force, commercial pressure sensor, and CBPDMS foam frequency content for U=0.3 m/s.

Figure 7-19: Frequency spectra for pressure and force measurements at U=0.3 m/s.

2 are located at approximately x/c=0.3, and the STD of the pressure coefficient was found to be higher in the presence of the sensor array protrusion than on a clean foil section, as shown in Figure 7-13. The over-prediction at low flow velocities may also be due to the < 4 Pa pressure signals measured by the commercial MPXV sensors

U [m/s]	RMS of Pressure MPXV [Pa]	RMS of Pressure CBPDMS [Pa]	Percent Difference of RMS
0.1	1.11	5.74	135.12
0.15	2.50	5.33	72.2
0.2	3.45	4.13	17.83
0.3	6.93	5.21	28.37

Table 7.7: Root mean square of the pressure fluctuations measured using the MPXV and CBPDMS sensors with percent difference. RMS is calculated for 20 shedding cycles starting 12 seconds after the initiation of the carriage motion, as seen in Figure 7-20. Because of the 3D instability of vortex shedding from a cylinder, differences in magnitude and phase along the foil span are expected.

being at the limit of the CPDMS foam array resolution.

7.8 Chapter Summary

For Kármán vortex shedding experiments conducted at towing speeds of 0.2 and 0.3 m/s, the RMS pressure was measured to be 3.45 and 6.93 Pa respectively using commercial MPXV series pressure sensors. Despite the very low RMS pressure, the CBPDMS foam sensor arrays were able to detect the peak shedding frequency within 3% of the value found using pressure and lift force measurements from commercial sensors, as given in Tables 7.5 and 7.6. In addition to accurately detecting the Kármán vortex shedding frequency, the CBPDMS foam sensor arrays were found to measure the RMS pressure for the 0.2 and 0.3 m/s cases with percent difference compared to the commercial pressure sensors of 18% and 28% respectively, as seen in Table 7.7. These results provided strong evidence that the 7.8 mm thick CBPDMS foam sensor array was capable of measuring the characteristic periodic pressure drop due to vortices at frequencies below 1 Hz and with RMS pressure of ~4 Pa.

For vortex identification experiments at towing speeds of 0.1 and 0.15 m/s, the signal to noise ratio in the CBPDMS pressure measurements was not sufficient to clearly identify the peak vortex shedding frequency. For the case of 0.1 m/s, the com-

mercial pressure sensors measured an RMS pressure of 1.11 Pa, below the anticipated resolution of the sensor array found from the plunging experiments. As expected, the CBPDMS foam sensor array over-predicted the RMS pressure for the 0.1 m/s case, and a clear frequency peak was not identified within the power spectrum, as seen in Figure 7-16. For the experiments at 0.15 m/s, the CBPDMS sensor similarly over-predicted the RMS pressure, although the error was reduced as the signal to noise ratio improved with towing speed. When considering the frequency spectra in Figure 7-17, a dual frequency peak was observed within the expected vortex shedding frequency range, with one of these peaks matching the frequency measurement from the commercial pressure sensors and lift force measurement. This partial identification of the vortex shedding frequency is consistent with the RMS pressure measurement from the commercial pressure sensors of 2.50 Pa, which is at the very limit of the CBPDMS sensor resolution and consistent with the results of the dipole experiments in Chapter 6.

In addition to measuring the vortex shedding frequency and RMS pressure for the 0.2 and 0.3 m/s cases, the decrease in the intensity of pressure fluctuations measured from the leading edge to the trailing edge of the foil by the CBPDMS foam array was consistent with measurements from the MPXV commercial sensors and simulations of the flow found using the Lily-Pad CFD solver. The variation in measurements along the chord-wise direction of the foil demonstrated the simultaneous use of the full CBPDMS foil sensor array, and reinforced the need for distributed pressure sensor arrays to characterize the development of flow structures along the length of a body.

The results of the Kármán vortex street identification experiments proved the viability of the CBPDMS foam sensor array to measure meaningful hydrodynamic stimulus. The experiments demonstrated the sensor array was successful at measuring periodic stimulus at the low end of its resolution while surface mounted on a curved hydrofoil being subjected to vibrations from being towed. The experiments also allowed for a confirmation of the sensor array robustness, as the sensors were left submerged for periods of over 24 hours during the series of experiments, and the performance was not impacted. Finally, the Kármán vortex street identification

experiments provided a verification of the sensor array calibration, and further evidence of the resolution of the CBPDMS foam sensor array as $\sim$5 Pa with a frequency range of 0.5-35 Hz, using a different stimulus type from the time-varying hydrostatic pressure, periodic water waves, or dipole.

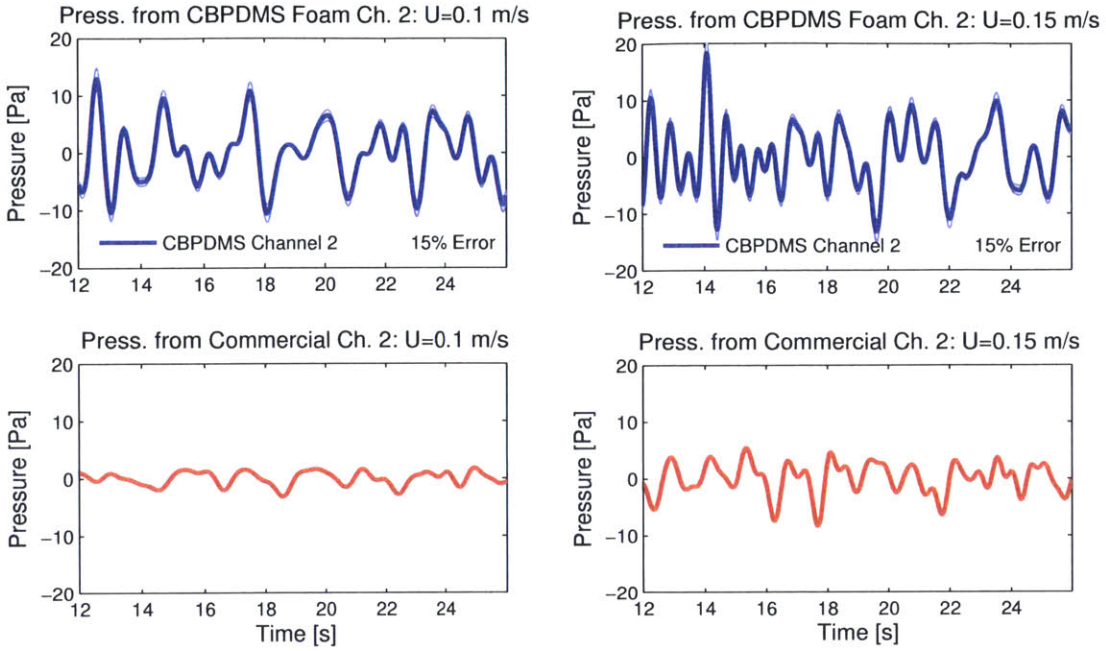

(a) Time series pressure results for U=0.1 m/s (b) Time series pressure results for U=0.15 m/s

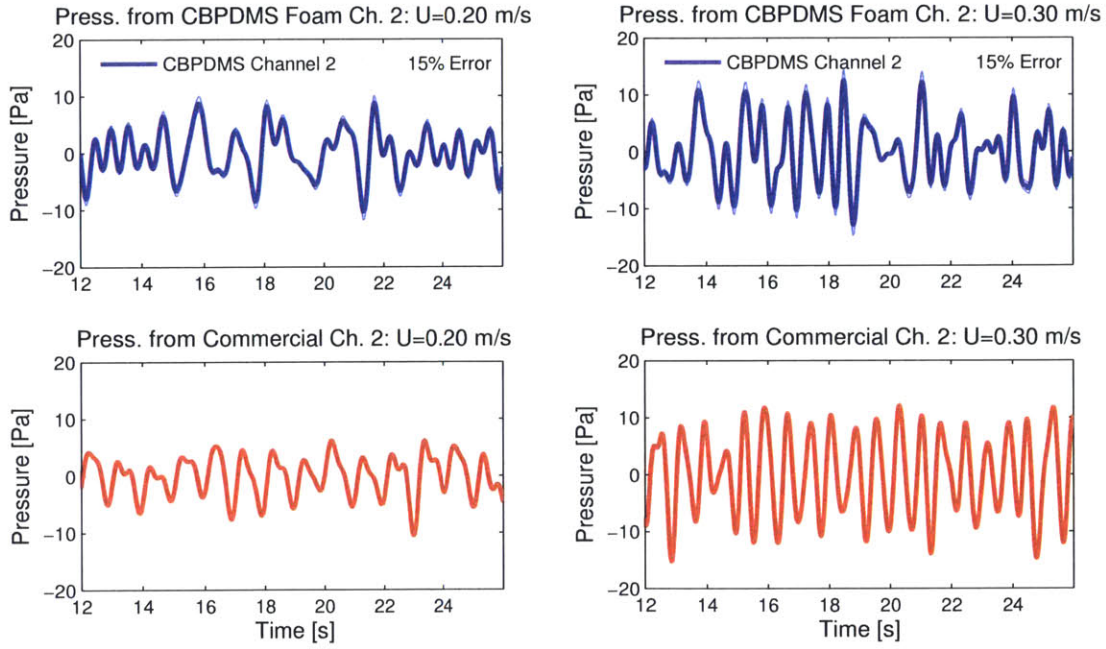

(c) Time series pressure results for U=0.2 m/s (d) Time series pressure results for U=0.3 m/s

Figure 7-20: Time series pressure results for the channel 2 of the CBPDMS foam sensor array and MPXV sensor 2 which are co-located in the chord-wise direction along the foil. Results are shown for 20 shedding cycles beginning 12 seconds after the initiation of carriage motion to avoid transients. The CBPDMS foam array and the MPXV sensors are located at different span-wise positions along the foil, and variations in phase and magnitude are expected as discussed in Section 7.4. A 15% error region is shown based on the RMS error found during plunging and wave experiments using the CBPDMS foam array.

Chapter 8

Conclusion

8.1 Overview

The performance of marine vehicles is largely influenced by near-field flows, both self-generated and environmentally driven. Examples of self-generated flows include leading edge vortex shedding from hydrofoils (Section 2.2), helical vortex shedding from ship hulls at non-zero drift angles (Section 2.1), and separation from the sharp bow of a surface vehicle at large angles of attack or during maneuvers (Sections 2.1 and 2.3). Environmentally driven flows cover an incredible frequency and amplitude range, from the periodic shedding of a Kármán vortex street behind an obstruction in the free-stream (Chapter 7), to surface water waves generated by wind or passing surface vessels (Section 5.4), to high frequency oscillatory flows generated by flapping or vibrating sources in the far field (Chapter 6). In each case, the fluid-structure interaction exerts forces on the marine vehicle, requiring a control action to either minimize a negative performance impact, or optimize a beneficial interaction.

For manned surface and aerial vehicles, performance evaluations are made in-situ and continuously through a variety of sensory inputs, and control decisions are made in real-time to optimize vehicle performance. In the case of marine vehicles, the operational environment presents a profound sensory deficit that must be overcome in order to operate successfully. While land and aerial vehicles often rely on visual feedback systems for navigation and RF signals for communication, underwater vehicles

are limited by low light transmission, turbidity, and the attenuation of RF signals in water. In nature, fish have developed a unique sensory organ known as the lateral line which overcomes this sensory deficit and allows for the detection of near-field flow structures through the use of distributed pressure and velocity sensing. The lateral line sensory organ in fish has been found to mediate such flow-field dependent behaviors as obstacle detection and avoidance, rheotaxis, vortex synchronization, and prey tracking (Section 1.3.2).

The goal of this thesis has been to bring detailed and real-time near-field flow measurements to unmanned marine vehicles through distributed pressure sensing inspired by the fish lateral line sensory organ. Experiments were first conducted using distributed arrays of commercially available pressure sensors to test the applicability of the sensing approach to hydrodynamic applications. The use of arrays of commercially available sensors validated the utilization of distributed pressure sensing for hydrodynamic stimulus, and demonstrated that the current landscape of pressure sensor technologies was ill-suited for scaling to real-world applications while maintaining spatial resolution and allowing for surface mounting. To satisfy the requirements of distributed pressure sensing on unmanned marine vehicles presented in Section 3.1, a conformal, waterproof, and highly sensitive pressure sensor array was developed using a PDMS (silicone) based material set. The use of a closed-cell carbon-black doped silicone foam allowed for sensitivity useful to hydrodynamic stimuli, while taking advantage of the flexibility, moisture resistance, and robustness of the PDMS bulk matrix material.

The following section describes the principal contributions of this thesis, including the validation of distributed pressure sensing for hydrodynamic applications, the design and fabrication of a conformal silicone based pressure sensor array, and the characterization and calibration of the sensor array using a series of biologically inspired fluid flows. As an experimental sensor array meant to demonstrate a novel approach to distributed hydrodynamic pressure sensing on curved bodies, this work revealed a series of paths for further study. The final section contains recommendations for future work, and a discussion of refinements that could be made to the

current experimental sensor arrays.

8.2 Principal Contributions of the Thesis

8.2.1 Distributed Pressure Sensing for use in Near-Body Flow Measurement

In nature, the fish lateral line provides an example of a distributed pressure sensing network for use in hydrodynamic flow sensing applications. The knowledge of the flow field gained from this distributed sensor network mediates behaviors including vortex detection, obstacle avoidance, and flow alignment (rheotaxis), which would benefit marine vehicle operations. To validate the use of a distributed array of pressure sensors to measure near-field flows, a series of experiments of increasing flow complexity were conducted using commercially available sensors. Experiments included the detection of leading edge vortex shedding on an instrumented hydrofoil [27], studying the growth of the separated region on a model sailboat hull as a function of towing angle of attack, and monitoring the dynamics of an unmanned surface vehicle during forced and self-propelled experiments.

Distributed Pressure Sensing on a Towed Surface Vehicle

Using a model sailboat hull in the MIT towing tank, the pressure distribution on a surface vehicle at non-zero angle of attack was investigated using an array of Honeywell 19 mm series pressure sensors. At low angles of attack the pressure was found to be highest at the bow stagnation point, and then decreased towards the vehicle midship, consistent with accelerating flow as the vessel beam increased. At angles of attack greater than 15 degrees, this trend reversed, with pressure increasing along the bow. This indicated a region of re-circulating flow brought on by separation occurring at the vehicle's sharp bow, as shown in Figure 2-2(b). Dye visualization and pressure measurements just aft of the maximum beam of the hull indicated additional vortex separation likely occurring at the sharp keel line, as seen in Figure 2-5. Most

importantly, the pressure at the bow-most tap exhibited a consistent decreasing trend with increasing angle of attack, allowing for the accurate estimation of towing angle based on pressure measurements.

The model sailboat hull experiments validated the use of surface pressure measurements to provide useful insight into the nature of the flow field past the hull. The experiments also provided insight into the placement of pressure taps on the hull, and the need for increased sensor coverage in the vicinity of the maximum beam where a pressure minimum was expected to have occurred, but was unable to be measured. Finally, the towed model experiments provided the first set of guidelines for the design of pressure sensor arrays intended specifically for hydrodynamic sensing applications. Instrumentation of the hull required pressure taps to be drilled through the hull, and mounting hardware to be epoxied to the hull's inner skin to accept pressure transmission tubes from the Honyewell sensors. These mounting limitations made clear the need for conformal and surface-mountable sensor arrays.

Distributed Pressure Sensing on a Self-Propelled Unmanned Surface Vehicle

An unmanned kayak vehicle was used as a test platform to evaluate the utility of distributed pressure sensing to measure vehicle dynamics during basic forced motion experiments and self-propelled tests. The unmanned surface vehicle was instrumented with an array 20 Honeywell SPT series commercial pressure sensors, as well as two experimental arrays featuring silicon piezoresistive sensor dyes mounted on conformal substrates, and a carbon-black silicone composite strain gauge sensor array. Basic forced vehicle motion experiments were conducted in the swimming pool at the National University of Singapore, and it was found that pressure measurements provided a comparable evaluation of vehicle motions in pitch, roll, and heave to the vehicles inertial motion unit (IMU). Additionally, the operation of all three experimental sensor arrays while surface mounted on a vehicle outside of the laboratory environment was confirmed.

Self-propelled experiments were conducted using the kayak vehicle in Singapore's

Pandan Reservoir, and provided a proof-of-concept for the experimental conformal sensor arrays in a real-world setting. It was found that the distributed pressure sensor arrays, both commercial and experimental, were able to detect the characteristic pressure variations associated with the non-zero yaw acceleration at the initiation of a turning maneuver, as seen in Figures 2-19 and 2-20. Additionally, the vehicles pitch and roll dynamics during maneuvers or when traversing an area of disturbed water were readily visible in the pressure sensor output.

The experiments conducted in Singapore with the unmanned kayak vehicle reinforced the utility of distributed pressure sensing on the hull of surface vehicles that was demonstrated in the towed model sailboat experiments. Like the towed model sailboat experiments, the size, cost, and mounting of the commercial pressure sensors was a limiting factor in capturing the kayak near-field flow structures. To begin to address this limitation, the unmanned kayak experiments were the first attempt at incorporating experimental conformal pressure sensor arrays on the surface of a marine vehicle hull. While the size and sensitivity of the sensor arrays required further optimization, the unmanned kayak experiments served as an important proof-of-concept for the continued development of conformal distributed pressure sensor arrays.

Design Guidelines for Distributed Hydrodynamic Sensor Arrays

Based on experiments using the towed model sailboat hull, the unmanned kayak vehicle, and an instrumented hydrofoil discussed briefly in Section 2.2 and in great depth in [27], a set of design guidelines were developed for distributed hydrodynamic pressure sensor arrays, as presented in Section 3.1. Primary among these design guidelines were an increase in sensor waterproofing, flexibility, and robustness to allow for surface mounting of the sensor arrays, easing the mounting challenges experienced in previous studies. The design guidelines also emphasized a reduction in individual sensor cost to allow for distributed arrays to be scaled up to real-world applications while maintaining spatial density on the order of millimeters to centimeters. Finally, previous experimental results demonstrated that for use in hydrodynamic sensing applications on marine vehicles of length $\sim$1-3 m, dynamic pressure stimuli range

from ~10 - 400 Pa with ~10 Pa sensitivity, as stated in Section 3.1.

Each design guideline presented in Section 3.1 was based on lessons learned through experimentation and experience with commercially available sensor technologies. By basing the design of a next-generation distributed sensor array on a foundation of experimental results using commercial sensors, the key areas in need of development were identified early in the design process, providing focus to the sensor array development.

8.2.2 Development of a Closed-Cell CBPDMS Foam Sensor Array

Informed by the experience gained using commercial pressure sensors for hydrodynamic sensing, a waterproof and conformal pressure sensor array was developed for use on marine vehicles, as shown in Figure 4-1. To achieve the goal of a robust, waterproof, and conformal array, a silicone-based material set was utilized, and piezoresistivity was achieved by selectively doping regions of the array with conductive carbon black particles. The array layout was designed to minimize contact resistance between the piezoresistive sensing material and the electrodes, and soft sensor fabrication techniques were extended to increase sensitivity through the use of a closed-cell silicone foam.

PDMS Based Material Set

Sensor arrays were developed using a completely PDMS (silicone) based material set to take advantage of the material's moisture resistance, flexibility, ease and safety of use, and inexpensive availability. The primary sensing component of the arrays was a commercially available platinum silicone foam doped with 5% by weight carbon black. The carbon black-PDMS (CBPDMS) foam composite was piezoresistive and displayed an inverse relationship between pressure and resistance, following the compressible model of piezoresistivity shown in Figure 4-2(a). The use of a closed-cell foam retained the reduction in Young's modulus observed in previous work in

CBPDMS foam composites (Section 3.4.3), while creating an inherently waterproof material well-suited for marine applications, without the need for encapsulation.

The sensor array electrodes were composed of a silver-carbon black-PDMS composite which offered excellent conductivity, low piezoresistivity, and maintained overall array flexibility. The continuity of PDMS base material provided excellent adhesion between the electrodes of the CBPDMS foam active sensing material, and a layer of pure PDMS on the bottom of the array provided for support during the fabrication process as well as a smooth and flexible backing for surface mounting applications.

The use of a PDMS based material set allowed for the fabrication of a completely flexible and waterproof sensor array. By varying material properties through the introduction of PDMS foam, and electrical properties through the selection of dopant type and concentration, segments of the sensor array were designated as either active sensing channels or electrodes. Because PDMS is a cheap and readily available base material, the overall material cost of the sensor arrays was kept below $40, and little specialized safety equipment was necessary to handle the PDMS base material or carbon black dopant.

Array Design and Fabrication Technique

The CBPDMS foam sensor arrays utilized a four-point probe measurement technique to eliminate the imapct of contact resistance on the voltage measurements. As tested, the array was comprised of a 4 x 1 linear array of 5 mm wide sensor channels, with a spacing of 17 mm between sensing locations, as shown in Figure 4-1. The total array dimensions were 80 mm x 20 mm, and array thicknesses of 7.8 mm and 6.2 mm were tested.

The use of a PDMS based material set for sensor array fabrication eliminated much of the need for specialized fabrication techniques or equipment, and arrays were fabricated in a series of component steps, utilizing delrin molds to reduce unwanted adherence between the PDMS material and the mold walls. The sensor molds were designed to be modular, allowing for the thickness of the electrode/sensor active layer to be varied. The Soma Foama PDMS foam used to fabricate the active sensing

material was commercially available from Smooth-On, and the foaming reaction took place as soon as the A and B components were mixed. Carbon black particles were pre-mixed into part A using a mechanical mixer with the goal of equal distribution of the dopant throughout the polymer matrix. Despite having a lack of precise control over the distribution of conductive particles within the matrix, or the density and distribution of pores from the foaming reaction, the performance of the individual sensor channels was found to be more consistent than expected, as evidence by the application of the calibration curve for 7.8 mm thick channel 2 to 7.8mm thick channel 1 with less than 10% RMS error when measuring the pressure field from water waves, as discussed in Section 5.4.5, and shown in Table 5.14 and Figure 5-26.

8.2.3 Experimental Validation of CBPDMS Foam Sensor Arrays as a New Tool for Hydrodynamic Sensing

Prototype CBPDMS foam devices were experimentally evaluated against a set of characteristics, given in Section 5.1.1, that are necessary for the device to be considered a viable sensor. Experiments were performed on the array using a series of hydrodynamic stimuli ranging from time-varying hydrostatic pressure from oscillatory plunging, to biologically motivated flows such as Kármán vortex shedding, water waves, and a dipole source. The sensor arrays were characterized over a range of frequencies consistent with the fish lateral line, and a calibration between pressure stimulus and output voltage was developed. Finally, the viability of the device for use in measuring flows consistent with the unmanned marine vehicle applications presented in Table 2.1 was evaluated.

Repeatability

For a prototype device to be considered a viable sensor, it must show repeatability within an experiment, across multiple trials with the same stimulus, and across different stimuli. The repeatability of the CBPDMS foam arrays was demonstrated using the results from periodic plunging experiments as discussed in Section 5.3.3.

Plunging experiments demonstrated the pressure-voltage pairs from within an experiment, as well as from six independent experiments with varying amplitude, followed a consistent non-linear trend, as shown in Figure 5-12(a). It was found that with outliers removed, a third degree polynomial curve fit represented the experimental data trend with less than 11% normalized RMS error.

Repeatability across pressure stimuli was demonstrated by applying the calibration curves found from the plunging experiments to measurements of water wave pressure. Using the plunging calibration curves, the water wave pressure was reproduced with less than 17% normalized RMS error, as shown in Table 5.15.

Ability to Be Calibrated

The ability to convert voltage output measurements to physical measures of the stimulus of interest is fundamental to the viability of a sensor. In the case of the CBPDMS foam sensor arrays, calibration curves were developed for each sensor channel using the results from six independent plunging experiments where the stimulus was a time-varying hydrostatic pressure. Initial calibration was performed using polynomial curve fits, with cross-validation used to determine the optimal polynomial order. A third degree polynomial was found to represent the experimental data well, and outliers were removed to further refine the calibration curves. With outliers removed, the third degree polynomial fits were found to have normalized RMS error less than 11%, and R^2 values greater than 0.85. A first order correction was added for low pressures to eliminate the non-physical behavior of the third degree polynomial at the ends of the training data set, creating a piecewise polynomial calibration for the arrays. The calibration curves for each sensor channel can be found in Tables 5.8 and 5.10 for the 7.8 mm and 6.2 mm thick arrays respectively.

Calibration curves were initially evaluated using time-series results from the plunging experiments at 10 mm, 20 mm, and 30 mm peak-to-peak amplitudes. For both the thick and thin arrays, the time-series pressure measurements were reproduced with less than 16% normalized RMS error, as seen in Tables 5.9 and 5.11. Calibration curves were further evaluated by applying the calibration to measurements of

water wave stimulus. With the DC voltage offset adjusted for consistency with the plunging experiments, and output voltage scaled for the supply current, the periodic water wave pressure was reproduced with less than 17 % normalized RMS error for all four channels of the 7.8 mm thick array, as seen in Table 5.15. Results from both the plunging and water wave experiments demonstrated conclusively that the CBPDMS foam sensor array was able to be calibrated, and that the calibration was applicable to multiple types of stimulus.

Ability to Measure Flows Useful for Ocean Engineering Applications

For use as a hydrodynamic pressure sensor, the CBPDMS foam array needed to be capable of measuring flows useful for ocean engineering applications. For this study, the primary application of interest was flow sensing on unmanned marine vehicles with length ~1-3 m, and example unsteady flows of interest were given in Table 2.1. From the guidelines outlined in Section 3.1 for hydrodynamic sensor development, dynamic pressure stimuli consistent with unmanned vehicles on this scale range from ~10-400 Pa with ~10 Pa sensitivity, and frequency from 0.25-3 Hz. The fulfillment of these dynamic pressure range and frequency guidelines was demonstrated through a series of experiments with a variety of hydrodynamic pressure stimuli.

During the plunging experiments with a vertically mounted linear stage, the peak-to-peak amplitude of the time-varying hydrostatic pressure was varied from 100-300 Pa, and the nominal frequency of the stage was 0.5 Hz. By studying the pressure-voltage pairs from all six independent plunging experiments, the pressure measured by the CBPDMS foam array was found to cover a range of ~50-500 Pa, and the sensitivity of the array was found to be ~5 Pa. Similarly, during the water wave experiments, the peak-to-peak pressure amplitude was ~75 Pa and the wave frequency was 1 Hz. Based on the plunging and wave experiments with periodic pressure stimuli, the dynamic range of the sensor arrays was approximately 50-500 Pa with a sensitivity of approximately 5 Pa. Additional experiments using a dipole source and the wake behind a circular cylinder were used to investigate the performance of the CBPDMS foam array in response to pressure stimuli with magnitude less than 50 Pa.

In nature the fish lateral line is used for detecting both low frequency near-field flows such as vortex shedding and water gravity waves, and high frequency flows such as the vibrations from an insect trapped on the water's surface. The upper frequency range of the CBPDMS foam sensor arrays was investigated using a vibrating sphere as a dipole source. From the dipole experiments, the CBPDMS foam sensor array was found to be sensitive to periodic pressure signals up to a maximum tested value of 35 Hz. For successful identification of the sphere vibration frequency, it was found that the RMS pressure had to exceed a cutoff value of ~3-5 Pa, consistent with the minimum sensitivity predicted from the plunging experiments.

In addition to the low-frequency experiments using time-varying hydrostatic pressure and water waves, the ability of the CBPDMS foam sensor array to detect the frequency of Kármán vortex shedding was studied. It was found that the ability of the CBPDMS foam array to detect periodic vortex shedding in the wake of a circular cylinder was highly dependent on the magnitude of the pressure signals generated by the shed vortices. For towing speeds of 0.1 and 0.15 m/s, the RMS pressure value was measured with commercial sensors as 1.11 and 2.50 Pa respectively, and the CBDPMS foam array was unsuccessful at clearly identifying the vortex shedding frequency due to low signal to noise ratio. For towing speeds of 0.2 and 0.3 m/s, the RMS pressure was found to be 3.45 and 6.93 Pa, and the CBPDMS foam array identified the vortex shedding frequencies within 3% of the value measured using commercial pressure sensors and the foil lift force, as given in Tables 7.5 and 7.6. For the experiments with towing speeds of 0.2 and 0.3 m/s, the percent difference between the RMS pressure measured using the MPXV series commercial sensors and the CBPDMS foam array was 18% and 28% respectively, which can be partially attributed to expected variations in pressure along the foil span due to the 3D instability of Kármán vortex shedding. The time-series results from the Kármán vortex experiments demonstrated the ability of the array to measure RMS pressure in the 3-5 Pa range, near the lower limit of the array as identified during plunging and dipole experiments. The results of the Kármán vortex street identification experiments further confirmed the resolution of the CBPDMS foam sensor array as ~5 Pa, and the frequency range as ~0.5-35 Hz.

While the experiments with water waves, the dipole source, and in the wake of a circular cylinder demonstrated the ability of the sensor array to measure a variety of hydrodynamic stimulus relevant to both biology and engineering applications, the stimuli were confined to laboratory scale flows due to the dynamic range of the sensor array. By using a low Young's modulus CBPDMS foam as the active sensing material in the array, the sensitivity of the piezoresistive material was increased compared to solid CBPDMS, but the dynamic range of the array was reduced. Above a hydrostatic pressure of ~500 Pa, the array was found to reach saturation, and the sensitivity of the array decreased. This saturation may be caused by the composite reaching a point where due to compression, the majority of conductive pathways have been formed from the available carbon black particles, and additional changes in resistance are minor. Alternatively, a change in the mechanical properties of the PDMS foam matrix material may occur as the interior cells collapse and the material reacts in a similar manner to a solid. The investigation of array saturation and the optimization of dynamic range is a rich path for future work.

Robustness and Cost

For use in real-world ocean engineering applications, CBPDMS foam sensor arrays must be robust enough for prolonged exposure to fluids and able to withstand repeated handling and potential impacts. The CBPDMS foam sensor arrays discussed in this study were used in hundreds of experiments over six different experimental setups, in five different tanks, and in two countries. The sensors were surface mounted on both flat and curved surfaces using double sided tape and silicone adhesive. Throughout the experiments, the sensor arrays were the most robust component of the experimental setup, with failures occurring in connectors, amplifiers, batteries, and software. To specifically test the robustness of the 7.8 mm thick CBPDMS foam array, the array was left submerged in the small towing tank at MIT for over 24 hours. Following this submergence test, the array was used for a full series of Kármán vortex street identification experiments and was found to operate normally.

To bring distributed pressure sensing with high spatial resolution to full-scale

ocean engineering systems, pressure sensors must be low cost. The cost of current commercially available sensors was strongly illustrated by the unmanned kayak vehicle which was equipped with an array of 20 Honeywell SPT series sensors at a total cost of ~$5000 or ~$250 per sensor. Despite this large investment in sensors, only a fraction of the kayak's hull was instrumented, leaving large portions of the near-body flow field unmeasured. The CBPDMS foam sensor arrays were fabricated using approximately ~$40 worth of materials for a 4x1 array, or ~$10 per sensor. With some modifications to the sensor electronics and data acquisition technique, the array could be converted to a 7x1 array, reducing the cost per sensor to ~$6. The largest contributor to the material cost was the silver used in the fabrication of the sensor array electrodes. With a modification to the materials used in the electrodes, the sensor cost could be reduced further, representing a greater benefit over commercially available sensors for large-area distributed applications.

8.3 Recommendations for Future Work

8.3.1 Reduction in Sensor Thickness

At present, the CBDPMS foam sensor arrays are too thick for use in surface mounting applications, as evidenced by the 7.8 mm thick sensor's protrusion from the hydofoil surface during Kármán vortex street identification experiments, as discussed in Section 7.5. While the 6.2 mm thick sensor array offered similar performance to the thick sensor, the imapct of sensor thickness on array performance has not been studied thoroughly. In particular, the impact of thickness on the sensor array's dynamic range is of great interest. For use in future hydrodynamic sensing applications, the thickness of the array must be reduced so as to not disturb the flow field.

8.3.2 Improved Control of Dopant and Pore Distribution

The use of a commercially available foaming platinum silicone enabled the fabrication of CBPDMS foam sensor arrays with very little specialized equipment and at low

cost. The downside of using a foaming silicone was little control over the size and distribution of pores within the PDMS bulk material, which led to poor control over material properties between sensor channels. Additionally, the distribution of carbon black particles within the composite was not well controlled. Efforts were made to ensure equal distribution by mixing the CB particles into Part A of the foaming silicone using a Mazerustar mechanical mixer, but the sensor channels were found to have varying initial resistance values and required individual calibration curves. If sensor arrays are to be scaled up to real-world applications, and the number of sensing channels greatly increased, the ability to use a single calibration for the entire array would be a great benefit. To ensure consistent performance between sensor channels, the sensor fabrication method needs to be improved to better control the pore size and pore and dopant distribution. If such a method were developed, the impact of pore size on sensitivity and dynamic range could be studied, allowing for the pressure sensitive foam to be optimized for different applications. Additionally, if fine control of pore size and distribution was available, an array could be developed with variable material properties to accommodate a variety of dynamic range and sensitivity combinations.

8.3.3 Modified Electrode Dopant for Cost Reduction

As discussed previously, the largest contributor to the cost of the CBPDMS foam sensor arrays was the silver used in the fabrication of the array electrodes. Substituting a less expensive conductive dopant for silver would reduce the material cost of the arrays and increase the viability of scaling to real-world applications. The use of nickel in the array electrodes is of particular interest, and a study of additional material options would be valuable.

8.3.4 Two-dimensional Sensor Arrays

In some areas along a fish's body, the lateral line is highly two-dimensional, especially near the head. The density and two-dimensionality of the lateral line in this

region indicates that fluid structures near the leading edge of the fish are of particular interest, and that measurements in two-dimensions are important for mediating certain behaviors. Extending the CBPDMS foam sensor array to two-dimensions in regions of particular interest would allow for better characterization of near-body fluid structures. Creating a two-dimensional array while maintaining a four-point probe measurement presents a challenge in both sensor layout and fabrication technique. To achieve the goal of full coverage of a marine vehicle hull with a network of distributes pressure sensors, extending the current array technology to two dimensions is essential.

8.3.5 CBPDMS foam array validation outside of laboratory

The final recommendation for the CBPDMS foam arrays is to validate the utility of the arrays outside of the laboratory environment through a series of experiments on actual marine vehicles. The transition from laboratory experiments to real world applications introduces an array of unknowns that provide the ultimate test of a sensor array's viability. Real-world experiments were used to validate the experimental sensor arrays in the unmanned kayak experiments, and a similar series of experiments is recommended for the CBPDMS foam arrays.

Appendix A

Thick CBPDMS Array (7.8 mm) Plunging Data

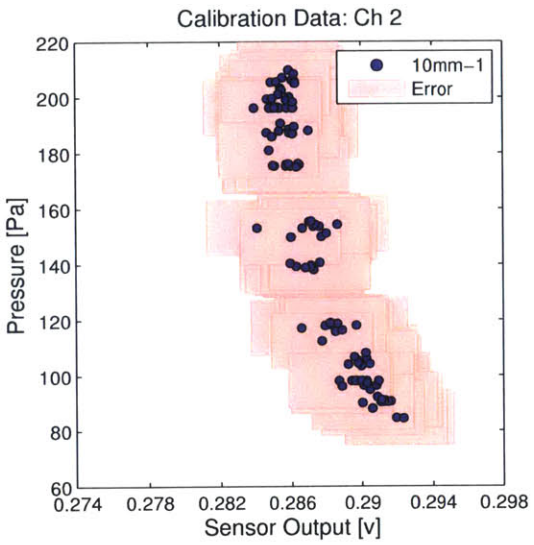

(a) Plunging results for 10mm peak-to-peak amplitude run 1 channel 2.

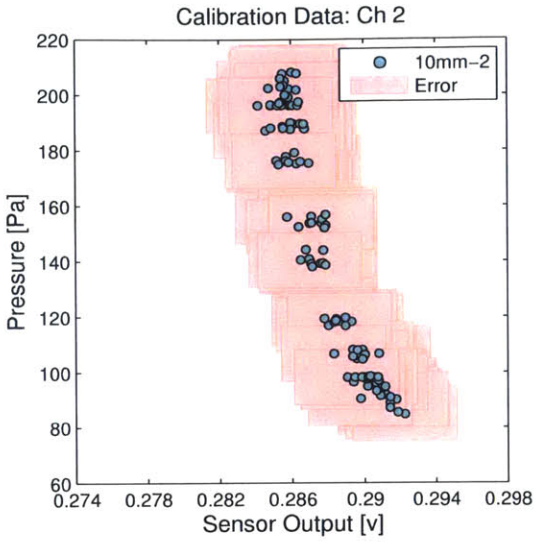

(b) Plunging results for 10mm peak-to-peak amplitude run 2 channel 2.

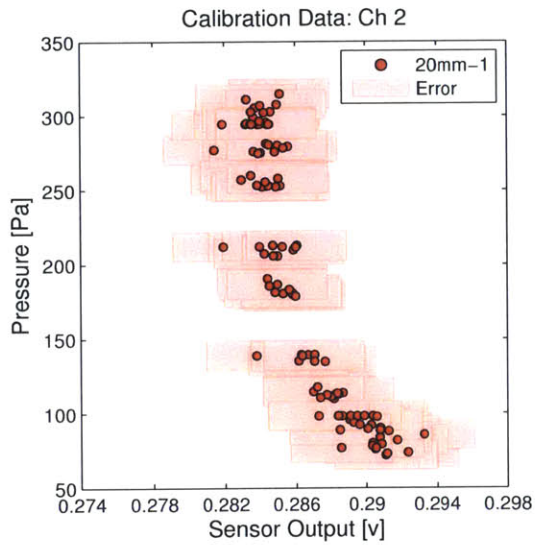

(c) Plunging results for 20mm peak-to-peak amplitude run 1 channel 2.

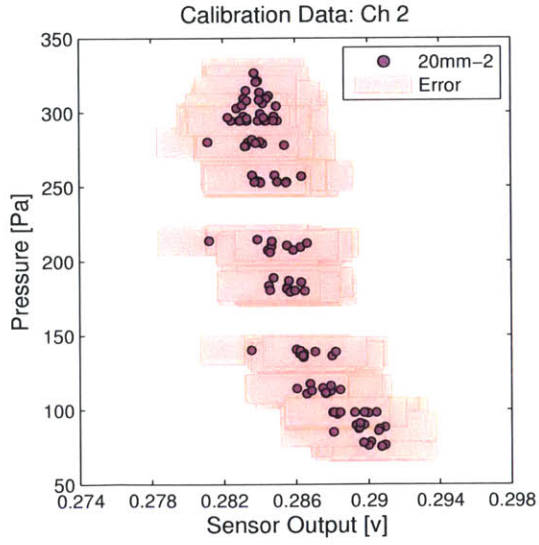

(d) Plunging results for 20mm peak-to-peak amplitude run 2 channel 2.

Figure A-1: Plunging data for 7.8 mm thick array channel 2. Boxes designate the experimental error in pressure and voltage.

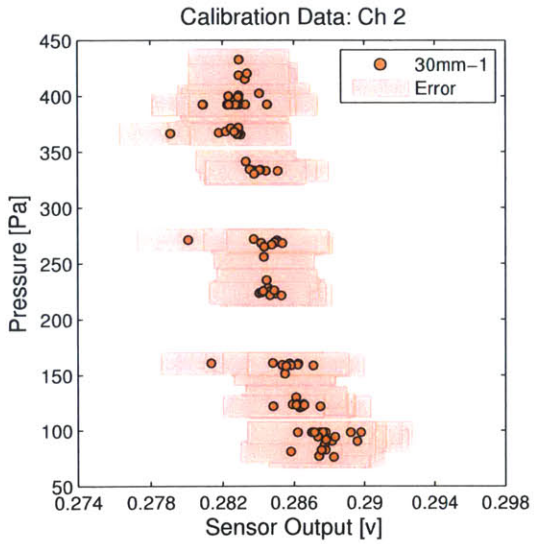

(a) Plunging results for 30mm peak-to-peak amplitude run 1 channel 2.

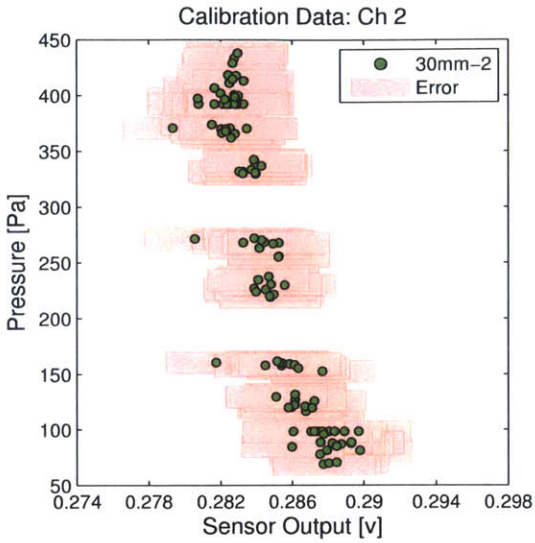

(b) Plunging results for 30mm peak-to-peak amplitude run 2 channel 2.

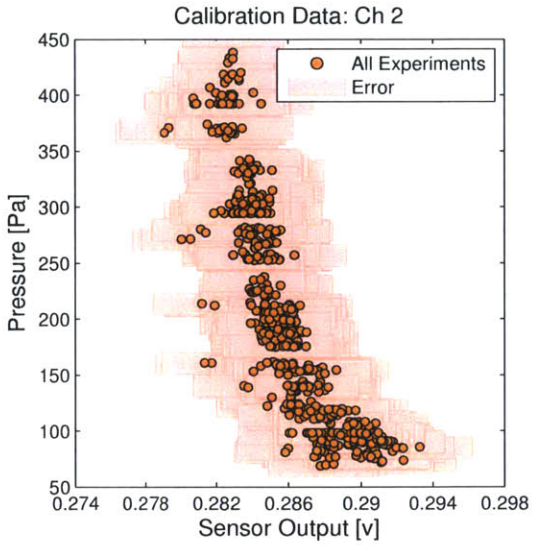

(c) Plunging results for all experiments channel 2.

Figure A-2: Plunging data for 7.8 mm thick array channel 2. Boxes designate the experimental error in pressure and voltage.

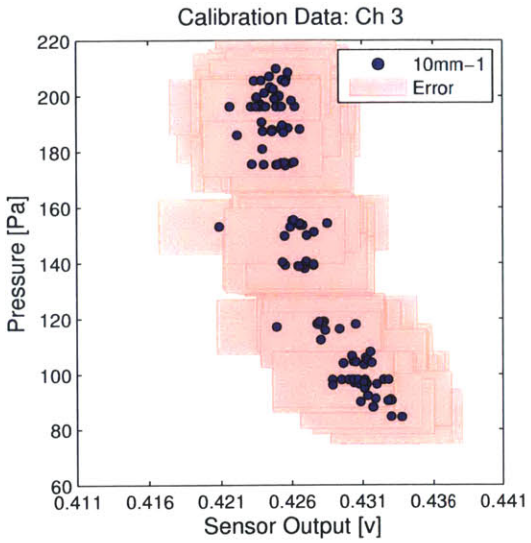

(a) Plunging results for 10mm peak-to-peak amplitude run 1 channel 3.

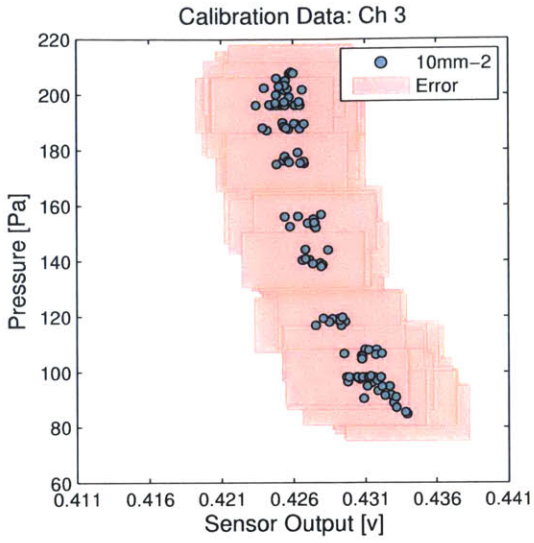

(b) Plunging results for 10mm peak-to-peak amplitude run 2 channel 3.

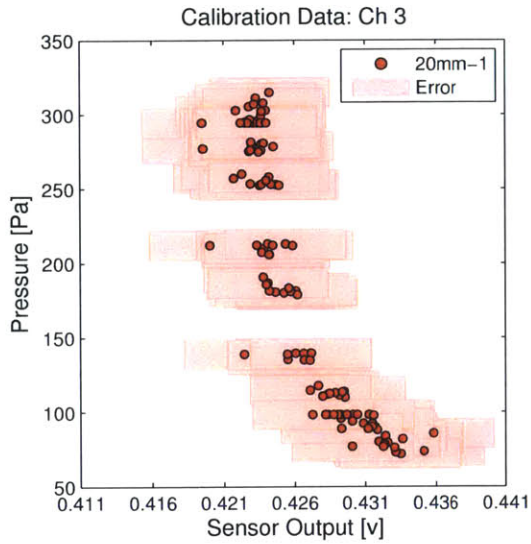

(c) Plunging results for 20mm peak-to-peak amplitude run 1 channel 3.

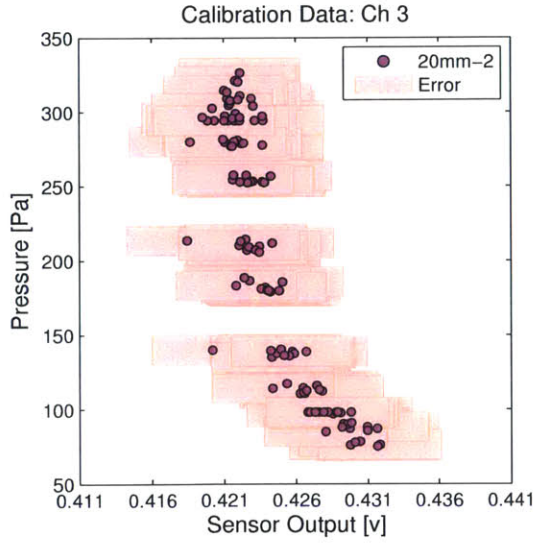

(d) Plunging results for 20mm peak-to-peak amplitude run 2 channel 3.

Figure A-3: Plunging data for 7.8 mm thick array channel 3. Boxes designate the experimental error in pressure and voltage.

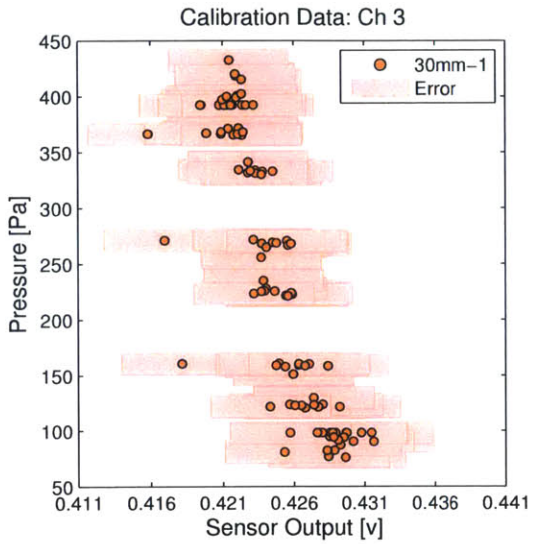

(a) Plunging results for 30mm peak-to-peak amplitude run 1 channel 3.

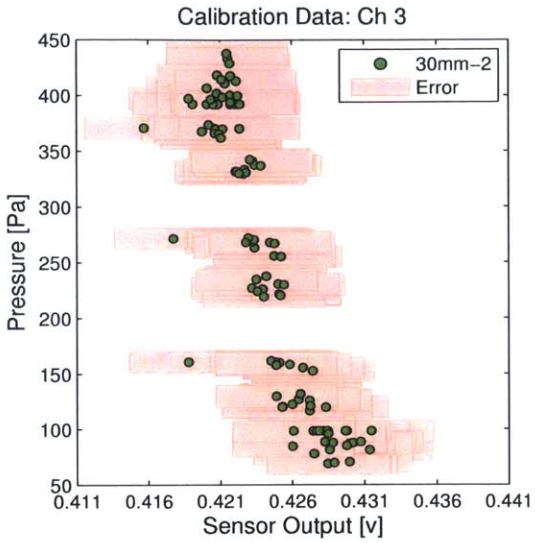

(b) Plunging results for 30mm peak-to-peak amplitude run 2 channel 3.

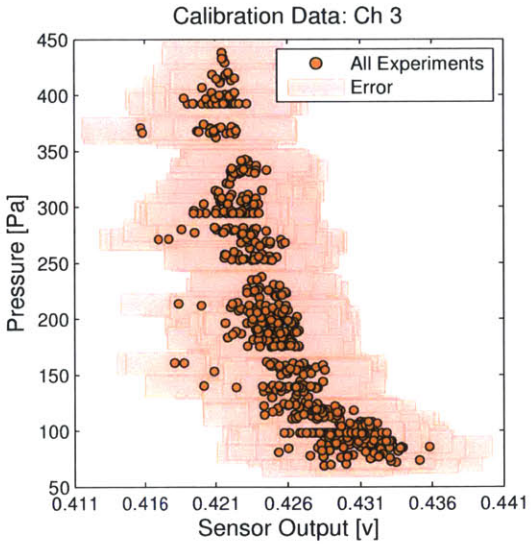

(c) Plunging results for all experiments channel 3.

Figure A-4: Plunging data for 7.8 mm thick array channel 3. Boxes designate the experimental error in pressure and voltage.

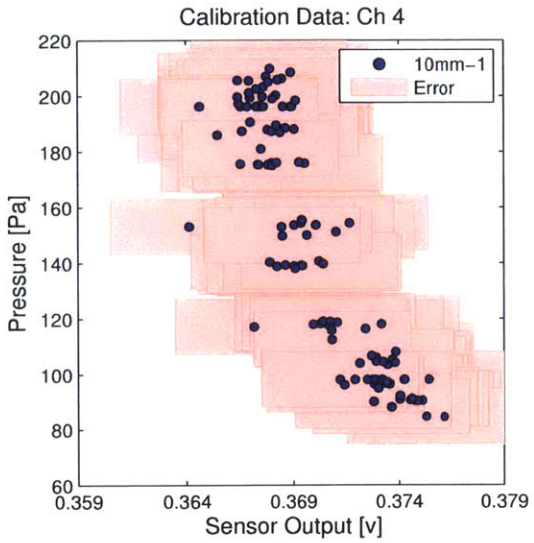

(a) Plunging results for 10mm peak-to-peak amplitude run 1 channel 4.

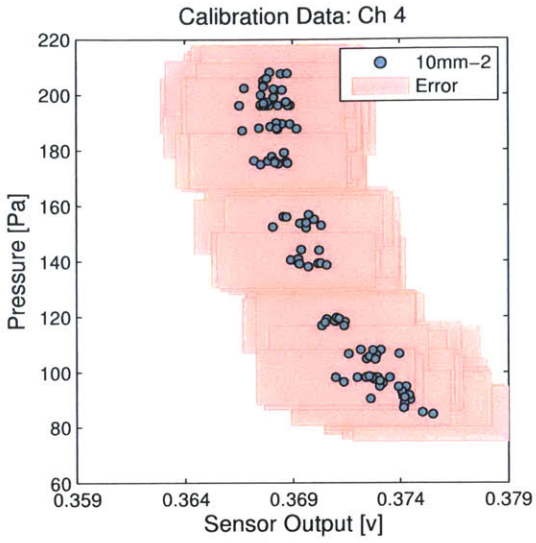

(b) Plunging results for 10mm peak-to-peak amplitude run 2 channel 4.

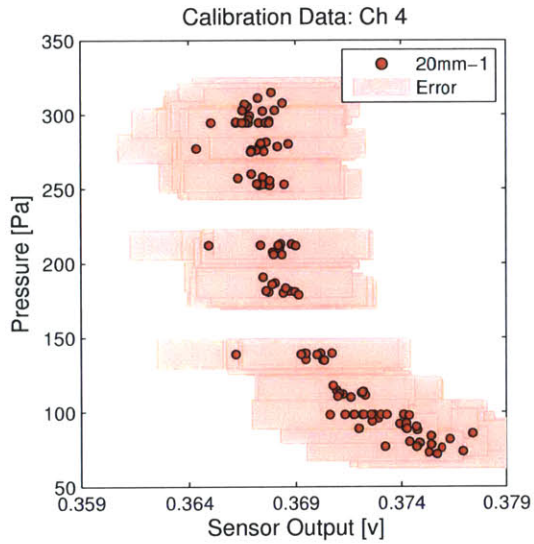

(c) Plunging results for 20mm peak-to-peak amplitude run 1 channel 4.

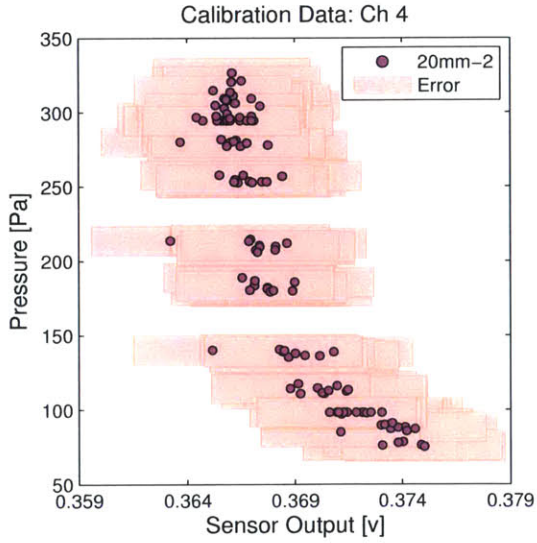

(d) Plunging results for 20mm peak-to-peak amplitude run 2 channel 4.

Figure A-5: Plunging data for 7.8 mm thick array channel 4. Boxes designate the experimental error in pressure and voltage.

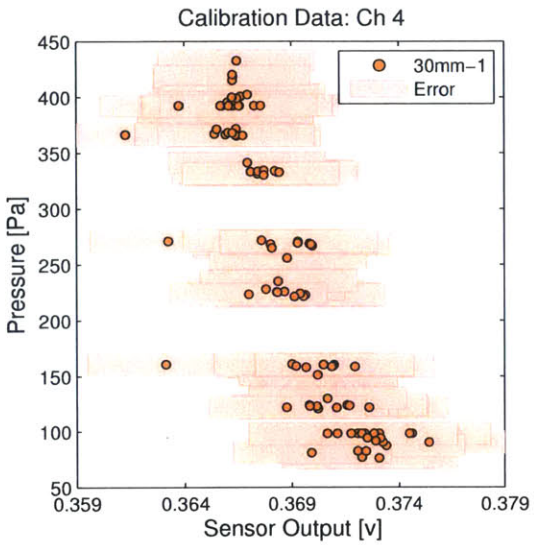

(a) Plunging results for 30mm peak-to-peak amplitude run 1 channel 4.

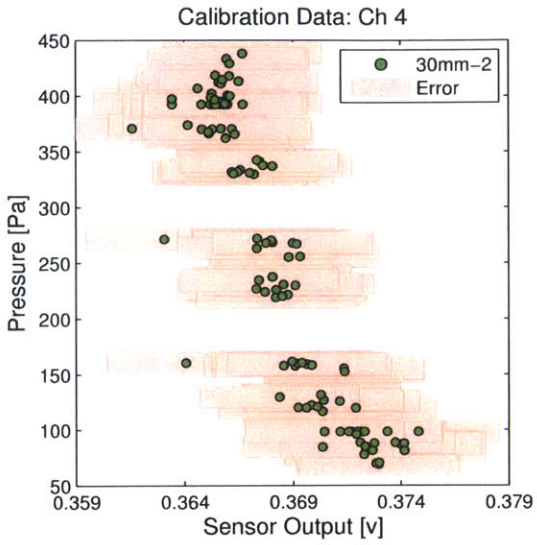

(b) Plunging results for 30mm peak-to-peak amplitude run 2 channel 4.

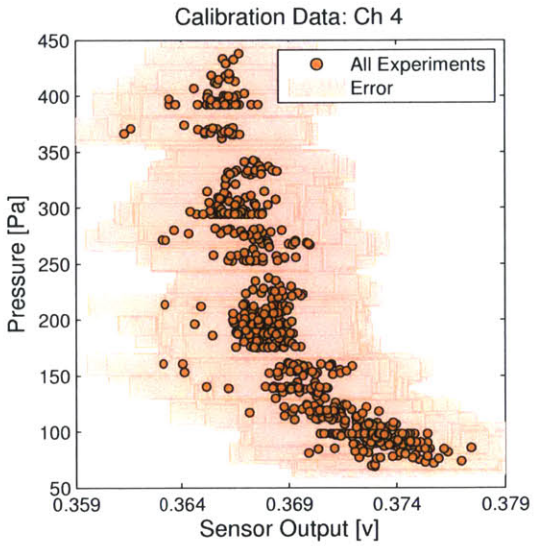

(c) Plunging results for all experiments channel 4.

Figure A-6: Plunging data for 7.8 mm thick array channel 4. Boxes designate the experimental error in pressure and voltage.

Appendix B

Thin CBPDMS Array (6.2 mm) Plunging Data

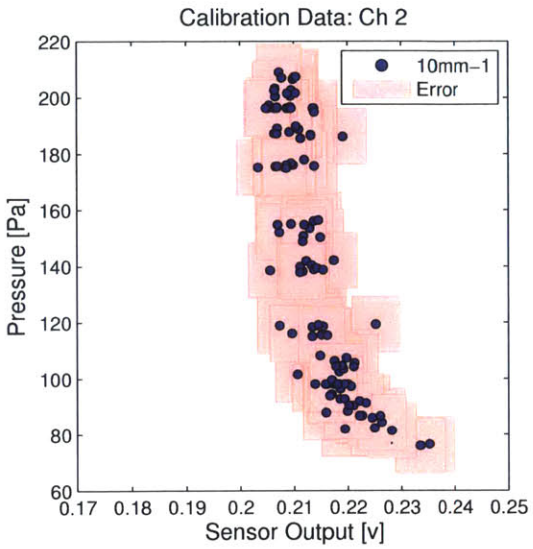

(a) Plunging results for 10mm peak-to-peak amplitude run 1 channel 2.

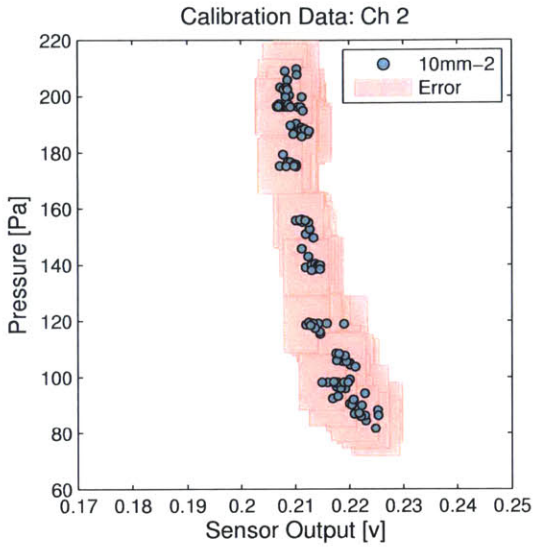

(b) Plunging results for 10mm peak-to-peak amplitude run 2 channel 2.

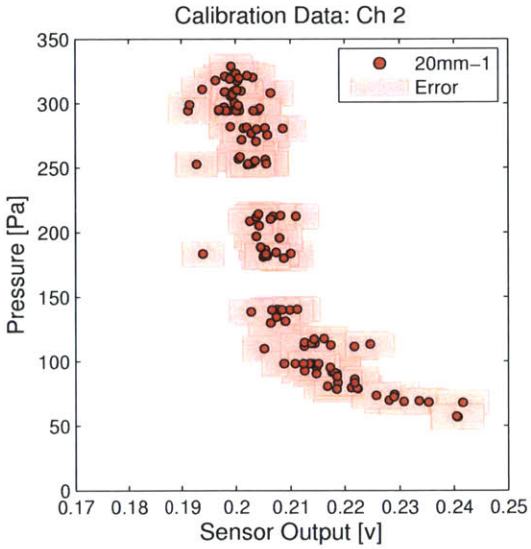

(c) Plunging results for 20mm peak-to-peak amplitude run 1 channel 2.

Figure B-1: Plunging data for 6.2 mm thick array channel 2. Boxes designate the experimental error in pressure and voltage.

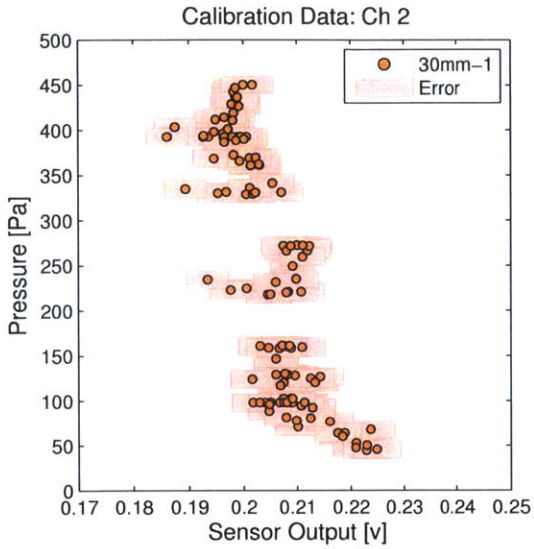

(a) Plunging results for 30mm peak-to-peak amplitude run 1 channel 2.

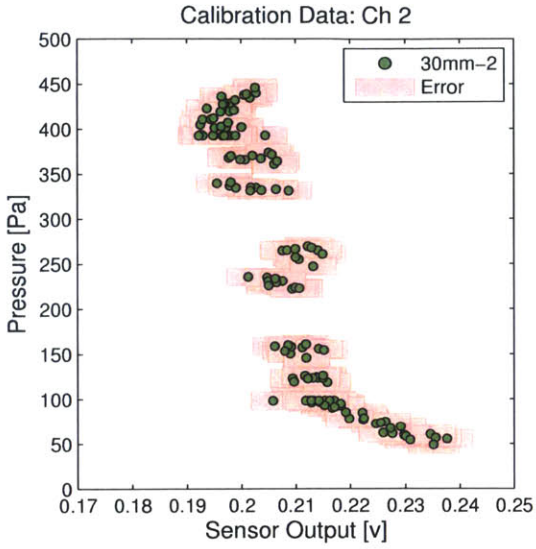

(b) Plunging results for 30mm peak-to-peak amplitude run 2 channel 2.

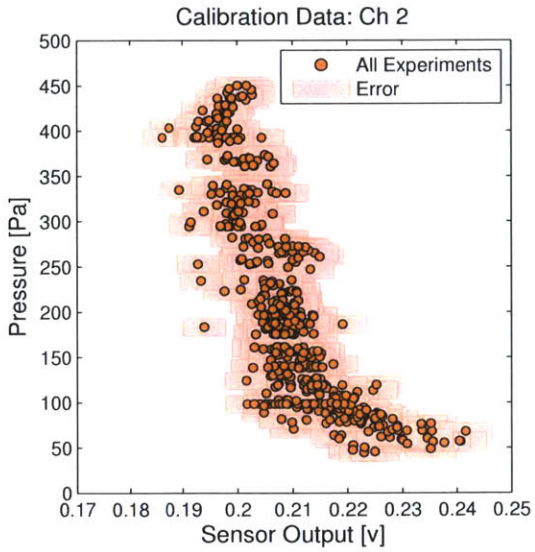

(c) Plunging results for all experiments channel 2.

Figure B-2: Plunging data for 6.2 mm thick array channel 2. Boxes designate the experimental error in pressure and voltage.

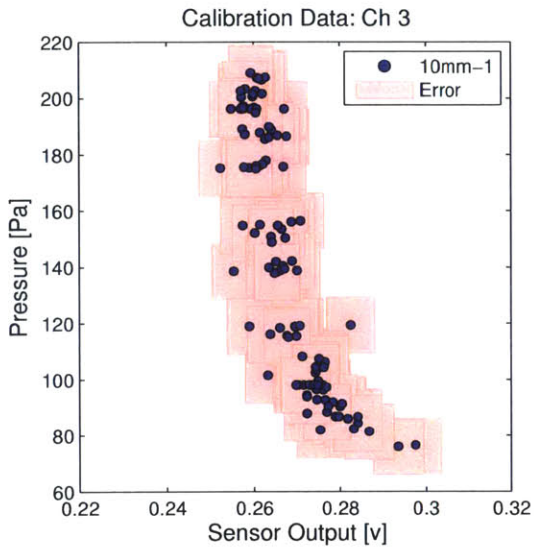

(a) Plunging results for 10mm peak-to-peak amplitude run 1 channel 3.

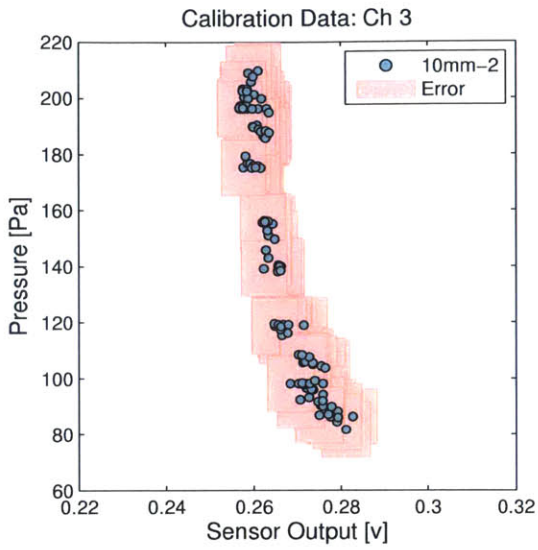

(b) Plunging results for 10mm peak-to-peak amplitude run 2 channel 3.

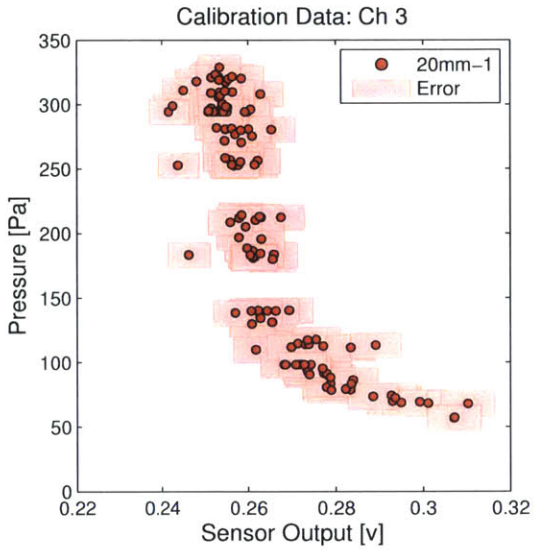

(c) Plunging results for 20mm peak-to-peak amplitude run 1 channel 3.

Figure B-3: Plunging data for 6.2 mm thick array channel 3. Boxes designate the experimental error in pressure and voltage.

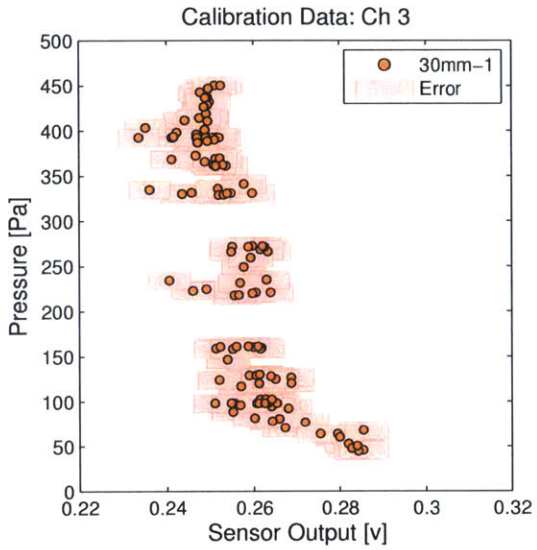

(a) Plunging results for 30mm peak-to-peak amplitude run 1 channel 3.

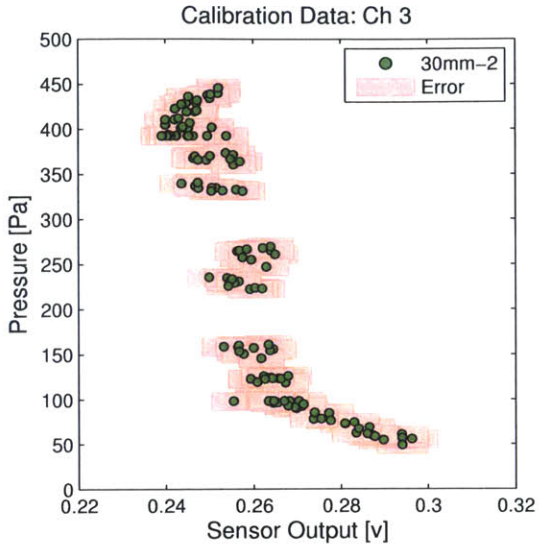

(b) Plunging results for 30mm peak-to-peak amplitude run 2 channel 3.

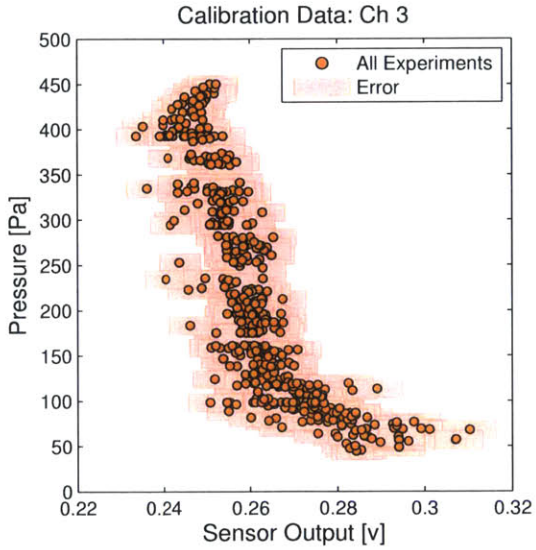

(c) Plunging results for all experiments channel 3.

Figure B-4: Plunging data for 6.2 mm thick array channel 3. Boxes designate the experimental error in pressure and voltage.

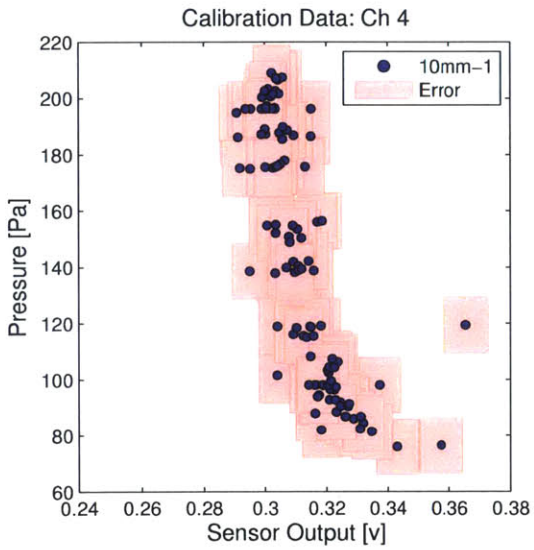

(a) Plunging results for 10mm peak-to-peak amplitude run 1 channel 4.

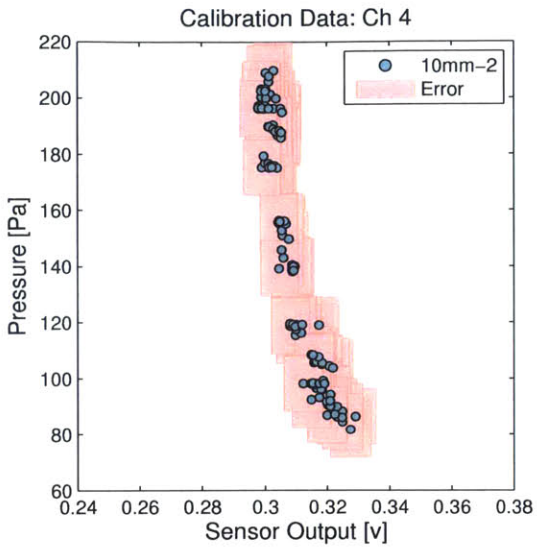

(b) Plunging results for 10mm peak-to-peak amplitude run 2 channel 4.

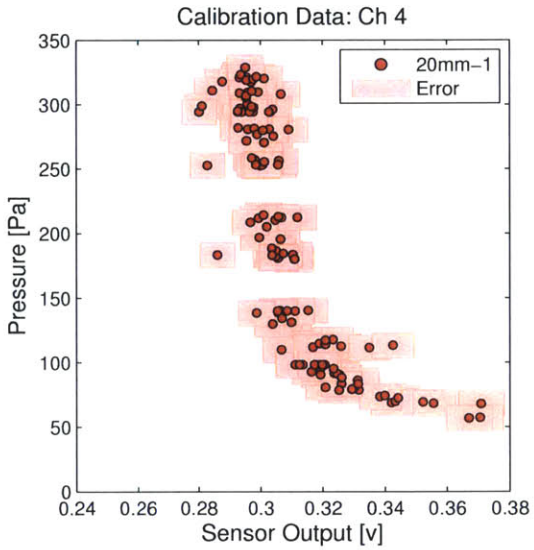

(c) Plunging results for 20mm peak-to-peak amplitude run 1 channel 4.

Figure B-5: Plunging data for 6.2 mm thick array channel 4. Boxes designate the experimental error in pressure and voltage.

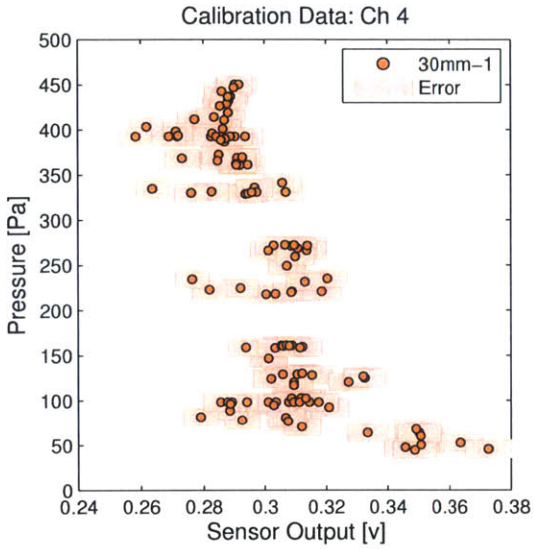

(a) Plunging results for 30mm peak-to-peak amplitude run 1 channel 4.

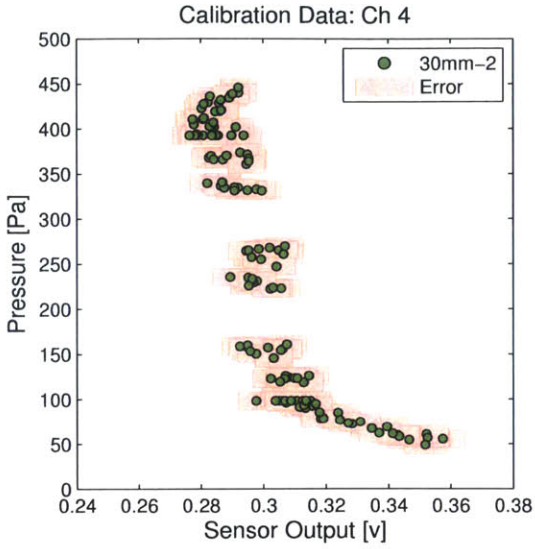

(b) Plunging results for 30mm peak-to-peak amplitude run 2 channel 4.

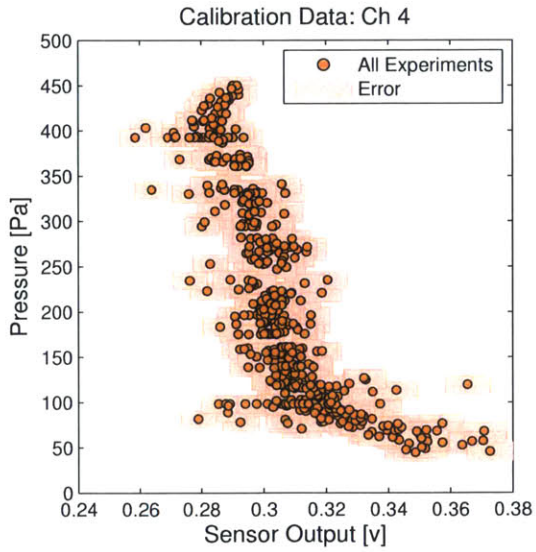

(c) Plunging results for all experiments channel 4.

Figure B-6: Plunging data for 6.2 mm thick array channel 4. Boxes designate the experimental error in pressure and voltage.

Appendix C

Thin CBPDMS Array (6.2 mm) Calibration Plots

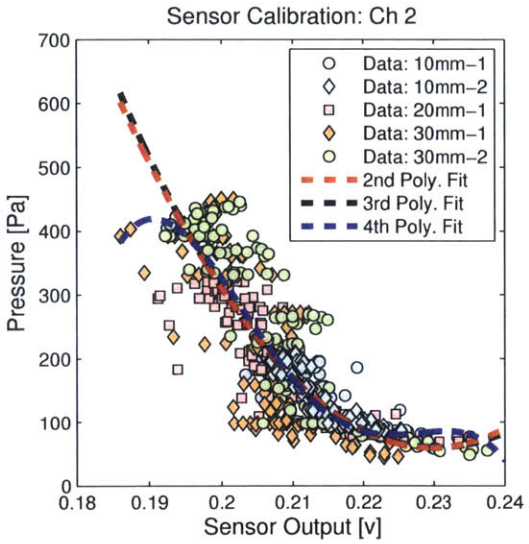

(a) Polynomial curve fits for Channel 2

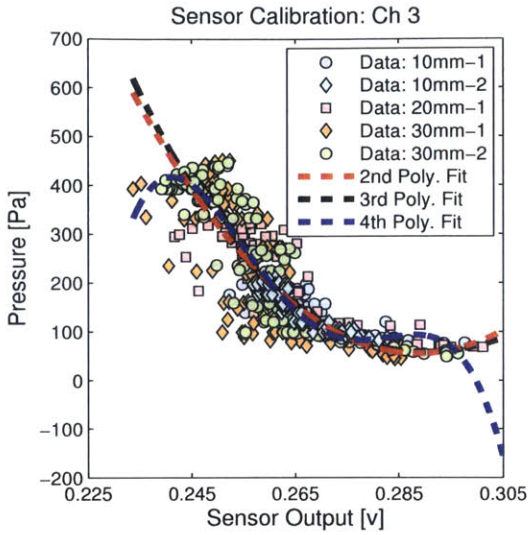

(b) Polynomial curve fits for Channel 3

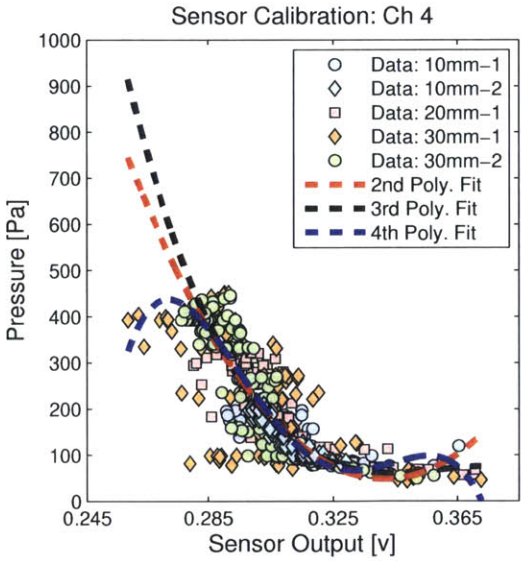

(c) Polynomial curve fits for Channel 4

Figure C-1:]
Second, third, and fourth order polynomial curve fits were found for the plunging experiments results from the 6.2 mm thick (Thin) CBPDMS foam sensor array.

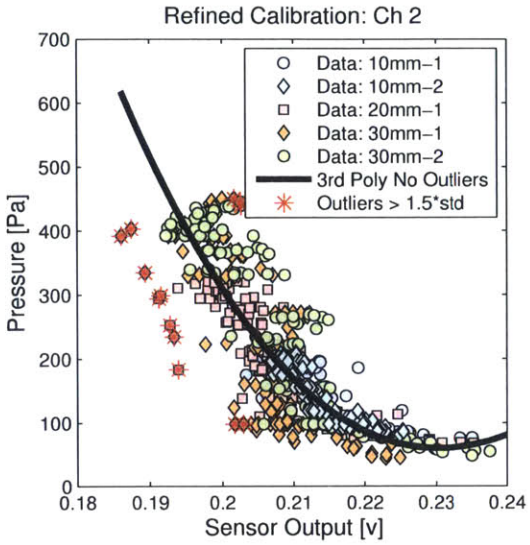

(a) Outliers and refined third order polynomial fit for channel 2.

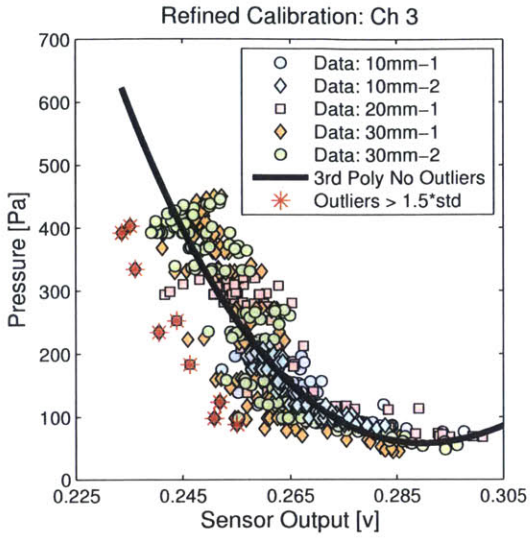

(b) Outliers and refined third order polynomial fit for channel 3.

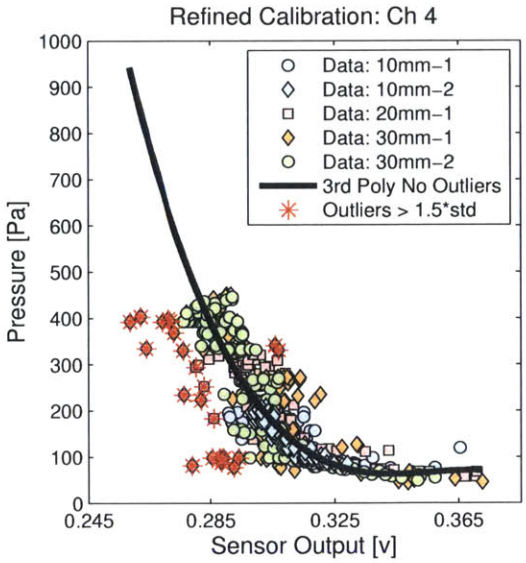

(c) Outliers and refined third order polynomial fit for channel 4.

Figure C-2: Outliers were designated as samples falling further than 1.5 standard deviations away from the third degree polynomial fits shown in Figure C-1. A refined third degree polynomial fit was found for each sensor channel of the 6.2 mm thick (Thin) array with the outliers excluded.

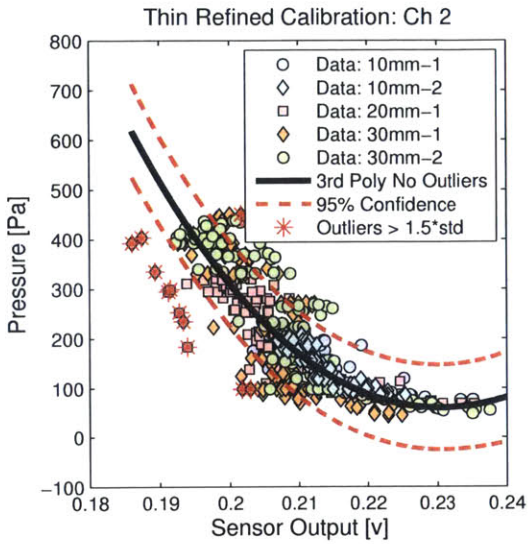

(a) Refined third degree polynomial fit for channel 2 with 95% confidence bounds.

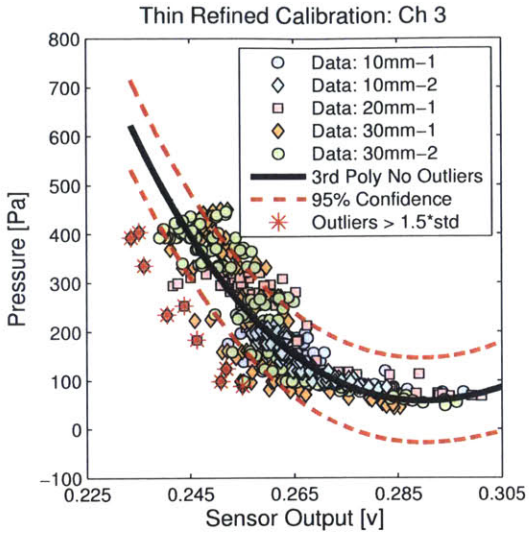

(b) Refined third degree polynomial fit for channel 3 with 95% confidence bounds.

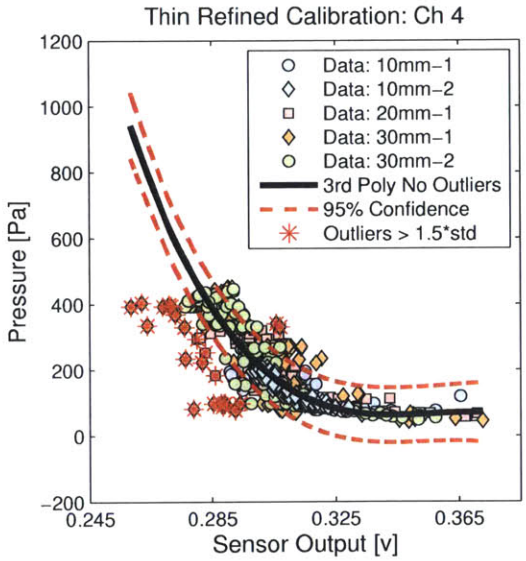

(c) Refined third degree polynomial fit for channel 4 with 95% confidence bounds.

Figure C-3: Polynomial fits for the 6.2 mm thick (Thin) CBDPMS foam sensor array refined through the removal of outliers.

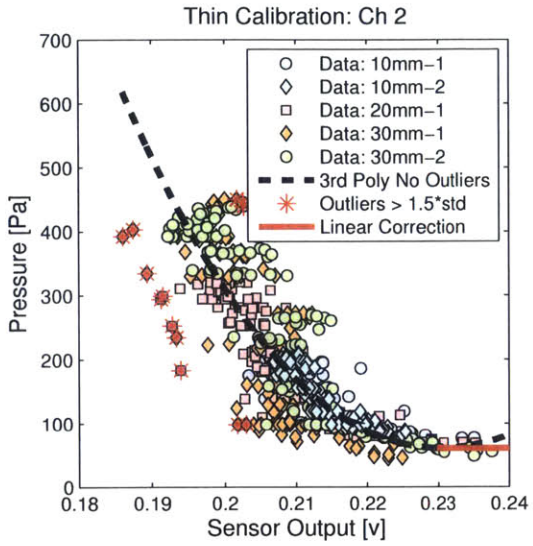

(a) Piecewise polynomial calibration for 6.2 mm thick CBPDMS foam array Channel 2.

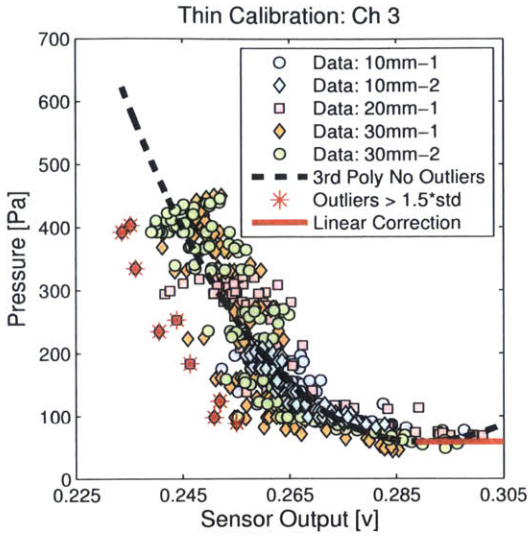

(b) Piecewise polynomial calibration for 6.2 mm thick CBPDMS foam array Channel 3.

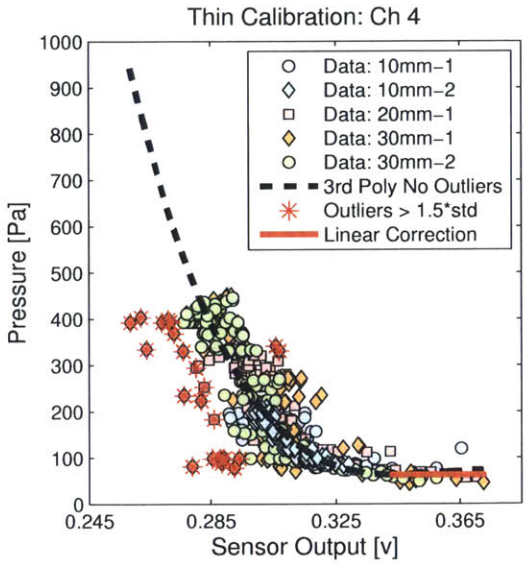

(c) Piecewise polynomial calibration for 6.2 mm thick CBPDMS foam array Channel 4.

Figure C-4: Piecewise polynomial calibrations for the 6.2 mm (Thin) CBPDMS foam sensor array.

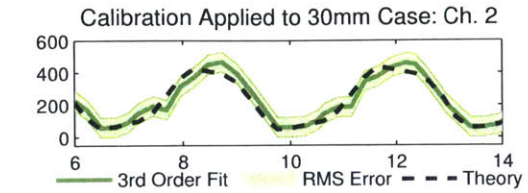

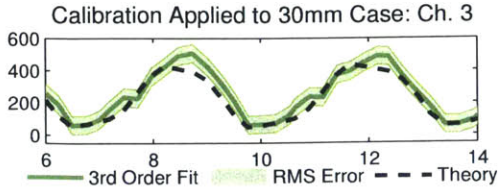

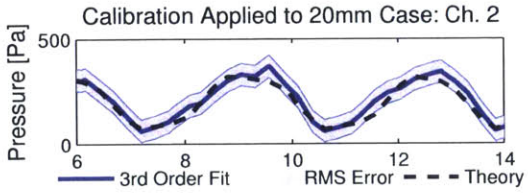

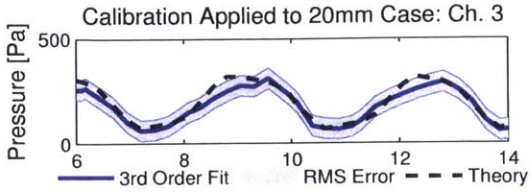

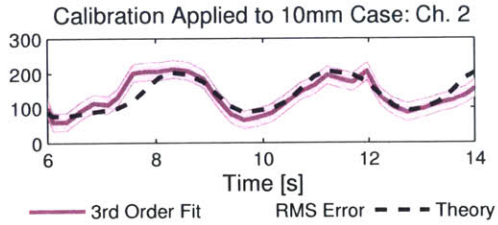

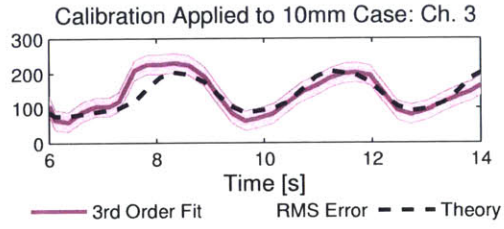

(a) Channel 2 polynomial calibration applied to plunging time series data.

(b) Channel 3 polynomial calibration applied to plunging time series data.

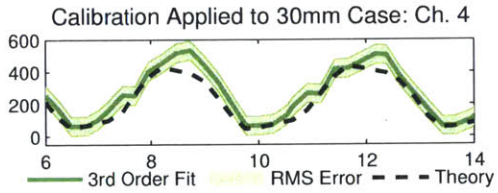

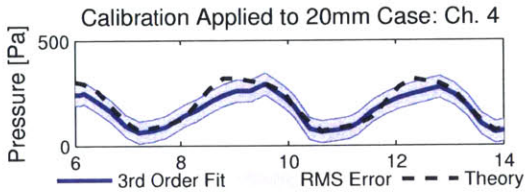

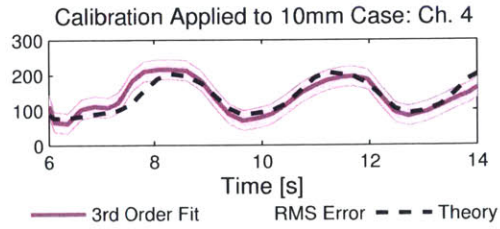

(c) Channel 4 polynomial calibration applied to plunging time series data.

Figure C-5: The refined third degree polynomial calibration for the 6.2mm thick (Thin) sensor array was applied to time series data from plunging experiments.

Appendix D

Commercial Sensor Calibrations

Axis							Max
Fx	-0.02084	0.00709	0.16508	-3.60303	-0.06136	3.73227	30 lbf
Fy	-0.07221	4.22837	0.10019	-2.08236	0.03623	-2.16487	30 lbf
Fz	6.60827	-0.33435	6.66040	-0.32223	6.53237	-0.28294	100 lbf
Tx	-0.03912	2.01414	-7.50994	-0.61275	7.40439	-1.37069	100 lbf-in
Ty	8.73372	-0.43266	-4.41910	1.91123	-4.23543	-1.60265	100 lbf-in
Tz	0.08075	-4.51588	0.14203	-4.43269	0.12753	-4.56767	100 lbf-in

Table D.1: Gamma force transducer calibration

Channel	C1	C0
1	3901.4	-9511.6
2	2529.4	-613.4
3	2455.3	-586.0
4	2697.6	-953.8

Table D.2: MPXV pressure sensor calibration of form P=C1*x+C0.

Bibliography

[1] O Akanyeti, J C Brown, L D Chambers, H el Daou, M C Fiazza, P Fiorini, J Jezov, D S Jung, M Kruusmaa, M Listak, A Liszewski, J L Maud, W M Megill, L Rossi, A Qualtieri, F Rizzi, T Salumae, G Toming, R Venturelli, F Visentin, and M De Vittorio. Filose for svenning: A flow sensing bioinspired robot. *IEEE Robotics and Automation Magazine*, September:51–62, 2014.

[2] D M Anderson. Approaches to monitoring, control and management of harmful algal blooms (habs). *Ocean & Coastal Management*, 52(7):342–347, Jul 2009.

[3] M Asadnia, A G P Kottapalli, J M Miao, and M S Triantafyllou. Ultra-sensitive and stretchable strain sensor based on piezoelectric polymeric nanofibers. *Proceedings of MEMS 2015*, pages 678–681, Nov 2015.

[4] M Asadnia, A G P Kottapalli, Z Shen, J M Miao, and M S Triantafyllou. Flexible and surface-mountable piezoelectric sensor arrays for underwater sensing in marine vehicles. *IEEE Sensors Journal*, 13(10):3918–3925, Aug 2013.

[5] D T Beruto, M Capurro, and G Marro. Piezoresistance behavior of silicone–graphite composites in the proximity of the electric percolation threshold. *Sensors and Actuators A*, 117:301–308, Sep 2005.

[6] H Bleckmann. Reaction time and stimulus frequency in prey localization in the surface-feeding fish aplocheilus lineatus. *Journal of Comparative Physiology*, 140:163–172, Oct 1980.

[7] H Bleckmann, A Klein, and G Meyer. Nature as a model for technical sensors. *Frontiers in Sensing*, pages 1–16, Sep 2012.

[8] H Bleckmann and G Topp. Surface wave sensitivity of the lateral line organs of the topminnow aplocheilus lineatus. *Naturwissenschaften*, 68:624–625, Aug 1981.

[9] J J Boland. Flexible electronics: Within touch of artificial skin. *Nature Materials*, pages 1–2, Sep 2010.

[10] K J Cha and D S Kim. A portable pressure pump for microfluidic lab-on-a-chip systems using a porous polydimethylsiloxane (pdms) sponge. *Biomed Microdevices*, 13(5):877–883, Oct 2011.

[11] L D Chambers, O Akanyeti, R Venturelli, J Jezov, J Brown, M Kruusmaa, P Fiorini, and W M Megill. A fish perspective: detecting flow features while moving using an artificial lateral line in steady and unsteady flow. *Journal of the Royal Society Interface*, 11(20140467):1–14, Jul 2014.

[12] J Chen, J Engel, N Chen, S Pandya, S Coombs, and C Liu. Artificial lateral line and hydrodynamic object tracking. *Micro Electro Mechanical Systems, 2006. MEMS 2006 Istanbul. 19th IEEE International Conference on*, pages 694–697, 2006.

[13] N Chen, C Tucker, J M Engel, Y Yang, S Pandya, and C Liu. Design and characterization of artificial haircell sensor for flow sensing with ultrahigh velocity and angular sensitivity. *Journal of Microelectromechanical Systems*, 16(5):999–1013, 2007.

[14] R A Conley and S Coombs. Dipole source localization by mottled sculpin. iii. orientation after site-specifc, unilateral denervation of the lateral line system. *J Comp Physiol A*, 183:335–344, Sep 1998.

[15] S Coombs. Smart skins: Information processing by lateral line flow sensors. *Autonomous Robots*, 11:255–261, 2001.

[16] S Coombs, H Bleckmann, R R Fay, and A N Popper. The lateral line system. *Springer Handobook of Auditory Research*, pages 1–360, Jan 2014.

[17] S Coombs, C B Braun, and B Donovan. The orienting response of lake michigan mottled sculpin is mediated by canal neuromasts. *The Journal of Experimental Biology*, 204:337–348, 2001.

[18] S Coombs and R A Conley. Dipole source localization by mottled sculpin. i. approach strategies. *J Comp Physiol A*, 180:387–399, Mar 1997.

[19] S Coombs and R A Conley. Dipole source localization by the mottled sculpin ii. the role of lateral line excitation patterns. *J Comp Physiol A*, 180:401–415, Mar 1997.

[20] S Coombs, M Hastings, and J Finneran. Modeling and measuring lateral line excitation patterns to changingdipolesourcelocations. *J Comp Physiol A*, 178:359–371, May 1996.

[21] R G Dean and R A Dalrymple. *Water wave mechanics for engineers and scientists*, volume 2 of *Advanced Series of Ocean Engineering*. World Scientific, 1984.

[22] L Devries, F D Lagor, H Lei, X Tan, and D A Paley. Distributed flow estimation and closed-loop control of an underwater vehicle with a multi-modal artificial lateral line. *Bioinspiration & Biomimetics*, 10(2):1–15, Mar 2015.

[23] S Dijkgraaf. Untersuchungen uber die funktion der seitenorgane an fischen. *Zeitschrift fur Vergleichende Physiology*, 20:162–164, 1934.

[24] T Ding, L Wang, and P Wang. Changes in electrical resistance of carbon-black-filled silicone rubber composite during compression. *Journal of Polymer Science: Part B: Polymer Physics*, 45:2700–2706, 2007.

[25] H Droogendijk, A M K Dagamseh, R G P Sanders, D R Yntema, and G J M Krijnen. Characterization of bio-inspired hair flow sensors for oscillatory airflows: techniques to measure the response for both flow and pressure. *Measurement Science and Technology*, 25:095005–095015, Jul 2014.

[26] J Dusek, A G P Kottapalli, M E Woo, M Asadnia, J Miao, J H Lang, and M S Triantafyllou. Development and testing of bio-inspired microelectromechanical pressure sensor arrays for increased situational awareness for marine vehicles. *Smart Materials and Structures*, 22:014002–014015, 2013.

[27] J Dusek and M Triantafyllou. Leading edge vortex detection using bio-inspired on-body pressure sensing. Master's thesis, Massachusetts Institute of Technology, Jan 2011.

[28] J Dusek, M E Woo, J H Lang, and M S Triantafyllou. Carbon black-pdms composite conformal pressure sensor arrays for near-body flow detection. *IEEE Oceans 2014- Taipei*, 2014.

[29] M Van Dyke. *An Album of Fluid Motion.* The Parabolic Press, Stanford, California, 1982.

[30] K Faucher, E Parmentier, C Becco, N Vandewalle, and P Vandewalle. Fish lateral system is required for accurate control of shoaling behaviour. *Animal Behaviour*, 79(3):679–687, Jul 2010.

[31] V Fernandez, J Dusek, J Schulmeister, A Maertens, S Hou, K Srivatsa, J Lang, and M.S Triantafyllou. Pressure sensor arrays to optimize the high speed performance of ocean vehicles. *11th International Conference on Fast Sea Transportation*, pages 1–8, Jul 2011.

[32] V I Fernandez, A Maertens, F M Yaul, J Dahl, J H Lang, and M S Triantafyllou. Lateral-line-inspired sensor arrays for navigation and object identification. *Marine Technology Society Journal*, 45(4):130–146, Jan 2011.

[33] V I Fernandez and M S Triantafyllou. *Performance Analysis for Lateral-Line-Inspired Sensor Arrays.* PhD thesis, Massachusetts Institute of Technology, Oct 2011.

[34] J M P Franosch, S Sosnowski, N K Chami, K K hnlenz, S Hirche, and J L van Hemmen. Biomimetic lateral-line system for underwater vehicles. *IEEE Sensors 2010 Conference*, pages 1–6, Jul 2010.

[35] A Gao and M S Triantafyllou. Bio-inspired pressure sensing for active yaw control of underwater vehicles. *Proceedings of MTS/IEEE Oceans*, 2012.

[36] P Gorner. The importance of the lateral line system for the perception of surface waves in the claw toad, xenopus laevis daudin. *Experientia*, 29:295–296, Sep 1973.

[37] J Goulet, J Engelmann, B P Chagnaud, JM P Franosch, MD Suttner, and JL Van Hemmen. Object localization through the lateral line system of fish: theory and experiment. *J Comp Physiol A*, 194(1):1–17, Jan 2008.

[38] B Gray. Artificial arrays could help submarines make like a fish. *Science*, 313:1382–1383, Sep 2006.

[39] EI-S Hassan. Mathematical description of the stimuli to the lateral line system of fish derived from a three-dimensional flow field analysis: I. the cases of moving in open water and of gliding towards a plane surface. *Biological Cybernetics*, 66:443–452, Jun 1992.

[40] EI-S Hassan. Mathematical description of the stimuli to the lateral line system of fish derived from a three-dimensional flow field analysis: Ii. the case of gliding alongside or above a plane surface. *Biological Cybernetics*, 66:453–461, Jun 1992.

[41] J A Herring. Mechanical and electrical characterization of carbon black-doped closed-cell polydimethylsiloxane (pdms) foam. *Bachelor's Thesis*, pages 1–54, May 2015.

[42] B Hofer. Studien uber die hautsinnesorgane der fische. i. die funktion de sietenorgane be den fischen. *Berichte der koniglichen Bayerischen Biologischen Versuchsstation Munchen*, 1:115–164, 1908.

[43] M J Holmes and S M Teo. Toxic marine dinoflagellates in singapore waters that cause seafood poisonings. *Clinical and Experimental Pharmacology and Physiology*, 29:829–836, Jul 2002.

[44] M Hussain, Y Choa, and K Niihara. Fabrication process and electrical behavior of novel pressure-sensitive composites. *Composites: PartA*, 32:1689–1696, Oct 2001.

[45] J Janssen. Comparison of response distance to prey via the lateral line in the ruffe and yellow perch. *J Fish Biol*, 51:921–930, Oct 1997.

[46] C Jones, E Creed, S Glenn, J Kerfoot, J Kohut, C Mudgal, and O Schofield. Slocum gliders – a component of operational oceanography. Technical report, Webb Research Corporation, Jul 2005.

[47] M G King, A J Baragwanath, M C Rosamond, D Wood, and A J Gallant. Porous pdms force sensitive resistors. *Procedia Chemistry*, 1(1):568–571, Oct 2009.

[48] A Klein and H Bleckmann. Determination of object position, vortex shedding frequency and flow velocity using artificial lateral line canals. *Beilstein J. Nanotechnol.*, 2:276–283, Jun 2011.

[49] M Knite and J Zavickis. *Contemporary Robotics- Challenges and Solutions.* InTech, 2009.

[50] A G P Kottapalli, M Asadnia, J M Miao, G Barbastathis, and M S Triantafyllou. A flexible liquid crystal polymer mems pressure sensor array for fish-like underwater sensing. *Smart Materials and Structures*, 21(11):115030, Oct 2012.

[51] A G P Kottapalli, M Asadnia, J M Miao, and M S Triantafyllou. Biomechanical canal sensors inspired by canal neuromasts for ultrasensitive flow sensing. *MEMS 2015*, pages 500–503, Nov 2015.

[52] A G P Kottapalli, CW Tan, M Olfatnia, JM Miao, G Barbastathis, and M Triantafyllou. A liquid crystal polymer membrane mems sensor for flow rate and flow direction sensing applications. *Journal of Micromechanics and Microengineering*, 21:085006, 2011.

[53] M Kulpa. The lateral line is necessary for blind cavefish rheotaxis in non-uniform flow. Masters of science, Bowling Green State University, Nov 2014.

[54] M Lacasse, V Duchaine, and C Gosselin. Characterization of the electrical resistance of carbon-black-filled silicone: Application to a flexible and stretchable robot skin. *2010 IEEE International Conference on Robotics and Automation*, pages 4842–4848, Jun 2010.

[55] H Lamb. *Hydrodynamics.* Cambridge University Press, 6 edition, 1932.

[56] I Lee and H J Sung. Development of an array of pressure sensors with pvdf film. *Experiments in Fluids*, 26:27–35, Nov 1999.

[57] F Leydig. Ueber organe eines sechsten sinnes. *Nova Acta Academia Curios*, 34(5), 1868.

[58] J C Liao. Neuromuscular control of trout swimming in a vortex street: implications for energy economy during the karman gait. *Journal of Experimental Biology*, 207(20):3495–3506, 2004.

[59] J C Liao. The role of the lateral line and vision on body kinematics and hydrodynamic preference of rainbow trout in turbulent flow. *Journal of Experimental Biology*, 209(20):4077, 2006.

[60] J C Liao, D N Beal, G V Lauder, and M S Triantafyllou. Fish exploiting vortices decrease muscle activity. *Science*, 302(5650):1566–1569, Jul 2003.

[61] H Liu, K Zhong, Y Fu, G Xie, and Q Zhu. Pattern recognition for robotic fish swimming gaits based on artificial lateral line system and subtractive clustering algorithms. *Sensors & Transducers*, 182(11):207–216, Nov 2014.

[62] J C Lotters, W Olthuis, P H Veltink, and P Bergveld. The mechanical properties of the rubber elastic polymer polydimethylsiloxane for sensor applications. *Journal of Micromechanics and Microengineering*, 7:145–147, 1997.

[63] W Luheng, D Tianhuai, and W Peng. Influence of carbon black concentration on piezoresistivity for carbon-black-filled silicone rubber composite. *Carbon*, 47(14):3151–3157, Nov 2009.

[64] A Maertens. Fish swimming optimization and exploiting multi-body hydrodynamic interactions for underwater navigation. *MIT PhD Thesis*, pages 1–161, Dec 2014.

[65] A Maertens and M Triantafyllou. Touch at a distance: underwater object identification using pressure sensors. Master's thesis, Massachusetts Institute of Technology, Jan 2011.

[66] S C B Mannsfeld, B Tee, R M Stoltenberg, C V Chen, S Barman, B V O Muir, A N Sokolov, C Reese, and Z Bao. Highly sensitive flexible pressure sensors with microstructured rubber dielectric layers. *Nature Materials*, 9(10):859–864, Sep 2010.

[67] M E McConney, N Chen, D Lu, H A Hu, S Coombs, C Liu, and V V Tsukruk. Biologically inspired design of hydrogel-capped hair sensors for enhanced underwater flow detection. *Soft Matter*, 5:292–295, Jan 2009.

[68] M J McHenry, K E Feitl, J A Strothr, and W J Van Trump. Larval zebrafish rapidly sense the water flow of a predator's strike. *Biology Letters*, 5:477–479, Mar 2009.

[69] J Montgomery, S Coombs, and C Baker. The mechanosensory lateral line system of the hypogean form of astyanax fasciatus. *Environmental Biology of Fishes*, 62:87–96, Sep 2001.

[70] J C Montgomery, C.F Baker, and A.G Carton. The lateral line can mediate rheotaxis in fish. *Nature*, 389:960–963, Oct 1997.

[71] J N Newman. *Marine Hydrodynamics*. The MIT Press, Cambridge, Ma, 1977.

[72] J O'Neill, J Lu, R Dockter, and T Kowalewski. Practical, stretchable smart skin sensors for contact-aware robots in safe and collaborative interactions. *2015 IEEE International Conference on Robotics and Automation (ICRA)*, pages 1–6, Jun 2015.

[73] S Pandya, Y Yang, D L Jones, J Engel, and C Liu. Multisensor processing algorithms for underwater dipole localization and tracking using mems artificial lateral-line sensors. *EURASIP Journal on Applied Signal Processing*, 2006(1):1–9, Jan 2006.

[74] M Rapo, H Jiang, and M Grosenbaugh. Using computational fluid dynamics to calculate the stimulus to the lateral line of a fish in still water. *J Exp Biol*, Jan 2009.

[75] K. Rapoza. The world's 10 busiest ports. www.Forbes.com, November 2014.

[76] N Ryvkina, I Tchmutin, J Vilcakova, M Peliskova, and P Saha. The deformation behavior of conductivity in composites where charge carrier transport is by tunneling: theoretical modeling and experimental results. *Synthetic Materials*, 148(2):141–146, 2005.

[77] F E Schulze. Uber die sinnesorgane der seitenlinie bei fischen und amphibien. *Archiv fur Mikroskopie un Anatomie*, 6:62–88, 1870.

[78] S E Shumway. A review of the effects of algal blooms on shellfish and aquaculture. *Journal of the World Aquaculture Society*, 21(2):65–104, Feb 1990.

[79] T Someya, Y Kato, T Sekitani, S Iba, Y Noguchi, Y Murase, H Kawaguchi, T Sakurai, and G M Whitesides. Conformable, flexible, large-area networks of pressure and thermal sensors with organic transistor active matrixes. *Proceedings of the National Academy of Sciences of the United States of America*, 102(35):12321–12325, Mar 2005.

[80] T Someya, T Sekitani, S Iba, Y Kato, H Kawaguchi, T Sakurai, and G M Whitesides. A large-area, flexible pressure sensor matrix with organic field-effect transistors for artificial skin applications. *Proceedings of the National Academy of Sciences of the United States of America*, 101(27):9966–9970, Mar 2004.

[81] A H Techet. Mit 13.42 lecture: Vortex induced vibrations. *MIT Open Courseware*, 2005.

[82] C von Campenhausen, I Riess, and R Weissert. Detection of stationary objects by the blind cave fish anoptichthysjordani (characidae)*. *Journal of Comparative Physiology*, 143:369–374, Oct 1981.

[83] M Walter, F Hover, and J Leonard. Slam for autonomous ship hull inspection using exactly sparse extended information filters. *2008 IEEE International Conference on Robotics and Automation*, pages 1–8, Apr 2008.

[84] G D Weymouth and D K P Yue. Conservative volume-of-fluid method for free-surface simulations on cartesian-grids. *Journal of Computational Physics*, 229(8):2853–2865, 2010.

[85] S P Windsor and M J McHenry. The influence of viscous hydrodynamics on the fish lateral-line system. *Integrative and Comparative Biology*, 49(6):691–701, Dec 2009.

[86] S P Windsor, S E Norris, S M Cameron, G D Mallinson, and J C Montgomery. The flow fields involved in hydrodynamic imaging by blind mexican cave fish (astyanax fasciatus). part i: open water and heading towards a wall. *Journal of Experimental Biology*, 213(22):3819–3831, Nov 2010.

[87] S P Windsor, S E Norris, S M Cameron, G D Mallinson, and J C Montgomery. The flow fields involved in hydrodynamic imaging by blind mexican cave fish (astyanax fasciatus). part ii: gliding parallel to a wall. *Journal of Experimental Biology*, 213(22):3832–3842, Nov 2010.

[88] S P Windsor, D Tan, and J C Montgomery. Swimming kinematics and hydrodynamic imaging in the blind mexican cave fish (astyanax fasciatus). *Journal of Experimental Biology*, 211(18):2950–2959, Sep 2008.

[89] M E Woo. Development of a porous piezoresistive material and its applications to underwater pressure sensors and tactile sensors. Master's thesis, Massachusetts Institute of Technology, Jun 2013.

[90] K A Wróbel. Underwater vehicles' applications in offshore industry. *Maritime Transport & Shipping – Marine Navigation and Safety of Sea Transportation*, pages 1–6, May 2013.

[91] Y Yang, J Chen, J Engel, S Pandya, N Chen, C Tucker, S Coombs, D L Jones, and C Liu. Distant touch hydrodynamic imaging with an artificial lateral line. *PNAS*, 103(50):18891–18895, Dec 2006.

[92] Y Yang, A Klein, H Bleckmann, and C Liu. Artificial lateral line canal for hydrodynamic detection. *Appl. Phys. Lett.*, 99(2):023701, Jan 2011.

[93] Y Yang, N Nguyen, N Chen, M Lockwood, C Tucker, H Han, H Bleckmann, C Liu, and D L Jones. Artificial lateral line with biomimetic neuromasts to emulate fish sensing. *Bioinspiration and Biomimetics*, 5:1–10, Mar 2010.

[94] F M Yaul. A flexible underwater pressure sensor array for artificial lateral line applications. Masters of engineering thesis, Massachusetts Institute of Technology, 2011.

[95] F M Yaul, V Bulovic, and J H Lang. A flexible underwater pressure sensor array using a conductive elastomer strain gauge. *Journal or Microelectromechanical Systems*, 21(4):897–907, Jul 2012.